Super-resolution Compressed Sensing for Resolving Time-of-Flight Multipath Interferences

DISSERTATION
zur Erlangung des akademischen Grades

eines Doktor der Ingenieurwissenschaften
(Dr. Ing.)

vorgelegt von
M.Sc. Xuan Vinh Nguyen

eingereicht bei der Naturwissenschaftlich -Technischen Fakultät
der Universität Siegen
Siegen 2018

Gutachter der Dissertation

1.Gutachter: Prof. Dr. Otmar Loffeld, Universität Siegen, Siegen

2.Gutachter: Prof. Dr. Andreas Kolb, Universität Siegen, Siegen

Tag der mündlichen Prüfung: 30.08.2018

Gedruckt auf alterungsbeständigem holz- und säurefreiem Papier.

Acknowledgments

First of all, I would like to thank my supervisor Prof.Dr. Otmar Loffeld for his great support and the good opportunity he gave me to work in his research group. Thanks to him, i gained a lot of advanced knowledge on the compressed sensing techniques and applied them into the development of time-of-flight depth sensing systems.

Besides, i also would like to thank the project "DFG Graduiertenkollegs 1564 - Imaging New Modalities" for their financial support during three years of my PhD research.

Furthermore, i would like to thank to all of my colleagues for their support and company.

A deepest love to my family and all my friends for supporting me.

And finally, the thesis is my special gift for my father who passed away three years ago. He always wished that i would become a good researcher and the things which i have done in this thesis will hopefully make him proud of me.

Thank you

Vinh Nguyen Xuan

Abstract

Nowadays, time-of-flight (TOF) cameras have become more popular in many practical applications, e.g., robot navigation, 3D reconstruction. Typically, they produce depth map of the entire scene through a low-cost and high-frame-rate system. Nevertheless, there exist many TOF problems, e.g., linearity errors, ambiguity range, multipath interferences (MPIs). Especially, MPIs which are usually caused by transparent object imaging or broaden illumination influence negatively on depth reconstruction results of the traditional phase-stepping method. For this reason, this thesis aims to resolve the MPI problem by carrying out multiple-frequency TOF (MFT) acquisition. According to the compressed sensing (CS) theory, since the amount of MPIs in real-life scenes is small, only a few MFT measurements are required to estimate the sparse time profile of the MPIs. However, this CS-MFT model suffers from hardware design limitation. To be concrete, under the Rayleigh resolution theorem, the low-frequency modulation of a commercial TOF camera leads to poor depth accuracy and low range resolution of the CS-MFT model. Whereas, increasing the modulation frequency is a significantly complicated task. Thus, our solution approach is to construct a super-resolution CS-MFT model with a large refinement factor. From this model, super-resolution CS techniques can reduce mismatch model errors but simultaneously cause poor sparse reconstruction performance with a highly coherent sensing matrix. This thesis introduces a variety of CS techniques to improve these reconstruction results as well as to maintain high-processing speed. They include exploring new CS reconstruction algorithms and optimizing the super-resolution CS-MFT sensing matrix structure. Besides, an alternative relaxed metric with a tolerance offset is introduced for gauging the quality of spike recovery in a more accurate way. The results achieved through numerical and practical experiments show a significant improvement in accuracy and resolution of the MPI time profile reconstruction.

Keywords: Compressed sensing, time-of-flight, multipath interferences, super-resolution, reconstruction algorithm.

Zusammenfassung

Heutzutage ist die Time-of-flight-Kamera (TOF-Kamera) in vielen praktischen Anwendungen sehr populär geworden, z.B., bei der Roboternavigation oder der 3D-Rekonstruktion. Sie erzeugt ein Tiefenbild der gesamten Szene ohne einen aufwendigen Scanvorgang. Daher sind die meisten der kommerziell erhältlichen TOF-Kameras kostengünstige Systeme, die mit der heute üblichen Videorate arbeiten. Dennoch gibt es weiterhin viele TOF-spezifische Probleme, wie z.B. Linearitätsfehler, Mehrdeutigkeitsbereiche und Mehrwegsinterferenzen (MPIs). Insbesondere MPIs, die durch eine transparente Objektabbildung oder eine überlappende Beleuchtung verursacht werden können, beeinflussen die Tiefenrekonstruktionsergebnisse des herkömmlichen Phasenschrittverfahrens negativ. Aus diesem Grund zielt diese Arbeit darauf ab, das MPI-Problem zu lösen, indem Mehrfrequenz-TOF (MFT)-Messungen durchgeführt werden. Unter der Annahmen, dass die Anzahl der MPIs in realen Szenen gering ist, sind gemäßder Theorie der komprimierten Erfassung (Compressed Sensing, CS) nur wenige MFT-Messungen erforderlich, um das dünnbesetztes Zeitprofil der MPIs abzuschätzen. Ein solches CS-MFT-Modell leidet jedoch unter Hardwarebeschränkungen. Konkret führt die Modulation bei den niedrigen Frequenzen einer kommerziellen TOF-Kamera unter dem Rayleigh-Auflösungssatz zu einer schlechten Tiefengenauigkeit und niedrigen Bereichsauflösung bei Anwendung des CS-MFT-Modells. Die nötige Erhöhung der Modulationsfrequenz ist dagegen nicht einfach möglich und ist meist nicht realisierbar. Unser Lösungsansatz besteht daher darin, das CS-MFT-Modell durch Superresolution-Techniken mit hohen Verfeinerungsfaktoren zu verbessern. Diese Superresolution-CS-Technik kann Fehlanpassungen des Modellsreduzieren, liefert aber gleichzeitig aufgrund der im hohen Maße kohärenten Messmatrix eine sehr schlechte Rekonstruktion. Wir schlagen in dieser Arbeit einige CS-Techniken vor, um diese Rekonstruktionsergebnisse zu verbessern und trotzdem eine hohe Verarbeitungsgeschwindigkeit beizubehalten. Sie umfassen die Erforschung neuer CS-Rekonstruktionsalgorithmen und die Optimierung des Designs der Superresolution-CS-MFT-Messmatrix. Außerdem wird eine alternative Metrik mit einem Toleranzausgleich eingeführt, um die Qualität der Rekonstruktion besonders bei heterogenen Szenen (Absätze, Sprünge) zu verbessern. Die erzielten Ergebnisse, die durch numerische und praktische Experimente demonstriert wurden, zeigen eine signifikante Verbesserung der Genauigkeit und Auflösung der MPI-Zeitprofilrekonstruktion.

Schlagwörter: Compressed Sensing, Time-of-flight, Mehrweginterfrenzen, Super-Resolution, Rekonstruktion-Methode.

List of publications

1. **Xuan. V. N.**, Weihs. W, and Loffeld. O
   Illumination, Phase Step Optimization and Improvements in Simultaneous Multiple Frequency Measurement for Time-of-Flight Sensors
   In 2015 International Conference on 3D Imaging (IC3D), pages 1–6.

2. **Xuan. V. N.**, Hartmann. K, Weihs. W, and Loffeld. O
   Multi-target Super-resolution using Compressive Sensing Arguments for Multipath Interference Recovery
   In 2016 4th International Workshop on Compressed Sensing Theory and its Applications to Radar, Sonar and Remote Sensing (CoSeRa), pages 148–152.

3. **Xuan. V. N.**, Hartmann. K, Weihs. W, and Loffeld. O
   Combined based on Minimum Distance Orthogonal Matching Pursuit Method for Support Recovery Improvement in Super-Resolution Compressed Sensing
   In 2016 4th International Workshop on Compressed Sensing Theory and its Applications to Radar, Sonar and Remote Sensing (CoSeRa), pages 257–261.

4. **Xuan. V. N.**, Hartmann. K, Weihs. W, and Loffeld. O
   Modified Orthogonal Matching Pursuit for Multiple Measurement Vector with Joint Sparsity in Super-resolution Compressed Sensing
   In 2017 51st Asilomar Conference on Signals, Systems, and Computers, Pacific Grove, CA, 2017, pp. 840-844..

Contents

Abstract iv

Zussamenfassung v

List of figures viii

List of tables ix

List of abbreviations x

1 Introduction 1
- 1.1 Time-of-flight imaging camera and multipath interference problem 1
- 1.2 Multi-frequency TOF acquisition using CS 3
  - 1.2.1 Super-resolution CS techniques 4
  - 1.2.2 Motivation and key contribution 5
- 1.3 Outline 5

2 Time-of-flight principle 9
- 2.1 Pulsed modulation 9
- 2.2 Continuous wave modulation 11
  - 2.2.1 Basic principles 11
  - 2.2.2 TOF measurement accuracy and precision 13
- 2.3 Main hardware components 13
- 2.4 State-of-art TOF problems and solutions 14
  - 2.4.1 Measurement linearity error 14
  - 2.4.2 Photon shot noise 16
  - 2.4.3 Saturation 17
  - 2.4.4 Ambiguity range 17
  - 2.4.5 Multipath interferences 18
- 2.5 Summary 19

3 Compressed sensing and TOF multipath problem 21
- 3.1 Compressed sensing (CS) and sparse recovery 22
  - 3.1.1 l_1 minimization or basis pursuit 23

3.1.2 Greedy pursuit . . . 26
3.2 Sparse time profile of TOF multipath problem . . . 27
3.2.1 Single modulation-frequency measurement . . . 27
3.2.2 Discretization of time profile . . . 29
3.3 Multiple frequency TOF (MFT) measurements . . . 30
3.3.1 Mismatch model errors . . . 32
3.3.2 Depth resolution of target discrimination . . . 33
3.3.3 TOF modulation frequency limitation problem . . . 34
3.4 Super-resolution MFT compressed sensing . . . 34
3.4.1 Preliminary . . . 35
3.4.2 High coherence of super-resolution sensing matrix . . . 37
3.4.3 Minimum distance . . . 41
3.4.4 Relaxed sparse support evaluation . . . 41
3.4.5 Numerical analysis . . . 43
3.5 Summary . . . 50

4 Super-resolution compressed sensing methods 51
4.1 Band exclusion and local optimization . . . 51
4.1.1 Band exclusion . . . 51
4.1.2 Local optimization . . . 53
4.1.3 BLOOMP . . . 54
4.2 Modified cyclic orthogonal matching pursuit -OMP3 . . . 56
4.2.1 Global optimization . . . 56
4.2.2 Modified cyclic OMP - OMP3 . . . 57
4.2.3 Combination between OMP3 and LO technique . . . 59
4.3 Non-negative least squares optimization - POMP . . . 59
4.3.1 Non-negative constraints . . . 59
4.3.2 Negative atom removal module . . . 59
4.3.3 Advantages and disadvantages . . . 60
4.4 Non-negative magnitude adjustment orthogonal matching pursuit . . . 61
4.4.1 Basic idea . . . 61
4.4.2 Non-negative magnitude adjustment orthogonal matching pursuit - Ma-OMP . . . 61
4.4.3 Modified non-negative magnitude adjustment orthogonal matching pursuit - Ma-OMP3 . . . 62
4.4.4 Optimized adjustment factor . . . 63
4.5 Numerical results . . . 63
4.5.1 Preliminaries . . . 63
4.5.2 Optimized adjustment factor of Ma-OMP3 . . . 64
4.5.3 Comparison between different methods . . . 66
4.5.4 Considered parameters . . . 69

4.6 Combined OMP based on predicted minimum distance - CMD-OMP . . . 74
4.6.1 Basic idea . . . 74
4.6.2 Tuning parameter estimation . . . 76
4.6.3 Minimum distance prediction . . . 77
4.6.4 Numerical results . . . 78
4.7 Summary . . . 82

5 Multi-frequency selection optimization 83
5.1 Frequency selection optimization . . . 83
5.1.1 Cyclic difference set . . . 83
5.1.2 DFT sensing matrix . . . 84
5.1.3 Proposed optimization method . . . 88
5.2 Frequency and initial phase-offset optimization . . . 92
5.3 Numerical results . . . 94
5.3.1 CDS selection and the proposed frequency optimization method . 94
5.3.2 Free parameter settings . . . 100
5.4 Summary . . . 103

6 Multiple measurement vector in super-resolution compressed sensing 105
6.1 Multipolarization TOF signal model . . . 105
6.1.1 Polarized light . . . 105
6.1.2 Multiple polarization . . . 106
6.2 Multiple measurement vector (MMV) model . . . 106
6.3 Conventional OMPMMV . . . 107
6.3.1 Basic principle . . . 107
6.3.2 Recovery guarantee . . . 108
6.4 Modified variants of greedy pursuits for MMV model . . . 108
6.4.1 Modified OMPMMV . . . 108
6.4.2 Modified global optimization - GO-MMV . . . 110
6.4.3 Cyclic orthogonal matching pursuit for MMV model - OMP3-MMV 110
6.4.4 Cyclic magnitude adjustment orthogonal matching pursuit for MMV model - Ma-OMP3-MMV . . . 112
6.4.5 POMP for MMV model . . . 113
6.5 Numerical results . . . 113
6.5.1 Comparison between OMPMMV variants . . . 114
6.5.2 Comparison between OMP3-MMV variants . . . 115
6.5.3 Comparison between Ma-OMP3-MMV variants . . . 117
6.5.4 Comparison between MMVs and SMV . . . 118
6.5.5 Number of MMVs . . . 123
6.6 Summary . . . 124

7 Simultaneous multiple frequency acquisition **127**
7.1 Projection matrix model . . . 128
7.1.1 Dictionary matrix . . . 128
7.1.2 MFT sensing matrix . . . 128
7.1.3 Multiple-SMF sensing matrix . . . 128
7.2 Projection matrix optimization in SMF acquisition . . . 130
7.2.1 Projection matrix optimization method . . . 130
7.2.2 Modified projection matrix modification . . . 131
7.2.3 SMF model parameters . . . 133
7.3 Numerical results . . . 134
7.3.1 Coherence histogram . . . 136
7.3.2 Support recovery performance . . . 136
7.3.3 Multiple-SMF acquisition using MMV techniques . . . 145
7.3.4 Relaxed super-resolution problem . . . 146
7.3.5 Summary . . . 147
7.4 Joint multiple frequency calibration . . . 147
7.4.1 Numerical results . . . 148
7.4.2 Summary . . . 150

8 Experimental results **153**
8.1 PMD Multicam System and measurement matrix formulation . . . 153
8.1.1 PMD Multicam System . . . 154
8.1.2 Dictionary matrix formulation . . . 154
8.2 Transparent object imaging . . . 155
8.3 Comparison of various reconstruction methods . . . 159
8.3.1 POMP and OMP3 . . . 159
8.3.2 BPIC . . . 168
8.3.3 Ma-OMP3 . . . 169
8.3.4 Supportive affects of LO techniques . . . 169
8.3.5 Summary . . . 171
8.4 CMD-OMP . . . 171
8.5 Frequency and phase-offset selection optimization . . . 172
8.6 SMF and joint multiple-frequency calibration . . . 175
8.7 Summary . . . 179

9 Conclusion **181**
9.1 Super-resolution compressed sensing algorithms . . . 181
9.2 Super-resolution MFT sensing matrix design . . . 182
9.3 Relaxed super-resolution factor . . . 183

A Appendix **184**
A.1 Derivative of $\mathrm{E}(f_i)$ w.r.t. f_i 184
A.1.1 Computation of $\Delta u_{i,q_1,q_2}$ 185
A.1.2 Computation of $\Delta v_{i,q_1,q_2}$ 185
A.2 Derivative of $\mathrm{E}(\tau_i)$ w.r.t. τ_i 186

Bibliography **187**

List of Figures

1.1 The operating principle of a CW-TOF camera 2
1.2 Different cases of MPIs in a TOF imaging camera 3

2.1 Overview pictures of many commercial TOF cameras 10
2.2 Pulsed-light TOF modulation and demodulation 10
2.3 Continuous-sinusoidal-wave modulation and demodulation scheme through fast sampling 11
2.4 Continuous-squared-wave modulation and demodulation schemes through window sampling 14
2.5 RMS linearity error: three-phase (green), four-phase(blue), five-phase(red) with different duty cycles from 10% to 50% 16

3.1 Schematic diagram of the MFT measurements for the reconstruction of two multipath interferences using CS model 31
3.2 A visual example of mismatch model errors before and after the grid system refinement 32
3.3 Resized Gram matrix or coherence pattern of two real-valued sensing matrices with two different refinement factors F 39
3.4 Mean mutual coherence value of 200 sensing matrix trials for different kinds of MFT acquisitions at different refinement factors F from 1 to 100 40
3.5 Relaxed sparse support recovery rates ($\delta = 2$) of OMP and BP for two MFT sensing matrices with two different refinement factors F in the SNR domain (1000 trials for each SNR case) 44
3.6 Relaxed sparse support recovery rates ($\delta = 2$) of OMP and BP for different types of MFT sensing matrices with a large refinement factor $F = 100$ in the SNR domain (1000 trials for each SNR case) 46
3.7 Relaxed support recovery rates ($\delta = 2$) of BP and OMP using a real-valued MFT acquisition at different MDs (500 trials for each MD). Choose $N = 500, M = 20, L = 5, f_{max} = 30$ MHz, $F = 100, K = 3$ 48

4.1 Mutual coherence versus the band radius for different types of MFT sensing matrices at $F = 100, N = 500$ 53

4.2 Relaxed support recovery rates ($\delta = 2$) of OMP and BLOOMP (band radius =40 and $\Delta_{LO} = 20$) for four sensing matrices with a large refinement factor $F = 100$ at various SNRs (1000 trials for each SNR). Choose f_{max} = 30 MHz, $K = 3$, $\Delta T > 40\Delta r$ (bins) 55
4.3 Relaxed support recovery rates ($\delta = 2$) of OMP and different variants of BLOOMP (different settings of band radius and LO range) for a real-valued MFT sensing matrix $\Phi \in \mathbb{R}^{20\times500}$ with the large refinement factor F=100 at various SNRs (1000 trials for each SNR). Choose $N = 500$, $L = 5$, $f_{max} = 30$ MHz, $K = 3, \Delta T > 4\Delta r$ (bins) 56
4.4 Comparison between support recovery performance of different Ma-OMP3 variants with different values of ρ for the real sensing matrix $\Phi^{20\times500}$ at different SNRs (3000 trials for each SNR). Choose $N = 500, L = 5, f_{max}$ = 30 MHz, $F = 100, K = 3$, $\Delta r = 5$ cm. 64
4.4 Comparison between support recovery performance of different Ma-OMP3 variants with different values of ρ for the real sensing matrix $\Phi^{20\times500}$ at different SNRs (3000 trials for each SNR). Choose $N = 500, L = 5, f_{max}$ = 30 MHz, $F = 100, K = 3$, $\Delta r = 5$ cm (cont). 65
4.5 Comparison between support recovery performance of different Ma-OMP3 variants with different values of ρ for the real sensing matrix $\Phi^{20\times500}$ at different MDs (500 trials for each MD). Choose $N = 500, L = 5, f_{max} =$ 30 MHz, $F = 100, K = 3$, $\Delta r = 5$ cm. 65
4.5 Comparison between support recovery performance of different Ma-OMP3 variants with different values of ρ for the real sensing matrix $\Phi^{20\times500}$ at different MDs (500 trials for each MD). Choose $N = 500, L = 5, f_{max} =$ 30 MHz, $F = 100, K = 3$, $\Delta r = 5$ cm (cont). 66
4.6 Comparison between support recovery performance of different methods for the real sensing matrix $\Phi^{20\times500}$ at different SNRs (3000 trials for each SNR). Choose $N = 500, L = 5, f_{max} = 30$ MHz, $F = 100, K = 3$, $\Delta r = 5$ cm 67
4.7 Comparison between support recovery performance of different methods for the real sensing matrix $\Phi^{20\times500}$ at different MDs (500 trials for each MD). Choose $N = 500, L = 5, f_{max} = 30$ MHz, $F = 100, K = 3$, $\Delta r = 5$ cm 68
4.8 Comparison between support recovery performance of different real sensing matrices $\Phi^{20\times500}$, $\Phi^{40\times500}$ and $\Phi^{60\times500}$ at different MDs (500 trials for each MD). Choose $L = 5, f_{max} = 30$ MHz, $F = 100, K = 3$, $\Delta r = 5$ cm. . 70
4.8 Comparison between support recovery performance of different real sensing matrices $\Phi^{20\times500}$, $\Phi^{40\times500}$ and $\Phi^{60\times500}$ at different MDs (500 trials for each MD). Choose $L = 5, f_{max} = 30$ MHz, $F = 100, K = 3$, $\Delta r = 5$ cm (cont). 71

4.9 Comparison between support recovery performance for the cases of two different DRs at different MDs (500 trials for each MD). Choose $N = 500$, $M = 20$, $L = 5$, $f_{max} = 30$ MHz, $F = 100$, $K = 3$, $\Delta r = 5$ cm. 72
4.10 Comparison between support recovery performance for different sparsity K at different MDs (500 trials for each MD). Choose $N = 1200$, $M = 40$, $L = 5$, $f_{max} = 30$ MHz, $F = 100$, $\Delta r = 5$ cm. 73
4.10 Comparison between support recovery performance for different sparsity K at different MDs (500 trials for each MD). Choose $N = 1200$, $M = 40$, $L = 5$, $f_{max} = 30$ MHz, $F = 100$, $\Delta r = 5$ cm (cont). 74
4.11 3D representation of the relaxed support recovery performance ($\delta = 2$) of OMP3, POMP and Ma-OMP3 at different MDs and SNRs (500 trials for each pair of SNR and MD). Choose $N = 500, M = 20, L = 5, f_{max} = 30$ MHz, $F = 100, K = 3$, $\Delta r = 5$ cm 75
4.12 Comparison rate of the selection results using different settings (F_0,ΔT_{tuning}) at different MD cases. Choose $N = 500$, $L = 5$, $M = 20$, $f_{max} = 30$ MHz, $F = 100, \Delta r = 5$ cm 78
4.13 Relaxed support recovery performance ($\delta = 2$) of CMD-OMP using different settings (F_0,ΔT_{tuning}) at different SNRs (3000 trials for each SNR). Choose $N = 500, L = 5, M = 20, f_{max} = 30$ MHz, $F = 100, \Delta r = 5$ cm . . 79
4.14 Relaxed support recovery performance ($\delta = 2$) of CMD-OMP using different settings (F_0,ΔT_{tuning}) at different MDs (500 trials for each MD). Choose N=500, L=5, M=20, $f_{max} = 30$ MHz and F=100 80

5.1 Coherence histograms of DFT and MFT sensing matrices structured by a CDS of frequencies in the conventional ($F = 1$) and super-resolution ($F = 100$) configurations. 86
5.2 Coherence histogram of the sensing matrices structured by the CDS (31,15,7) and our proposed frequency selection optimization method. Choose $M = 15$, $F = 100$, $f_{max} = 31$ MHz 95
5.3 Relaxed support recovery rates ($\delta = 2$) at different SNRs (3000 trials for each SNR) for the CDS (31,15,7) and the proposed frequency optimization method with a large range of interest configuration. Choose $N = 1500, L = 5, M = 15, F = 100, K = 3$, $f_{max} = 31$ MHz 96
5.4 Relaxed support recovery rates ($\delta = 2$) at different MDs (500 trials for each MD) for the CDS (31,15,7) and the proposed frequency optimization method with a large range of interest configuration. Choose $N = 1500, L = 5, M = 15, F = 100, K = 3$, $f_{max} = 31$ MHz 97
5.5 Relaxed support recovery rates ($\delta = 2$) at different SNRs (3000 trials for each SNR) for the CDS (31,15,7) and the proposed frequency optimization method with a short range of interest configuration. Choose $N = 750$, $L = 5$, $M = 15$, $F = 100$, $K = 3$, $f_{max} = 31$ MHz 98

5.6 Relaxed support recovery rates ($\delta = 2$) at different MDs (500 trials for each MD) for the CDS (31,15,7) and the proposed frequency optimization method with a short range of interest configuration. Choose $N = 750, L = 5, M = 15, F = 100, K = 3$, $f_{max} = 31$ MHz 99
5.7 Coherence histogram of the MFT sensing matrices structured by a random selection and the proposed methods. Choose $N = 500$, $L = 5$, $M = 20$, $F = 100$, $f_{max} = 30$ MHz. 100
5.8 Relaxed support recovery rates ($\delta = 2$) at different SNRs (3000 trials for each SNR) for a random selection and the proposed optimization method. Choose $N = 500, L = 5, M = 20, F = 100, \Delta r = 5$cm, $K = 3$. 101
5.9 Relaxed support recovery rates ($\delta = 2$) at different MDs (500 trials for each MD) for a random selection and the proposed optimization method. Choose $N = 500, L = 5, M = 20, F = 100, \Delta r = 5$cm, $K = 3$. 102

6.1 Comparison between the relaxed support recovery performances of Modified OMPMMV and the conventional variants of OMPMMV in the cases of different SNRs (3000 trials for each SNR). Choose $N = 500$, $L = 5$, $M = 20$, $Q = 3$, $f_{max} = 30$ MHz, $F = 100$, $K = 3$, $\Delta r = 5$ cm for a super-resolution MMV-MFT acquisition. 115
6.2 Comparison between the relaxed support recovery performances of Modified OMPMMV and the conventional variants of OMPMMV in the cases of different MDs (500 trials for each MD). Choose $N = 500$, $L = 5$, $M = 20$, $Q = 3$, $f_{max} = 30$ MHz, $F = 100$, $K = 3$, $\Delta r = 5$ cm for a super-resolution MMV-MFT acquisition. 116
6.3 Comparison between the relaxed support recovery performances of our proposed OMP3-MMV and the other variants of OMP3-MMV in the cases of different SNRs (3000 trials for each SNR). Choose $N = 500$, $L = 5$, $M = 20$, $Q = 3$, $f_{max} = 30$ MHz, $F = 100$, $K = 3$, $\Delta r = 5$ cm for a super-resolution MMV-MFT acquisition. 117
6.4 Comparison between the relaxed support recovery performances of our proposed OMP3-MMV and the other variants of OMP3-MMV in the cases of different MDs (500 trials for each MD). Choose $N = 500$, $L = 5$, $M = 20$, $Q = 3$, $f_{max} = 30$ MHz, $F = 100$, $K = 3$, $\Delta r = 5$ cm for a super-resolution MMV-MFT acquisition. 118
6.5 Comparison between the relaxed support recovery performances of many variants of Ma-OMP3-MMV in the cases of different SNRs (3000 trials for each SNR). Choose $N = 500$, $L = 5$, $M = 20$, $Q = 3$, $f_{max} = 30$ MHz, $F = 100$, $K = 3$, $\Delta r = 5$ cm for a super-resolution MMV-MFT acquisition. 119

6.6 Comparison between the relaxed support recovery performances of many variants of Ma-OMP3-MMV in the cases of different MDs (500 trials for each MD). Choose $N = 500$, $L = 5$, $M = 20$, $Q = 3$, $f_{max} = 30$ MHz, $F = 100$, $K = 3$, $\Delta r = 5$ cm for a super-resolution MMV-MFT acquisition. 119
6.6 Comparison between the relaxed support recovery performances of Ma-OMP3-MMV and the other variants of Ma-OMP3-MMV in the cases of different MDs (500 trials for each MD). Choose $N = 500$, $L = 5$, $M = 20$, $Q = 3$, $f_{max} = 30$ MHz, $F = 100$, $K = 3$, $\Delta r = 5$ cm for a super-resolution MMV-MFT acquisition (cont). 120
6.7 Comparison between the relaxed support recovery performances ($\delta = 2$) in MMV model and SMV model in the cases of different SNRs (3000 trials for each SNR). Choose $N = 500$, $L = 5$, $M = 20$, $Q = 3$, $f_{max} = 30$ MHz, $F = 100$, $K = 3$, $\Delta r = 5$ cm for the construction of MMV and SMV models. 121
6.8 Comparison between the relaxed support recovery performances ($\delta = 2$) in MMV model and SMV model in the cases of different MDs (500 trials for each MD). Choose $N = 500$, $L = 5$, $M = 20$, $Q = 3$, $f_{max} = 30$ MHz, $F = 100$, $K = 3$, $\Delta r = 5$ cm for the construction of MMV and SMV models. 122
6.9 Comparison between the relaxed support recovery performances ($\delta = 2$) in two MMV models with different settings of Q in the case of different SNRs (3000 trials for each SNR). Choose $N = 500$, $L = 5$, $M = 20$, $f_{max} = 30$ MHz, $F = 100$, $K = 3$, $\Delta r = 5$ cm for the construction of MMV models 123
6.10 Comparison between the relaxed support recovery performances ($\delta = 2$) in two MMV models with different settings of Q in the cases of different MDs (500 trials for each MD). Choose $N = 500$, $L = 5$, $M = 20$, $f_{max} = 30$ MHz, $F = 100$, $K = 3$, $\Delta r = 5$ cm for the construction of MMV models 124
6.10 Comparison between the relaxed support recovery performances ($\delta = 2$) in two MMV models with different settings of Q in the cases of different MDs (500 trials for each MD). Choose $N = 500$, $L = 5$, $M = 20$, $f_{max} = 30$ MHz, $F = 100$, $K = 3$, $\Delta r = 5$ cm for the construction of MMV models (cont) 125

7.1 Single-frequency and simultaneous multi-frequency MFT acquisition . . . 129
7.2 Coherence histogram of various SMF measurement matrices 136
7.3 Comparison between the relaxed support recovery performances ($\delta = 2$ bins) of multiple-SMF acquisition and MFT acquisition at different SNRs (3000 trials for each SNR). Choose $N = 500$, $L = 5$, $f_{max} = 30$ MHz, $F = 100$, $\Delta r = 5$ cm, $K = 3$. 137

7.3 Comparison between the relaxed support recovery performances ($\delta = 2$ bins) of multiple-SMF acquisition and MFT acquisition at different SNRs (3000 trials for each SNR). Choose $N = 500$, $L = 5$, $f_{max} = 30$ MHz, $F = 100$, $\Delta r = 5$ cm, $K = 3$ (cont). 138
7.4 Comparison between the relaxed support recovery performances ($\delta = 2$ bins) of multiple-SMF acquisition and MFT acquisition at different MDs (500 trials for each MD) in the case of SNR = 15dB. Choose $N = 500$, $L = 5$, $f_{max} = 30$ MHz, $F = 100$, $\Delta r = 5$ cm, $K = 3$. 138
7.4 Comparison between the relaxed support recovery performances ($\delta = 2$ bins) of multiple-SMF acquisition and MFT acquisition at different MDs (500 trials for each MD) in the case of SNR = 15dB. Choose $N = 500$, $L = 5$, $f_{max} = 30$ MHz, $F = 100$, $\Delta r = 5$ cm, $K = 3$ (cont). 139
7.5 Comparison between relaxed support recovery performances ($\delta = 2$ bins) of multiple-SMF acquisition and MFT acquisition at different MDs (500 trials for each MD) in the case of SNR = 30dB. Choose $N = 500$, $L = 5$, $f_{max} = 30$ MHz, $F = 100$, $\Delta r = 5$ cm, $K = 3$. 139
7.5 Comparison between relaxed support recovery performances ($\delta = 2$ bins) of multiple-SMF acquisition and MFT acquisition at different MDs (500 trials for each MD) in the case of SNR = 30dB. Choose $N = 500$, $L = 5$, $f_{max} = 30$ MHz, $F = 100$, $\Delta r = 5$ cm, $K = 3$ (cont). 140
7.6 Comparison between the relaxed support recovery performances ($\delta = 2$ bins) of different reconstruction methods for the multiple-SMF model at different SNRs (3000 trials for each SNR). Choose $N = 500$, $L = 5$, $f_{max} = 30$ MHz, $F = 100$, $\Delta r = 5$ cm, $K = 3$. 142
7.7 Comparison between the relaxed support recovery performances ($\delta = 2$ bins) of different reconstruction methods for the multiple SMF model at different MDs (500 trials for each MD). Choose $N = 500$, $L = 5$, $f_{max} = 30$ MHz, $F = 100$, $\Delta r = 5$ cm, $K = 3$. 143
7.8 Tuning border image of the relaxed support recovery rates ($\delta = 2$) between POMP and OMP3 for the multiple SMF model in the super-resolution configuration. Choose $N = 500$, $L = 5$, $f_{max} = 30$ MHz, $F = 100$, $\Delta r = 5$ cm, $K = 3$. 144
7.9 Relaxed support recovery performances ($\delta = 2$) for a MMV-SMF model (Q=3) at different MDs (500 trials for each MD) with SNR= 20dB. Choose $N = 500$, $L = 5$, $f_{max} = 30$ MHz, $F = 100$, $\Delta r = 5$ cm, $K = 2$, $h = 5$, $M = 20$. 146
7.10 Relaxed support recovery performances ($\delta = 2$) of OMP3 and POMP after joint multiple-frequency calibration with different projection matrices at different SNRs (3000 trials for each SNR). Choose $N = 500$, $L = 5$, $f_{max} = 30$ MHz, $F = 100$, $\Delta r = 5$ cm, $K = 3$. 149

7.11 Relaxed support recovery performances ($\delta = 2$) of OMP3 and POMP after joint multiple-frequency calibration with different projection matrices at different MDs (500 trials for each MD) with SNR=30 dB. Choose $N = 500$, $L = 5$, $f_{max} = 30$ MHz, $F = 100$, $\Delta r = 5$ cm, $K = 3$. 150

8.1 Multicam System 153
8.2 Transparent object imaging with two reflecting components from a transparent bottle and a wall. 156
8.3 The recovered depth images of the transparent bottle using different recovery methods (traditional four-phase method, OMP3, POMP, CMD-OMP) and different super-resolution MFT models (random frequency selection Γ_0, frequency selection optimization Γ_1, frequency and phase-offset selection optimization Γ_2) at a small MD $\Delta T = 54\Delta r$ in scenario E1. 162
8.4 Histogram of the reconstructed support results into the transparent bottle region of different recovery methods (traditional four-phase method, OMP3, POMP, CMD-OMP) using different super-resolution MFT models (random frequency selection Γ_0, frequency selection optimization Γ_1, frequency and phase-offset selection optimization Γ_2) at a small MD $\Delta T = 54\Delta r$ in scenario E1. 163
8.5 The recovered depth images of the transparent bottle using different recovery methods (traditional four-phase method, OMP3, POMP, CMD-OMP) and different super-resolution MFT models (random frequency selection Γ_0, frequency selection optimization Γ_1, frequency and phase-offset selection optimization Γ_2) at a medium MD $\Delta T = 73\Delta r$ in scenario E4. 164
8.6 Histogram of the reconstructed support results into the transparent bottle region of different recovery methods (traditional four-phase method, OMP3, POMP, CMD-OMP) using different super-resolution MFT models (random frequency selection Γ_0, frequency selection optimization Γ_1, frequency and phase-offset selection optimization Γ_2) at a medium MD $\Delta T = 73\Delta r$ in scenario E4. 165
8.7 The recovered depth images of the transparent bottle using different recovery methods (traditional four-phase method, OMP3, POMP, CMD-OMP) and different super-resolution MFT models (random frequency selection Γ_0, frequency selection optimization Γ_1, frequency and phase-offset selection optimization Γ_2) at a large MD $\Delta T = 90\Delta r$ in scenario E8. 166
8.8 Histogram of the reconstructed support results into the transparent bottle region of different recovery methods (traditional four-phase method, OMP3, POMP, CMD-OMP) using different super-resolution MFT models (random frequency selection Γ_0, frequency selection optimization Γ_1, frequency and phase-offset selection optimization Γ_2) at a large MD $\Delta T = 90\Delta r$ in scenario E8. 167

8.9 Joint multiple frequency calibration: the recovered depth images of transparent bottle using OMP3 in scenario B1. 178
8.10 The joint multiple frequency calibration: the histogram of reconstruction results using OMP3 in scenario B1. 178
8.10 The joint multiple frequency calibration: the histogram of reconstruction results using OMP3 in scenario B1 (cont). 179

List of Tables

2.1 Harmonics being suppressed by various phase-stepping algorithms 15
2.2 Optimized duty cycles of an emitted rectangular waveform signal for various phase stepping algorithms 17

4.1 Average run time of different recovery methods in 3000 trials for each 3-MPI reconstruction of one pixel (N =500, M=20, $f_{max} = 30$, F=100) . . 81

7.1 Different SMF measurement matrices with different parameter settings . . 135

8.1 Nine scenarios E1-E9 with different MDs, 1 bin = $\Delta r = 5$ cm 158
8.2 Numerical count n for the comparison between OMP3 and POMP in nine scenarios E1-E9 160
8.3 Numerical count n of BPIC in nine scenarios E1-E9 169
8.4 Numerical count n of Ma-OMP3 in nine scenarios E1-E9 170
8.5 Numerical count n of OMP3 and POMP with the support of LO technique in nine scenarios E1-E9 170
8.6 Numerical count n of CMD-OMP variants with different settings 172
8.7 Numerical count n of OMP3 and POMP using the frequency or phase-offset optimization. 174
8.8 SMF model : five scenarios with different MDs, $f_{max} = 15$ MHz, F=100, $\Delta r = 10$ cm 176
8.9 The count n of POMP with different settings of joint multiple-frequency calibration 176
8.10 The count n of OMP3 with different settings of joint multiple-frequency calibration 177

List of abbreviations

TOF Time of flight.

LIDAR Light Detection and Ranging.

PMD Photo Mixer Device.

CMOS Complementary metal-oxide-semiconductor.

CCD Charge-coupled device.

TI Texas Instrument

AMCW Amplitude modulated continuous wave.

IR Infrared-red.

MPI Multipath interference.

LED Light-emitting diode.

CS Compressed sensing.

MFT Multiple different frequency TOF acquisition.

BP Basis Pursuit.

BPIC Basis Pursuit Inequality Constraint.

OMP Orthogonal Matching Pursuit.

OMPMMV Orthogonal Matching Pursuit for MMV model.

OMP3 Modified Cyclic Orthogonal Matching Pursuit.

Ma-OMP Non-Negative Magnitude Adjustment Orthogonal Matching Pursuit.

Ma-OMP3 Modified Cyclic Non-Negative Magnitude Adjustment Orthogonal Matching Pursuit.

POMP Non-Negative Least Square Optimization.

CMD-OMP Combined based on Minimum Distance Orthogonal Matching Pursuit.

DFT Discrete Fourier Transformation.

MWBE Maximum Welch bound equality.

CDS Cyclic difference set.

SMV Single measurement vector.

MMV Multiple measurement vector.

SMF Simultaneous multiple frequency.

ADC Analog-to-digital converter.

SBI Suppression of Background Illumination.

RIP Restricted isometry property.

SNR Signal noise ratio.

BOMP Band-excluded Orthogonal Matching Pursuit.

BLOOMP Band-excluded, Locally Optimized Orthogonal Matching Pursuit.

3D Three dimension.

Fig. Figure.

$s(t)$ Emitted optical signal.

$s_r(t)$ Reflected optical signal.

f_{max} Highest modulation frequency.

Δt Grid spacing in time.

Δr Grid spacing in space.

ΔT Minimum separation or minimum distance.

τ Phase offset.

$\boldsymbol{y}$ Measurement vector.

$\boldsymbol{Y}$	Multiple measurement vectors.
Q	Number of multiple measurement vectors.
$\boldsymbol{X}$	Multiple joint sparse signal vector.
$\boldsymbol{x}$	Signal vector.
$\boldsymbol{\Phi}$	Sensing matrix or measurement matrix.
$\tilde{\boldsymbol{\Phi}}$	Normalized-column version of sensing matrix.
K	Signal sparsity.
L	Maximum concerned harmonics.
N	Dimensionality of sensing matrix.
M	Amount of TOF measurements at different modulation frequencies.
f	Modulation frequency.
$\boldsymbol{\sigma}$	Noise vector.
ϵ	Upper bound on noise variance.
Ψ	Modulation frequency set.
F	Refinement factor.
R_{max}	Ambiguity range.
R	Range of interest.
μ	Mutual coherence of sensing matrix.
ρ	Adjustment factor of Ma-OMP.
DR	Dynamic range of signal vector.
E	Coherence cost.
$\boldsymbol{C}$	Coherence pattern matrix.
H	Set of chosen frequencies.
J	Set of chosen phase-offsets.
$\boldsymbol{P}$	Projection matrix in simultaneous multiple frequency or calibration matrix in joint multiple frequency technique.

h	Number of different frequency components in a SMF measurement.

1 Introduction

1.1 Time-of-flight imaging camera and multipath interference problem

In recent decades, time-of-flight (TOF) cameras have been used popularly in many various daily applications, e.g., robotics [1], computer graphics, human interaction [2, 3]. Especially, the continuous-wave TOF (CW-TOF) camera is a type of commercial sensors, e.g., Photo Mixer Device (PMD) [4], Texas Instruments [5], which are able to generate three-dimensional (3D) measurements with high quality and speed. From these reasons, the thesis focuses on this type of commercial CW-TOF camera, particularly PMD 19k imaging system [4]. Due to its operating principle, it produces the depth map of an observing scene through calculating the phase-shift between the reflected and emitted optical signals, as described in Fig. 1.1. This phase-shift calculation is proceeded through phase-stepping algorithms, for instance, the four-phase method in a PMD-19k camera [2].

However, these CW-TOF phase-stepping methods suffer from multipath interference (MPI) problems as described in Fig. 1.2 [6, 7]. To be concrete, multiple light rays which are scattered from complex environmental geometry (see Fig. 1.2b and Fig. 1.2c) or transparent objects (see Fig. 1.2a), arrive at the same pixel. Each flight path possesses different phase-shift. Therefore, the achieved TOF measurements comprising of those various components can lead to a wrong phase-shift and subsequently depth estimation [8, 6]. Many studies have been implemented to reduce the adverse effects of MPIs in CW-TOF camera by many depth correction calibration techniques [8, 9, 10]. Nevertheless, the applicability scopes of these compensation methods are highly scene-dependent. A more effective solution approach for resolving the MPI problem is to reconstruct the time profile of MPIs through a new TOF acquisition. In particular, many publications [11, 12, 13] carried out multiple TOF measurements at different frequencies or phase-offsets and then estimated the time profile through solving a sparse optimization problem modeled from these measurements. However, they spent a long acquisition time of over 30 seconds for generating a large amount of measurements .

For a high acquisition speed, many recent studies [14, 6] acquired only a few TOF measurements at different modulation frequencies. For instance, Dorrington et al. [14] reconstructed the time profile of two return components through two TOF measurements at two different modulation frequencies. However, because the number of measurements

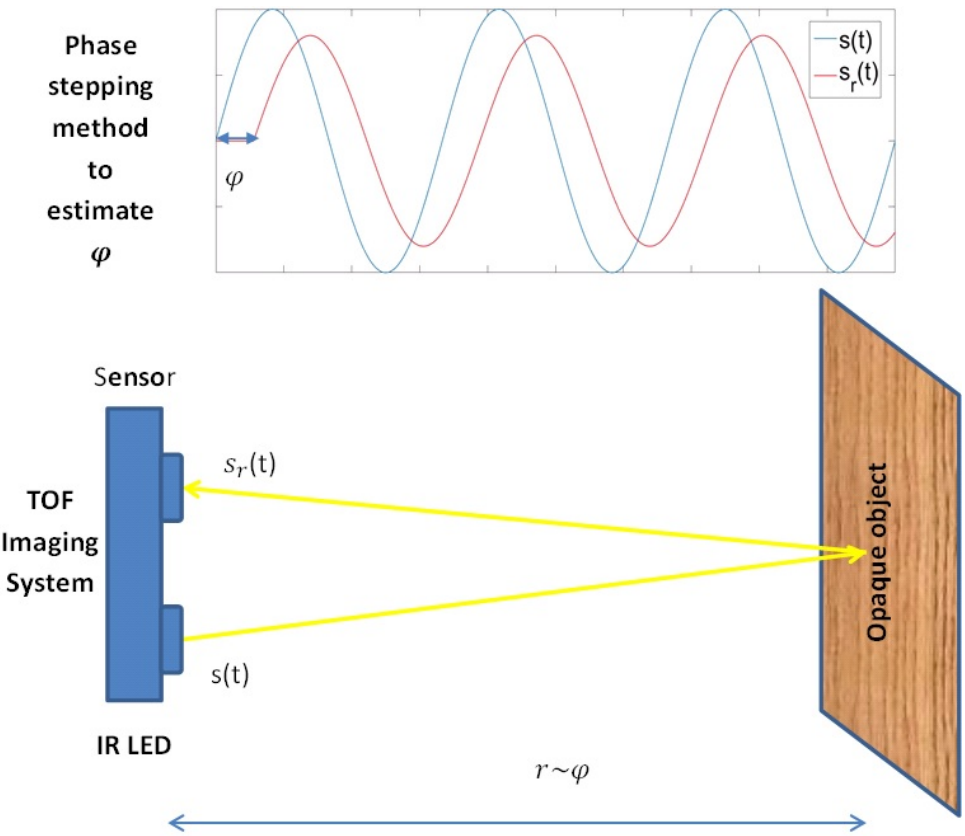

Figure 1.1. The operating principle of a CW-TOF camera

is tiny, the reconstruction performance of their method is sensitive to measurement noise. Moreover, this technique cannot be extended for a complex scattering scene comprising more than two scatterers. More interestingly, Bhandari et al. [6] estimated successfully the depth images of a scattering scene comprising three targets. Their solution approach is formulating a linear optimization problem based on 77 TOF frames at different modulation frequencies and then using a greedy pursuit (Orthogonal matching pursuit-OMP) method for a fast time-profile reconstruction. Nevertheless, the formulation of their sensing matrix model relies on the assumption of an emitted sinusoidal optical signal, that is hard to design in a commercial TOF camera. Moreover, their experimental results are only correct for a defined scenario. But, a diverse analysis of sparse recovery performance in different scenarios has not been implemented yet.

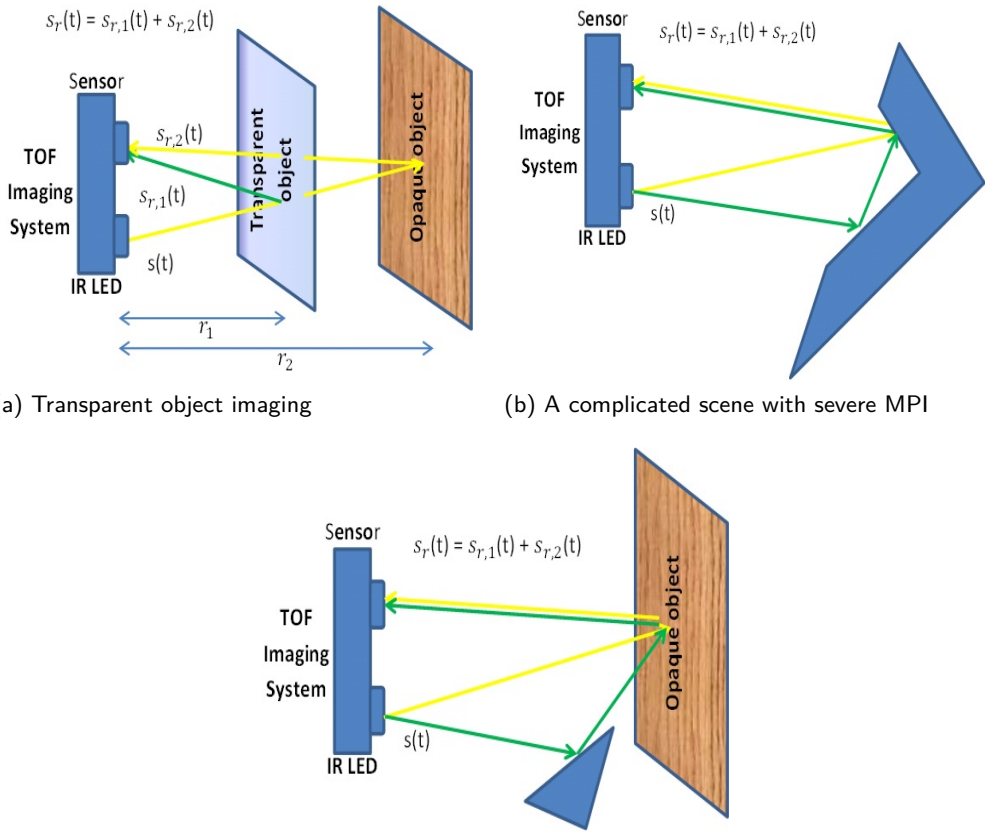

(a) Transparent object imaging

(b) A complicated scene with severe MPI

(c) Mirror-like reflections produce MPI

Figure 1.2. Different cases of MPIs in a TOF imaging camera

1.2 Multi-frequency TOF acquisition using CS

The primary research goal of this thesis is to resolve MPI problems of a TOF camera. Typically, we aim to reconstruct the time profile of the MPIs based on multiple TOF measurements at different modulation frequencies (MFT), similar to the study by Bhandari et al. [6]. The continuous time profile is discretized through an equi-distant grid system and then the time profile estimation based on the MFT model is converted to a linear optimization problem. On the contrary to the previous studies, on one hand, our sensing model is not restricted by the assumption of an emitted sinusoidal optical signal or sinusoidal cross-correlation function. In other words, we construct this model for any emitted or demodulation CW signal, e.g., square or sinusoidal wave [15]. Eventually, our MFT acquisition requires no complex illumination system or chip design for such a sinusoidal-waveform signal generation. On the other hand, since the number of tar-

gets is tiny, compressed sensing (CS) techniques are efficient tools to apply to the MFT acquisition. There have been many studies [16, 17, 18] which used CS techniques in a PMD CW-TOF camera for more advantages. Firstly, they can reduce the number of measurements and further shorten the acquisition time. Secondly, they improve sparse recovery performance through optimizing the MFT sensing matrix design.

A MFT sensing matrix represents the mathematical TOF response of MPIs to different modulation frequencies. And hence, its structure is similar to a discrete Fourier transformation (DFT) matrix. For DFT sensing matrices, Candes et al. [19] proved that there exists the following restricting condition on the grid length Δt of the equi-distant grid system in the time-profile discretization process to guarantee the perfect sparse recovery of a basis pursuit (BP) method:

$$f_{max}\Delta t = 1 \tag{1.1}$$

where f_{max} is the highest modulation frequency. According to (1.1), we have the following properties of a CS-MFT model in numbers regarding the hardware capabilities of a commercial TOF camera:

- If $f_{max} = 30$ MHz, then the spatial grid spacing should be configured as 5 m in the reflection mode.
- If $f_{max} = 100$ MHz, then the spatial grid spacing should be configured as 1.5 m in the reflection mode.

Apparently, with maximum frequency of 100 MHz, according to (1.1), a grid length of 1.5 m would not be well-refined enough to achieve a high depth accuracy and resolution in a MFT model. Eventually, for the reduction of mismatch model errors as well as the enhancement of depth resolution [20, 21], this grid spacing should be set as small as possible but simultaneously satisfy the condition (1.1). Therefore, an increase of modulation frequency in a TOF camera is an important task in our proposed MFT acquisition to obtain a high stability of exact sparse recovery. However, this frequency increase capability is highly dependent on the illumination driving and digital shuttering systems [2, 4]. Currently, a low-cost CW-TOF camera can only modulate and demodulate optical signals at a low frequency of a few tens of MHz. It is significantly difficult to design a new low-cost hardware system to acquire high-frequency TOF measurements.

1.2.1 Super-resolution CS techniques

Super-resolution CS techniques have been applied in many signal-processing applications over the past few years, e.g., high-frequency component extraction from low-frequency samples, target discrimination [22, 21]. The basic principle is to refine the grid spacing with a large refinement factor ($F \gg 1$) [19, 21, 23]. In other words, a refined grid

spacing $\Delta t \ll 1/f_{max}$ is configured for a super-resolution CS-MFT model without any frequency increase. However, this refinement process simultaneously causes a lot of disadvantages in the form of poor recovery performances. Through Theorem 1.2 in [22], Candes et al. indicated a lower bound on a minimum distance (MD) ($\Delta T \geq 2F\Delta t$) of a sparse signal to guarantee an exact sparse recovery using Basis Pursuit (BP) in a super-resolution DFT-CS model. From this theorem, many studies [22, 21] reduced mismatch model errors successfully without any hardware updates. Nevertheless, this restricting condition on MD limits the capability of near-target discrimination or in other words the depth resolution. In summary, a low-cost TOF camera with low-frequency measurements can only acquire a low-depth resolution of the time-profile reconstruction with an acceptably high accuracy.

1.2.2 Motivation and key contribution

Unlike the previous research [22, 21], we aim to analyze the sparse reconstruction capabilities of super-resolution CS algorithms in all cases of various MDs. There is no restricting condition on MD [15, 24] in this thesis with $\Delta T \ll 2F\Delta t$. Therefore, we have to face the problem of poor reconstruction performance due to a highly coherent sensing matrix. To be concrete, super-resolution CS algorithms seem to be impossible to reconstruct sparse signals exactly with a high probability, especially in the cases of small MDs. For these reasons, we introduce an alternative relaxed metric to gauge the quality of the estimated signal more accurately with a tolerance offset, similar to some previous studies [21, 23]. This tolerance offset denotes the requirement of depth accuracy in a 3D application. A small offset value represents a high accuracy requirement and inversely.

This thesis proposes to use a variety of CS techniques to progressively improve the relaxed sparse reconstruction performance in a super-resolution MFT model ($F \gg 1$). They categorize into two main parts, i.e., exploring new super-resolution CS reconstruction algorithms and optimizing a MFT sensing matrix design. Apparently, if we can guarantee a high stability of good relaxed sparse recovery, then near-distant MPI separation can be done successfully through a commercial TOF camera without any hardware update for an increase of modulation frequency. Besides, such a super-resolution MFT model aims to maintain a high frame rate of the time-profile reconstruction as well.

1.3 Outline

Firstly, the fundamental operating principle of a TOF camera is reviewed in Chapter 2. Especially, the CW-TOF modulation and demodulation schemes are the underlying techniques in this thesis. Therefore, this chapter introduces some main properties and state-of-art problems of a currently commercial CW-TOF camera. Besides, we overview some solution approaches for each issue as well as their technical drawbacks.

As mentioned before, a CS model can be efficiently used for the sparse time profile reconstruction. Chapter 3 begins with an overview of some restricting conditions, i.e., Null Space Property, Restricted Isometry Property, Coherence Property, on a sensing matrix to guarantee an exact sparse recovery with high probability [25, 26]. Next, we construct a super-resolution CS model based on MFT measurements with a large refinement factor $F \gg 1$. There are some concerned properties of the above super-resolution MFT model for improving the reconstruction performance of MPI time profile. This chapter demonstrates these useful properties through numerical experiments.

In Chapter 4, we introduce several super-resolution CS greedy pursuits, e.g., Modified Cyclic OMP (OMP3), Non-negative least square optimization (POMP), and Non-negative Magnitude Adjustment OMP (Ma-OMP3). Their achieved reconstruction results are then compared to those of the other state-of-art super-resolution CS algorithms through numerical experiments. Furthermore, each algorithm possesses own advantages in the cases of different MDs. Therefore, this chapter introduces a new combination method based on pre-estimated minimum distance (CMD-OMP) to enhance the stability of a good relaxed sparse recovery.

Chapter 5 proposes a gradient steepest descent method to optimize the frequency and phase-offset selection in a MFT acquisition. It aims to increase the incoherence of a MFT sensing matrix and throughout improve the sparse recovery performance of a greedy pursuit. The results are demonstrated through numerical experiments.

Multiple Measurement Vectors (MMVs) with joint-sparsity recovery is an emerging CS technique which can improve the sparse recovery performance in many target localization applications [27, 28]. Thus, Chapter 6 analyzes a MMV data based on a super-resolution MFT model. For this MMV-MFT model, we introduce many modified variants of greedy pursuits, i.e., OMP3-MMV, Ma-OMP3-MMV, POMP-MMV. All of them aim to improve the sparse recovery performance or in other words increase the accuracy of the time-profile reconstruction. The effectiveness of a MMV-MFT model is proven through numerical results.

Simultaneous multiple-frequency (SMF) TOF acquisition was proposed firstly by Payne et al. [29] to extend ambiguity range of a CW-TOF camera. In principle, each SMF measurement comprises multiple TOF components of different frequencies. Chapter 7 applies this new type of measurement to increase the incoherence of a super-resolution MFT sensing matrix in the configuration of a large refinement factor. In particular, we optimize the sensing matrix structure through a gradient steepest descent method, which was proposed in [30]. Eventually, this technique aims to guarantee a higher stability of a good sparse recovery. Nevertheless, there are some crucial problems regarding hardware design complexity in the acquisition of multiple real SMF measurements. Under these hardware limitations, the gradient steepest descent method in [30] is modified to enhance MPI reconstruction capabilities which will be shown through numerical experiments.

Chapter 8 carries out some practical experiments to prove the confidentiality and practicality of our proposed super-resolution CS models and reconstruction algorithms

which are mentioned in the previous chapters. Nevertheless, raw TOF images which are needed for our reconstruction process, are not available in a commonly commercial TOF camera. For this reason, we use our ZESS Multicam system [2] with some modification steps for the generation of the expected raw images. Finally, Chapter 9 concludes this thesis with some arguments and our future work.

2 Time-of-flight principle

Range measurements play a significant role in many 3D reconstruction applications, e.g., object recognition, human motion tracking, human-computer interaction [2, 31]. Several techniques, i.e., triangulation, interferometry, time-of-flight (TOF), have different approaches to depth estimation. Each one possesses its disadvantages and advantages and hence different scopes of applicability. TOF is the underlying technology of this thesis. It is used in a variety of commercial systems, e.g., TOF camera or Light Detection and Ranging (LiDAR) [31]. These systems illuminate the objects with a modulated light and then measure the time until the reflected light is incident on a photodetector [2]. Subsequently, the distance is computed through the estimated time of flight and the light velocity in propagation medium. LIDAR is a typical system using TOF technology for a high-resolution 3D map. However, for applications requiring an array of depth measurements, this system uses a scanning device for capturing the entire scene and hence consumes a long acquisition time [32]. Whereas, a TOF camera chip comprises a two-dimensional array of CCD or CMOS photo-detectors. Due to this property, it can generate a depth image of the entire scene without scanning. Fig. 2.1 demonstrates several commercial TOF cameras, e.g., PMD [4], Swiss Ranger, CanestaVision [33], Texas Instrument [5], ZCam [34]. There are currently two classes of TOF cameras with different modulation and demodulation schemes, i.e., pulsed-wave (PW) and continuous-wave (CW) modulation. Section 2.1 and Section 2.2 overview fundamental principles of each one respectively. CW-TOF camera is under our concern for resolving MPIs. Thus, Section 2.3 and Section 2.4 describe some main hardware components and subsequently state-of-art problems of this camera type.

2.1 Pulsed modulation

Pulsed-wave (PW) TOF sensors, e.g., ZCam [34], emit an extremely short-width light pulse of a few nanoseconds. Their operating principle is to estimate the time delay between the reflected and emitted optical signals in a direct way. Typically as described in Fig. 2.2, the time-delay estimation relies on two samples of the reflected energy with two out-of-phase demodulation windows (0° and 180°). These windows have the same time duration as the emitted light. Given that the emitted light has the period T_0 and two measured samples are V_1 and V_2. The distance of the target point is computed

(a) PMD (b) Swiss Ranger (c) Texas Instruments

Figure 2.1. Overview pictures of many commercial TOF cameras

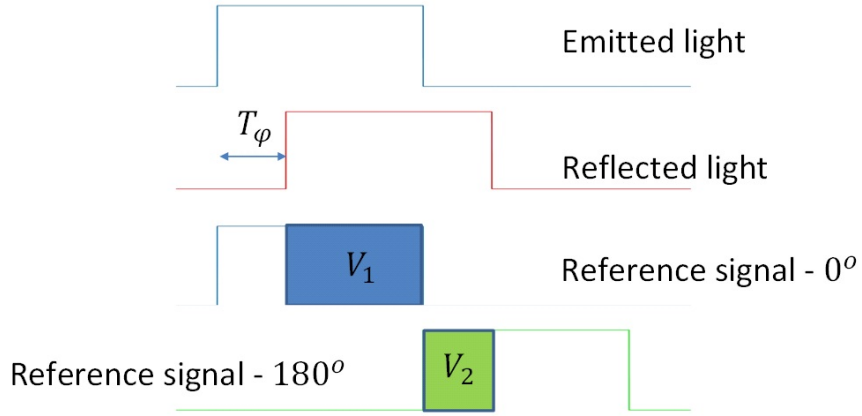

Figure 2.2. Pulsed-light TOF modulation and demodulation

through:

$$d = \frac{1}{2}cT_\varphi = \frac{1}{2}cT_0\left(\frac{V_2}{V_2 + V_1}\right) \tag{2.1}$$

where c is the light speed in application medium.

A PW-TOF camera is used for many outdoor applications under adverse conditions, e.g., surveying (static and mobile), autonomous driving, cultural heritage, planetary missions. According to (2.1), this PW modulation technique does not suffer from a phase ambiguity problem, which will be explained in Section 2.4.4. However, it requires a high-speed shutter operating with extremely short pulses for a high depth resolution. For instance, the receiver of a PW-TOF camera has to demodulate with picosecond (ps)

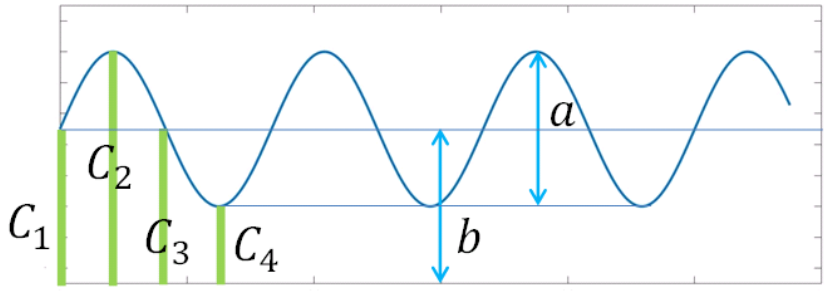

Figure 2.3. Continuous-sinusoidal-wave modulation and demodulation scheme through fast sampling

accuracy to achieve depth resolution and precision up to a few millimeters. And apparently such kind of system is a high-cost device under the current technologies. Moreover, the pulse irradiance power should be set significantly high to ignore background noises. From these reasons, a PW-TOF camera cannot suit for daily low-cost applications.

2.2 Continuous wave modulation

2.2.1 Basic principles

Instead of short light pulses, CW-TOF camera emits a modulated continuous light wave to the scene. Unlike PW-TOF camera, it measures the flight time of the emitted light indirectly through estimating the phase difference between the emitted and received CW signals. The CW-TOF camera chip estimates the phase shift through a phase-stepping algorithm. To be concrete, it acquires several samples of cross-correlation between the demodulation $s(t)$ and received signals $s_r(t)$ at different time-offsets $\Delta\tau$ [2]:

$$C(\Delta\tau) = (s \otimes s_r)(\Delta\tau) = \lim_{T\to\infty} \frac{1}{T} \int_{-T/2}^{T/2} s^*(t - \Delta\tau) s_r(t) dt \tag{2.2}$$

where s^* represents the conjugate of the complex signal s.

Assume that the emitted and demodulation signals are given as the same sinusoidal function with a basic frequency f then (2.2) can be rewritten as:

$$C(\Delta\tau) = C(\tau) = \frac{a}{2} \cos(\varphi + \tau) \tag{2.3}$$

where $\tau = 2\pi f \Delta\tau$ is phase-offset, a is amplitude of the received signal $s_r(t)$ and φ is the unknown phase-shift.

A phase-stepping algorithm acquires N_{phase} samples of the correlation function (2.3) with a phase step of $2\pi/N_{phase}$. Then it estimates the phase shift φ due to the principle

of Discrete Fourier Transform (DFT):

$$\varphi = \tan^{-1}(\frac{W_1}{W_2}) = \tan^{-1}\left(\frac{\sum_{k=1}^{N_{phase}} V_k \sin(2\pi\frac{k-1}{N_{phase}})}{\sum_{k=1}^{N_{phase}} V_k \cos(2\pi\frac{k-1}{N_{phase}})}\right) \tag{2.4}$$

where $V_1, V_2 \ldots, V_{N_{phase}}$ are samples of the correlation function at different phase offsets τ. Additionally, the pixel amplitude a and offset b can be calculated as follows:

$$a = \frac{2}{N_{phase}}\sqrt{{W_1}^2 + {W_2}^2} \tag{2.5}$$

$$b = \frac{\sum_{k=1}^{N_{phase}} V_k}{N_{phase}} \tag{2.6}$$

where

$$W_1 = \sum_{k=1}^{N_{phase}} V_k \sin(2\pi\frac{k-1}{N_{phase}}) \tag{2.7}$$

and

$$W_2 = \sum_{k=1}^{N_{phase}} V_k \cos(2\pi\frac{k-1}{N_{phase}}) \tag{2.8}$$

Finally, the depth information of each pixel can be inferred from the estimated phase-shift φ:

$$d = \frac{c}{4\pi f}\varphi \tag{2.9}$$

Based on mathematical principles, three above unknown variables φ, a, b can be estimated through at least three sampling points ($N_{phase} = 3$). From this point, a three phase-stepping method brings some advantages upon short acquisition time and read-out time. However, there are some drawbacks with low depth accuracy which can be solved through acquiring more phase-measurements [35, 36]. Certainly, more measurements consume more acquisition time.

Typically, a commercial PMD CW-TOF camera [4] uses a four-phase-stepping algorithm ($N_{phase} = 4$) for higher frame rate and moderately higher depth accuracy and precision. In particular, each TOF acquisition acquires four samples V_1, V_2, V_3 and V_4 at four phase offsets 0°, 90°, 180°, 270° respectively. Due to (2.4), (2.5), (2.10), we have:

$$\varphi = \tan^{-1}\left(\frac{V_2 - V_4}{V_1 - V_3}\right) \tag{2.10}$$

$$a = \frac{\sqrt{(V_1 - V_3)^2 + (V_2 - V_4)^2}}{2} \tag{2.11}$$

and

$$b = \frac{V_1 + V_2 + V_3 + V_4}{4} \tag{2.12}$$

2.2.2 TOF measurement accuracy and precision

The term accuracy refers to the closeness of a measurement or an estimate to the true one or a bias value. A low accuracy of a CW-TOF measurement usually suffers from system or measurement non-linearity errors.

The term precision is a measure of how similar multiple measurements or estimates are to each other. It denotes the variability of depth measurements in a TOF camera for the same captured scene. Its magnitude is only dependent on the estimated or measured values and is completely independent of the true value. Conventionally, the precision of CW-TOF measurement is dependent on photon shot noises or external lighting conditions.

2.3 Main hardware components

A commercial CW-TOF camera conventionally comprises the following main hardware components:

- An illumination source emits a CW signal at a modulation frequency. Unlike a pulsed-modulation, this optical signal has no fast rise and fall time. Thus, a variety of light sources is applicable in this system. Light emitting diodes (LED) and laser diodes are two popular sources in many commercial TOF cameras. Each one has own disadvantages and advantages. In particular, a LED modulation circuitry is a low-cost and high-optical-power system. However, it can modulate only low-frequency optical signals, e.g., 60 MHz for a PMD 19k. Whereas, a laser diode driving system is capable of generating an optical signal with higher modulation frequencies. Nevertheless, this type of laser system is significantly complicated and expensive to design. For these reasons, the selection between LED and laser systems highly depends on some application requirements.

- An imaging chip comprises a two-dimensional array of pixels or photon-detectors. For instance, each pixel of a PMD 19k chip is a MOS capacitor with two photogates, which are controlled by two out-of-phase modulation signals and called as channel A and channel B. It collects photons from each distinct part of the scene during the integration time. Subsequently, the collected photons are converted to a charge through an electronic circuit and then read out as a TOF sample in (2.3). For

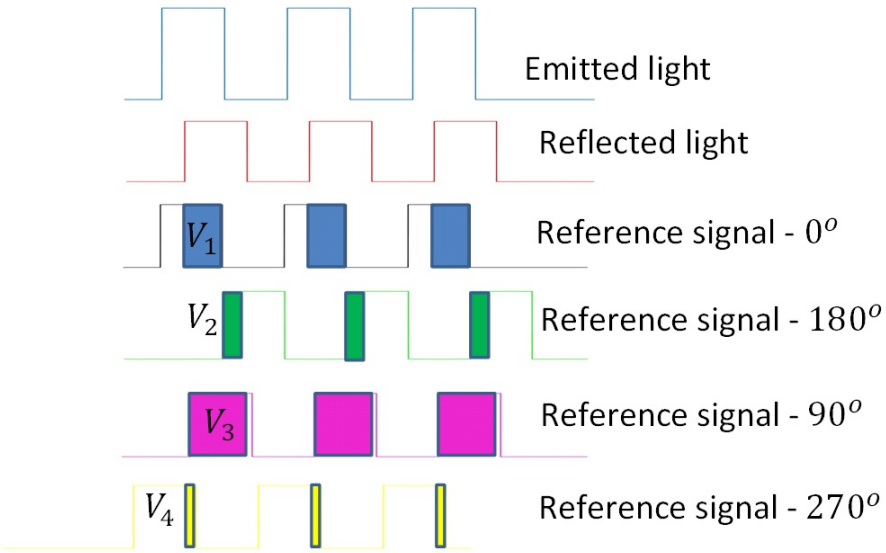

Figure 2.4. Continuous-squared-wave modulation and demodulation schemes through window sampling

a PMD 19k chip, totally eight samples from two photo-gates are read out for four measurements V_1, V_2, V_3 and V_4 in (2.10). The above TOF acquisition is mentioned as window sampling and described in Fig. 2.4. Since a large number of analog-to-digital-converters (ADCs) reads out the samples for thousands of pixels simultaneously, a CW-TOF camera consumes a short acquisition time and hence has a high frame rate.

2.4 State-of-art TOF problems and solutions

Some technical issues of the above hardware components cause errors to the reconstruction of a depth image using a four-phase stepping algorithm. Particularly, there are many state-of-art problems in a commercial CW-TOF camera.

2.4.1 Measurement linearity error

As mentioned in Section 2.2, the phase-shift estimation in (2.4) is only accurate if either demodulation signal or reflected signal is sinusoidal. Whereas, a commercial CW-TOF system controls a light source through digital squared-wave signals. Thus, the emitted optical output lies somewhere between square and sinusoidal waves. This waveform contains some higher order harmonic components which lead to a wrong phase estimation.

This measurement linearity error is mentioned as aliasing problem [2]. For solving this problem, a new hardware design is required for the generation of a sinusoidal waveform but currently acquires high cost and high complexity. Besides, the non-linearity of a TOF measurement can also be caused by other problems, e.g., saturation, system loss. Many studies [37, 38] proposed some correction methods to reduce these linearity errors, e.g., using a look-up table or parametric fit. However, these methods are time-exhausting and highly system-dependent.

Another effective solution for linearity error reduction is to diminish high-order harmonics through synthesizing the waveform of the transmitted signal. For instance, Payne et al. [39] transmitted multiple parts of square signals with the same modulation frequency but different phase-offsets. This technique aims to eliminate two odd high-order harmonics, i.e., 3^{rd} and 5^{th} components, from a TOF measurement. Meanwhile, another study of Payne et al. [40] proposed to transmit a rectangular illumination waveform and then explored the optimized duty cycle (29%) for minimizing measurement linearity errors of a four-phase-stepping method. For extending this approach, we used the illumination waveform optimization into a variety of phase-stepping methods, e.g., three-phase and five-phase stepping methods [41]. Apparently, as can be seen in Table 2.1 [35], various phase-stepping algorithms are sensitive to different high-order harmonic components so each one acquires different optimized duty cycle of rectangular illumination waveform.

Table 2.1. Harmonics being suppressed by various phase-stepping algorithms

Algorithms	Harmonics Being Suppressed								
	2	3	4	5	6	7	8	9	10
3 phase (120°)	_	Y	_	_	Y	_	_	Y	_
4 phase (90°)	Y	_	Y	_	Y	_	Y	_	Y
5 phase (72°)	Y	Y	_	Y	_	Y	Y	_	Y
6 phase (60°)	Y	Y	Y	_	Y	_	Y	Y	Y

The numerical results which are demonstrated in Fig. 2.5, show the linearity root-mean-square (RMS) errors of various duty cycles for three-phase and five-phase algorithms. Apparently, we explore the optimum duty cycle of 37% for three-phase method and 42% for five-phase method. Additionally, both of these methods have other small optimum values of duty cycle for tiny RMS errors, e.g., 18% for three-phase method and 10%, 20%, 31% for five-phase method, with some advantages upon measurement precision. Concretely, as explained in the study of Payne et al. [40], the amplitude of a laser optical signal is inversely proportional to the duty cycle of a rectangular illumination waveform while fixing the optical transmission power. In other words, according

to (2.13) demonstrated in the next section, a rectangular waveform with a smaller duty cycle results in a higher precision of a TOF measurement.

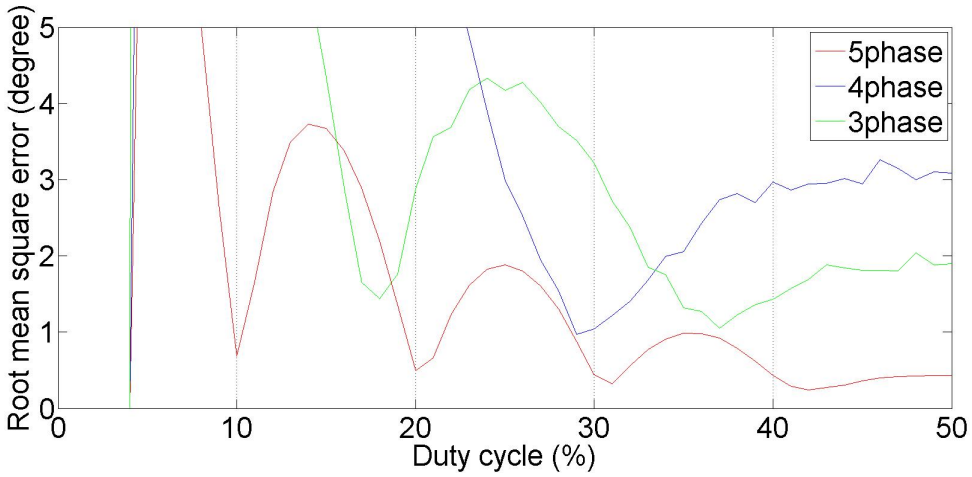

Figure 2.5. RMS linearity error: three-phase (green), four-phase(blue), five-phase(red) with different duty cycles from 10% to 50%

Table.2.2 lists up the optimum duty cycle values as well as some related properties of three various phase-stepping methods. It should be remembered that more measured samples consume longer acquisition time and read-out time and hence the camera has a low frame rate.

2.4.2 Photon shot noise

In the demodulation phase, a TOF chip acquires several samples of the cross-correlation function in (2.3) through the photon generation and the conversion of photons to electrons. Both of two these processes follow a Poisson distribution [4, 42, 2]. Eventually, the more photons are incident on the sensor chip, the more precise these TOF measurements are. Based on [29], the precision (standard deviation) of a depth measurement in a CW-TOF camera is defined as follows:

$$\sigma_d = \frac{c}{4\pi f\sqrt{2}} \frac{\sqrt{b_{ambient} + b_{active}}}{c_d b_{active}} \tag{2.13}$$

where

$$c_d = \frac{a}{b_{active}} \tag{2.14}$$

where $b_{ambient}$ and b_{active} are the offset of the ambient and the active illumination sources respectively. More extended exposure and integration time can increase the active light

Table 2.2. Optimized duty cycles of an emitted rectangular waveform signal for various phase stepping algorithms

N-phase	Optimized duty cycle (%)	RMS linearity error (degree)	Properties
4-phase	29	0.9682	Moderate frame rate and accuracy
3-phase	18	1.436	High frame rate and low accuracy
	37	1.049	
5-phase	10	0.6875	Low frame rate and high accuracy
	20	0.4914	
	31	0.3223	
	42	0.2451	

intensity b_{active} and hence improve the measurement precision, according to (2.13). However, this solution slows down the camera speed. Alternatively, there are two common ways to enhance the TOF measurement precision, by either increasing the modulation frequency or increasing the emitted total optical power [40]. However, these solutions are restricted by hardware design complexity or light safety conditions.

2.4.3 Saturation

Each pixel or photo-detector has a limited storage to collect and store incident photons. Too many incident photons may lead to the saturation problem. And hence some active photons are inevitably lost in the external environment. Eventually, this loss causes low measurement accuracy and precision. The saturation problems usually occur under many outside environments with high external light power. Currently, some PMD chips have featured methods to suppress ambient light efficiently, e.g., Suppression of Background Illumination - SBI [4].

2.4.4 Ambiguity range

The phase-shift estimation in (2.4) contains an arctangent function. Thus, the estimated value lies into [-π,π) and hence the reconstructed depth in (2.9) ranges from 0 to $c/2f$. The maximum value $c/2f$ is defined as ambiguity range of a CW-TOF camera. If

objects locate beyond this range, their true locations cannot be estimated accurately by the phase-stepping method in (2.4) and (2.9). Apparently, a lower modulation frequency can lead to a longer ambiguity range. However, according to (2.13), a TOF measurement at a low modulation frequency acquires a low precision. Therefore, the selection of modulation frequency should satisfy the application requirements of both ambiguity range and measurement precision.

Recently, many studies aim to extend ambiguity range through two TOF measurements at different frequencies [43, 29]. Given two frequencies be f_a and f_b, then this two-frequency acquisition can extend ambiguity range to:

$$R_{max} = \frac{c}{2|f_a - f_b|} \tag{2.15}$$

However, this approach requires more TOF samples for each depth reconstruction, e.g., 8 times 2 (A- and B-channel are acquired simultaneously) samples for two TOF measurements in a PMD 19k camera. Thus, it has negative influences on the depth reconstruction speed or frame rate of this camera. For this reason, Payne et al. [29] introduced simultaneous multiple frequency (SMF) acquisition to reduce the number of samples for two TOF measurements. Nevertheless, this type of acquisition causes much more linearity errors. Based on the illumination waveform optimization method in [40], we successfully reduced these errors of a SMF acquisition in a literature [41].

2.4.5 Multipath interferences

As described in Fig. 1.2, multipath interferences (MPIs) usually incur in real-life scenes, e.g., transparent object imaging, broaden illumination. However, the phase-stepping algorithms of a commercial CW-TOF camera apparently suffer from these MPI problems. For more concreteness, the estimation of phase-shift in (2.10) becomes inaccurate since multiple reflections from scattering environments are incident on the same pixel [14]. It seems to be impossible to resolve the MPIs and subsequently correct TOF depth measurements through selecting an appropriate phase-stepping method or modifying the transmitted signal waveform.

For resolving MPI problem, many studies proposed many depth correction calibration techniques to correct the wrong TOF measurements [8, 9, 10]. However, these methods are highly scene-dependent. For instance, the direct and global separation [9] relies on the assumption of a spatially smooth global component and hence becomes ineffective in some specular corner cases. Meanwhile, the computational optimization methods depend on the radiometric assumption [10] or Lambertian radiator assumption [8].

The current approach for resolving MPI problem focuses on reconstructing the time profile of MPIs at each observed scene point. Many publications [14, 11, 12, 44, 13] carried out multiple TOF measurements at different frequencies or phase-offsets and then constructed sparse models based on these measurements. Various sparse regularization

methods are used for the target depth estimation. Although these models bring robust reconstruction results, they consume extremely long acquisition and computation time. For instance, Kadambi et al. [13] carried out a lot of measurements (i.e., 3000 raw frames at different phase-shifts) to localize only two targets. Whereas, Heide et al. [11] reconstructed the time profile of MPIs with a larger number of TOF measurements at different phase-shifts and frequencies. Both of the above models consume an acquisition time of over 30 seconds. Furthermore, Heide et al. [11] used a l_1-optimization method with smoothing constraints which takes a few hours for the sparse reconstruction of the whole depth map. For more simplicity, Dorrington et al. [14] reconstructed the time profile of two return components through two TOF measurements at two different modulation frequencies. For the case of three or more returns, Freedman et al. [44] proposed Sparse Reflections Analysis (SRA) for a fast real-time multipath separation or Bhandari et al. [6] estimated successfully the depth images of a scattering scene comprising three targets by using 77 TOF frames at different modulation frequencies and a greedy pursuit (Orthogonal matching pursuit-OMP) method for a fast time-profile reconstruction. Nevertheless, these fast-processing methods have not implemented a diverse analysis of reconstruction capabilities under various scenarios, especially near-target cases.

2.5 Summary

CW-TOF cameras are low-cost devices to produce depth images with a high frame rate. As mentioned in this chapter, their current modulation and demodulation schemes suffer from many state-of-art TOF problems. Thus, many studies have been implemented to improve technical properties of a CW-TOF camera, e.g., accuracy, precision, frame rate, ambiguity range. Nevertheless, MPIs are still severe problems which seem to be hard to resolve through the modifications of phase-stepping modulation and demodulation methods. Apparently, the approach of MPI time profile reconstruction based on TOF measurements at different frequencies or phase-offsets are more practical and efficient solutions. However, these models consume heavy acquisition time and computation time. From these points, this thesis aims to develop them by many CS techniques to guarantee a high frame rate of a commercial TOF camera and simultaneously resolve MPIs successfully.

3 Compressed sensing and TOF multipath problem

MPI problems are inherent to the working principle of a commercial TOF camera. Typically, there is not only one light ray reflected from a complex scattering scene. Instead, multiple optical reflections are incident simultaneously on the sensor side. Therefore, the phase-shift estimation of the traditional phase-stepping algorithms in (2.4) contains much errors if the contribution of the unexpected MPI components is significant. Many previous studies [8, 9, 10] successfully reduced these adverse effects by depth correction calibration methods. However, these compensation methods are highly scene-dependent. For instance, the direct and global separation [9] is only applicable for specular corner cases. Therefore, in recent years, a more efficient solution approach [6, 14, 11] has been developed to reconstruct the time profile of MPIs through multiple TOF measurements at various frequencies and phase-offsets. Its operating principle is similar to multi-target localization based on the TOF imaging system. However, this approach presents a lot of challenges, e.g., large acquisition and computation time or low depth resolution regarding the hardware design limitation. Thus, this chapter aims to construct a CS model of a general MPI problem based on CW-TOF measurements at different frequencies (MFT), similar to the study by Bhandari et al. [6]. However, there are significant advances of our model, compared to their research work. While their model can be only applied to TOF cameras with the sinusoidal cross-correlation function, our model is extended to a variety of transmitted or demodulation signal waveforms. Besides, our analysis under CS approaches are also efficient to not only reduce the number of TOF measurements as well as shorten the acquisition time but also explore the depth resolution problem of a MFT acquisition.

Firstly, Section 3.1 overviews some restricting conditions on the sensing matrix, i.e., Null Space Property, Restricted Isometry Property (RIP), Coherence Property, to guarantee an exact sparse signal recovery with a high probability. Additionally, two main classes of CS recovery algorithms, i.e., Basis Pursuit (BP) and Greedy Pursuit, are introduced with their advantages and disadvantages. Secondly, we construct a linear equation system based on multiple TOF measurements at various modulation frequencies (MFT) for a general MPI case in Section 3.2 and Section 3.3. Finding a sparse solution of this system can reconstruct the time profile of MPIs. Nevertheless, the structure of this MFT acquisition introduces new challenges regarding low depth resolution and big mismatch model errors because the modulation frequency of a commercial CW-TOF camera is

significantly low. These problems are explained clearly in Section 3.3. A new hardware design for the implementation of real high-frequency TOF measurements is apparently a direct solution to develop the capabilities of a MFT acquisition. But this task requires high cost and high complexity. Another solution approach in many studies [19, 23, 21] is to refine the grid length without hardware updates. This refinement process leads to the construction of a super-resolution MFT acquisition in Section 3.4, but simultaneously a highly coherent MFT sensing matrix and consequently poor sparse recovery performance. Subsequently, this section indicates some useful settings of a super-resolution MFT acquisition to improve the sparse reconstruction performance and simultaneously maintain a high frame rate of a TOF camera. These arguments are proven through numerical experiments. Additionally, a relaxed metric is introduced to gauge the quality of the estimated sparse signal more accurately. Finally, Section 3.5 concludes the primary goals of our super-resolution MFT acquisition.

3.1 Compressed sensing (CS) and sparse recovery

Compressed sensing (CS) offers a framework for reconstructing a high-dimensional sparse vector $\boldsymbol{x} \in \mathbb{C}^N$ that relies on linear dimensionality reduction [45, 46, 25]. Instead of acquiring $\boldsymbol{x}$ directly, it carries out $M < N$ linear measurements

$$\boldsymbol{y} = \boldsymbol{\Phi}\boldsymbol{x} \tag{3.1}$$

using a sensing matrix $\boldsymbol{\Phi} \in \mathbb{C}^{M \times N}$ where $\boldsymbol{y} \in \mathbb{C}^M$ is referred as the measurement vector. Solving the linear equation system in (3.1) brings many different solutions when $M \ll N$. Thus, it is hard to estimate the correct vector $\boldsymbol{x}$ among these solutions without any additional conditions.

Definition 1. A complex-valued signal vector $\boldsymbol{x} \in \mathbb{C}^N$ is K-sparse if

$$||\boldsymbol{x}||_0 \leq K \tag{3.2}$$

meaning that the number of non-zero elements, namely atoms, of vector $\boldsymbol{x}$ is smaller or equal to K ($K \ll N$). The set of non-zero indices is mentioned as the support of vector $\boldsymbol{x}$.

If vector $\boldsymbol{x}$ is K-sparse, then the problem (3.1) is converted to searching the sparsest solution or solving the following l_0-norm optimization problem:

$$(P_0): \quad \min_{\boldsymbol{z} \in \mathbb{C}^N} ||\boldsymbol{z}||_0 \qquad \text{subject to} \qquad \boldsymbol{y} = \boldsymbol{\Phi}\boldsymbol{z} \tag{3.3}$$

Apparently, this l_0 quasi-norm optimization problem is non-convex. An intuitive approach to this optimization problem is employing exhaustive search routines through all

possible sparse subsets for an exact decomposition. However, this search algorithm is hugely time-consuming.

3.1.1 l_1 minimization or basis pursuit

An alternative approach to solve the non-convex problem P_0 is converting it to the following convex problem, e.g., [47]

$$(P_1): \quad \min_{\boldsymbol{z}\in\mathbb{C}^N} ||\boldsymbol{z}||_1 \qquad \text{subject to} \qquad \boldsymbol{y} = \boldsymbol{\Phi z} \tag{3.4}$$

where $||\cdot||_1$ denotes l_1-norm of a vector. Apparently, the l_1-optimization problem P_1 in (3.4) can be solved by linear programming methods or efficient convex optimization algorithms. Besides, it can be simply extended for the noisy recovery problem $\boldsymbol{y} = \boldsymbol{\Phi z} + \boldsymbol{\sigma}$ to the basis pursuit inequality constraints (BPIC) problem:

$$(P_2): \quad \min_{\boldsymbol{z}\in\mathbb{C}^N} ||\boldsymbol{z}||_1 \qquad \text{subject to} \qquad ||\boldsymbol{y} - \boldsymbol{\Phi z}||_2 \leq \epsilon \tag{3.5}$$

where ϵ is an appropriately chosen upper bound on the noise variance or to basis pursuit denoising with a Lagrangian relaxation:

$$(P_3): \quad \min_{\boldsymbol{z}\in\mathbb{C}^N} ||\boldsymbol{z}||_1 + \lambda||\boldsymbol{y} - \boldsymbol{\Phi z}||_2 \tag{3.6}$$

where λ is a appropriately chosen positive parameter.

However, there are some restricting conditions on the sensing matrix $\boldsymbol{\Phi}$ to ensure that the solutions of the l_0-optimization problem (P_0) and the l_1-optimization problem (P_1, P_2, P_3) coincide [46].

3.1.1.1 Null Space Property and Restricted Isometry Property

Definition 2. A matrix $\boldsymbol{\Phi} \in \mathbb{C}^{M\times N}$ satisfies the null space property of order K if for all subsets $T \subset [N]$ with $|T| = K$, it holds

$$||\boldsymbol{v}_T||_1 < ||\boldsymbol{v}_{T^c}||_1 \quad \forall\, \boldsymbol{v} \in \ker(\boldsymbol{\Phi})\backslash\{0\} \tag{3.7}$$

where T^c is complement of subset T.

Due to [46], the solutions of P_0 and P_1 coincide through the following restricting condition:

Remark 1. Every K-sparse vector $\boldsymbol{x} \in \mathbb{C}^N$ is the unique solution of the l_1-minimization problem P_1 if and only if $\boldsymbol{\Phi}$ satisfies the null space property of order K.

Nevertheless, according to (3.7), it is difficult to verify the null space property of a sensing matrix. Thus, the restricted isometry property (RIP) which was introduced by Candes et al. [48], is used more popularly in CS theory.

Definition 3. The restricted isometry constant β_K of a matrix $\mathbf{\Phi} \in \mathbb{C}^{M\times N}$ is defined as the smallest β_K such that

$$(1-\beta_K)||\boldsymbol{x}||_2^2 \leq ||\mathbf{\Phi}\boldsymbol{x}||_2^2 \leq (1+\beta_K)||\boldsymbol{x}||_2^2 \tag{3.8}$$

for all K-sparse vector $\boldsymbol{x} \in \mathbb{C}^N$

As proven in [49], there exists a restricting condition on sensing matrix relating to the restricted isometry constant β_{2K} :

Remark 2. Suppose the restricted isometry constant β_{2K} of a matrix $\mathbf{\Phi} \in \mathbb{C}^{M\times N}$ satisfies

$$\beta_{2K} < \sqrt{2}-1, \tag{3.9}$$

the solution $\hat{\boldsymbol{x}}$ of the problem P_1 coincides with that of the problem P_0 in noiseless recovery and obeys:

$$||\hat{\boldsymbol{x}}-\boldsymbol{x}||_2 \leq C_0 K^{-1/2}||\boldsymbol{x}-\boldsymbol{x}_K||_1 \tag{3.10}$$

where C_0 is some constant given in [49]. Moreover, the above RIP condition is also applied for noisy recovery. Assume that $\beta_{2K} < \sqrt{2}-1$ and $||\boldsymbol{y}-\mathbf{\Phi}\boldsymbol{z}||_2 \leq \epsilon$. Then the solution of the problem P_2 coincides with that of the problem P_0 and obeys:

$$||\hat{\boldsymbol{x}}-\boldsymbol{x}||_2 \leq C_0 K^{-1/2}||\boldsymbol{x}-\boldsymbol{x}_K||_1 + C_1\epsilon \tag{3.11}$$

where C_0 and C_1 are some constants given in [49].

3.1.1.2 Coherence

The estimation of RIP constant for a sensing matrix is also non-convex and time-consuming. Eventually, the sensing matrix design based on this RIP constant seems to be complicated. For this reason, we use a more effective way to evaluate the reconstruction capabilities of a sensing matrix $\mathbf{\Phi}$ through its coherence property.

Definition 4. The normalized coherence between the p^{th} - and q^{th} columns of a sensing matrix $\mathbf{\Phi} \in \mathbb{C}^{M\times N}$ can be computed as:

$$c_{pq} = \frac{|\boldsymbol{\phi}_p^H \boldsymbol{\phi}_q|}{||\boldsymbol{\phi}_p||_2||\boldsymbol{\phi}_q||_2} \tag{3.12}$$

and the mutual coherence of $\mathbf{\Phi}$ is defined as the largest absolute inner product between any two columns of $\mathbf{\Phi}$:

$$\mu(\mathbf{\Phi}) = \max_{1 \leq p \neq q \leq N} c_{pq} \tag{3.13}$$

Remark 3. If the mutual coherence is significantly small, then the columns of the sensing matrix $\mathbf{\Phi}$ are almost mutually orthogonal. Consequently, the signal recovery based on the orthogonal observations is entirely exact. Thus, the primary task of CS techniques turns into minimizing mutual coherence of the sensing matrix.

It can be shown that $\mu(\mathbf{\Phi}) \in [\sqrt{\frac{N-M}{M(N-1)}}, 1]$, where $\sqrt{\frac{N-M}{M(N-1)}}$ is known as the Welch bound [45, 50]. This Welch bound is the optimized mutual coherence value that one wishes to achieve for the sensing matrix design.

Remark 4. As proven in [46, 51, 52], the slightly weaker sufficient condition

$$K < \frac{1}{2}\Big(1 + \frac{1}{\mu(\mathbf{\Phi})}\Big) \tag{3.14}$$

ensures the perfect K-sparse noiseless recovery by l_1-minimization methods and even by greedy algorithms.

The condition (3.14), together with the Welch bound, gives an upper bound on the sparsity that guarantees the equivalence between the solutions of P_0 and P_1. Nevertheless, it is only valid for noiseless recovery. Therefore, the following restricting condition is used to guarantee the stability of exact noisy recovery [46, 45]. It represents the correspondence between the mutual coherence property and RIP.

Remark 5. If $\mathbf{\Phi}$ has unit-norm columns and mutual coherence satisfying $\beta \leq (K-1)\mu(\mathbf{\Phi})$, then $\mathbf{\Phi}$ has RIP-condition with $\beta_K = \beta$.

In summary, three above restricting conditions on a sensing matrix ensure an exact recovery of the K-sparse vector $\boldsymbol{x}$ by using l_1-minimization. Two of them, i.e., Null Space Property and RIP are the strongest conditions for a guarantee for the high stability of a perfect sparse reconstruction even in the noisy cases. Whereas, the condition (3.14) based on mutual coherence is a weaker one. But it is a more efficient and fast-processing tool to evaluate a structured sensing matrix. Many CS studies [53, 54] successfully designed a structured sensing matrix with the minimized mutual coherence for improving the sparse reconstruction quality.

There are two common classes of sparse reconstruction algorithms, i.e., basis pursuit (BP) and greedy pursuit. Three above restricting conditions ensure uniqueness properties of l_1 solutions of the linear equation system P_1 and P_2 (BP problem). However, l_1-minimization algorithms [55, 56, 57, 58] for solving the above BP problem typically rely on the linear programming that takes a long running time, especially in noisy recovery, even for signals of moderate length. Many recent studies [59, 60] have proposed

a variety of faster-processing BP methods but the computation time is still challenging. Therefore, the current CS research aims to explore greedy algorithms [61, 62] with a higher processing speed.

3.1.2 Greedy pursuit

Greedy pursuit algorithms estimate the support of K-sparse signal vector $\boldsymbol{x}$ iteratively. Therefore, a distinct advantage of these methods is low computation time if the largest sparsity of $\boldsymbol{x}$ is small ($K \ll N$). Nevertheless, they also present new challenges.

3.1.2.1 Orthogonal Matching Pursuit

Orthogonal Matching Pursuit (OMP) algorithm is a stepwise forward selection method as described in Algorithm 1. At each iteration, a new non-zero atom is selected through finding the column of the sensing matrix $\boldsymbol{\Phi}$ which is best-matching to the residual measurement vector. Subsequently, the pseudo-inverse of the sensing matrix respect to the selected columns $\boldsymbol{\Phi}_{T_t}^{\dagger}$ is used to estimate non-zero magnitudes. This magnitude estimation follows the least mean squares minimization. Assume that the expected vector $\boldsymbol{x}$ contains K non-zero atoms. If the sparsity K is known, then OMP stops after K iterations.

Algorithm 1 Orthogonal Matching Pursuit- OMP

Input: $\boldsymbol{y}$, $\boldsymbol{\Phi}$, K
Output: $\boldsymbol{x}$ and T
1: Compute the normalized-column version $\tilde{\boldsymbol{\Phi}}$ of $\boldsymbol{\Phi}$
2: Initialization: $\boldsymbol{x}_0 = \emptyset, T_0 = \emptyset$, $\boldsymbol{r}_0 = \boldsymbol{y}$
3: **for** $t = 1$ **to** K **do**
4: Choose the column $\tilde{\boldsymbol{\phi}}_i$ of $\tilde{\boldsymbol{\Phi}}$ which satisfies
$i = \text{argmax}_{1 \le k \le N} |z_k|$ where $z_k = \tilde{\boldsymbol{\phi}}_k^H \boldsymbol{r}_{t-1}$
5: $T_t = T_{t-1} \bigcup i$
6: Compute $\boldsymbol{x}_{T_t} = \boldsymbol{\Phi}_{T_t}^{\dagger} \boldsymbol{y}$ where $\boldsymbol{\Phi}_{T_t}^{\dagger} = (\boldsymbol{\Phi}_{T_t}^H \boldsymbol{\Phi}_{T_t})^{-1} \boldsymbol{\Phi}_{T_t}^H$
7: Set $\boldsymbol{r}_t = \boldsymbol{y} - \boldsymbol{\Phi}_{T_t} \boldsymbol{x}_{T_t}$
8: **end for**
9: Set $T = T_K$, $\boldsymbol{x} = 0^{N \times 1}$ and $\boldsymbol{x}(T) = \boldsymbol{x}_{T_K}$

As Algorithm 1 shows, OMP is quite fast with a few iterations. Besides, the largest sparsity must be known priorly for the stopping condition of OMP. Nevertheless, an estimate of the largest sparsity before signal reconstruction is a difficult task in practical applications. Another approach for stopping condition relies on the predicted noise level. To be precise, OMP stops whenever the residual energy is smaller than the given noise threshold [62]. In general, both approaches require the prior information for the stopping

condition. Moreover, the sparse reconstruction performance of OMP is not good as that of Basis Pursuit [61]. In summary, greedy methods have advantages of faster processing speed, but disadvantages regarding poorer recovery performance. Additionally, they require the prediction of the largest sparsity or the measurement noise variance before each reconstruction.

3.2 Sparse time profile of TOF multipath problem

As stated in Section 3.1, CS techniques are capable of recovering a sparse signal exactly with a few measurements. Therefore, a CS model of a general MPI problem based on CW-TOF measurements is constructed in this section to estimate the sparse time profile of the MPIs.

Now suppose that K targets are located on the observing line of one-pixel view and have K different distances reference to the camera side (r_1, r_2, ..., r_K). The reflected signal incident on this pixel comprises K reflectance components. Each one represents each optical light reflected from each target. In the reflection mode, the corresponding time delays (t_1, t_2, ..., t_K) of reflected optical components for traveling forth and back from K targets are computed as follows:

$$t_i = 2\frac{r_i}{c} \quad , \quad 1 \leq i \leq K \tag{3.15}$$

where c is the light speed in application medium.

Given that $s(t)$ is the emitted signal. And hence the return signal which is sum of K reflections, is represented by:

$$s_r(t) = \sum_{i=1}^{K} a_i \cdot s(t - t_i) \tag{3.16}$$

where a_i denotes the complex-valued reflective factor of the corresponding target i.

The time profile (t_1, t_2, ..., t_K) and the corresponding reflective properties (a_1, a_2, ..., a_K) of K existing targets are the expected variables. The distances of K targets in the observed pixel can be estimated through finding the time profile (t_1, t_2, ..., t_K).

3.2.1 Single modulation-frequency measurement

A CW-TOF camera emits a time-modulated intensity signal $s(t)$. The discrete Fourier series of this signal with an arbitrary waveform shape can be represented by a function of a modulation frequency f_0:

$$s_{f_0}(t) = \sum_{l=-\infty}^{+\infty} c_l e^{j2\pi l f_0 t} \tag{3.17}$$

where c_l is the l^{th} Fourier coefficient of the transmitted signal. Assume that only L first coefficients are significant. Employing (3.16), we rewrite the reflected signal as follows:

$$\begin{aligned} s_{r,f_0}(t) &= \sum_{i=1}^{K} a_i \sum_{l=-L}^{L} c_l e^{j2\pi l f_0 (t-t_i)} \\ &= \sum_{l=-L}^{L} c_l e^{j2\pi l f_0 t} \sum_{i=1}^{K} a_i e^{-j2\pi l f_0 t_i} \end{aligned} \tag{3.18}$$

Set $G(lf_0) = \sum_{i=1}^{K} a_i e^{-j2\pi l f_0 t_i}$ then:

$$s_{r,f_0}(t) = \sum_{l=-L}^{L} c_l e^{j2\pi l f_0 t} G(lf_0) \tag{3.19}$$

Assume that the demodulation signal $s_{d,f_0}(t)$ has the following discrete Fourier series:

$$s_{d,f_0}(t) = \sum_{l=-L}^{L} d_l e^{j2\pi l f_0 t} \tag{3.20}$$

where d_l is the l^{th} Fourier coefficient of the demodulation signal.

As described in Fig. 2.4, each TOF sample is the sampling of cross-correlation function between the demodulation and reflected signals at a phase offset τ or equivalently a time offset $\Delta\tau$:

$$\begin{aligned} g_{f_0}(\Delta\tau) &= (s_d \otimes s_r)(\Delta\tau) \\ &= \lim_{T_0\to\infty} \frac{1}{T_0} \int_0^{T_0} s^*_{d,f_0}(t-\Delta\tau) s_{r,f_0}(t) dt \\ &= \lim_{T_0\to\infty} \frac{1}{T_0} \int_0^{T_0} \sum_{l=-L}^{L} \sum_{l'=-L}^{L} c_l d^*_{l'} G(lf_0) e^{j2\pi f_0 (l-l')t + jl'2\pi f_0 \Delta\tau} dt \end{aligned} \tag{3.21}$$

or can be rewritten with phase offset $\tau = 2\pi f_0 \Delta\tau$:

$$\begin{aligned} g_{f_0}(\tau) &= \lim_{T_0\to\infty} \frac{1}{T_0} \int_0^{T_0} \sum_{l=-L}^{L} \sum_{l'=-L}^{L} c_l d^*_{l'} G(lf_0) e^{j2\pi f_0 (l-l')t + jl'\tau} dt \\ &= \sum_{l=-L}^{L} \sum_{l'=-L}^{L} c_l d^*_{l'} G(lf_0) e^{jl'\tau} \lim_{T_0\to\infty} \frac{1}{T_0} \int_0^{T_0} e^{j2\pi f_0 (l-l')t} dt \end{aligned} \tag{3.22}$$

Besides, we have:

$$\lim_{T_0\to\infty} \frac{1}{T_0} \int_0^{T_0} e^{j2\pi f_0 (l-l')t} dt = \begin{cases} 1 & \text{if } l = l' \\ 0 & \text{if } l \neq l' \end{cases} \tag{3.23}$$

From (3.22) and (3.23):

$$\begin{aligned} g_{f_0}(\tau) &= \sum_{l=-L}^{L} c_l d_l^* G(lf_0) e^{jl\tau} \\ &= \sum_{l=-L}^{L} c_l d_l^* e^{jl\tau} \sum_{i=1}^{K} a_i e^{-j2\pi l f_0 t_i} \end{aligned} \tag{3.24}$$

3.2.2 Discretization of time profile

In order to construct a sparse model from the TOF measurement $g_{f_0}(\tau)$ in (3.24), a equidistant grid system is used to discretize the continuous value t_i. In other words, the viewing line of one pixel is subdivided in space by the equidistant grid. Each grid has a length of Δr. In the aspect of the flight time, the time grid spacing of the time profile is defined as:

$$\Delta t = \frac{2\Delta r}{c} \tag{3.25}$$

Given each target i locates at the n_i^{th}-grid point whose distance to TOF camera is r_i, then we have:

$$r_i = n_i \Delta r \quad \text{or} \quad t_i = n_i \Delta t \tag{3.26}$$

From (3.24) and (3.26), a TOF sample $g_{f_0}(\tau)$ after discretization can be rewritten as:

$$\begin{aligned} g_{f_0}(\tau) &= \sum_{l=-L}^{L} c_l d_l^* e^{jl\tau} \sum_{i=1}^{K} a_i e^{-j2\pi l f_0 n_i \Delta t} \\ &= \sum_{i=1}^{K} a_i \sum_{l=-L}^{L} c_l d_l^* e^{-j2\pi l f_0 n_i \Delta t + jl\tau} \end{aligned} \tag{3.27}$$

Set $\phi_{f_0,n_i,\tau} = \sum_{l=-L}^{L} c_l d_l^* e^{-j2\pi l f_0 n_i \Delta t + jl\tau}$, then (3.27) is rewritten as:

$$g_{f_0}(\tau) = \sum_{i=1}^{K} a_i \phi_{f_0,n_i,\tau} \tag{3.28}$$

The term $\phi_{f_0,n_i,\tau}$ represents the cross-correlation function response to a target at the n_i^{th} grid point. If the discretization system comprises N grids, then the row vector $\boldsymbol{\phi}_{f_0,\tau}$=($\phi_{f_0,1,\tau}$, $\phi_{f_0,2,\tau}$, ..., $\phi_{f_0,N,\tau}$) represents N delay responses. From this representation, the TOF sample $g_{f_0}(\tau)$ can be rewritten as a linear equation:

$$g_{f_0}(\tau) = \boldsymbol{\phi}_{f_0} \boldsymbol{x} \tag{3.29}$$

where $\boldsymbol{x}$=(x_1, x_2, ..., x_N)^T with $x_{n_i} = a_i$, $\forall\ 1 \leq i \leq K$. The K-sparse vector $\boldsymbol{x}$ has K non-zero indices representing the grid locations of K targets, according to (3.26).

3.3 Multiple frequency TOF (MFT) measurements

Now carry out M TOF measurements at different modulation frequencies $(f_1, f_2 \cdots f_M)$ and formulate the measurement vector $\boldsymbol{y}$ with:

$$\boldsymbol{y} = \begin{pmatrix} g_{f_1}(\tau_1) \\ g_{f_2}(\tau_2) \\ \vdots \\ g_{f_M}(\tau_M) \end{pmatrix} = \boldsymbol{\Phi x} \tag{3.30}$$

where the sensing matrix $\boldsymbol{\Phi}$ comprises M row vectors $\phi_{f,\tau}$:

$$\Phi = \begin{pmatrix} \sum_{l=-L}^{L} c_l d_l^* e^{-j2\pi l f_1 \Delta t + jl\tau_1} & \sum_{l=-L}^{L} c_l d_l^* e^{-j2\pi l f_1 2\Delta t + jl\tau_1} & \cdots & \sum_{l=-L}^{L} c_l d_l^* e^{-j2\pi l f_1 N\Delta t + jl\tau_1} \\ \sum_{l=-L}^{L} c_l d_l^* e^{-j2\pi l f_2 \Delta t + jl\tau_2} & \sum_{l=-L}^{L} c_l d_l^* e^{-j2\pi l f_2 2\Delta t + jl\tau_2} & \cdots & \sum_{l=-L}^{L} c_l d_l^* e^{-j2\pi l f_2 N\Delta t + jl\tau_2} \\ \vdots & \vdots & \ddots & \vdots \\ \sum_{l=-L}^{L} c_l d_l^* e^{-j2\pi l f_M \Delta t + jl\tau_M} & \sum_{l=-L}^{L} c_l d_l^* e^{-j2\pi l f_M 2\Delta t + jl\tau_M} & \cdots & \sum_{l=-L}^{L} c_l d_l^* e^{-j2\pi l f_M N\Delta t + jl\tau_M} \end{pmatrix} \tag{3.31}$$

If TOF measurements are noisy then:

$$\boldsymbol{y} = \boldsymbol{\Phi x} + \boldsymbol{\sigma} \tag{3.32}$$

where $\boldsymbol{\sigma}$ is the noise vector. These noises can originate from external environment or system error sources.

Unlike the traditional phase-stepping scheme in Fig. 2.3, a MFT acquisition carries out multiple TOF measurements at different modulation frequencies. The goal of this MFT acquisition is to estimate the signal vector $\boldsymbol{x}$ in the linear equation system (3.32). Consequently, the non-zero indices and magnitudes of the estimate represent for the time profiles t_i and reflective properties a_i of K targets in the observing view of one pixel (see Fig. 3.1). Assume that the number of MPIs is small in a scattering scene, then it is promising to apply CS techniques into the MFT acquisition to solve (3.32) with two advantages. Firstly, only a few measurements are needed for the sparse time

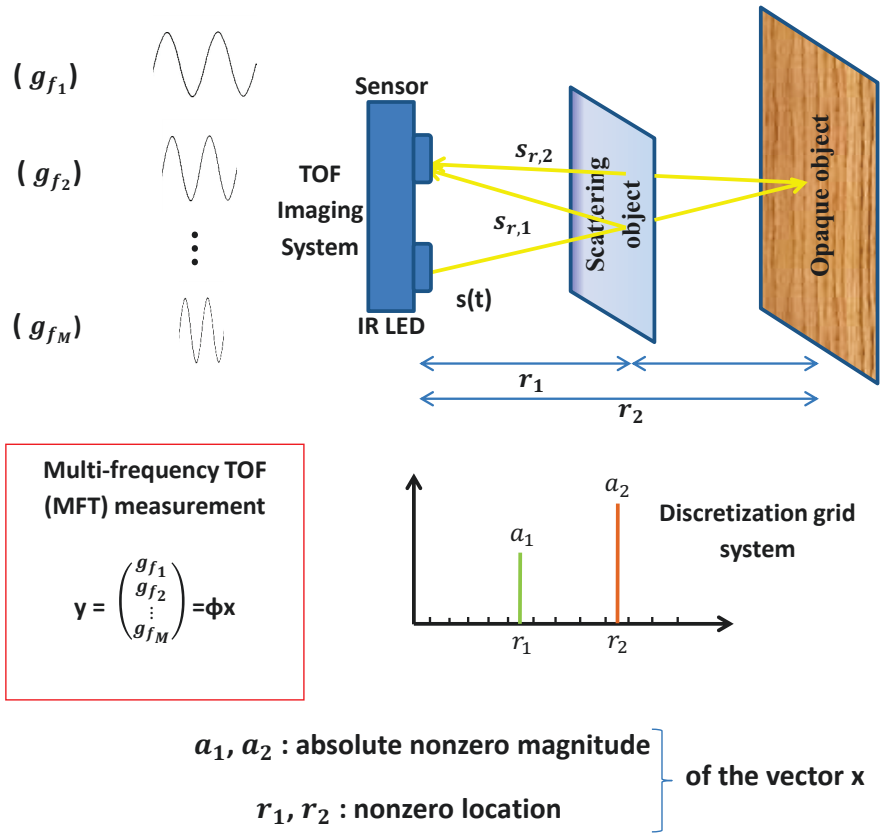

Figure 3.1. Schematic diagram of the MFT measurements for the reconstruction of two multipath interferences using CS model

profile reconstruction. Thus, it consumes a short acquisition time. Secondly, designing the sensing matrix $\mathbf{\Phi}$ efficiently leads to the improvement of sparse recovery performance in (3.32).

It should be noted that the signal support or non-zero indices denote the time profile of MPIs. Therefore, resolving MPIs relies on the accuracy of sparse signal support reconstruction in (3.32).

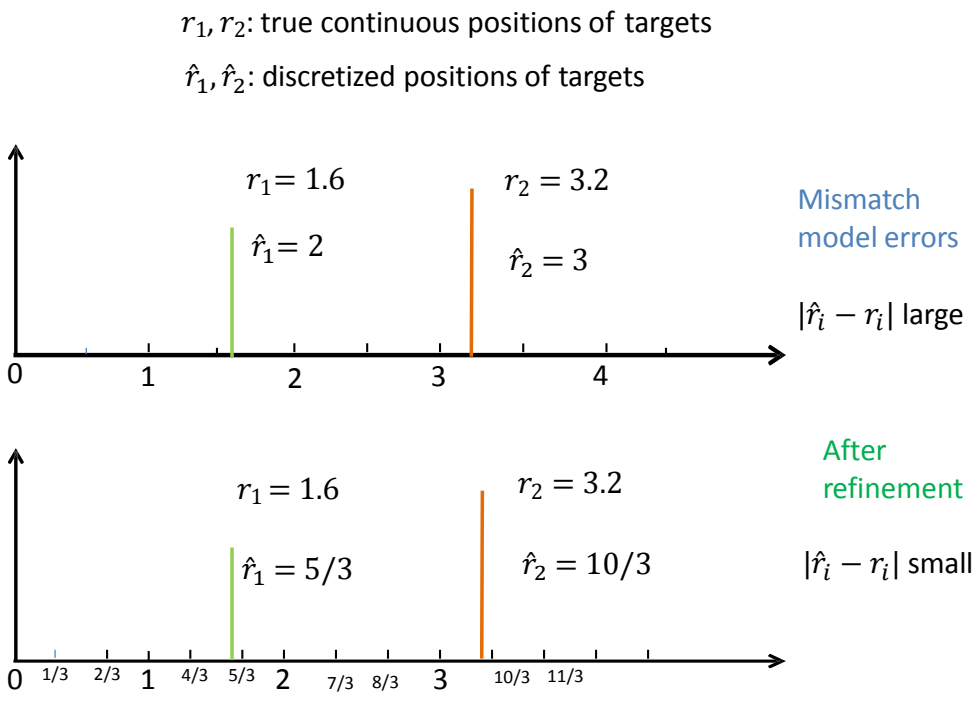

Figure 3.2. A visual example of mismatch model errors before and after the grid system refinement

3.3.1 Mismatch model errors

The above discretization step of time profile in MFT acquisition causes mismatch errors as the true continuous parameters t_i do not lie exactly at the grid points:

$$t_i = n_i \Delta t + \sigma_{t_i} \tag{3.33}$$

where σ_{t_i} is mismatch model error caused by discretization step.

Suppose that the non-zero indices can be estimated exactly after solving the MFT problem (3.32) or $\hat{n}_i = n_i$. Then the corresponding time delay is estimated as $\hat{t}_i = \hat{n}_i \Delta t$. Despite an exact support recovery, there is a gap σ_{t_i} between the estimated time delay $\hat{t}_i$ and the actual one t_i. A large grid length Δt can easily lead to a big mismatch error σ_{t_i} with a high probability, as described in Fig. 3.2. However, the reduction of this error

cannot rely on the development of sparse reconstruction methods.

Besides, if the above model mismatch occurs, then the optical TOF measurement at a modulation frequency f_0 in (3.26) can be rewritten as:

$$\begin{aligned} g_{f_0}(\tau) &= \sum_{i=1}^{K} a_i \sum_{l=-L}^{L} c_l d_l^* e^{-j2\pi l f_0 (n_i \Delta t + \sigma_{t_i}) + jl\tau} \\ &= \sum_{i=1}^{K} a_i \sum_{l=-L}^{L} c_l d_l^* e^{-j2\pi l f_0 (n_i \Delta t) + jl\tau} e^{-j2\pi l f_0 \sigma_{t_i}} \end{aligned} \tag{3.34}$$

Set $e^{-j2\pi l f_0 \sigma_{t_i}} = 1 - \sigma_{f_0,l,i}$, then

$$\begin{aligned} g_{f_0}(\tau) &= \sum_{i=1}^{K} a_i \sum_{l=-L}^{L} c_l d_l^* e^{-j2\pi l f_0 (n_i \Delta t) + jl\tau} (1 - \sigma_{f_0,l,i}) \\ &= \sum_{i=1}^{K} a_i \phi_{f_0,n_i} + \sigma_{f_0} \end{aligned} \tag{3.35}$$

where $\sigma_{f_0,l,i}$ are non-zero mean noises. If the mismatch noise σ_{f_0} is significantly high, the sparse estimation in (3.32) based on the much noisy measurements is no longer accurate or $\hat{n}_i \neq n_i$. Consequently, these big mismatch model errors can cause a poor sparse support recovery performance.

3.3.2 Depth resolution of target discrimination

Depth resolution is mentioned as the minimum separation between two targets which can be distinguished accurately. Suppose that two targets stay in the same grid, then it is impossible to discriminate them. In a CS-MFT acquisition, the increase of the depth resolution as well as the reduction of the mismatch model errors does require a smaller length of a discretization grid. Nevertheless, according to the Rayleigh resolution theorem [22], there exists a relationship between the length of a grid or grid spacing and the highest modulation frequency:

$$\Delta r_{min} = \frac{c}{2 f_{max}} \tag{3.36}$$

or

$$\Delta t_{min} = \frac{1}{f_{max}} \tag{3.37}$$

where f_{max} is the highest modulation frequency in a MFT acquisition. Particularly, if a grid spacing is equal to Δr_{min}, a high stability of an exact signal reconstruction in (3.32) is guaranteed. In many applications, e.g., target discrimination or radar processing techniques [22, 63], this minimum threshold Δr_{min} is considered as the minimum depth

resolution of a target sensing system or referred as the Rayleigh length. As (3.36) indicates, an increase of the highest modulation frequency in a MFT acquisition can improve its minimum depth resolution.

3.3.3 TOF modulation frequency limitation problem

The highest modulation frequency of a low-cost CW-TOF camera is low (e.g, 50 MHz for PMD 19k)[4]. The equation (3.36) indicates that the minimum target discrimination resolution or in this thesis mentioned as minimum range resolution of this camera is equal to:

$$\Delta r_{min} = \frac{c}{2f_{max}} = \frac{3 \times 10^8 \text{ m s}^{-1}}{2 \times 50 \text{ MHz}} = 3 \text{ m} \tag{3.38}$$

and hence not good enough for a MFT acquisition to discriminate targets separated under 3 m. From this result, this model cannot resolve MPIs accurately in a real-life scattering environment. Conventionally, the distance between scatters is small, from a few centimeters to a few meters. Therefore, the modulation frequency in a commercial TOF camera should be increased to improve the depth resolution. Nevertheless, the frequency increase requires the design of a new illumination driving circuit and faster clock generator which is hugely complicated and simultaneously insufficient for a low-cost system.

Remark 6 (Modulation Frequency Set)**.** Theoretically, the modulation frequencies of a MFT acquisition can be selected arbitrarily in the range $(0, f_{max}]$. However, manufacturers produce their CW-TOF camera which can only modulate a set of frequencies. For instance, a PMD 19k chip that is used in this thesis has an operating range of modulation frequencies from 1 MHz up to 60 MHz with a frequency step of 0.25 MHz. However, the TOF measurements over 30 MHz have low confidentiality and demodulation contrast [4, 64]. Thus, 30 MHz is considered as the maximum modulation frequency of a TOF acquisition in this thesis. And hence from (3.36), $\Delta r_{min} = 5$ m. Concisely, we select the frequencies of a MFT acquisition from the set $\Psi = \{1 \text{ MHz}, 1.25 \text{ MHz}, ..., 29.75 \text{ MHz}, 30 \text{ MHz}\}$ with totally 117 different choices.

3.4 Super-resolution MFT compressed sensing

Many super-resolution CS studies [19, 23, 21] aim to reduce the mismatch model errors through refining the grid system with a smaller grid length $\Delta r \ll \Delta r_{min}$ (see Fig. 3.2).

3.4.1 Preliminary

3.4.1.1 Refinement factor

In a super-resolution CS-MFT acquisition, an equidistant grid length is set much smaller than the minimum range resolution ($\Delta r \ll \Delta r_{min}$). This refinement process is adjusted through a given refinement factor:

$$F = \frac{\Delta r_{min}}{\Delta r} = \frac{c}{2 f_{max} \Delta r} \tag{3.39}$$

According to (3.39), a larger refinement factor leads to a smaller grid length and inversely. Thus, one expects to set a large refinement factor to enhance depth resolution and reduce mismatch model errors. However, this significant refinement factor also presents new challenges which will be discussed later.

3.4.1.2 Complex-valued and real-valued measurements

In a commercial PMD CW-TOF camera, the emitted and demodulation signals are squared waves with the following Fourier coefficients:

$$c_l = d_l = \begin{cases} \frac{4}{\pi |l|} & \text{if } |l| \text{ is odd} \\ 0 & \text{if } |l| \text{ is even} \end{cases} \tag{3.40}$$

In the principle of DFT transformation, the auto-correlation function of a square wave possesses the Fourier coefficients of a triangle wave. Thus,:

$$c_l d_l^* = \begin{cases} \frac{16}{\pi^2 |l|^2} & \text{if } |l| \text{ is odd} \\ 0 & \text{if } |l| \text{ is even} \end{cases} \tag{3.41}$$

There are two kinds of TOF measurements, i.e., real-valued or complex-valued measurements. The former one is a sample of cross-correlation at a particular phase-offset τ as described in (3.24). The latter one is the composition of two TOF samples at two

phase-offsets τ and $\tau + \pi/2$:

$$\begin{aligned} g_{complex,f_0,\tau} &= g_{f_0}(\tau) + j g_{f_0}(\tau + \frac{\pi}{2}) \\ &= \sum_{i=1}^{K} a_i \sum_{l=0}^{L} c_l d_l^* \cos\left(-j2\pi l f_0 n_i \Delta t + jl\tau\right) \\ &+ j \sum_{i=1}^{K} a_i \sum_{l=0}^{L} c_l d_l^* \sin\left(-j2\pi l f_0 n_i \Delta t + jl\tau\right) \\ &= \sum_{i=1}^{K} a_i \sum_{l=0}^{L} c_l d_l^* e^{-j2\pi l f_0 n_i \Delta t + jl\tau} \end{aligned} \tag{3.42}$$

The selection between complex-valued and real-valued measurement approaches is a great importance when designing a super-resolution MFT system. Ordinarily, the previous super-resolution CS models [19, 23, 21] have used complex-valued DFT measurements for the estimation of spike locations and complex-valued reflectivity magnitudes. Nevertheless, as explained in Section 3.3, our MFT acquisition aims to reconstruct only the time profile of MPIs through estimating the support of sparse signal $\boldsymbol{x}$. Therefore, the imaginary parts of $\boldsymbol{x}$ can be ignored in this sparse optimization problem. From this point, both complex-valued and real-valued MFT acquisitions are applicable for resolving MPIs. However, according to (3.42), a complex-valued TOF measurement comprising two real-valued samples eventually consumes a doubled acquisition time in a commercial TOF camera. For this reason, it apparently brings a clear disadvantage of long acquisition time despite a higher measurement quality.

3.4.1.3 High order harmonics

The parameter L in (3.24) denotes the highest-order harmonic existing in the cross-correlation function at each modulation frequency. In an ideal case, L equals to one when the transmitted optical signal or the demodulation signal is sinusoidal. However, in a commercial CW-TOF camera, the value of L is larger than one but finite. According to (3.41), the value of a low-order Fourier coefficient $c_l d_l^*$, e.g., $l = 1$, is large while a higher-order one is extremely smaller. As a result, only a few low-order Fourier coefficients have a significant contribution to a practical TOF measurement [2].

3.4.1.4 The ambiguity range and range of interest

As introduced in Section 2.4, ambiguity range is the maximum distance which can be estimated accurately by a depth estimation method. This parameter of a commercial TOF camera using the traditional phase-stepping method is $c/(2f)$ and hence depends on the modulation frequency. Eventually, a higher frequency leads to a smaller ambiguity range and inversely. To extend this ambiguity range, many studies [29, 43] utilized

multiple TOF measurements at different frequencies. Given a set of various modulation frequencies is $\Psi_c \subset \Psi$, then the ambiguity range R_{max} can be extended to:

$$R_{max} = c/(2\,\mathrm{gcd}(\Psi_c)) \tag{3.43}$$

where gcd is greatest common divisor operator.

Similarly, a complex-valued MFT acquisition possesses the same ambiguity range R_{max} in (3.43). For instance, as mentioned in Remark 6, the available frequency pool Ψ with $\mathrm{gcd}(\Psi) = 0.25$ MHz leads to $R_{max} = 600$ m, according to (3.43). Nevertheless, the ambiguity range of a real-valued MFT acquisition $R_{max} = 300$ m is only a half of that of a complex-valued one since the values of cosine functions repeat after a half of period.

Besides, unlike the traditional phase-stepping method, the range of interest using MFT acquisition can be configured through defining a dimension N (the number of grids in the MFT discretization) and a grid length Δr:

$$R = N\Delta r = N\frac{c\Delta t}{2} \tag{3.44}$$

With a conventional grid-length configuration ($F = 1$), for instance $\Delta r = 5$ m for $f_{max} = 30$ MHz, a real-valued MFT acquisition has $R_{max} = N_{max}\Delta r = 300$ m or correspondingly the largest dimension $N_{max} = 60$. However, the value of N_{max} grows larger if the grid length is set smaller or the refinement factor is larger:

$$N_{max} = \frac{R_{max}}{\Delta r} = \frac{R_{max}F}{\Delta r_{min}} = R_{max}F\frac{2f_{max}}{c} \tag{3.45}$$

For instance, $F = 100$ leads to a higher largest dimension $N_{max} = 6000$ to cover the whole ambiguity range of 300 m. Obviously, the setting of a large value $N = N_{max}$ wastes much time for any CS algorithm [26, 65] to reconstruct a sparse signal in (3.32) with a large sensing matrix. However, such a large range of interest $R = 300$ m usually overrides the requirements of a practical TOF application. For these reasons, the dimension should be set small enough to satisfy the application requirements as well as to speed up the reconstruction process. In this thesis, our super-resolution CS-MFT acquisition with $F = 100$ ($f_{max} = 30$ MHz and $\Delta r = 5$ cm) selects $N = 500$ or $R_{MFT} = 25$ m for numerical experiments and $N = 200$ or $R_{MFT} = 10$ m for practical experiments.

3.4.2 High coherence of super-resolution sensing matrix

If two columns of a sensing matrix are similar to each other, two corresponding entries of a sparse vector $\boldsymbol{x}$ show similar observations. Consequently, it is impossible for any reconstruction algorithm based on the observations to distinguish two these entries precisely. Eventually, a highly coherent sensing matrix leads to a low accuracy of signal reconstruction.

Many studies [19, 66] have indicated that the neighboring columns of a DFT sensing matrix are highly coherent to each other in the configuration of a large refinement factor. In this part, we aim to prove that a MFT sensing matrix suffers from similar problems. For this purpose, we construct two different MFT sensing matrices at two different refinement factors, i.e., $F = 1$ and $F = 100$ with the same setting of additional parameters, i.e., $f_{max} = 30$ MHz, $L = 5$, $R = 150$ m. For the simplicity, both of two sensing matrices are real-valued, and the phase offsets τ are zero for all real-valued TOF measurements. In summary, we have two following MFT sensing matrices:

- A structured sensing matrix $\mathbf{\Phi} \in \mathbb{R}^{40\times 30}$ with conventional grid length configuration $F = 1$.
- A structured sensing matrix $\mathbf{\Phi} \in \mathbb{R}^{40\times 3000}$ with super-resolution grid length configuration $F = 100$.

3.4.2.1 Gram matrix

The Gram matrix of a sensing matrix $\mathbf{\Phi}$ is defined as $\boldsymbol{C} = \tilde{\mathbf{\Phi}}^H \tilde{\mathbf{\Phi}}$, where $\tilde{\mathbf{\Phi}}$ is the column-normalized version of $\mathbf{\Phi}$. Each Gram matrix element represents the similarity between two corresponding columns of the sensing matrix $\mathbf{\Phi}$. For instance, the value of c_{12} denotes the coherence between the 1^{st} and 2^{nd} columns. If this value is approximate to zero, then two corresponding columns are nearly orthogonal. Inversely, if this value is approximate to one, then two corresponding columns are similar or highly coherent. Conventionally, the elements of a Gram matrix on the diagonal line are equal to one because they denote auto-correlation of one column. However, in our Gram matrix representation, all of these diagonal elements are set to zero to distinguish them from the high-value elements representing the high coherence between neighboring columns in a super-resolution configuration.

Fig. 3.3 demonstrates the coherence patterns or Gram matrices of two structured MFT sensing matrices. Apparently, according to Fig. 3.3a, the elements of the Gram matrix are small and hence the columns of the sensing matrix $\mathbf{\Phi} \in \mathbb{R}^{40\times 30}$ without a grid refinement ($F = 1$) are incoherent. Whereas, according to Fig. 3.3b, the sensing matrix $\mathbf{\Phi} \in \mathbb{R}^{40\times 3000}$ with a large refinement factor ($F = 100$) possesses a Gram matrix with a high coherence, especially at the diagonal line. In other words, the refinement process breaks out the restricting condition of mutual coherence on a sensing matrix in (3.14). Eventually, the high stability of a good sparse recovery is no longer guaranteed in this super-resolution configuration.

3.4.2.2 Mutual coherence

Nevertheless, only one random selection of 40 frequencies seems to be not enough for a statistical comparison between various MFT acquisitions with different refinement

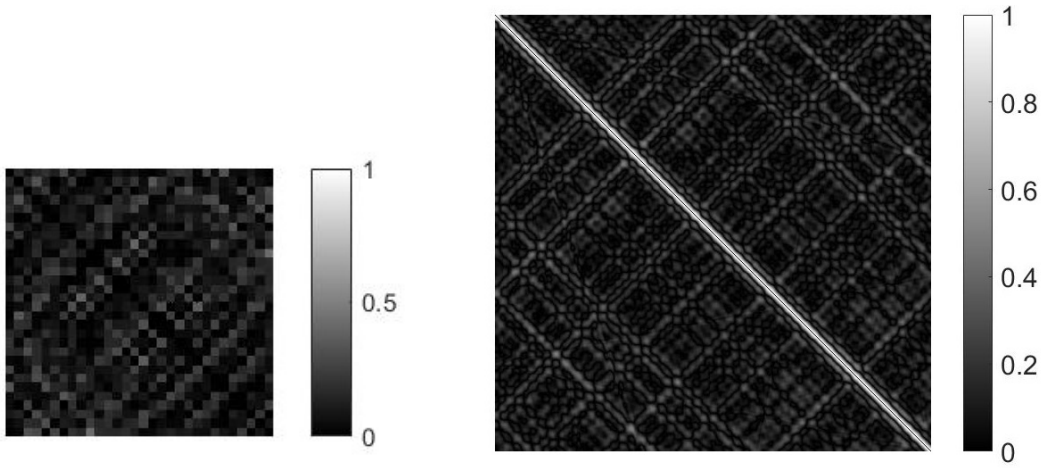

(a) F=1 (b) F=100

Figure 3.3. Resized Gram matrix or coherence pattern of two real-valued sensing matrices with two different refinement factors F

factors. For each case of a refinement factor, we repeat random selection 200 times to formulate 200 real-valued MFT sensing matrix trials. All other parameters, i.e., $L = 5$ and $R = 150$ m are fixed. For each MFT sensing matrix trial, the mutual coherence or the maximum coherence value is computed. The mean value of all mutual coherences of 200 trials is demonstrated in Fig. 3.4. There are 100 different refinement factors (from 1 to 100) which are analyzed in this part.

As can be seen in Fig. 3.4 that a refinement factor over 20 leads to a highly coherent MFT sensing matrix with a considerable mutual coherence close to one (blue line). According to (3.14), this large mutual coherence theoretically cannot guarantee a high stability of an exact sparse recovery using BP or greedy pursuit algorithms.

3.4.2.3 Number of measurements

Remark 7. Due to the CS theory [45, 46, 25], a small number of TOF measurements ($M \ll N$) is necessary for recovering a sparse signal vector $\boldsymbol{x} \in \mathbb{R}^N$ with a small sparsity ($K \ll M$). But this number suffers from lower bound conditions [65]:

$$M \geq CKN\mu^2(\boldsymbol{\Phi}) \log(N/\gamma) \tag{3.46}$$

and

$$M \geq C' \log^2(N/\gamma) \tag{3.47}$$

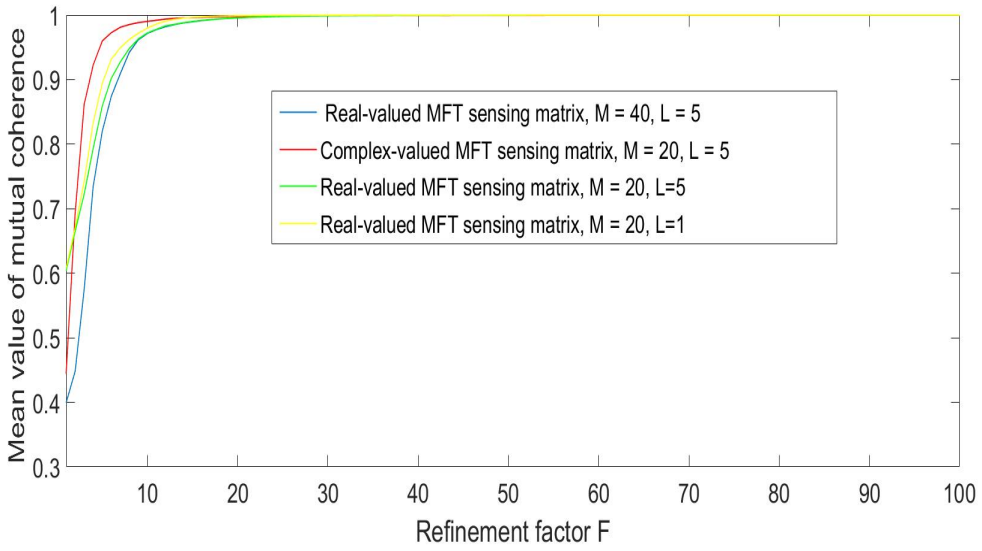

Figure 3.4. Mean mutual coherence value of 200 sensing matrix trials for different kinds of MFT acquisitions at different refinement factors F from 1 to 100

for fixed values of $\gamma < 1$, C, C', to guarantee an exact signal recovery using l_1-minimization algorithm with a probability at least $1 - \gamma$.

According to (3.46), the number of measurements M is linearly proportional to the sparsity property of the scene structure K, the dimension N and the mutual coherence $\mu(\mathbf{\Phi})$ of a sensing matrix. Conventionally, the number of MPIs in a real-life scattering scene is small. Therefore, if the MFT sensing matrix is highly incoherent ($\mu(\mathbf{\Phi}) \ll 1$), then a few TOF measurements are needed for an exact time profile reconstruction of (3.32). However, as can be seen in Fig. 3.4, a MFT acquisition with a large refinement factor configuration leads to a high mutual coherence of the sensing matrix. Eventually, the number of measurements has to be extremely large ($M > N$) to guarantee the high stability of an exact K-sparse signal reconstruction in a large refinement factor configuration. As a result, this super-resolution MFT acquisition consumes much acquisition and readout time and hence cannot maintain a video frame rate of a TOF camera. Thus, in this thesis, we only carry out a few TOF measurements ($M \ll N$), e.g., $M = 20$, for the K-sparse signal reconstruction, e.g., $K = 3$, with $F = 100$. According to (3.47), such a small measurement number causes poor reconstruction performances with a higher γ or in other words a lower detection rate of MPI.

3.4.3 Minimum distance

Definition 5. Given T is the support set of the sparse signal vector $\boldsymbol{x}$. The minimum distance (MD) of a support T is defined as the minimum distant separation between two arbitrary indices in T.

$$\Delta T = \inf_{n,n' \in T, n \neq n'} |n - n'| \tag{3.48}$$

This separation is given by the number of grids or namely bins. In a MFT acquisition, MD denotes the minimum separation between scatters in a MPI case with $\Delta R = \Delta T \Delta r$. In super-resolution CS-DFT problem, Theorem 1.2 of Candes et al. [22] gives a lower bound condition on MD:

$$\Delta T \geq 2F\Delta r \tag{3.49}$$

to guarantee for an exact complex-valued signal recovery using l_1-optimization or a looser lower bound

$$\Delta T \geq 1.87F\Delta r \tag{3.50}$$

for a real-valued sparse signal recovery using l_1-optimization.

According to (3.49) and (3.36), the minimum separation (ΔT) should be larger than $2F\Delta r = 2\Delta r_{min}$. However, Δr_{min} is extremely large if the maximum frequency is low, for instance $\Delta r_{min} = 5$ m with $f_{max} = 30$ MHz. Therefore, MD has to be large to ensure a good sparse reconstruction. This condition cannot be satisfied in a real-life MPI case as the separation between scatters is several 10 centimeters or slightly more. Most previous research [21, 23, 19] admitted this bound as a necessary condition to guarantee a high stability of good sparse reconstruction. They successfully reduced mismatch model errors through the grid refinement process, but the low depth resolution problem has not been solved yet. This thesis aims to analyze the reconstruction performance of a super-resolution CS-MFT model in all cases of both large and small MDs ($\Delta T \ll 2F\Delta t$) [24].

3.4.4 Relaxed sparse support evaluation

As mentioned previously, the set of non-zero indices or the support set of the sparse signal $\boldsymbol{x}$ reconstructed through (3.32) is equivalent to the time profile of MPIs. Therefore, the accuracy of time profile estimation is highly dependent on the accuracy of sparse support estimation. In an ordinary evaluation, a non-zero index or support index of the reconstructed sparse signal $\boldsymbol{x}$ is correct if it coincides with the true one. In this thesis, each sparse signal $\boldsymbol{x}$ achieved by solving (3.32), is evaluated by counting how many support indices in $\boldsymbol{x}$ are correct. The rate of the correctly detected support indices or namely sparse support recovery rate denotes the target detection probability of an analyzed MFT acquisition.

However, the neighboring columns of a MFT sensing matrix is highly coherent in a high-refinement configuration. Additionally, a lower bound on MD to guarantee the

high stability of an exact sparse recovery is not given in our super-resolution MFT acquisition. From these points, the reconstructed sparse signals have a small number of correctly detected support indices or more concisely a low support recovery rate. This low rate denotes low reconstruction capabilities of a super-resolution CS-MFT technique. Nonetheless, this perfect support evaluation with such a restricting detection condition is sometimes not necessary in some applications of target localization. In some cases, the estimation of a target location can be considered as a correct one if the offset between the estimated and true locations is tolerated. For example, a target has the true location of 3 m. For the regular evaluation, this target is missing if its location is estimated as 3.15 m. But for an application with the accuracy requirement of 20 cm, the estimated location of 3.15 m is considered as accurate. Under such a relaxed evaluation metric with a tolerance offset δ, a relaxed sparse support recovery rate is defined as follows:

$$R_b = \frac{1}{K}\Big|\{\hat{n}_k{:}|\hat{n}_k - n_k| \leq \delta, k = 1, 2 \cdots K\}\Big| \tag{3.51}$$

where $\Big|.\Big|$ denotes the cardinality of a set, n_k and $\hat{n}_k$ represent the true and estimated support indices respectively.

The value of the tolerance offset δ is an ordinal number. It represents how many grid lengths between the true and estimated target locations can be accepted as a robust detection. This value is equivalent to the accuracy requirement of some application through $\delta_{true} = \delta\Delta r$. For instance, if $F = 100$ and $f_{max} = 30$ MHz, then $\Delta r = 5$ cm. If $\delta = 2$, then the accuracy requirement is $2\Delta r = 10$ cm. A higher value of δ is corresponding to a lower accuracy requirement and inversely. This relaxed rate R_b becomes the conventional sparse support recovery rate if $\delta = 0$. A MFT model with a low conventional sparse support recovery rate may bring a high relaxed sparse support recovery rate with $\delta > 0$. For such a model, its MPI reconstruction capabilities are high despite its low conventional support recovery rate. Therefore, the relaxed sparse support recovery rate is apparently useful in this thesis for evaluating the performance of a super-resolution MFT acquisition more accurately.

However, for the localization of targets with MD smaller than $2\delta + 1$, the relaxed support evaluation may be inaccurate since an estimated target location may simultaneously satisfy the relaxed detecting conditions of both two actual ones. From this point, the cases of MD into [1, $2\delta + 1$] will be ignored in our analysis. More concretely, this thesis sets a lower bound condition of $2\delta + 1$ on MD between scatters in a MPI case. For instance, if $\delta = 2$ then the restricting condition is $\Delta T \geq 5$, meaning that the separation between MPIs has to be at least $5\Delta r$ in numerical and practical experiments. This small bound has no much negative influence on the depth resolution of our super-resolution CS-MFT acquisition. Our goal is to develop a MFT technique with a high relaxed sparse support recovery rate to guarantee the high stability of an accurate spare support reconstruction with some tiny tolerance offset.

3.4.5 Numerical analysis

3.4.5.1 Recovery performance in super-resolution MFT configuration

According to the Gram matrices in Fig. 3.3, a more significant refinement factor leads to a higher coherence of MFT sensing matrix. In this part, a numerical experiment is carried out to prove that such a higher coherence property causes a lower sparse support recovery rate.

Two different real-valued MFT sensing matrices $\mathbf{\Phi_1} \in \mathbb{R}^{40\times 500}$ and $\mathbf{\Phi_2} \in \mathbb{R}^{40\times 500}$ are constructed with two different refinement factors ($F_1 = 20$ and $F_2 = 100$ respectively). Given Δr_1 and Δr_2 be the grid lengths of the sensing matrices $\mathbf{\Phi_1}$ and $\mathbf{\Phi_2}$, and $f_{max,1}$ and $f_{max,2}$ be the maximum frequencies of the sensing matrices $\mathbf{\Phi_1}$ and $\mathbf{\Phi_2}$. For the construction of two these matrices such that $F_2 = 5F_1$, according to (3.39), there are two different approaches, i.e., setting $\Delta r_1 = 5\Delta r_2$ while fixing $f_{max,1} = f_{max,2}$ or setting $f_{max,1} = 5f_{max,2}$ while fixing $\Delta r_1 = \Delta r_2$. The latter one with the same grid length is selected in this part to guarantee a comparison in a fair manner between their relaxed support recovery rates with $\delta = 2\Delta r$. Besides, we choose $H_1 = 5H_2$ where H_1 and H_2 are two sets of 40 frequencies for two models of acquisition, to satisfy $f_{max,1} = 5f_{max,2}$. The phase offset $\tau = 0$ and the largest number of Fourier coefficients $L = 5$ are set for all TOF measurements.

A Monte Carlo simulation is carried out with 1000 trials for each case of signal-noise-ratio (SNR). At each trial, a sparse signal $\boldsymbol{x}$ with $K = 3$ and consequently two noisy measurement vectors $\boldsymbol{y_1} \in \mathbb{R}^{40}$ ($\mathbf{\Phi_1}$) and $\boldsymbol{y_2} \in \mathbb{R}^{40}$ ($\mathbf{\Phi_2}$) are randomly generated as follows:

Remark 8 (Numerical generation of K-sparse signal and noisy measurement vector for a MFT acquisition $\mathbf{\Phi}$)**.** A non-negative K-sparse vector $\boldsymbol{x} \in \mathbb{R}^N$ is generated with random non-zero indices and magnitudes such that $\Delta T \geq 2\delta + 1$(see Section 3.4.4). The non-negative magnitudes are randomly selected in the range [0.1, 10]. The noisy measurement vector $\boldsymbol{y} = \mathbf{\Phi}\boldsymbol{x} + \boldsymbol{\sigma}$ is then computed based on the generated signal vector $\boldsymbol{x}$ and the MFT sensing matrix $\mathbf{\Phi}$. A vector of white Gaussian noises $\boldsymbol{\sigma}$ is simulated through the Matlab function "awgn" for a specific signal-noise-ratio (SNR) case.

Based on two generated noisy measurement vectors $\boldsymbol{y}_1$ and $\boldsymbol{y}_2$ and two corresponding sensing matrices $\mathbf{\Phi_1}$ and $\mathbf{\Phi_2}$, two following reconstruction methods OMP and BP are used sequentially for recovering the sparse signal vector $\boldsymbol{x}$:

- OMP assumes the availability of the known sparsity $K = 3$.
- For Basis Pursuit, the CVX-package is used to solve the problem P_2 (3.5) or BPIC with an assumption that the upper noise variance ϵ is priorly known. In these simulations, a value of $\epsilon = 1.2||\boldsymbol{y} - \hat{\boldsymbol{y}}||_2$ is assumed as priorly known where $\hat{\boldsymbol{y}}$ is the noiseless measurement vector.

After the sparse reconstruction using OMP or BP, only K largest-magnitude atoms of the estimated signal $\hat{\boldsymbol{x}}$ are kept for calculating the relaxed sparse support recovery rates R_b with $\delta = 2$ as described in (3.51). These rates are averaged after 1000 trials for each case of SNR. There are many cases of different SNRs (from 5 dB to 40 dB with a step of 5 dB) in this numerical experiment. Subsequently, the achieved relaxed support recovery rates of OMP and BP in SNR domain for two different MFT sensing matrices $\boldsymbol{\Phi}_1$ and $\boldsymbol{\Phi}_2$ are shown in Fig. 3.5. From these results, we conclude some following arguments:

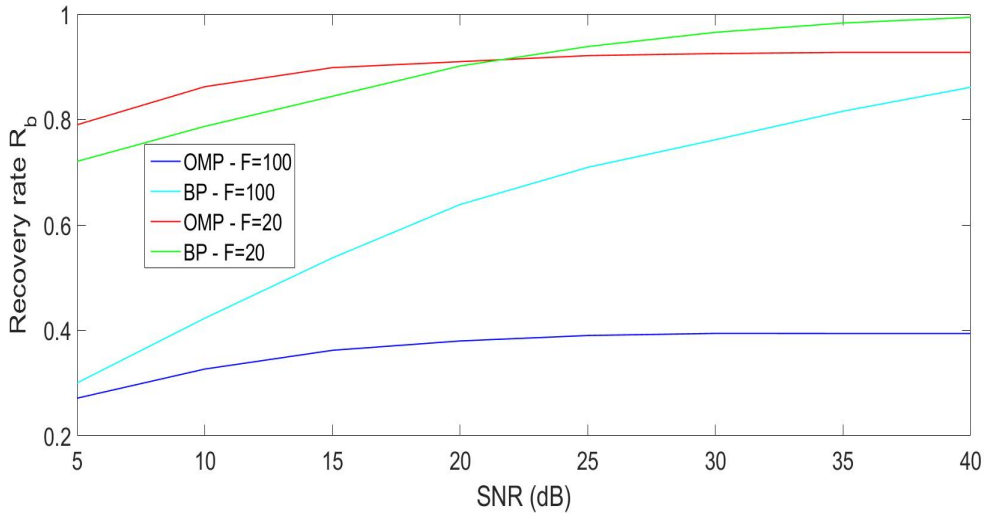

Figure 3.5. Relaxed sparse support recovery rates ($\delta = 2$) of OMP and BP for two MFT sensing matrices with two different refinement factors F in the SNR domain (1000 trials for each SNR case)

- A larger refinement factor configuration of a MFT acquisition leads to a poorer relaxed sparse support recovery performance of CS sparse reconstruction algorithms. As can be seen in Fig. 3.5, the relaxed support recovery rates of OMP and BP using the MFT acquisition $\boldsymbol{\Phi}_1$ with a smaller refinement factor $F = 20$ (red and green lines) are much higher than those using MFT acquisition $\boldsymbol{\Phi}_2$ with a larger refinement factor $F = 100$ (blue and cyan lines) in all cases of various noise levels. This result coincides with the analysis of coherence properties in Fig. 3.3.

- BP (cyan or green line) outperforms OMP (blue or red line) in most cases of different refinement factors ($F = 100$ or $F = 20$) and SNRs (from 5dB to 40 dB) apart from the case of $F = 20$ and SNR ≤ 22 dB, but consumes more computation time.

3.4.5.2 Appropriate MFT acquisition settings

This part analyzes the properties of a CS-MFT technique through numerical experiments. It aims to answer two following questions:

- As shown in Fig. 3.4, a real-valued MFT sensing matrix (green line) has a smaller mutual coherence at a medium refinement factor ($2 \leq F \leq 20$), in comparison to the complex-valued one (red line). However, in a large refinement factor configuration ($F \geq 20$), both real-valued and complex-valued MFT models possess large mutual coherences close to one. From these results, we consider the selection between the complex-valued and real-valued TOF measurements for a higher performance in a super-resolution MFT acquisition.
- In a commercial CW-TOF camera, high-order harmonics are the unexpected components which cause measurement linearity errors [2, 4]. And hence many previous studies [37, 38] tried to eliminate them from a TOF depth measurement. However, as Fig. 3.4 illustrates, these high-order harmonics can enhance the incoherence of a super-resolution MFT sensing matrix. To be concrete, the mean mutual coherence value of a MFT sensing matrix with an emitted sinusoidal optical signal ($L = 1$, yellow line) is higher than that of a MFT sensing matrix with the contribution of high-order harmonics ($L = 5$, green line) at most different refinement factors. From these results, a question arises whether the high-order harmonics in a TOF measurement have positive influence on a super-resolution MFT acquisition.

For the above purposes, we construct the following four MFT acquisitions with the same refinement factor $F = 100$ and maximum frequency $f_{max} = 30$ MHz:

- A complex-valued MFT sensing matrix $\boldsymbol{\Phi}_3 \in \mathbb{C}^{20\times 500}$ with $L = 5$.
- A real-valued MFT sensing matrix $\boldsymbol{\Phi}_4 \in \mathbb{R}^{20\times 500}$ with $L = 5$.
- A real-valued MFT sensing matrix $\boldsymbol{\Phi}_5 \in \mathbb{R}^{40\times 500}$ with $L = 5$
- A real-valued MFT sensing matrix $\boldsymbol{\Phi}_6 \in \mathbb{R}^{20\times 500}$ with $L = 1$.

For the construction of $\boldsymbol{\Phi}_3$, $\boldsymbol{\Phi}_4$ and $\boldsymbol{\Phi}_6$, the same set of 20 frequencies with $f_{max} = 30$ MHz is chosen to guarantee a comparison in a fair manner. Similar to the previous numerical experiment in Fig. 3.5, a Monte Carlo simulation is carried out with 1000 trials for each SNR case. At each trial, a 3-sparse signal $\boldsymbol{x}$ and four noisy measurements vectors $\boldsymbol{y}_3$, $\boldsymbol{y}_4$, $\boldsymbol{y}_5$ and $\boldsymbol{y}_6$, corresponding to $\boldsymbol{\Phi}_3$, $\boldsymbol{\Phi}_4$, $\boldsymbol{\Phi}_5$ and $\boldsymbol{\Phi}_6$, are randomly generated, similarly as in Remark. 8. The reconstruction results of OMP and BP based on four above different MFT acquisitions are analyzed at different SNRs (from 5 dB to 40 dB with a step of 5 dB). The relaxed support recovery rates with $\delta = 2$ after 1000 trials are then shown in Fig. 3.6.

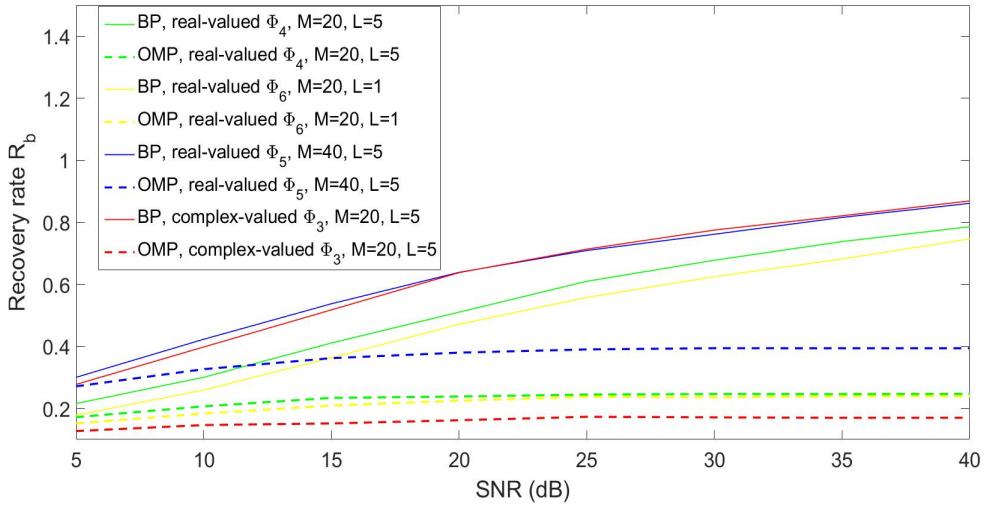

Figure 3.6. Relaxed sparse support recovery rates ($\delta = 2$) of OMP and BP for different types of MFT sensing matrices with a large refinement factor $F = 100$ in the SNR domain (1000 trials for each SNR case)

Complex- and real-valued measurements: are represented by two MFT acquisitions $\mathbf{\Phi}_3$ and $\mathbf{\Phi}_4$ respectively. As can be seen in Fig. 3.6 that the relaxed support recovery rate of OMP using the real-valued MFT acquisition $\mathbf{\Phi}_4$ (dashed green line) is higher than that using the complex-valued one $\mathbf{\Phi}_3$ (dashed red line). However, the relaxed rate of BP using $\mathbf{\Phi}_4$ (solid green line) is inversely lower than that using $\mathbf{\Phi}_3$ (solid red line).

Additionally, as shown in (3.43), a complex-valued TOF measurement comprises two real-valued TOF samples at the phase offsets τ and $\tau + \pi/2$. From this reason, the complex-valued MFT acquisition $\mathbf{\Phi}_3$ with 20 complex-valued TOF measurements have the same acquisition time as the real-valued one $\mathbf{\Phi}_5$ with 40 real-valued TOF measurements. As Fig. 3.6 illustrates, there is no significant difference between the reconstruction performances of BP using $\mathbf{\Phi}_5 \in \mathbb{R}^{40\times 500}$ (solid blue line) and $\mathbf{\Phi}_3 \in \mathbb{C}^{20\times 500}$ (solid red line) in nearly noiseless cases (SNR $\geq$ 20 dB). Whereas, the real-valued MFT acquisition $\mathbf{\Phi}_5$ brings slightly higher relaxed support recovery rates of BP in highly noisy cases (SNR $\leq$ 20 dB) and higher rates of OMP (dashed blue line) in all cases of various SNRs.

An additional comparison between the reconstruction results using $\mathbf{\Phi}_4$ (green lines) and $\mathbf{\Phi}_5$ (blue lines) in Fig. 3.6 reveals that a super-resolution MFT acquisition with more TOF measurements brings a higher stability of a good support recovery. These results are similar to the CS theory in (3.47). However, more measurements simultaneously waste more acquisition time.

In summary, real-valued TOF measurements have more advantages regarding both shorter acquisition time and better support recovery performance of OMP in a super-

resolution MFT acquisition. Therefore, this thesis uses real-valued TOF measurements for a MFT acquisition. Note that they possess a shorter ambiguity range in comparison to a complex-valued MFT acquisition, as mentioned in Section 3.4.1.4.

High-order harmonics: a comparison between the results of two real-valued MFT acquisitions $\boldsymbol{\Phi}_4$ and $\boldsymbol{\Phi}_6$ in Fig. 3.6 reveals that the high-order harmonic contribution ($L = 5$) brings the higher relaxed support reconstruction rates of both OMP and BP. These results empirically demonstrate the positive effects of high-order harmonics in a super-resolution MFT-CS model. Thus, the linearity error compensation methods in the previous studies [37, 38] are unnecessary in the camera calibration of a super-resolution CS-MFT technique.

3.4.5.3 Minimum distance

Our goal in this thesis is to guarantee the high stability of a good support recovery in both large and small MD cases. Therefore, the relaxed support recovery performance of any CS algorithm or MFT acquisition should be analyzed in the MD domain. This analysis can be achieved through a Monte Carlo simulation with a large amount of trials for each MD case (from 5 to 150 bins). At each trial, a sparse signal vector $\boldsymbol{x}$ and a noisy measurement vector $\boldsymbol{y}$ are generated as follows:

- A K-sparse signal vector $\boldsymbol{x}$ is generated with random non-zero indices whose MD is equal to the analyzing MD value. Their non-zero magnitudes similarly range from 0.1 to 10.
- The noisy measurement vector $\boldsymbol{y}$ is generated through $\boldsymbol{y} = \boldsymbol{\Phi x} + \boldsymbol{\sigma}$ with a given SNR. Conventionally, there are two cases of different SNRs, i.e., 15 dB and 30 dB, that denote high and low noise-level cases in this analysis.

Next, a recovery algorithm reconstructs the K-sparse signal based on the generated measurement vector and sensing matrix. The relaxed support recovery rate with a tolerance offset δ is averaged after all trials for each MD case. Fig. 3.7 demonstrates an example of the relaxed support performance analysis in the MD domain for the MFT acquisition $\boldsymbol{\Phi}_4 \in \mathbb{R}^{20\times 500}$ with $F = 100$. Two algorithms OMP and BP are used for sparse reconstruction. Then, their relaxed support recovery rates ($\delta = 2$) after 500 trials for each MD are illustrated by the blue and red lines respectively in Fig. 3.7. As this figure shows, both of two CS reconstruction methods bring poor support recovery performances in the case of a small MD and inversely a better one at a larger MD [24]. Besides, it can be seen through this analysis that BP (red lines) outperforms OMP (blue lines) in all cases of MDs and in both two various SNR cases (15 dB and 30 dB).

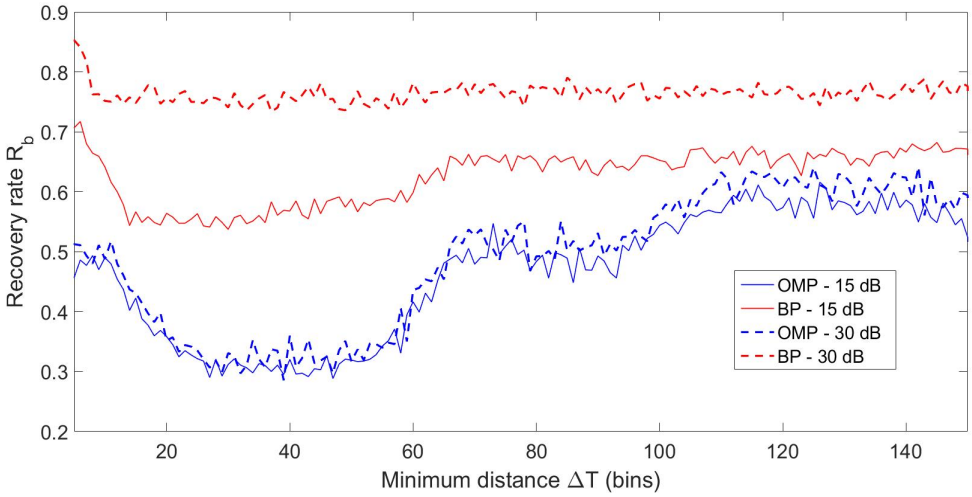

Figure 3.7. Relaxed support recovery rates ($\delta = 2$) of BP and OMP using a real-valued MFT acquisition at different MDs (500 trials for each MD). Choose $N = 500, M = 20, L = 5, f_{max} = 30$ MHz, $F = 100, K = 3$

3.4.5.4 Concerned MFT properties

The support set of a sparse signal vector $\boldsymbol{x}$ represents the time profile of MPIs at one pixel-view. To resolve the MPIs of the entire scene, the noisy sparse reconstruction in (3.32) has to be carried out for thousands of pixels, e.g., 160×120 pixels for a commercial PMD 19k chip [4]. Whereas, a TOF camera is expected to capture the scene depth with a video frame rate. For these reasons, the sparse reconstruction using a MFT acquisition has to run in a short computation time. Therefore, l_1- optimization algorithms (BP) with high run time are inappropriate sparse reconstruction methods for a super-resolution CS-MFT acquisition although they possess high relaxed support recovery rates in the previous numerical experiments. Our research aims to explore fast-processing greedy pursuit methods which bring the good performance in both recovery results and processing time.

Especially, through the above numerical results, a larger refinement factor causes poorer sparse signal recovery performance due to the higher coherence of MFT sensing matrix. From this result, one expects to design a MFT acquisition in the configuration of a small refinement factor. However, this acquisition would possess a high depth resolution only if the TOF camera can modulate an extremely high-frequency acquisition. For a currently commercial TOF camera, such high-frequency modulation and demodulation with a high hardware-design complexity cannot be implemented. Therefore, super-resolution CS techniques are good solution approaches to improve the depth resolution without hardware updates. However, according to (3.46), a huge amount of

TOF measurements ($M > N$) is needed to guarantee the high stability of an exact sparse recovery but simultaneously consume much acquisition time. Therefore, this thesis aims to design new super-resolution MFT acquisitions comprising only a few low-frequency TOF measurements to maintain a high frame rate but simultaneously improve the sparse recovery performance by many different super-resolution CS techniques.

The accuracy of time profile reconstruction is highly dependent on the accuracy of the sparse support recovery. Due to the accuracy requirements of target discrimination application, a relaxed metric is given to gauge the recovered signal support more correctly. A high relaxed support recovery rate is our goal for a MFT acquisition in the configuration of a large refinement factor. This good result can guarantee the high stability of a good support recovery with a tolerance offset δ. This tolerance offset is equivalent to the accuracy requirement. And it will be given as $\delta = 2$ in our next numerical experiments.

As shown in (3.43), the ambiguity ranges of both complex- and real-valued MFT acquisitions are extremely large if the frequency set Ψ has a small $\gcd(\Psi)$. For instance, the frequency set of a commercial PMD 19k chip has $\gcd(\Psi) = 0.25$ MHz and hence $R_{max} = 600$ m for a complex-valued MFT acquisition and $R_{max} = 300$ m for a real-valued one. Unlike the traditional phase-stepping method, a TOF camera using MFT acquisition can configure its range of interest through setting the dimension N of sensing matrix, according to (3.45). For some short-range TOF applications, a small value of dimension is set to cover a short range of interest. For instance, $N = 500$ is set to cover the range of interest $R = 25$ m in most numerical experiments.

A CS reconstruction method brings a poor support recovery performance at a small MD and inversely a better one at a larger MD. In the previous research [21, 23, 19], a lower bound condition on MD was set to guarantee a high sparse recovery performance. However, we have no restricting condition on MD in our analysis. This thesis aims to improve this reconstruction performance of MFT acquisition even in the cases of a small MD or consequently enhance the depth resolution. Note that all cases of MD smaller than $2\delta+1$ are unconcerned in our numerical and practical experiments to avoid a wrong relaxed support evaluation.

Besides, the achieved numerical results demonstrate the following important properties of a super-resolution MFT acquisition.

- The real-valued MFT acquisition is effective with shorter acquisition time and better recovery rate, in comparison with the complex-valued ones with the same large refinement factor ($F = 100$).
- The presence of high-order harmonics in the TOF cross-correlation function seems to improve the reconstruction performance of sparse support.

3.5 Summary

A refinement factor F represents the ratio between the minimum range resolution (Rayleigh threshold) and the grid spacing of a MFT sensing matrix. It should be noted that the refinement factor and the super-resolution factor do not always coincide. As proven in the numerical experiments, a larger refinement factor leads to a poorer signal reconstruction performance. If the high stability of a good signal reconstruction is not guaranteed, then the large refinement factor cannot be considered as a super-resolution factor. Therefore, our goal in this thesis is to improve this performance or more concisely enhance the relaxed support recovery rate of a MFT acquisition in a large refinement factor configuration, particularly $F = 100$. This research approach can be named shortly as the relaxed super-resolution CS, which has not been investigated in the previous studies of the TOF frequency diversity [6, 11, 13]. If a high relaxed support recovery rate R_b (≈ 1) with $\delta = 2$ can be achieved for all cases of various MDs ($\Delta T \geq 2\delta + 1$), then this MFT acquisition possesses a high relaxed super-resolution factor. The MFT acquisition with the above properties brings potentials to resolve MPIs successfully in a real-life scene through only a commercial low-cost TOF camera with low-frequency measurements. Besides, the time profile reconstruction consumes short acquisition time with only a few TOF measurements. For instance, only 20 TOF measurements are used for 3-sparse reconstruction. The presence of the high-order harmonics in the TOF cross-correlation function has some advantages regarding the better support reconstruction results. Thus, reducing these harmonics is unnecessary in the TOF camera calibration. Moreover, we solve (3.32) based on a real-valued MFT acquisition with some advantages regarding shorter acquisition time and better recovery performance. Since the unknown signal vector $\boldsymbol{x}$ is considered as real-valued and the reflective magnitudes of targets are non-negative, this thesis can solve (3.32) with non-negative constraints. Note that the randomly generated sparse signals in all numerical experiments in this thesis are non-negative.

4 Super-resolution compressed sensing methods

For the sparse reconstruction in (3.32), the selection of an appropriate CS algorithm is necessary to guarantee the high stability of accurate sparse reconstruction as well as fast processing speed for the time profile reconstruction of thousands of observed scene points or pixels. For these reasons, l_1-optimization algorithms with massive computation time cannot be used in a MFT acquisition although they bring good support recovery performances as proven in Fig. 3.5. Therefore, this chapter aims to introduce some greedy pursuit methods for a super-resolution MFT acquisition.

Section 4.1 firstly introduces a super-resolution greedy pursuit, i.e., Band Exclusion and Local Optimization proposed by Fannjiang et al. [66]. Subsequently, we propose three other methods, i.e., Modified Cyclic OMP (OMP3) in Section 4.2, Non-negative Least Squares (POMP) in Section 4.3 and Modified Cyclic Non-negative Magnitude Adjustment OMP (Ma-OMP3) in Section 4.4. Their reconstruction capabilities are analyzed for a super-resolution MFT acquisition through numerical experiments in Section 4.5. Each one possesses some distinct advantages and disadvantages in different cases. From these achieved results, a new algorithm, named as Combined based on Minimum Distance Orthogonal Matching Pursuit (CMD-OMP) is proposed in Section 4.6 to maintain the high stability of accurate support recovery. Section 4.7 will conclude some arguments drawn from numerical analysis.

4.1 Band exclusion and local optimization

4.1.1 Band exclusion

In a super-resolution CS problem, Theorem 1.2 of Candes et al. [19] gives a lower bound condition on MD to guarantee the high stability of an exact sparse signal reconstruction. Similarly, the band exclusion technique proposed by Fannjiang et al. [66] assumes that the non-zero atoms are separated by at least an excluded band.

Definition 6. Let $0 < \eta < 1$. Define the η-coherence band of the index element k to be the set

$$B_\eta(k) = \{i \quad | \quad c_{ik} \geq \eta\} \tag{4.1}$$

where c_{ik} represents coherence element of sensing matrix $\mathbf{\Phi}$ and the η-coherence band of

the index set T is the union of the above sets:

$$B_\eta(T) = \bigcup_{k \in T} B_\eta(k) \tag{4.2}$$

Apparently, the radius of the excluded band is considered as the lower bound condition on MD. It is highly dependent on the given coherence value η. Thus, there exists a relationship between this MD bound and the coherence value η. For a further analysis, the mutual coherences η versus the band radius of some super-resolution MFT sensing matrices are demonstrated by numerical experiments in Fig. 4.1, similar to the studies by Fannjiang et al. [66]. There are four examples of different MFT acquisitions with a large refinement factor $F = 100$, including:

- A real-valued MFT sensing matrix $\mathbf{\Phi}_1 \in \mathbb{R}^{20\times 500}$ with a sinusoidal cross-correlation function or $L = 1$.
- A real-valued MFT sensing matrix $\mathbf{\Phi}_2 \in \mathbb{R}^{20\times 500}$ with high-order harmonic contribution $L = 5$.
- A complex-valued MFT sensing matrix $\mathbf{\Phi}_3 \in \mathbb{C}^{20\times 500}$ with high-order harmonic contribution $L = 5$.
- A real-valued MFT sensing matrix $\mathbf{\Phi}_4 \in \mathbb{R}^{40\times 500}$ with high-order harmonic contribution $L = 5$.

For each case of different MFT acquisition and band radius, there are 200 randomly generated sensing matrix trials. The mutual coherences shown in Fig. 4.1 are the mean values of these 200 trials. The assumption of the band exclusion technique claims that there are no two non-zero atoms existing in one excluded band. Therefore, the radius of excluded band is considered as a lower bound condition on MD.

According to (4.1), the observations of any two non-zero atoms have coherence value smaller than η. In other words, the results in Fig. 4.1 indicate the excluded band radius and its corresponding mutual coherence between the observations of any two non-zero atoms under the restricting condition of excluded band. It can be seen in Fig. 4.1 that a larger band radius leads to a smaller coherence η. Whereas, if the observations are more incoherent, then an accurate signal recovery can be achieved by any CS method with a higher probability. In other words, a larger excluded band radius or a more relaxed lower bound on MD can bring a higher sparse recovery performance. This fact has been proven through the numerical studies of Fannjiang et al. [66]. They used OMP combined with the band exclusion technique (BOMP) for improving the quality of spike reconstruction. However, this improvement is significantly small. It seems possible that these unexpected results are due to that the band exclusion technique is inefficient if the selection of non-zero indices in OMP algorithm is inaccurate. Therefore, Fannjiang et al. [66] proposed local optimization (LO) method to fix the incorrectly estimated indices.

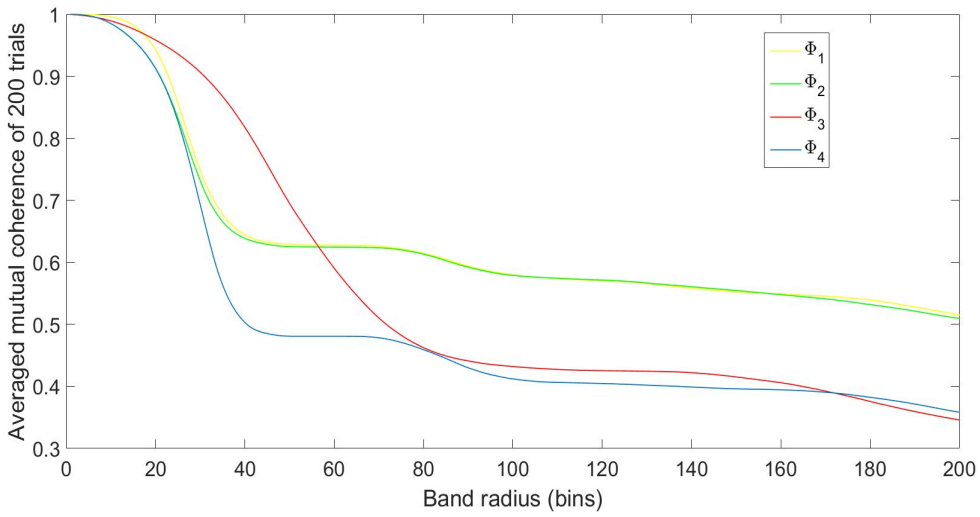

Figure 4.1. Mutual coherence versus the band radius for different types of MFT sensing matrices at $F = 100, N = 500$

4.1.2 Local optimization

Local optimization (LO) is a residual-minimization technique with an effort to fix the incorrectly estimated non-zero indices as described in Algorithm 2. The residual $||\boldsymbol{\Phi x} - \boldsymbol{y}||_2$ is minimized by varying one index while all other ones are held fixed. The replacing index is searched among the neighbors of the replaced one. The replacing process is implemented sequentially for all current non-zero indices.

If we search through all atom indices for a replacement, this process is quite time-consuming. Inversely, the search with a small local range runs in a short time but cannot fix the incorrectly estimated index which stays far away from the true one. Therefore, the local range of searching (LO range) plays a significant role in this LO technique.

Algorithm 2 Local Optimization (LO) with a LO range Δ_{LO}

Input: $\boldsymbol{y}$, $\boldsymbol{\Phi}$, k, $T_0 = \{i_1, i_2, \cdots, i_k\}$, Δ_{LO}
Output: T_k

1: **for** $n = 1$ to k **do**
2: $\boldsymbol{x}_n = \text{argmin}_{\boldsymbol{z}} ||\boldsymbol{\Phi z} - \boldsymbol{y}||_2$, s.t. $\text{supp}(z) = (T_{n-1} \backslash \{i_n\}) \bigcup \{j_n\})$,
where $j_n \in [i_n - \Delta_{LO}, i_n + \Delta_{LO}]$
3: $T_n = \text{supp}(\boldsymbol{x}_n)$
4: **end for**

4.1.3 BLOOMP

Embedding LO technique into BOMP as described in Algorithm 3, named Band-excluded Locally Optimized Orthogonal Matching Pursuit (BLOOMP), can strengthen the reconstruction capabilities of band exclusion technique, as proven in [66]. Conventionally, LO range Δ_{LO} is set equal to the excluded band radius.

Algorithm 3 Band-excluded, Locally Optimized Orthogonal Matching Pursuit (BLOOMP)

Input: $\boldsymbol{y}$, $\boldsymbol{\Phi}$, K
Output: $\boldsymbol{x}$, T
1: Initialization: $\boldsymbol{x}_0 = 0, \boldsymbol{r}_0 = y, T_0 = \emptyset$
2: **for** n:=1 to K **do**
3: $i_n = \arg\max_i |\langle \boldsymbol{r}_{n-1}, \boldsymbol{a}_i \rangle|$, with $i \notin B_\eta(T_{n-1})$
4: $T_n = \mathrm{LO}(T_{n-1} \bigcup i_n, \Delta_{LO})$
5: $\boldsymbol{x}_n = \mathrm{argmin}_{\boldsymbol{z}} ||\boldsymbol{\Phi z} - \boldsymbol{y}||_2 \quad$ s.t. $\mathrm{supp}(\boldsymbol{z}) = T_n$
6: $\boldsymbol{r}_n = \boldsymbol{y} - \boldsymbol{\Phi x}_n$
7: **end for**

A Monte Carlo simulation is carried out to prove the reconstruction capabilities of BLOOMP in a super-resolution MFT acquisition with 1000 trials for each SNR case. In particular, this part analyzes four above different MFT acquisitions $\boldsymbol{\Phi}_1$, $\boldsymbol{\Phi}_2$, $\boldsymbol{\Phi}_3$ and $\boldsymbol{\Phi}_4$ with a large refinement factor configuration $F = 100$. Their mutual coherence values versus band radius are shown in Fig. 4.1. Assume a lower bound condition on MD be 40 bins for this simulation. Concretely, at each trial, we generate a random 3-sparse signal vector $\boldsymbol{x}$ with $\Delta T \geq 40$. Subsequently, a noisy measurement vector $\boldsymbol{y} = \boldsymbol{\Phi x} + \boldsymbol{\sigma}$ is computed through the above sparse signal and MFT sensing matrix with a specific SNR. Two greedy pursuits OMP and BLOOMP are sequentially used for the sparse recovery with the known sparsity $K = 3$. For BLOOMP, we set the band radius to 39 but the LO range to only 20 for a high searching speed. After 1000 trials, the relaxed support recovery rates R_b with a tolerance offset $\delta = 2$ of both OMP and BLOOMP at various SNRs (from 5 dB to 40 dB) are shown in Fig. 4.2.

It can be seen in Fig. 4.2 that BLOOMP (solid lines) brings higher relaxed support recovery performances in all four different MFT acquisitions, compared with OMP (dashed lines). This comparison reveals the efficiency of BLOOMP in super-resolution MFT acquisitions ($F = 100$). However, the lower bound condition on MD or more concisely the band exclusion restricts the applicability scope of BLOOMP. For instance, in the above simulation, BLOOMP can only be useful to discriminate targets separated by at least $40\Delta r$. Apparently, this assumption is impractical in a real-life scene. In this thesis, we expect to resolve MPIs successfully with even a small MD ($\Delta T \geq 2\delta + 1$ as explained in Section 3.4.4) to obtain a higher depth resolution. For this reason, we modify BLOOMP

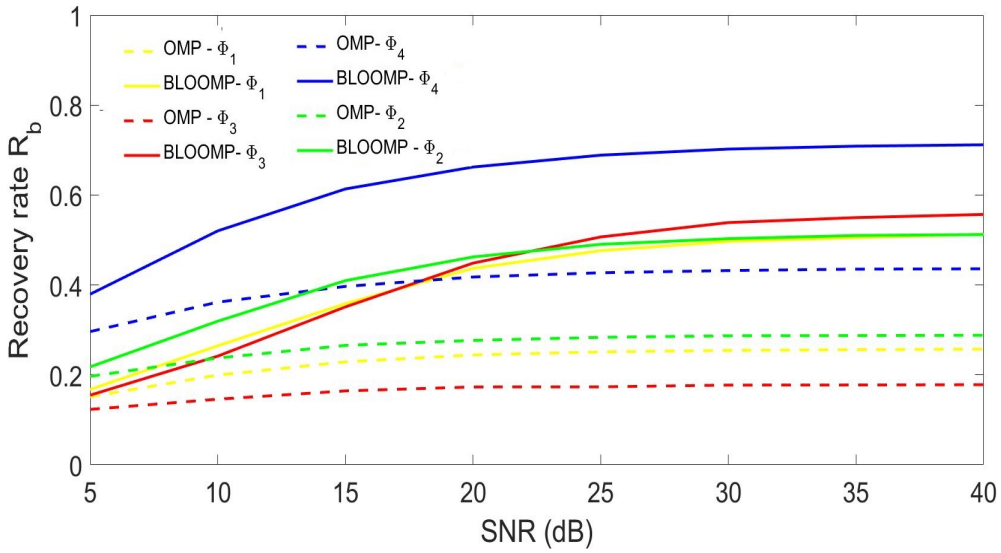

Figure 4.2. Relaxed support recovery rates ($\delta = 2$) of OMP and BLOOMP (band radius =40 and $\Delta_{LO} = 20$) for four sensing matrices with a large refinement factor $F = 100$ at various SNRs (1000 trials for each SNR). Choose $f_{max} = 30$ MHz, $K = 3$, $\Delta T > 40\Delta r$ (bins)

with a smaller band radius and LO range. To be concrete, we repeat the above Monte Carlo simulation with 1000 trials for each SNR, but the randomly generated 3-sparse signals acquire a smaller MD with $\Delta T \geq 2\delta + 1$ (choose $\delta = 2$ bins). Subsequently, 20 TOF measurements based on the real-valued MFT acquisition $\mathbf{\Phi}_2 \in \mathbb{R}^{20\times 500}$ are generated with a specific SNR. Many variants of BLOOMP with different settings of band radius and LO range are used for 3-sparse reconstruction. Since the lower bound on MD is 5 bins, the largest band radius is 4 bins. These achieved results are shown in Fig. 4.3.

As can be seen in Fig. 4.3 that there is no significant difference between the recovery results of BLOOMP with a small band radius of one bin (green line) and four bins (red line). These results indicate that the band exclusion technique seems to be useless with such a small band radius or more precisely a tiny lower bound condition on MD in a super-resolution CS problem. However, the sparse support recovery performance of a super-resolution MFT acquisition can be enhanced through LO technique with an extended searching range. For instance, as Fig. 4.3 shows, the relaxed support recovery rates of BLOOMP with a large LO range of 20 bins (cyan line) are significantly higher than those of BLOOMP with smaller LO ranges, i.e., four bins (red line) and ten bins (rose line). Note that these variants of BLOOMP have the same band radius of four bins. Nevertheless, it should be considered that this increase of LO range simultaneously consumes more searching time.

In summary, the band exclusion technique is only appropriate for our super-resolution

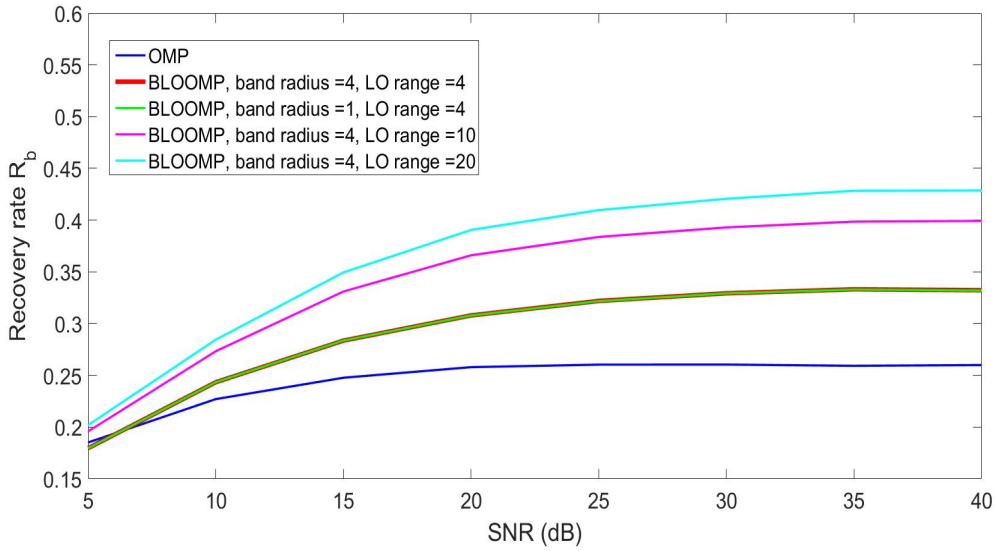

Figure 4.3. Relaxed support recovery rates ($\delta = 2$) of OMP and different variants of BLOOMP (different settings of band radius and LO range) for a real-valued MFT sensing matrix $\Phi \in \mathbb{R}^{20\times 500}$ with the large refinement factor F=100 at various SNRs (1000 trials for each SNR). Choose $N = 500$, $L = 5$, $f_{max} = 30$ MHz, $K = 3, \Delta T > 4\Delta r$ (bins)

MFT acquisition if the MD between targets is large. It becomes inefficient in the case of small MDs. Whereas, LO technique brings the significant improvements of the quality of the spike reconstruction in all cases of various MDs. Apparently, this atom updating technique is useful to interact with other greedy pursuit algorithms for fixing support estimate. However, the LO searching range should be adjusted to guarantee a balance between the support recovery performance improvement and the consumption of computation time.

4.2 Modified cyclic orthogonal matching pursuit -OMP3

4.2.1 Global optimization

The above LO technique is used to fix the incorrectly estimated indices but has some disadvantages regarding low processing speed. Additionally, the wrongly estimated index slowly converges to the true one within a small range of searching. Another atom updating approach, which has been introduced in Cyclic Orthogonal Matching Pursuit method [67], is an alternative solution to overcome the above drawbacks. In this technique, the replacing index is selected to minimize the residual $||\boldsymbol{\Phi}_T \boldsymbol{x}_T - \boldsymbol{y}||_2$ similar to LO technique, but through a different searching procedure. More precisely, it selects an

Algorithm 4 Global Optimization (GO)

Input: $\boldsymbol{y}$, $\boldsymbol{\Phi}$, k, $T = \{i_1, i_2, \cdots, i_k\}$, column-normalized matrix $\tilde{\boldsymbol{\Phi}}$
Output: T, $\boldsymbol{x}_T$

Compute $\boldsymbol{x}_T = \text{argmin}_{\boldsymbol{z}_T} ||\boldsymbol{\Phi}_T \boldsymbol{z}_T - \boldsymbol{y}||_2$
Compute $r_{min} = ||\boldsymbol{\Phi}_T \boldsymbol{x}_T - \boldsymbol{y}||_2$
while true **do**
  Set *stopping* = true
  for $n = 1$ to k **do**
    $T_{tmp} = T \backslash \{i_n\}$,
    $\boldsymbol{x}_{T_{tmp}} = \boldsymbol{x}_T \backslash \{x_{i_n}\}$,
    $\boldsymbol{r}_n = \boldsymbol{y} - \boldsymbol{\Phi}_{T_{tmp}} \boldsymbol{x}_{T_{tmp}}$
    Choose the column $\tilde{\boldsymbol{\phi}}_{i_{max}}$ of $\tilde{\boldsymbol{\Phi}}$ which satisfies
      $i_{max} = \text{argmax}_{1 \leq k \leq N} |z_k|$ where $z_k = \tilde{\boldsymbol{\phi}}_k^H \boldsymbol{r}_n$
    $T_{new} = T_{tmp} \bigcup i_{max}$
    Compute $\boldsymbol{x}_{T_{new}} = \text{argmin}_{\boldsymbol{z}_{T_{new}}} ||\boldsymbol{\Phi}_{T_{new}} \boldsymbol{z}_{T_{new}} - \boldsymbol{y}||_2$
    Compute $r_{new} = ||\boldsymbol{\Phi}_{T_{new}} \boldsymbol{x}_{T_{new}} - \boldsymbol{y}||_2$
    if $r_{min} > r_{new}$ **then**
      Update $T_{opt} = T_{new}$, $\boldsymbol{x}_{T_{opt}} = \boldsymbol{x}_{T_{new}}$, $r_{min} = r_{new}$
      Set stopping = false
    end if
  end for
  if *stopping*==false **then**
    Update $T = T_{opt}$ and $\boldsymbol{x}_T = \boldsymbol{x}_{T_{opt}}$
  else
    break
  end if
end while

appropriate replacing index through finding the best-matching component. This process is similar to the atom selection module of OMP as described in Algorithm 4. According to its operating principle, this technique has an advantage regarding high convergence speed over LO technique. Since the replacing indices are no longer restricted to a local range, a wrongly estimated index can quickly converge to the true one after only one iteration. This technique is referred as global optimization (GO) in this thesis.

4.2.2 Modified cyclic OMP - OMP3

Sturm et al. [67] have proposed Cyclic OMP to improve sparse recovery performance in a CS model. At the end of each non-zero selection iteration in OMP, they run GO technique as described in Algorithm 5 to correct the wrongly estimated indices quickly

without exhaustive searching.

Algorithm 5 Conventional Cyclic Orthogonal Matching Pursuit

Input: $\boldsymbol{y}$, $\boldsymbol{\Phi}$, K
Output: $\boldsymbol{x}$, T
1: Initialization: $\boldsymbol{x}_0 = 0, \boldsymbol{r}_0 = y, T_0 = \emptyset$
2: **for** $n = 1$ to K **do**
3: $i_n = \arg\max_i |\langle \boldsymbol{r}_{n-1}, \boldsymbol{a}_i \rangle|$
4: $T_n = \mathrm{GO}(T_{n-1} \bigcup i_n)$
5: $\boldsymbol{x}_n = \mathrm{argmin}_{\boldsymbol{z}} ||\boldsymbol{\Phi z} - \boldsymbol{y}||_2$ s.t. $\mathrm{supp}(\boldsymbol{z}) = T_n$
6: $\boldsymbol{r}_n = \boldsymbol{y} - \boldsymbol{\Phi x}_n$
7: **end for**

Conventionally, an atom updating procedure, e.g., GO technique in Cyclic OMP or LO technique in BLOOMP, runs after each iteration of OMP has done with a new non-zero index. It is aimed at correcting all selected non-zero indices in each iteration through minimizing the residual cost. As a result, the estimate of new index in the next

Algorithm 6 Modified Cyclic Orthogonal Matching Pursuit

Input: $\boldsymbol{y}$, $\boldsymbol{\Phi}$, K
Output: $\boldsymbol{x}$, T
1: Initialization: $\boldsymbol{x}_0 = 0, \boldsymbol{r}_0 = y, T_0 = \emptyset$
2: **for** $n = 1$ to K **do**
3: $i_n = \arg\max_i |\langle \boldsymbol{r}_{n-1}, \boldsymbol{a}_i \rangle|$
4: $T_n = T_{n-1} \bigcup i_n$
5: $\boldsymbol{x}_n = \mathrm{argmin}_{\boldsymbol{z}} ||\boldsymbol{\Phi z} - \boldsymbol{y}||_2$ s.t. $\mathrm{supp}(\boldsymbol{z}) = T_n$
6: $\boldsymbol{r}_n = \boldsymbol{y} - \boldsymbol{\Phi x}_n$
7: **end for**
8: $T = \mathrm{GO}(T_K)$
9: Additional step: $T = \mathrm{LO}(T, \Delta_{LO})$
10: $\boldsymbol{x} = \mathrm{argmin}_{\boldsymbol{z}} ||\boldsymbol{\Phi z} - \boldsymbol{y}||_2$ s.t. $\mathrm{supp}(\boldsymbol{z}) = T$

iteration becomes more accurate. However, this advantage cannot be guaranteed if the sensing matrix is highly coherent. According to Algorithm 4 or Algorithm 2, GO or LO technique corrects each index while the other ones are held fixed. If the set of all selected non-zero indices is incomplete, then the observation of the updated index and the residual vector may be highly coherent to each other. From this result, finding the replacing index becomes more inaccurate. Therefore, the atom updating procedure is only useful in a super-resolution CS problem if the estimated support set is complete. More concretely, this procedure should run after OMP has selected K non-zero indices. Thus, we add GO technique at the end of OMP to fix the incorrect indices efficiently

and simultaneously reduce the computation time. This method is named as Modified Cyclic OMP or shortly OMP3 in this thesis and described in Algorithm 6.

4.2.3 Combination between OMP3 and LO technique

GO and LO techniques are two various atom updating procedures with their disadvantages and advantages:

- Theoretically, LO techniques consume more time because of an extensive searching range. Additionally, it is only useful if the updated indices close to the actual ones.
- On the contrary, GO techniques can quickly correct the wrongly estimated indices even if the estimated and actual non-zero indices are far away to each other. However, the accuracy of these techniques is significantly low in a super-resolution CS problem because of a highly coherent sensing matrix. The replacing indices do not coincide with the actual ones but stay around them locally.

From these properties, LO technique can be a supportive solution to fix the wrongly updated results of GO technique, as described in Algorithm 6.

4.3 Non-negative least squares optimization - POMP

4.3.1 Non-negative constraints

As stated in Section 3.4.5.2, the time profile of MPIs can be reconstructed through the non-negative sparse support estimation using a MFT acquisition. Therefore, solving the following non-negative least squares minimization problem:

$$\boldsymbol{x} = \underset{\boldsymbol{z}}{\operatorname{argmin}} ||\boldsymbol{\Phi z} - \boldsymbol{y}||_2 \quad \text{s.t.} \quad \boldsymbol{z} \geq 0 \tag{4.3}$$

can also resolve MPIs successfully. Lawson [68] introduced a greedy pursuit method, namely Non-negative Least Squares, to estimate a non-negative solution for the above problem (4.3). In our research, it is shortly referred as POMP.

4.3.2 Negative atom removal module

POMP can be considered as a class member of greedy pursuit since it uses the same atom selection procedure of OMP, as described in Algorithm 7. At each iteration, after least squares minimization, the magnitude of some support indices may be negative. This result violates the non-negative constraint of the problem (4.3). Therefore, the Negative Atom Removal (NAR) approach aims to eliminate these negative indices from the current support set. As a result, the achieved solution is non-negative.

Algorithm 7 Negative Atom Removal Module (NAR)

Input: $\boldsymbol{y}$, $\boldsymbol{\Phi}$, $\boldsymbol{x}$, T, $\boldsymbol{x}_{prev}$
Output: $\boldsymbol{x}$, T
while $\exists x_j < 0$ for $j \in T$ **do**
  Let $\alpha = \min \frac{x_{prev,i}}{x_{prev,i} - x_i}$ for $i \in T$ and $x_i \leq 0$
  $\boldsymbol{x}_{prev} = \boldsymbol{x}_{prev} + \alpha(\boldsymbol{x} - \boldsymbol{x}_{prev})$
  Set $T = \text{supp}(\boldsymbol{x}_{prev})$
  $\boldsymbol{x} = \text{argmin}_{\boldsymbol{z}} ||\boldsymbol{\Phi z} - \boldsymbol{y}||_2$ s.t. $\text{supp}(\boldsymbol{z}) = T$
end while

Algorithm 8 Non-negative least squares - POMP

Input: $\boldsymbol{y}$, $\boldsymbol{\Phi}$, tolerance ϵ
Output: $\boldsymbol{x}_n$, T_n
Initialization: $\boldsymbol{x}_0 = 0, \boldsymbol{r}_0 = y, T_0 = \emptyset$ and n=1
while $||\boldsymbol{\Phi x} - \boldsymbol{y}||_2 \geq \epsilon$ **do**
  $i_n = \arg\max_i |\langle \boldsymbol{r}_{n-1}, \boldsymbol{a}_i \rangle|$
  $T_n = T_{n-1} \bigcup i_n$
  $\boldsymbol{x}_n = \text{argmin}_{\boldsymbol{z}} ||\boldsymbol{\Phi z} - \boldsymbol{y}||_2$ s.t. $\text{supp}(\boldsymbol{z}) = T_n$
  if $\exists x_j < 0$ for $j \in T_n$ **then**
    $(T_n, \boldsymbol{x}_n) = \text{NAR}(\boldsymbol{x}_n, \boldsymbol{x}_{n-1}, \text{T})$
  end if
  Set $\boldsymbol{x}_{n-1} = \boldsymbol{x}_n$
  $\boldsymbol{r}_n = \boldsymbol{y} - \boldsymbol{\Phi x}_n$
end while

4.3.3 Advantages and disadvantages

As described in Algorithm 8, POMP stops until finding a linear combination of observations closest to the measurement vector. Therefore, the signal reconstruction is exact if measurements are noiseless. Additionally, POMP requires no priorly known information of the sparsity. Nevertheless, it runs with a significant amount of iterations to obtain the final result and hence consumes much computation time and brings non-negative solutions with a higher sparsity ($||\boldsymbol{x}||_0 \geq K$). Thus, only K largest-magnitude atoms are kept for a relaxed support evaluation in our numerical experiments.

4.4 Non-negative magnitude adjustment orthogonal matching pursuit

For a fast non-negative estimation, we propose a new reconstruction algorithm, named Non-negative magnitude adjustment orthogonal matching pursuit (Ma-OMP) in this part.

4.4.1 Basic idea

In each atom selection iteration of the greedy pursuits, the estimate of the atom magnitudes conventionally relies on least-mean-squares minimization. However, in a super-resolution CS problem, this magnitude estimation is inaccurate if the observations of non-zero atoms are highly coherent. Suppose that the residual is the linear combination of two highly coherent columns $\boldsymbol{\phi}_{i_1}$ and $\boldsymbol{\phi}_{i_2}$ of a super-resolution CS sensing matrix:

$$\boldsymbol{r} = a_1\boldsymbol{\phi}_{i_1} + a_2\boldsymbol{\phi}_{i_2} \tag{4.4}$$

where a_1 and a_2 are the actual non-negative magnitudes. Then, a new non-zero index is selected through finding the best matching between the residual vector $\boldsymbol{r}$ and all sensing matrix columns $\boldsymbol{\phi}_i$:

$$i_{new} = \underset{i}{\operatorname{argmax}}\, \boldsymbol{\phi}_i^H \boldsymbol{r} \tag{4.5}$$

Since the coherence of columns from i_1 to i_2 is high and a_1, a_2 are non-negative, the newly selected non-zero index stays around i_1 or i_2 and due to least mean square (LMS) minimization, its estimated magnitude will be:

$$a_{new} = \lambda_1 a_1 + \lambda_2 a_2 \tag{4.6}$$

where λ_1 and λ_2 are weighting factors which highly depend on the coherences between the observation of the wrongly estimated index $\boldsymbol{\phi}_{i_{max}}$ and two columns $\boldsymbol{\phi}_{i_1}$ and $\boldsymbol{\phi}_{i_2}$ respectively. Since a_1 and a_2 are non-negative, λ_1 and λ_2 are also non-negative. In the worst case, if all three columns $\boldsymbol{\phi}_{i_{new}}$, $\boldsymbol{\phi}_{i_1}$ and $\boldsymbol{\phi}_{i_2}$ are likely similar then $\lambda_1 = \lambda_2 = 1$ and hence $a_{new} = a_1 + a_2$. These wrongly estimated magnitudes may cause the inaccuracy of atom selection in the next iterations.

4.4.2 Non-negative magnitude adjustment orthogonal matching pursuit - Ma-OMP

Due to the above analysis, this method uses an adjustment factor ($0 < \rho \leq 1$) to regulate the wrongly estimated magnitude a_{new} in (4.6). As described in Algorithm 9, this adjustment process is proceeded only if the newly selected atom index is not present in

the current support set T_{k-1}. The adjustment of the estimated non-negative magnitude is expected to bring a high accuracy of atom selection in the next iterations.

Algorithm 9 Non-negative Magnitude Adjustment Orthogonal Matching Pursuit - (Ma-OMP)

Input: $\boldsymbol{y}$, $\boldsymbol{\Phi}$, K
Output: $\boldsymbol{x}$, T
1: Initialization: $\boldsymbol{x} = 0, \boldsymbol{r}_0 = y, T_0 = \emptyset$, $k = 0$
2: **while** $||T_k||_0 < K$ **do**
3: $k = k + 1$
4: $i_k = \arg\max_i |\langle \boldsymbol{r}_{k-1}, \boldsymbol{a}_i \rangle|$
5: Compute $a_k = \text{argmin}_{a_k} ||a_k \boldsymbol{\phi}_{i_k} - \boldsymbol{r}_{k-1}||_2$
6: **if** $i_k \in T_{k-1}$ **then**
7: $x_{i_k} = x_{i_k} + a_k$
8: **else**
9: $T_k = T_{k-1} \bigcup i_k$
10: $x_{i_k} = \rho a_k$
11: **end if**
12: $\boldsymbol{r}_k = \boldsymbol{y} - \boldsymbol{\Phi x}$
13: **end while**
14: Set $T = T_K$
15: $\boldsymbol{x} = \text{argmin}_{\boldsymbol{z}>0} ||\boldsymbol{\Phi z} - \boldsymbol{y}||_2$ s.t. $\text{supp}(\boldsymbol{z}) = T$

4.4.3 Modified non-negative magnitude adjustment orthogonal matching pursuit - Ma-OMP3

Modified Non-negative Magnitude Adjustment Orthogonal Matching Pursuit or shortly Ma-OMP3 is the insertion of a GO step at the end of Ma-OMP to fix the wrongly estimated indices, similar to OMP3. This method is described in Algorithm 10. Besides, LO technique can additionally improve the quality of support recovery of Ma-OMP3.

Algorithm 10 Modified Cyclic Non-negative Magnitude Adjustment Orthogonal Matching Pursuit - Ma-OMP3

Input: $\boldsymbol{y}$, $\boldsymbol{\Phi}$, K
Output: $\boldsymbol{x}$, T
1: $[\boldsymbol{x}, T]$= Ma-OMP($\boldsymbol{y}$, $\boldsymbol{\Phi}$, K)
2: $T = \text{GO}(T_K)$
3: Additional step: $T = \text{LO}(T, \Delta_{LO})$
4: $\boldsymbol{x} = \text{argmin}_{\boldsymbol{z}>0} ||\boldsymbol{\Phi z} - \boldsymbol{y}||_2$ s.t. $\text{supp}(\boldsymbol{z}) = T$

Both POMP and Ma-OMP3 are non-negative greedy pursuits in this thesis. The number of running iterations in Ma-OMP is larger than that in OMP but significantly smaller than that in POMP. As a result, Ma-OMP3 has a short processing time.

4.4.4 Optimized adjustment factor

Different positive adjustment factors ρ can bring different support recovery performances of Ma-OMP3. For instance, if $\rho \approx 1$, Ma-OMP3 is equivalent to OMP3. Whereas, if the adjustment factor is significantly small, the atom selection module of Ma-OMP3 aims to select simultaneously neighboring indices with highly coherent observations. Therefore, an adjustment factor should be selected appropriately for enhancing the sparse reconstruction capabilities of Ma-OMP3.

4.5 Numerical results

In this part, the reconstruction performance of several proposed methods, i.e., BLOOMP, OMP3, POMP, Ma-OMP3, are analyzed for a super-resolution MFT acquisition in the configuration of a large refinement factor ($F = 100$). These results are then compared to those of some super-resolution l_1-optimization algorithms, i.e., BPIC, SURE-IR [23].

4.5.1 Preliminaries

Similar to the previous numerical experiments in Section 3.4, we carry out Monte Carlo simulations in this part to obtain the reconstruction capabilities of each CS algorithm in the cases of various SNRs and various MDs.

- The first analysis of a CS algorithm demonstrates its relaxed support recovery rates R_b with a tolerance offset δ in the cases of various SNRs (from 5dB to 40 dB). The results are achieved after 3000 trials for greedy pursuits or 500 trials for basis pursuits (BP) in each case of SNR. At each trial, a non-negative K-sparse signal is generated with a lower bound condition $\Delta T \geq 2\delta + 1$ and subsequently a noisy measurement vector.

- The second analysis is the relaxed support recovery rates R_b with a tolerance offset δ at various MDs (from $2\delta + 1$ to 150 bins). Different from the first analysis, we generate a non-negative K-sparse signal whose MD is equal to the analyzed MD value. All other procedures are similar to the first one. For this analysis, there are two cases of SNRs, i.e., 15 dB (high noise level) and 30 dB (low noise level). The achieved results are averaged after 500 trials for greedy pursuits or 200 trials for basis pursuits in each case of MD.

For the comparison between CS reconstruction algorithms, the same parameters of a MFT acquisition are set in all Monte Carlo simulations. For 3-sparse reconstruction, a set of 20 different frequencies are selected randomly from the full set Ψ with $f_{max} = 30$ MHz. According to (3.31), we construct a real-valued super-resolution MFT sensing matrix $\boldsymbol{\Phi} \in \mathbb{R}^{20\times 500}$ with $L = 5$ and a large refinement factor $F = 100$.

4.5.2 Optimized adjustment factor of Ma-OMP3

This part aims to indicate which adjustment factor ρ is the best choice for the proposed recovery method Ma-OMP3. For a comparison, several variants of Ma-OMP3 with different values of $\rho \in \{0.9, 0.8, 0.75,\ 0.7, 0.5, 0.3\}$ are used for 3-sparse reconstruction based on the same realisation of the measurement vector $\boldsymbol{y}$ and MFT sensing matrix $\boldsymbol{\Phi}$. The achieved results in the cases of various SNRs and MDs are shown in Fig. 4.4 and Fig. 4.5 respectively.

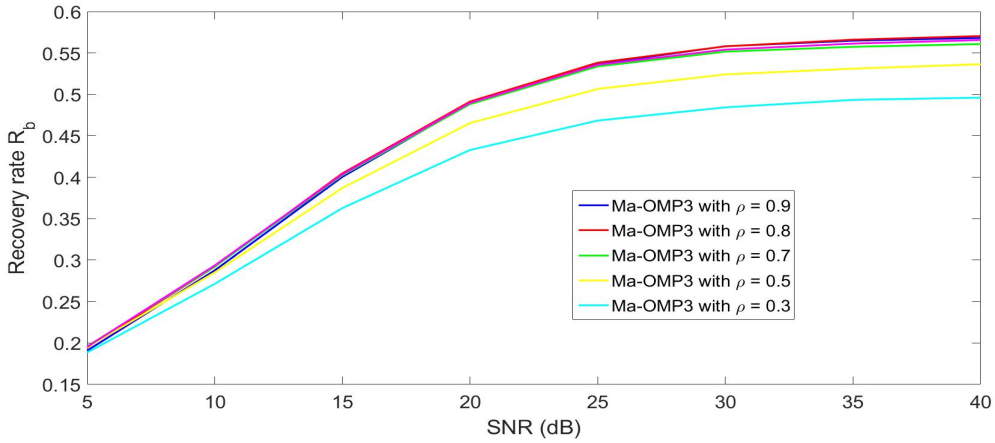

(a) Relaxed support recovery rate with $\delta = 2$

Figure 4.4. Comparison between support recovery performance of different Ma-OMP3 variants with different values of ρ for the real sensing matrix $\Phi^{20\times 500}$ at different SNRs (3000 trials for each SNR). Choose $N = 500, L = 5, f_{max} = 30$ MHz, $F = 100, K = 3, \Delta r = 5$ cm.

Firstly, as can be seen in Fig. 4.4 that the variants of Ma-OMP3 with $\rho = 0.8$ (red line) and $\rho = 0.9$ (blue line) bring higher relaxed support recovery rates with two different tolerance offsets, i.e., $\delta = 2$ and $\delta = 5$, when SNR is high. Whereas, the lower values of ρ (0.5 - yellow line and 0.3 - cyan line) are apparently the wrong choices with significantly low reconstruction rates. Secondly, as Fig. 4.5 shows, the variants of Ma-OMP3 with $\rho = 0.9$ (blue line) acquires the highest rate ($\delta = 2$) at large MDs. Whereas, the variant of Ma-OMP3 with $\rho = 0.7$ (green line) brings the highest rate ($\delta = 2$) at small MDs.

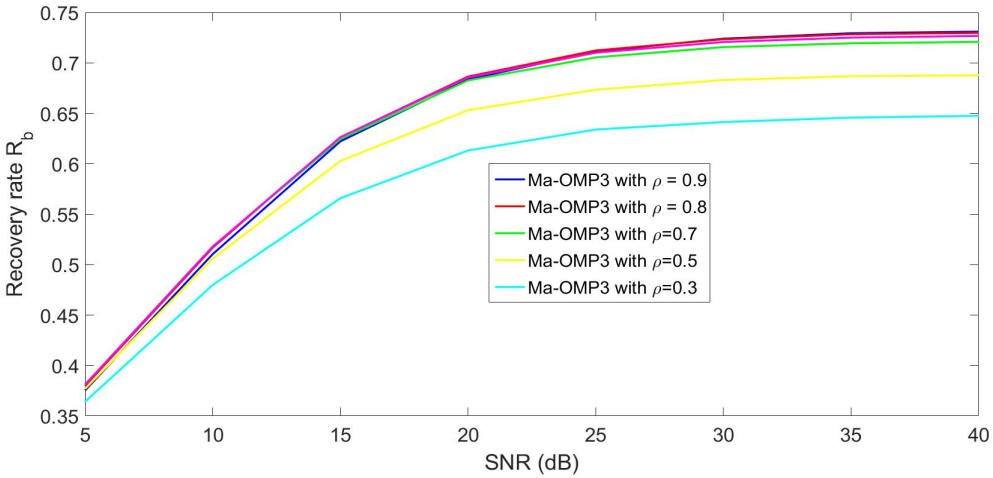

(b) Relaxed support recovery rate with $\delta = 5$

Figure 4.4. Comparison between support recovery performance of different Ma-OMP3 variants with different values of ρ for the real sensing matrix $\Phi^{20\times500}$ at different SNRs (3000 trials for each SNR). Choose $N = 500, L = 5, f_{max} = 30$ MHz, $F = 100, K = 3$, $\Delta r = 5$ cm (cont).

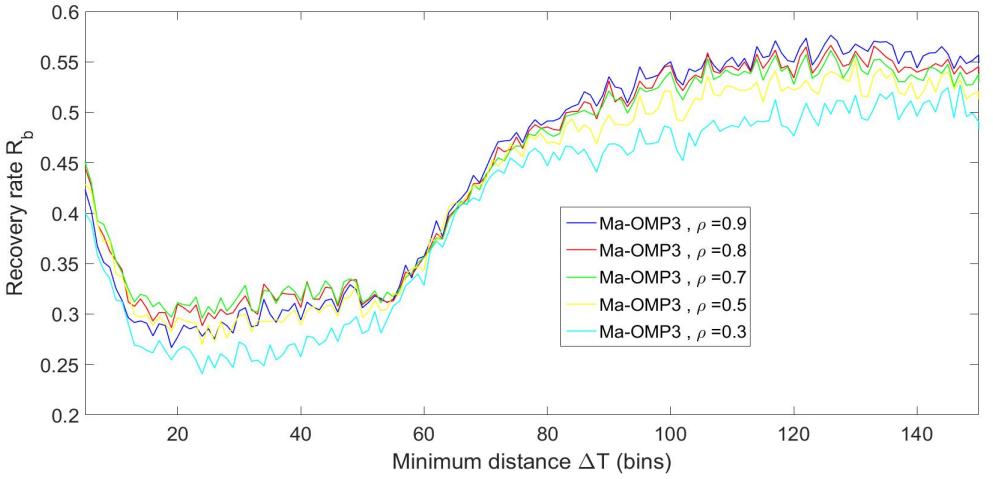

(a) 15dB, $\delta = 2$ (bins)

Figure 4.5. Comparison between support recovery performance of different Ma-OMP3 variants with different values of ρ for the real sensing matrix $\Phi^{20\times500}$ at different MDs (500 trials for each MD). Choose $N = 500, L = 5, f_{max} = 30$ MHz, $F = 100, K = 3$, $\Delta r = 5$ cm.

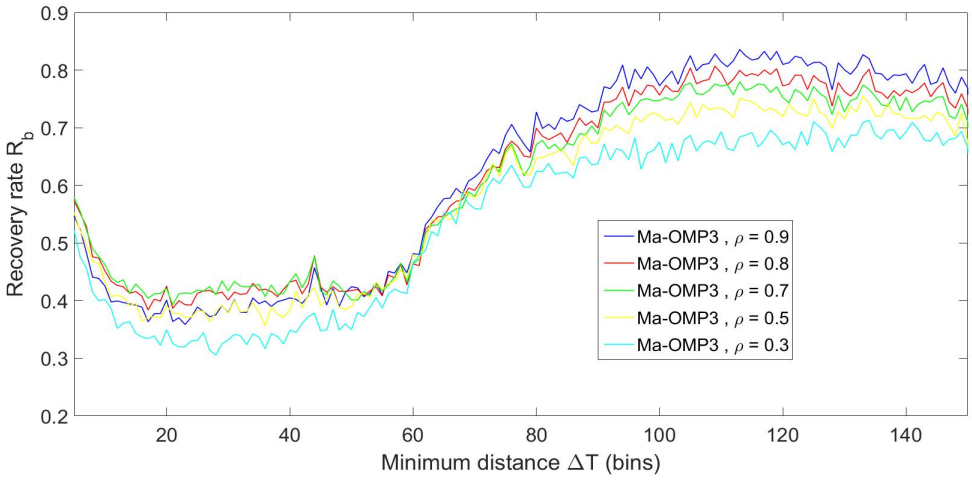

(b) 30dB, $\delta = 2$ (bins)

Figure 4.5. Comparison between support recovery performance of different Ma-OMP3 variants with different values of ρ for the real sensing matrix $\Phi^{20\times500}$ at different MDs (500 trials for each MD). Choose $N = 500, L = 5, f_{max} = 30$ MHz, $F = 100, K = 3$, $\Delta r = 5$ cm (cont).

For a balance between them, $\rho = 0.8$ (red line) is apparently an appropriate choice for Ma-OMP3 to achieve moderate reconstruction rates in all cases of various MDs and SNRs. Thus, we set $\rho = 0.8$ for Ma-OMP3 in our subsequent numerical and practical experiments.

4.5.3 Comparison between different methods

This part aims to compare the reconstruction capabilities of many proposed greedy pursuit methods, i.e., BLOOMP, OMP3, POMP, and Ma-OMP3. Besides, two other super-resolution CS methods, i.e., SURE-IR[23] and BPIC, are additionally analyzed. Before sparse signal reconstruction, each algorithm requires some following configurations:

- OMP3, POMP and Ma-OMP3 assume the availability of the known sparsity $K = 3$.
- BPIC is l_1 optimization method for the problem P_2 in (3.5). It assumes the availability of the known noise variance $\epsilon = 1.2||\boldsymbol{y} - \hat{\boldsymbol{y}}||_2$ where $\hat{\boldsymbol{y}}$ is the noiseless measurement vector. CVX-package is used for implementing this method in Matlab.
- BLOOMP is configured with an excluded band radius of 5 bins and a LO range of 20 bins.

- SURE-IR is a dictionary refinement algorithm proposed by Fang et al. [23]. The initial number of grids is set equal to $K = 3$ to reduce computation time.

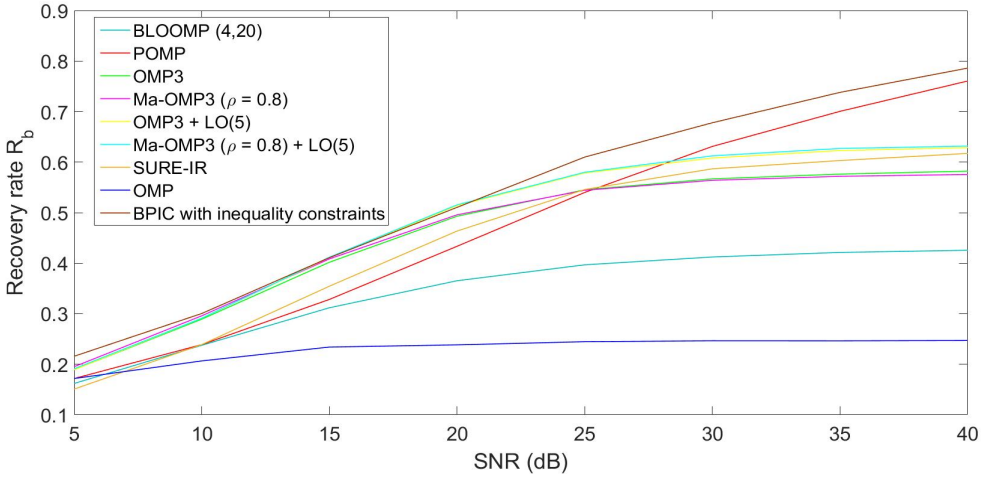

Figure 4.6. Comparison between support recovery performance of different methods for the real sensing matrix $\Phi^{20\times500}$ at different SNRs (3000 trials for each SNR). Choose $N = 500, L = 5, f_{max}$ = 30 MHz, $F = 100, K = 3$, $\Delta r = 5$ cm

After sparse reconstruction, the achieved results are evaluated under the relaxed detecting condition with a tolerance offset $\delta = 2$. Fig. 4.6 and Fig. 4.7 demonstrate these relaxed support recovery rates in the cases of different SNRs and MDs respectively.

Firstly, it can be seen in Fig. 4.6 that the relaxed support rate of l_1-optimization (BPIC) (brown line) is the highest one among all analyzed methods at most cases of SNRs. The significant strength of BPIC occurs at high SNRs (SNR $\geq$ 22 dB). It seems possible that these good results are due to the extremely accurate noise variance $\epsilon = 1.2||\boldsymbol{y} - \boldsymbol{y}_{noiseless}||$ in the cases of high SNRs. However, such a precise prediction of a noise variance is usually hard in a practical application. Whereas, as Fig. 4.7 shows, BPIC brings the highest rates at small MDs but the lower ones at large MDs. From these results, although BPIC consumes a massive computation time, it seems to be not the best method in all cases. For instance, OMP3 outperforms BPIC in the cases of large MDs ($\Delta T \geq 45$).

Secondly, SURE-IR (orange lines) can bring only a moderately good reconstruction results, in comparison to greedy pursuit methods. As Fig. 4.6 shows, the relaxed support rates of OMP3 and Ma-OMP3 are even higher than those of SURE-IR in the highly noisy cases (SNR$\leq$ 26 dB). Whereas, POMP outperforms SURE-IR in the cases of high SNRs. In general, SURE-IR brings no impressive reconstruction results.

Thirdly, BLOOMP (turkish blue lines) outperforms OMP in all cases of various SNRs

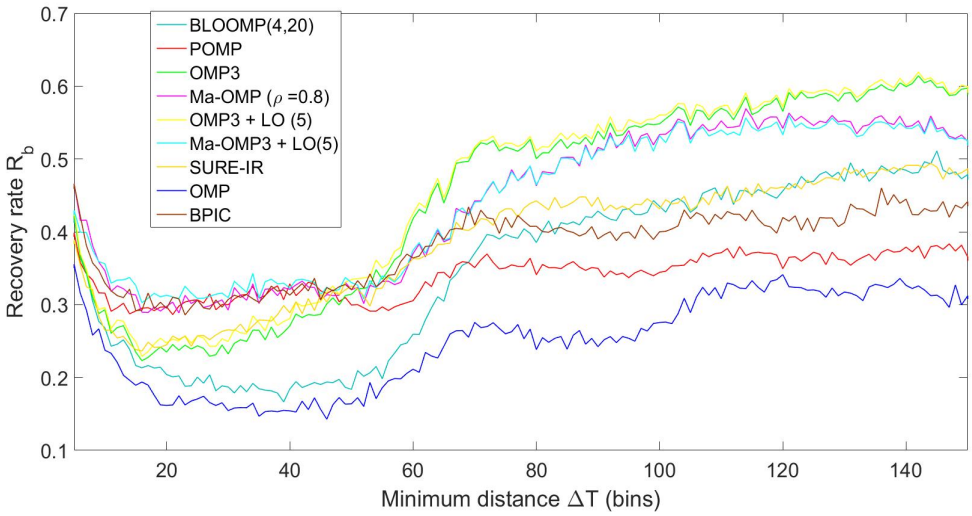

(a) 15dB, $\delta = 2$ (bins)

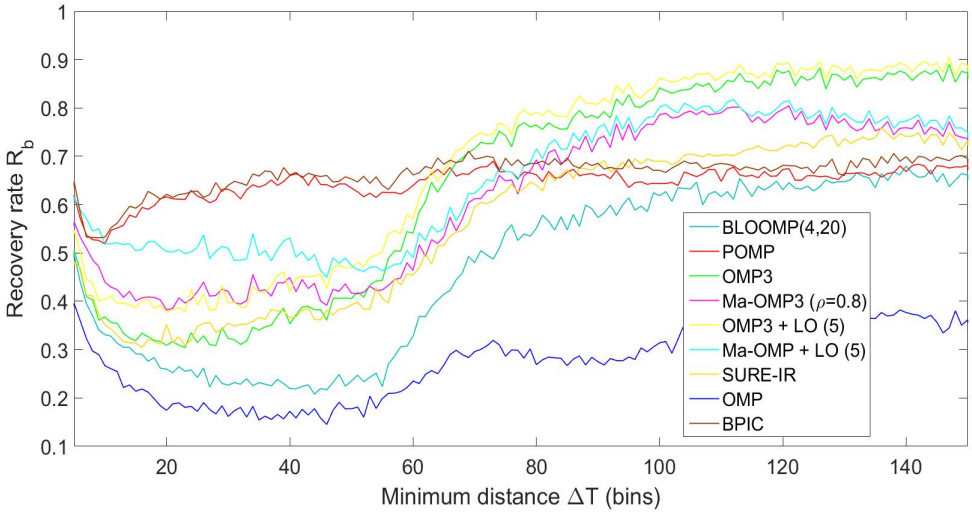

(b) 30dB, $\delta = 2$ (bins)

Figure 4.7. Comparison between support recovery performance of different methods for the real sensing matrix $\Phi^{20\times500}$ at different MDs (500 trials for each MD). Choose $N = 500, L = 5, f_{max} =$ 30 MHz, $F = 100, K = 3$, $\Delta r = 5$ cm

and MDs. But its relaxed support recovery rates are significantly lower than those of the other greedy pursuit methods, i.e., OMP3, POMP, and Ma-OMP3, (green, red, rose

lines) in most cases of SNRs and MDs. Exceptionally, in Fig. 4.7a, this method has some advantages over BPIC and POMP (brown and red lines) at large MDs when SNR is 15 dB.

Especially, as Fig. 4.6 shows, OMP3 and Ma-OMP3 (green and rose lines) have advantages in the cases of low SNRs while POMP (red line) performs better at high SNRs. Moreover, OMP3 and Ma-OMP3 with the support of LO technique (yellow and cyan lines) can even bring a significant improvement of support recovery performance in the cases of high SNRs. Additionally, as Fig. 4.7 shows, OMP3 (green lines) outperforms POMP and Ma-OMP3 (red and rose lines) at small MDs while POMP and Ma-OMP3 outperform OMP3 at large ones. From these results, we summarize:

- OMP3 is an appropriate method at large MDs without any concern of SNR.
- POMP is an appropriate method at small MDs without any concern of SNR. However, it consumes much computation time.
- Ma-OMP3 is an appropriate method at small MDs only in the cases of very low SNRs (SNR =15 dB). Besides, this method brings better support recovery rates at large MDs.

Eventually, the proposed greedy pursuits, i.e., POMP, Ma-OMP, and OMP3, have their reconstruction strengths in some cases of MDs or SNRs for a super-resolution MFT acquisition. More concisely, as can be seen in Fig. 4.7 that the sum of these strengths (red lines in small-MD cases and green lines in large-MD cases) outperforms the available super-resolution CS algorithms, e.g., BLOOMP, SURE-IR, BPIC. Besides, these greedy pursuits run with fast-processing speed. However, they require a known sparsity. Additionally, LO technique shows its capabilities to improve the relaxed support recovery performance of OMP3 and Ma-OMP in the cases of small MDs and high SNRs (see Fig. 4.7b).

4.5.4 Considered parameters

There are many different parameters which influence on the recovery performance of a CS algorithm. Thus, in this part, we aim to analyze three factors including number of measurements (M), dynamic range (DR) and signal sparsity (K) in a super-resolution MFT acquisition.

4.5.4.1 Number of measurements

According to CS theory in (3.46), there exists a lower bound on the number of measurements to guarantee a high stability of accurate K-sparse reconstruction. However, if the mutual coherence of the sensing matrix is significantly large, we theoretically

need a huge number of measurements for a good reconstruction quality. Although our super-resolution MFT sensing matrix with $F = 100$ is highly coherent, our current experiments uses only 20 TOF measurements to reconstruct a 3-sparse signal. For this reason, the quality of the previous sparse reconstruction is certainly poor. In this part, we analyze the variation of the recovery performance with an increase of the measurement number. To be concrete, three super-resolution MFT acquisitions with $M = 20$, $M = 40$ and $M = 60$ are constructed with the same parameters, i.e., $L = 5$, $N = 500$, $f_{max} = 30$ MHz, $F = 100$. Similar to the previous numerical experiments, a Monte Carlo simulation is carried out with 500 trials for each MD case to achieve the reconstruction results in three above MFT acquisitions at various MDs. Three greedy pursuit methods, i.e., OMP3, POMP, and Ma-OMP3 are used for the 3-sparse signal reconstruction. Their achieved relaxed support recovery rates are demonstrated with SNR = 15 dB in Fig. 4.8a and SNR = 30 dB in Fig. 4.8b.

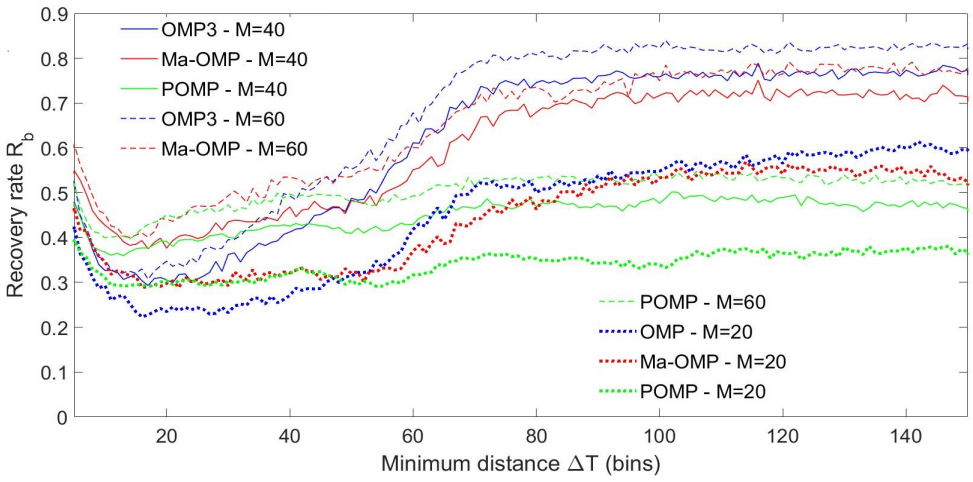

(a) 15dB, $\delta = 2$ (bins)

Figure 4.8. Comparison between support recovery performance of different real sensing matrices $\Phi^{20\times500}$, $\Phi^{40\times500}$ and $\Phi^{60\times500}$ at different MDs (500 trials for each MD). Choose $L = 5, f_{max} =$ 30 MHz, $F = 100, K = 3$, $\Delta r = 5$ cm.

Fig. 4.8 clearly shows that more measurements can bring higher relaxed support recovery rates ($\delta = 2$) of all three used methods in all cases of MDs when SNR is low (SNR = 15 dB) or high (SNR = 30 dB). However, the first increase of 20 measurements (from $M = 20$ - dot lines to $M = 40$ - solid lines) brings a significantly higher improvement of recovery quality, compared to the second increase (from $M = 40$ - solid lines to $M = 60$ - dashed lines). These results indicate that there may exist an upper bound on the measurement number at which the improvement of recovery performance is signifi-

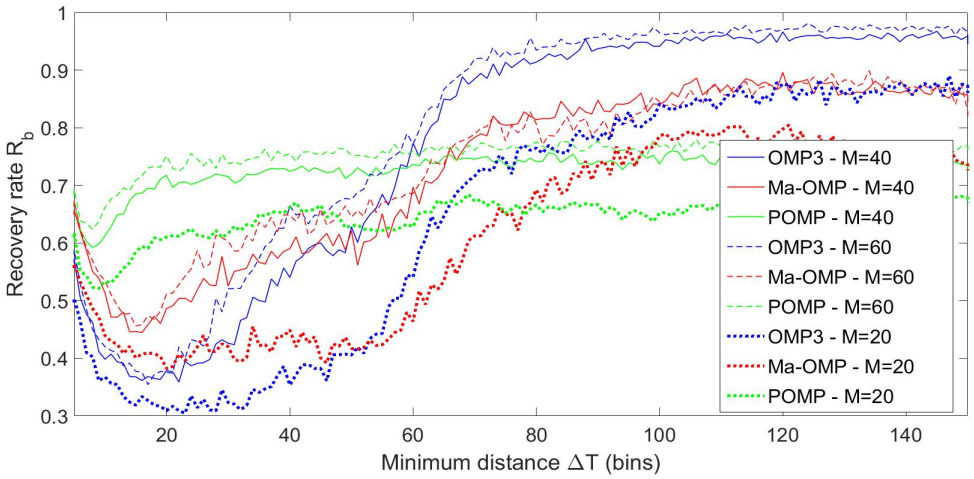

(b) 30dB, $\delta = 2$ (bins)

Figure 4.8. Comparison between support recovery performance of different real sensing matrices $\Phi^{20\times500}$, $\Phi^{40\times500}$ and $\Phi^{60\times500}$ at different MDs (500 trials for each MD). Choose $L = 5, f_{max} =$ 30 MHz, $F = 100, K = 3$, $\Delta r = 5$ cm (cont).

cantly small if increasing the number of measurements. Eventually, in a super-resolution CS problem, more measurements consume more acquisition time but apparently do not guarantee a highly better sparse reconstruction quality as in expectation.

4.5.4.2 Dynamic range

Let $\boldsymbol{x}$ be K-sparse vector. Dynamic range of $\boldsymbol{x}$ is defined by:

$$DR = \frac{x_{max}}{x_{min}} \tag{4.7}$$

where

$$x_{max} = \max_{k, x_k \neq 0} |x_k|, \quad x_{min} = \min_{k, x_k \neq 0} |x_k|, \tag{4.8}$$

As proven in [19, 66], dynamic range (DR) is a crucial factor which influences much on sparse recovery performance of any CS algorithm in a super-resolution CS problem. To be concrete, it hardly reconstructs a sparse signal support accurately in the case of a large DR. Therefore, this part carries out a similar numerical experiment to show the reconstruction capabilities of three concerned algorithms OMP3, POMP and Ma-OMP3 in the cases of two different DRs, i.e., $DR = 1$ (small) and $DR = 20$ (large). Their relaxed support recovery rates are averaged after 500 trials for each case of different MD (from 1 to 150 bins) and then demonstrated in Fig. 4.9.

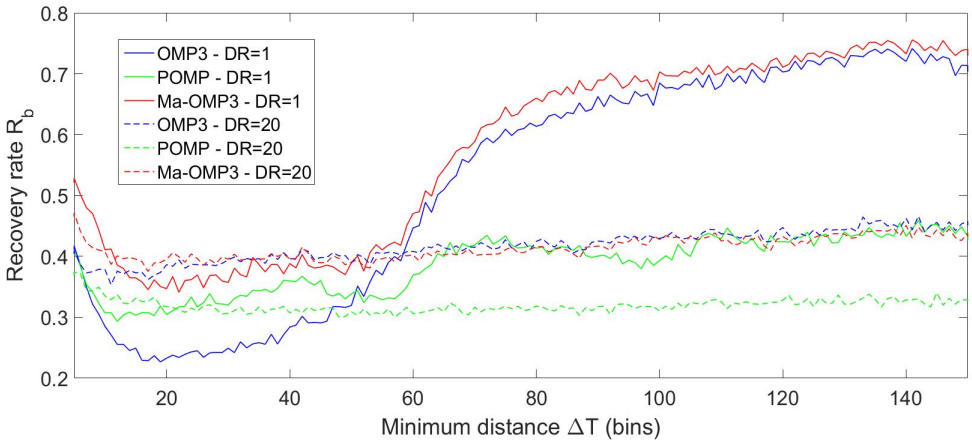

(a) 15dB, $\delta = 2$ (bins)

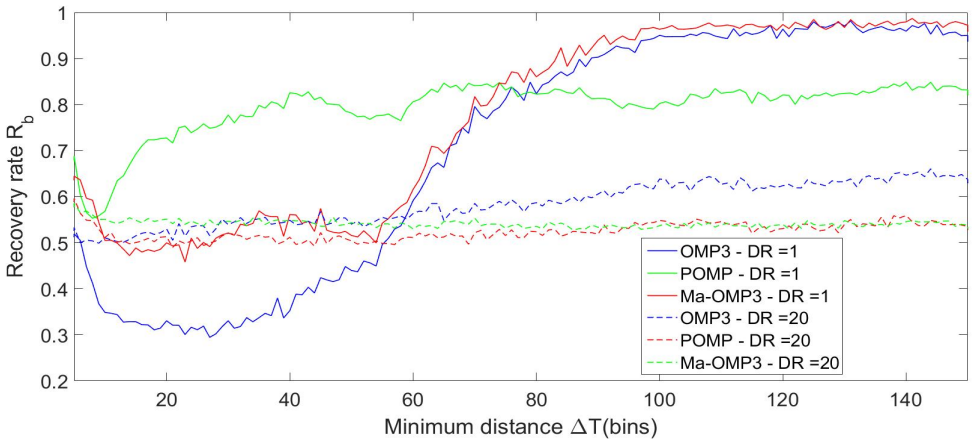

(b) 30dB, $\delta = 2$ (bins)

Figure 4.9. Comparison between support recovery performance for the cases of two different DRs at different MDs (500 trials for each MD). Choose $N = 500$, $M = 20$, $L = 5$, $f_{max} = 30$ MHz, $F = 100$, $K = 3$, $\Delta r = 5$ cm.

As Fig. 4.9 shows, the reconstruction quality of all three methods in the case of a small DR (solid lines) is much better than that in the case of a large DR (dash lines). These results coincide with the theorems proven by many previous studies [19, 66]. Additionally, Ma-OMP3 (red lines) outperforms OMP3 (blue lines) at a small DR but OMP3 inversely does at a large DR.

4.5.4.3 Sparsity

This part evaluates the recovery performance for a super-resolution MFT acquisition in the cases of different sparsity values ($K = 3$ or $K = 6$). For this analysis, we construct a real-valued MFT sensing matrix $\mathbf{\Phi} \in \mathbb{R}^{40\times1200}$ with a large refinement factor $F = 100$. Similar to the previous simulations, we use three greedy pursuit methods, i.e., OMP3, POMP, and Ma-OMP3 for K-sparse signal reconstruction. A larger dimension $N = 1200$ is selected so that many cases of different MDs from 1 to 150 bins can be included in this experiment. Besides, the maximum separation between non-zero atoms in sparse signal $\boldsymbol{x}$ is maintained below 180 bins for a comparison between 6-sparse and 3-sparse signal reconstruction in a fair manner. The achieved relaxed support recovery rates with a tolerance offset $\delta = 2$ are averaged after 500 trials for each MD case and then demonstrated for the case of SNR = 15 dB in Fig. 4.10a and SNR = 30 dB in Fig. 4.10b.

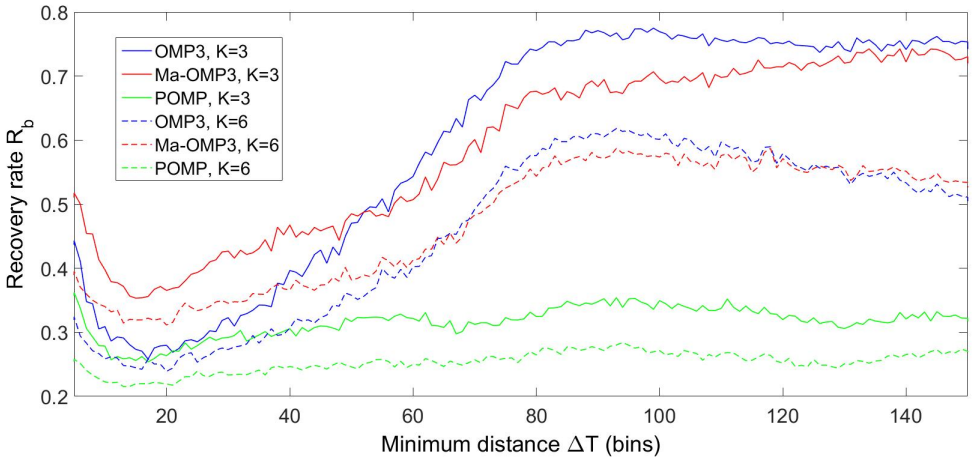

(a) 15dB, $\delta = 2$ (bins)

Figure 4.10. Comparison between support recovery performance for different sparsity K at different MDs (500 trials for each MD). Choose $N = 1200$, $M = 40$, $L = 5$, $f_{max} = 30$ MHz, $F = 100$, $\Delta r = 5$ cm.

The results in Fig. 4.10 indicate that the relaxed support recovery rates of all three methods become lower in all cases of MDs for the 6-sparse reconstruction. Eventually, we need more TOF measurements for resolving more MPIs in a real-life scene.

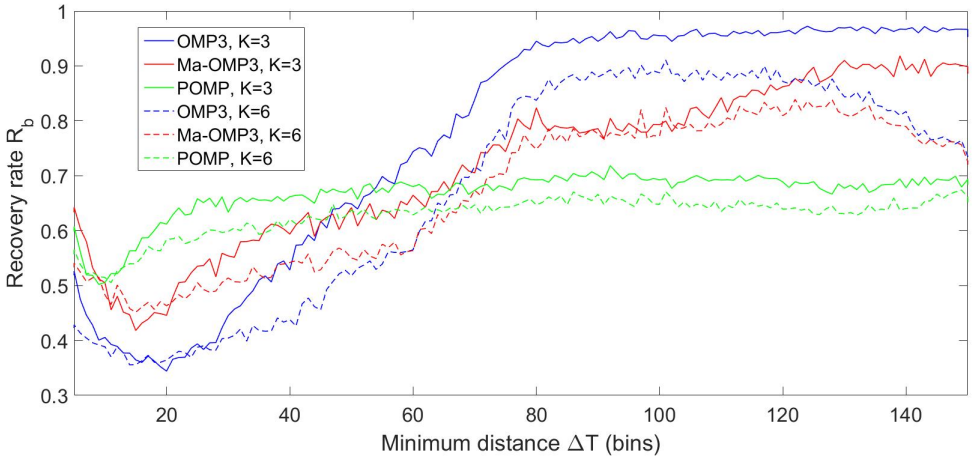

(b) 30dB, $\delta = 2$ (bins)

Figure 4.10. Comparison between support recovery performance for different sparsity K at different MDs (500 trials for each MD). Choose $N = 1200$, $M = 40$, $L = 5$, $f_{max} = 30$ MHz, $F = 100$, $\Delta r = 5$ cm (cont).

4.6 Combined OMP based on predicted minimum distance - CMD-OMP

4.6.1 Basic idea

As proven earlier in Fig. 4.7, three methods, i.e., OMP3, Ma-OMP3, and POMP possess their strengths in the cases of various MDs and SNRs. Therefore, if the minimum distance and noise level can be predicted, then one of three above methods can be chosen appropriately for a specific case. As a result, a higher stability of accurate sparse recovery can be obtained through this combination. Due to this solution approach, we introduce Combined OMP based on Predicted Minimum Distance (CMD-OMP).

Firstly, the strengths of all three methods should be explored more carefully in the cases of various MDs and SNRs. For this purpose, a Monte Carlo simulation is carried out to achieve the relaxed support recovery rates ($\delta = 2$) of each method in a specific case of MD and SNR. In this analysis, we construct a real-valued MFT sensing matrix $\mathbf{\Phi} \in \mathbb{R}^{20\times 500}$ with the same previous parameters $L = 5$, $f_{max} = 30$ MHz, $F = 100, M = 20$ and $N = 500$. Fig. 4.11a, Fig. 4.11c and Fig. 4.11e demonstrate the achieved results of POMP, OMP3 and Ma-OMP3 respectively for the 3-sparse reconstruction.

A comparison between the results of POMP in Fig. 4.11a and OMP3, Ma-OMP3 in Fig. 4.11c and Fig. 4.11e reveals that POMP outperforms at small MDs in most cases of

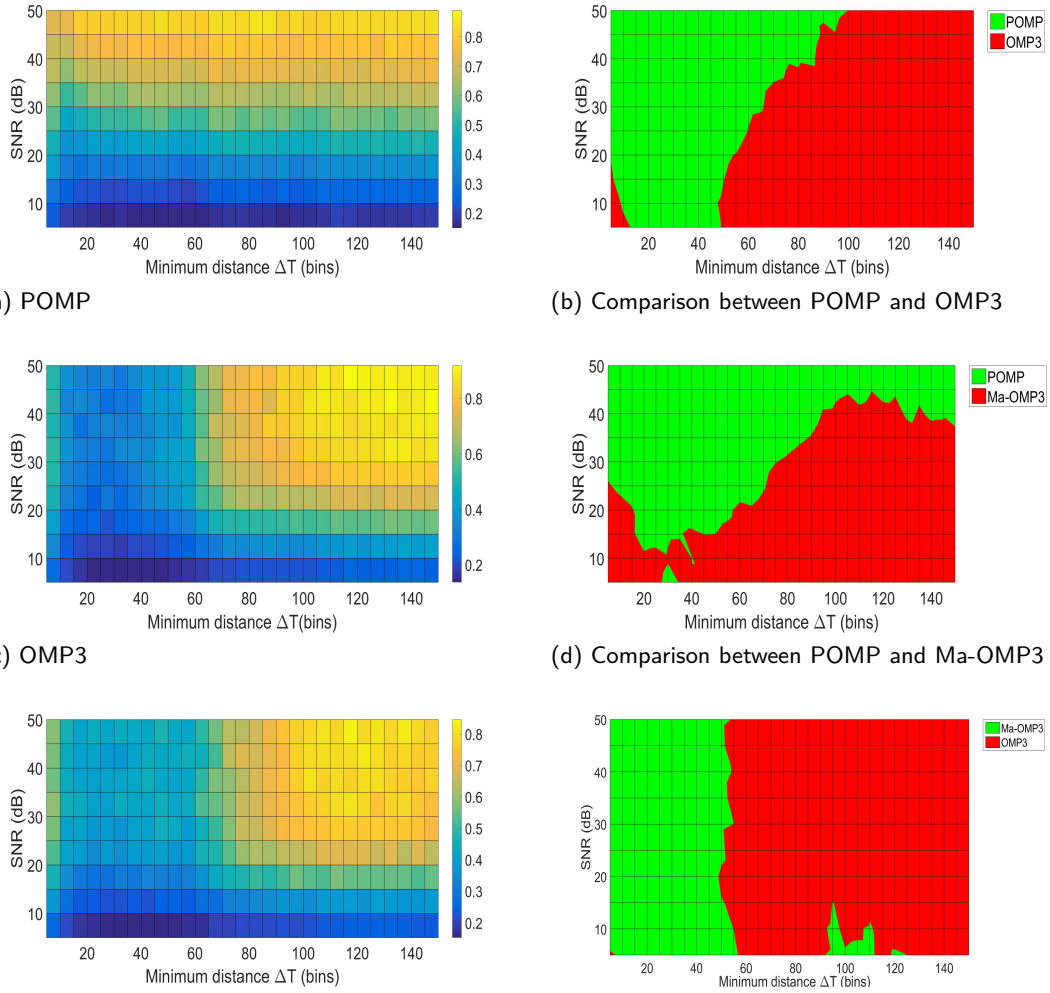

(a) POMP

(b) Comparison between POMP and OMP3

(c) OMP3

(d) Comparison between POMP and Ma-OMP3

(e) Ma-OMP3

(f) Comparison between OMP3 and Ma-OMP3

Figure 4.11. 3D representation of the relaxed support recovery performance ($\delta = 2$) of OMP3, POMP and Ma-OMP3 at different MDs and SNRs (500 trials for each pair of SNR and MD). Choose $N = 500, M = 20, L = 5, f_{max} = 30$ MHz, $F = 100, K = 3, \Delta r = 5$ cm

SNRs. However, these result demonstrations are apparently hard to give more arguments about the comparison between three methods. For this reason, the reconstruction results of each two algorithms are mapped together into the same 3D figure. Each point of the new image represents which method possesses a higher recovery rate in a specific case of MD and SNR. For instance, in Fig. 4.11b, the green points denote the cases of MDs and SNRs at which POMP outperforms OMP3. Inversely, the red region indicates

Algorithm 11 Combined based on Minimum Distance Orthogonal Matching Pursuit (CMD-OMP)

Require: $\boldsymbol{y}$, $\boldsymbol{\Phi}$, K
Ensure: $\hat{\boldsymbol{x}}$, T
1: Estimate ΔT_{pre}
2: **if** $(\Delta T_{pre} \geq \Delta T_{tuning})$ **then**
3: Run OMP3 with $\boldsymbol{y}$, $\boldsymbol{\Phi}$ to estimate the support T
4: **else**
5: Run POMP with $\boldsymbol{y}$, $\boldsymbol{\Phi}$ to estimate the support T
6: **end if**
7: Estimate $\hat{\boldsymbol{x}}(T) = \boldsymbol{\Phi}(:, T) \backslash \boldsymbol{y}$

where OMP3 outperforms POMP. Similarly, Fig. 4.11d and Fig. 4.11f show the visual comparison between POMP and Ma-OMP3 and the visual comparison between OMP3 and Ma-OMP3 respectively.

As can be seen in Fig. 4.11b and Fig. 4.11d, POMP brings better recovery performances in most cases of small MDs. Exceptionally, Ma-OMP3 outperforms POMP in the case of a significantly low SNR (SNR $\leq$ 12 dB) when MD is very small. In general, if the measurement noise level is not high, POMP is the best method for the cases of small MDs, compared to OMP3 and Ma-OMP3. On the contrary, as Fig. 4.11d and Fig. 4.11f show, OMP3 is the best one at large MDs. In summary, OMP3 and POMP have some advantages regarding reconstruction capabilities in the cases of various MDs. The newly proposed method CMD-OMP aims to integrate these strengths of both POMP and OMP3. Suppose that MD is priorly known in the current scenario, then a correct choice between POMP and OMP3 can bring a good support recovery result. The new method CMD-OMP is described in Algorithm 11. For an accurate selection of reconstruction algorithm, the tuning parameter ΔT_{tuning} and the predicted MD ΔT_{pre} of CMD-OMP should be estimated correctly for each specific scenario.

4.6.2 Tuning parameter estimation

Tuning parameter ΔT_{tuning} is the MD threshold at which CMD-OMP changes the selection from OMP3 to POMP or inversely. More precisely, OMP3 is selected for sparse recovery if the predicted MD is larger than this tuning parameter. Otherwise, POMP is selected for the case of a smaller MD. Therefore, the choice of tuning parameter plays a significant role in CMD-OMP. A correct choice of ΔT_{tuning} can promote the strengths of OMP3 and POMP, but inversely a wrong one causes a poor support recovery performance.

The results in Fig. 4.11b indicate the tuning region between POMP and OMP3 in the cases of different SNRs. To be concrete, a value $\Delta T_{tuning} \in [50, 100]$ is appropriate

for CMD-OMP in the super-resolution MFT acquisition $\mathbf{\Phi} \in \mathbb{R}^{20\times 500}$ with $F = 100$. Note that these values vary wiith different MFT system settings, e.g., refinement factor (F), amount of measurements (M), a range of interest or dimension (N). Therefore, for each various MFT acquisition, a comparison analysis between OMP3 and POMP which is similar to the results in Fig. 4.11b should be carried out again for re-identifying the tuning border of MD in CMD-OMP.

4.6.3 Minimum distance prediction

Besides tuning parameter, a correct selection of the appropriate recovery method (POMP or OMP3) highly depends on the predicted MD. However, the accurate estimation of the actual MD for a specific scenario seems to be impossible in practice if the MFT sensing matrix is highly coherent. Therefore, CMD-OMP aims to explore whether the MD is smaller or larger than the given tuning parameter. Furthermore, this procedure should run shortly in order not to slow down CMD-OMP.

As shown in Fig. 3.5, the support recovery performance of OMP is significantly higher in the configuration of a smaller refinement factor. Additionally, OMP is a fast-processing greedy pursuit. Therefore, the prediction of MD in our proposed CMD-OMP relies on these advantages of OMP. Firstly, based on the available super-resolution MFT sensing matrix $\mathbf{\Phi}$ with $F = 100$, we construct a MFT sensing matrix $\mathbf{\Phi}_0$ with the same parameters but a smaller refinement factor F_0. For the same range of interest, the dimension N_0 of $\mathbf{\Phi}_0$ is smaller than the dimension N of $\mathbf{\Phi}$ with a scaling factor:

$$\frac{N}{N_0} = \frac{F}{F_0} \tag{4.9}$$

The measurement vector $\boldsymbol{y} = \mathbf{\Phi}\boldsymbol{x} + \boldsymbol{\sigma}$ is also the multiplication between the MFT sensing matrix $\mathbf{\Phi}_0$ and the K-sparse signal $\boldsymbol{x}_0$. From this point, OMP is used to estimate the K-sparse signal support (T_0) of $\boldsymbol{x}_0$ based on the measurement vector $\boldsymbol{y}$ and the MFT sensing matrix $\mathbf{\Phi}_0$. From this result, the MD ΔT_0 is inferred. Since the refinement factor F_0 is small, the estimate of the support T_0 is highly accurate. Besides, the estimation using OMP runs very fast because the dimension N_0 of $\mathbf{\Phi}_0$ is extremely small. Subsequently, we calculate ΔT_{pre} by scaling ΔT_0:

$$\Delta T_{pre} = \frac{F}{F_0}\Delta T_0 \tag{4.10}$$

where ΔT_0 is inferred from the achieved support T_0. According to (4.10), ΔT_{pre} is a multiple of the factor F/F_0 because ΔT_0 is an integer. Note that the accuracy of this MD prediction procedure is highly dependent on the chosen small refinement factor F_0.

4.6.4 Numerical results

4.6.4.1 Minimum distance prediction

Apparently, the recovery performance of CMD-OMP highly depends on the accuracy of the comparison results between the predicted MD ΔT_{pre} and the tuning point ΔT_{tuning}. Thus, the choices of F_0 and ΔT_{tuning} play significant roles in CMD-OMP. In this part, four variants of CMD-OMP with different settings (F_0, ΔT_{tuning}) are analyzed to show their disadvantages and advantages through numerical experiments.

Initially, we construct a real-valued MFT acquisition $\mathbf{\Phi}$ with $N = 500, L = 5, M = 20$, $f_{max} = 30$ MHz and a large refinement factor $F = 100$, similar to the previous simulations. Subsequently, based on the above sensing matrix $\mathbf{\Phi}$, a MFT sensing matrix $\mathbf{\Phi}_0$ can be constructed with a given smaller refinement factor F_0. A Monte Carlo simulation is carried out with 500 trials for each MD case (from 5 to 150 bins). At each trial, we generate a non-negative 3-sparse signal whose MD is equal to the analyzed MD. Next, the noisy measurement vector $\boldsymbol{y} = \mathbf{\Phi}\boldsymbol{x} + \boldsymbol{\sigma}$ is generated with a fixed SNR = 30 dB. And then we predict MD through the proposed procedure (4.9)-(4.10). Due to Fig. 4.11b, the tuning parameter is about 65 when SNR is 30 dB. The selection between OMP3 and POMP depends on the comparison result between the predicted MD and the tuning parameter. Fig. 4.12 illustrates the rate of giving a correct choice in 500 trials for each case of different MD. Ideally, these rates should be equal to one in all cases of various MDs.

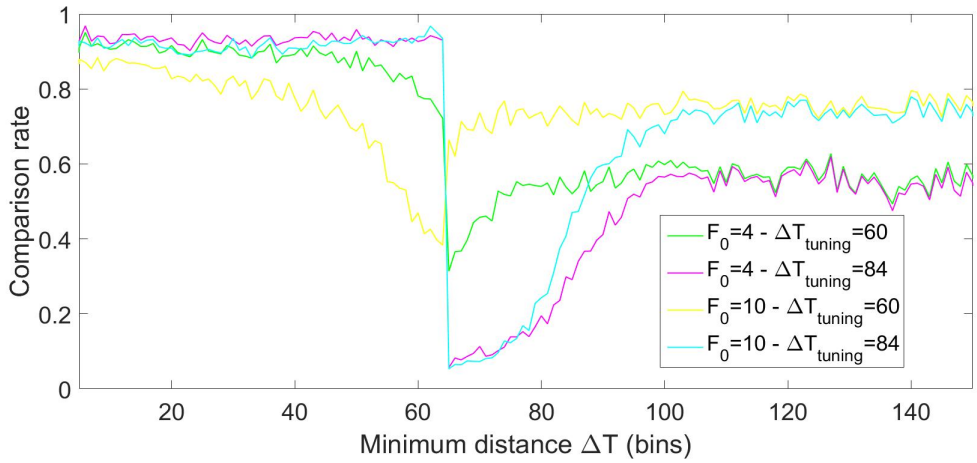

Figure 4.12. Comparison rate of the selection results using different settings (F_0,ΔT_{tuning}) at different MD cases. Choose $N = 500$, $L = 5$, $M = 20$, $f_{max} = 30$ MHz, $F = 100, \Delta r = 5$ cm

As can be seen in Fig. 4.12, each setting (F_0, ΔT_{tuning}) acquires various properties:

- The setting (4, 84) (rose lines) mostly makes the correct decision at small MDs but

the incorrect decision at large ones. These results reveal that this setting prefers to choose POMP as the favorite recovery method.

- Inversely, the setting (10, 60) (yellow lines) selects OMP3 most frequently.
- Two other settings (4, 60) and (10, 84) balance the selection rates of OMP3 and POMP. For instance, the setting (10, 84) (cyan lines) can guarantee the moderate stability of correct choice in the cases of both small and large MDs.

4.6.4.2 CMD-OMP

Subsequently, four variants of CMD-OMP with above settings (F_0, ΔT_{tuning}) are used to reconstruct 3-sparse signal in the super-resolution MFT acquisition $\mathbf{\Phi}$. Two Monte Carlo simulations are carried out with 3000 trials for each SNR (from 5 dB to 40 dB) and 500 trials for each MD (from 5 to 150 bins). The procedures of 3-sparse signal and noisy measurement vector generation repeat similarly as the previous numerical experiments. The achieved relaxed support recovery rates of CMD-OMP with a tolerance offset $\delta = 2$ are then compared to those of POMP and OMP3 in the same Fig. 4.13 for SNR domain and Fig. 4.14 for MD domain.

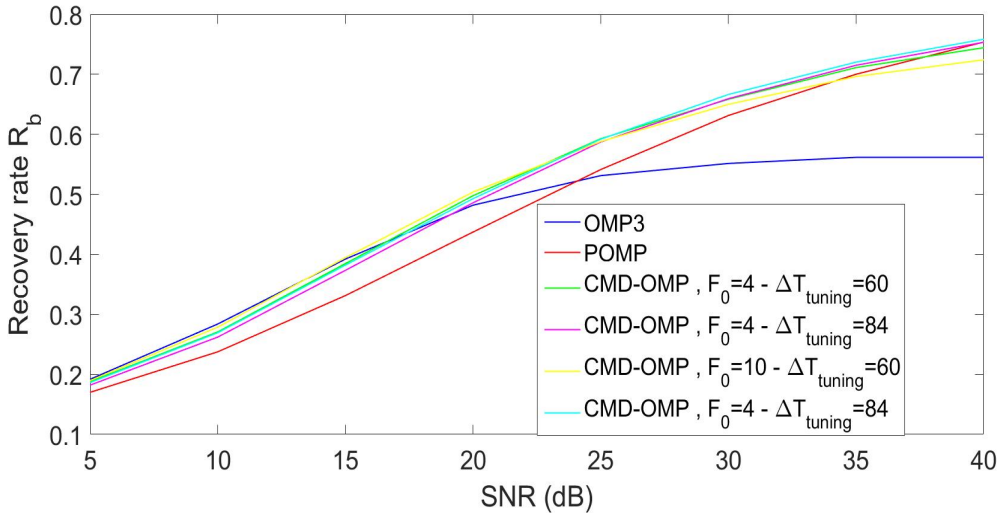

Figure 4.13. Relaxed support recovery performance ($\delta = 2$) of CMD-OMP using different settings (F_0,ΔT_{tuning}) at different SNRs (3000 trials for each SNR). Choose $N = 500, L = 5, M = 20, f_{max} = 30$ MHz, $F = 100, \Delta r = 5$ cm

As Fig. 4.13 shows, POMP (red lines) outperforms at high SNRs while inversely OMP3 (blue lines) does at low SNRs. Whereas, the reconstruction results of many variants of CMD-OMP with different settings can inherit from these strengths of both two methods.

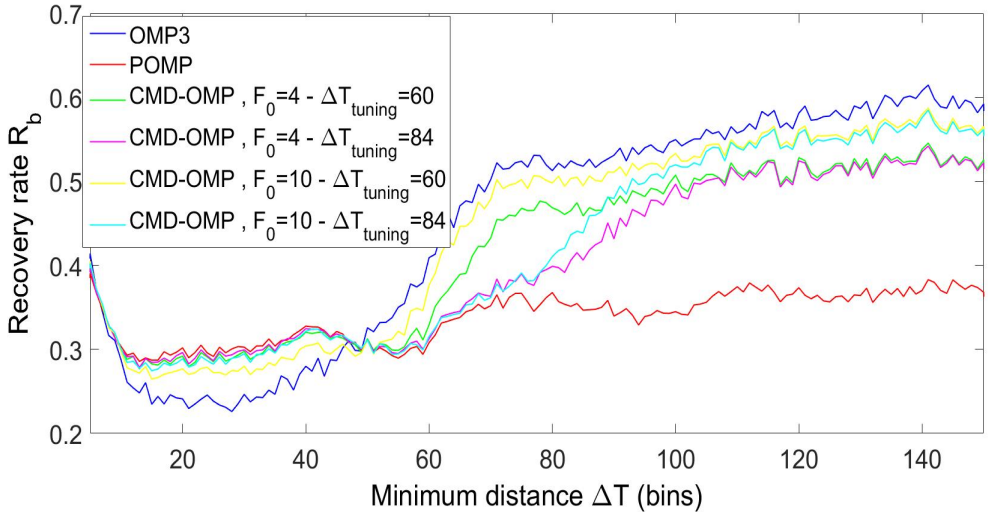

(a) 15dB, $\delta = 2$ (bins)

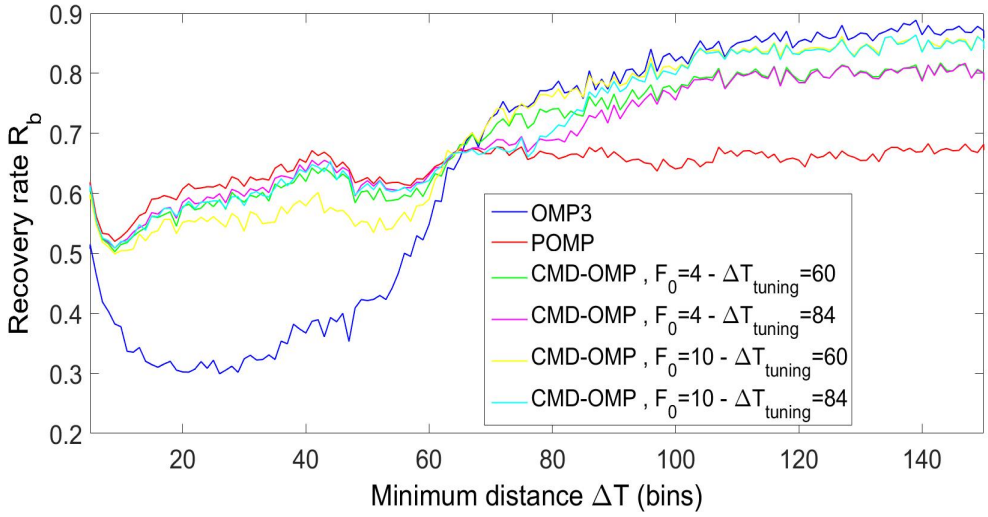

(b) 30dB, $\delta = 2$ (bins)

Figure 4.14. Relaxed support recovery performance ($\delta = 2$) of CMD-OMP using different settings (F_0,ΔT_{tuning}) at different MDs (500 trials for each MD). Choose N=500, L=5, M=20, $f_{max} = 30$ MHz and F=100

Besides, Fig. 4.14 indicates the following disadvantages and advantages of each setting (F_0, ΔT_{tuning}):

- The variant of CMD-OMP with the setting (10, 60) (yellow lines) is the best one among the four variants of CMD-OMP at large MDs but the worst ones at small MDs. These results indicate that this setting uses OMP3 most frequently. However, in a general comparison, this variant outperforms OMP3.
- Inversely, the variant of CMD-OMP with the setting (4, 84) (rose lines) has the highest rates at small MDs but the lowest rates at high MDs, among four variants of CMD-OMP. These results indicate that this setting uses POMP most frequently. However, in a general comparison, this variant of CMD-OMP outperforms POMP.

Table 4.1. Average run time of different recovery methods in 3000 trials for each 3-MPI reconstruction of one pixel (N =500, M=20, $f_{max} = 30$, F=100)

Algorithms	Average consuming time (seconds)
OMP3	0.0337
POMP (lsnonneg MATLAB function)	0.2606
CMD-OMP with $F_0 = 4$ and $\Delta T_{tuning} = 60$	0.1231
CMD-OMP with $F_0 = 10$ and $\Delta T_{tuning} = 60$	0.1678
CMD-OMP with $F_0 = 4$ and $\Delta T_{tuning} = 84$	0.0904
CMD-OMP with $F_0 = 10$ and $\Delta T_{tuning} = 84$	0.1239
BPIC (cvx package)	2

- Two other settings (10, 84) and (4, 60) (cyan and green lines) bring the moderate support recovery rates in the cases of both small and large MDs. More precisely, the variant with the setting (10, 84) has some advantages at large MDs ($\Delta T \geq 85$) while the variant with the setting (4, 60) does at medium MDs ($60 \leq \Delta T \leq 85$).
- CMD-OMP cannot improve the recovery performance in a specific scenario. It only inherits from the recovery capabilities of two member methods. Therefore, if one wishes to enhance this performance, two member methods should be replaced by other ones with a higher sparse reconstruction performance. For instance, a new method should replace POMP for an improvement of reconstruction performance in the cases of small MDs.

Moreover, Table 4.1 shows the averaged computation time of all used methods, i.e., OMP3, POMP, four variants of CMD-OMP, for each 3-MPI reconstruction of one pixel.

According to Table 4.1, POMP run extremely slowly while OMP3 runs in the shortest time. In comparison with POMP, the variants of CMD-OMP have additional advantages regarding a shorter computation time.

4.7 Summary

This chapter introduces several super-resolution CS greedy pursuits, i.e., OMP3, POMP, Ma-OMP3, CMD-OMP. Through the numerical results, the support recovery performances of these greedy pursuits are approximate to those of a l_1-optimization algorithm, e.g., BPIC. Whereas, they consume a very shorter computation time.

Besides, POMP and OMP3 possess other advantages regarding high recovery rates at small and large MDs respectively. The proposed method CMD-OMP can use up their strengths to maintain a higher stability of accurate support reconstruction in all cases of various MDs. Moreover, the performance of CMD-OMP can be improved in the future if we explore two new member methods for replacing POMP or OMP3.

An accurate support recovery with a tolerance offset should be guaranteed for all cases of various MDs with a high probability, even in highly noisy environments. However, the achieved support recovery results of OMP3, POMP, Ma-OMP3, and even CMD-OMP seem to be not good enough to apply for a practical TOF application. Therefore, other CS techniques regarding the design of MFT sensing matrix will be investigated in next chapters to enhance the current reconstruction stability.

5 Multi-frequency selection optimization

Due to the CS theory in Section 3.1, there are some restricting conditions on the sensing matrix $\mathbf{\Phi}$ to guarantee for the high stability of an exact sparse reconstruction. Therefore, the design of the sensing matrix plays an important role in the improvement of the reconstruction results. In the context of a MFT acquisition, the structure of the MFT sensing matrix is highly dependent on some modulation parameters, i.e., the set of frequencies or phase-offsets, according to (3.31). However, an efficient method for selecting these parameters has not been introduced so far. Therefore, this chapter proposes a gradient steepest descent method for optimizing these parameters. It aims to formulate the MFT sensing matrix which brings a higher reconstruction performance of the greedy pursuit algorithms, i.e., OMP3, POMP. There are three main goals of this chapter. Firstly, cyclic difference set (CDS) is proven as the optimum set of frequencies for the DFT sensing matrix in the conventional grid configuration ($F = 1$) [45, 50]. Secondly, CDS is proven to be not the optimum selection for both the DFT and MFT models in a super-resolution grid configuration ($F > 1$). Thirdly, a gradient steepest descent method is then proposed for optimizing the frequency selection in Section 5.1 as well as both frequency and phase-offset selection in Section 5.2. The improvements in the sparse reconstruction performance in the super-resolution MFT acquisition ($F = 100$) are demonstrated through numerical experiments in Section 5.3. The results are concluded in Section 5.4.

5.1 Frequency selection optimization

Recently, the deterministic construction of the partial Fourier CS matrices has been received a lot of attraction from scientific community [46, 20, 65]. The work aims at the high stability of exact signal recovery through finding the optimized set of Fourier samples. Many publications [45, 50] proved that the CDS of frequencies formulates a DFT sensing matrix satisfying the maximum Welch-bound equality (MWBE).

5.1.1 Cyclic difference set

Definition 7. A cyclic (N_0, M, λ)-difference set $H = \{f_1, f_2, \cdots, f_M\}$ is a collection of M distinct residues modulo N_0 such that for any residue $b \not\equiv 0 \pmod{N_0}$, there exist precisely λ ordered pairs (f_i,f_j) from H such that $b \equiv f_i - f_j \pmod{N_0}$ [69], where

$$M(M-1) = \lambda(N_0 - 1) \tag{5.1}$$

For instance, the set $H = \{1, 3, 4, 5, 9\}$ of residues modulo 11 is a cyclic difference set (11, 5, 2).

5.1.2 DFT sensing matrix

After the discretization of a fine grid spacing $1/N_0$ ($\Delta t = 1/N_0$), each element of DFT sensing matrix $\boldsymbol{A}$ can be represented by:

$$a_{pq} = e^{-j2\pi f_p q \Delta t} = e^{-j2\pi f_p q/N_0} \tag{5.2}$$

where $f_p \in \mathbb{Z}_N$, $f_p \neq f_l$, $\forall p \neq l$ and $1 \leq q \leq N_0$. For each signal reconstruction phase, there are M Fourier samples $H = \{f_1, f_2, \cdots, f_M\}$ which are chosen with $f_p \in \mathbb{Z}_N$.

Definition 8. A $M \times N_0$ sensing matrix $\boldsymbol{A}$ ($N_0 > M$) satisfies the maximum Welch Bound Equality (MWBE) if and only if all coherence components

$$c_{nn'} = \sqrt{\frac{N_0 - M}{(N_0 - 1)M}} \quad \forall 0 < n \neq n' \leq N_0 \tag{5.3}$$

and hence according to 3.13, the mutual coherence of the sensing matrix $\boldsymbol{A}$

$$\mu(\boldsymbol{A}) = \max_{c \neq c'} c_{nn'} = \sqrt{\frac{N_0 - M}{(N_0 - 1)M}} \tag{5.4}$$

Theorem 1. As shown in [20, 50], a $M \times N_0$ DFT sensing matrix $\boldsymbol{A}$ satisfies the maximum Welch Bound Equality (MWBE) if and only if the Fourier sampling set H is a cyclic difference set (N_0, M, λ).

According to 3.12, the normalized coherence between two arbitrary columns $\boldsymbol{a}_n$ and $\boldsymbol{a}'_n$ ($1 \leq n \neq n' \leq N_0$) of a DFT sensing matrix can be represented by:

$$c_{nn'} = \frac{|\boldsymbol{a}_n^H \boldsymbol{a}'_n|}{||\boldsymbol{a}_n||_2 ||\boldsymbol{a}_{n'}||_2} = \frac{1}{M} \left| \sum_{p=1}^{M} e^{j2\pi \frac{f_p}{N_0}(n'-n)} \right| \tag{5.5}$$

Set $g = n' - n \in Z_{N_0}$ then

$$c(g) = \frac{1}{M} \left| \sum_{p=1}^{M} e^{j2\pi \frac{g}{N_0} f_p} \right| \tag{5.6}$$

and we have:

$$\begin{aligned} c^2(g) &= \frac{1}{M^2}\left(\sum_{p=1}^{M} e^{j2\pi\frac{g}{N_0}f_p}\right)\left(\sum_{k=1}^{M} e^{-j2\pi\frac{g}{N_0}f_k}\right) \\ &= \frac{N_0-M}{(N_0-1)M} + \frac{M-1}{(N_0-1)M} + \frac{1}{M^2}\sum_{p=1}^{M}\sum_{k=1,k\neq p}^{M} e^{j2\pi\frac{g}{N_0}(f_p-f_k)} \end{aligned} \tag{5.7}$$

If the set H is a CDS (N_0,M,λ) then $(f_p - f_k) \mod N_0$ takes all values $i = 1, 2, \cdots N_0-1$ with the same number of occurrences λ. Thus, (5.7) can be rewritten as:

$$c^2(g) = \frac{N_0-M}{(N_0-1)M} + \frac{M-1}{(N_0-1)M} + \frac{\lambda}{M^2}\sum_{i=1}^{N_0-1} e^{j2\pi\frac{g}{N_0}i} \tag{5.8}$$

According to [50], $\lambda = \frac{(M-1)M}{(N_0-1)}$ and hence:

$$\begin{aligned} c^2(g) &= \frac{N_0-M}{(N_0-1)M} + \frac{M-1}{(N_0-1)M} + \frac{M-1}{(N_0-1)M}\sum_{i=1}^{N_0-1} e^{j2\pi\frac{g}{N_0}i} \\ &= \frac{N_0-M}{(N_0-1)M} + \frac{M-1}{(N_0-1)M}\left(1 + \sum_{i=1}^{N_0-1} e^{j2\pi\frac{g}{N_0}i}\right) \\ &= \frac{N_0-M}{(N_0-1)M} + \frac{M-1}{(N_0-1)M}\sum_{i=0}^{N_0-1} e^{j2\pi\frac{g}{N_0}i} \end{aligned} \tag{5.9}$$

We have $\sum_{i=0}^{N_0-1} e^{j2\pi\frac{g}{N_0}i} = 0 \ \forall g \in \mathbb{N}^*$ and $\sum_{i=0}^{N_0-1} e^{j2\pi\frac{g}{N_0}i} = N_0$ if $g = 0$. Therefore, from (5.9):

$$c^2(g) = \begin{cases} \frac{N_0-M}{(N_0-1)M} & \text{if} \quad g \in \mathbb{N}^* \\ 1 & \text{if} \quad g = 0 \end{cases} \tag{5.10}$$

According to (5.10), the DFT sensing matrix structured by a CDS of Fourier samples satisfies the MWBE. For instance, the red line in Fig. 5.1a denotes the coherence histogram of the sensing matrix structured by the CDS (31, 15, 7). It is intuitive that all the normalized coherence elements are equal to the Welch-bound (= 0.1886). Due to the restricting condition in (3.14), this sensing matrix with a low mutual coherence μ is potential to bring the high stability of exact signal reconstruction, in comparison to a random selection of frequencies [20].

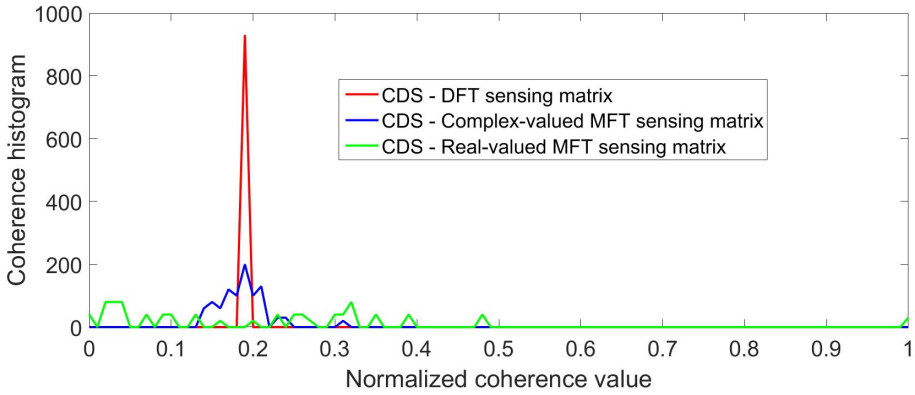

(a) $F = 1$

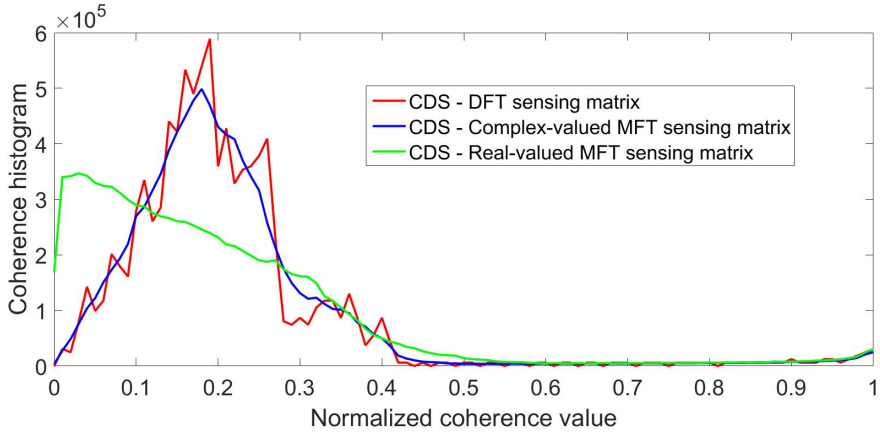

(b) $F = 100$

Figure 5.1. Coherence histograms of DFT and MFT sensing matrices structured by a CDS of frequencies in the conventional ($F = 1$) and super-resolution ($F = 100$) configurations.

5.1.2.1 DFT super-resolution sensing matrix

In a super-resolution configuration, the current discretized grid is refined with a large refinement factor ($F > 1$) [66, 21]

$$\Delta t = \frac{1}{N_0 F} \tag{5.11}$$

and hence (5.6) is rewritten to:

$$c(g) = \frac{1}{M}\left|\sum_{p=1}^{M} e^{j2\pi\frac{f_p}{N_0F}g}\right|,\ 0 \leq g \leq N_0F-1 \tag{5.12}$$

Now, according to (5.7), if the set H is a CDS (N_0, M, λ) then $\Big((f_p - f_k) \mod N_0\Big)$ takes all values $i = 1, 2, \cdots N_0 - 1$ but $\Big((f_p - f_k) \mod N_0F\Big)$ where $F > 1$ cannot cover all values $i = 1, 2, \cdots N_0F - 1$. Hence,

$$\sum_{p=1}^{M}\sum_{k=1,k\neq p}^{M} e^{j2\pi\frac{g}{N_0F}(f_p-f_k)} \neq \sum_{i=1}^{N_0F-1} e^{j2\pi\frac{g}{N_0F}i} \tag{5.13}$$

leads to the invalidity of (5.8) and consequently breaks the MWBE in the super-resolution configuration. Definitely, there exists at least one integer $g \in Z_{N_0F-1}$ such that $c(g) \neq \sqrt{\frac{N_0-m}{(N_0-1)m}}$. The red line in Fig. 5.1b denotes the coherence histogram of the DFT sensing matrix structured by the CDS (31, 15, 7) at $F = 100$. Compared to the DFT matrix at $F = 1$ (red line in Fig. 5.1a), the coherence histogram of DFT matrix in a super-resolution configuration of $F = 100$ no longer satisfies the MWBE.

5.1.2.2 MFT super-resolution compressed sensing

The selection of frequencies in a MFT acquisition as described in (3.31) is similar to the selection of Fourier samples in a DFT model. In the conventional grid configuration ($F = 1$), there are two different kinds of MFT sensing matrices:

- If the cross-correlation function in (3.27) is sinusoidal ($L = 1$) and the phase-offset is zero ($\tau = 0$), a complex-valued TOF measurement possesses the same mathematical representation as a DFT measurement in (5.2). Therefore, as proven previously, a CDS of frequencies $H = \{f_1, f_2, \cdots, f_M\}$ leads to the formulation of a MFT sensing matrix satisfying the MWBE with the minimum mutual coherence.
- If the cross-correlation function in (3.27) is not sinusoidal and contains higher-order harmonics, i.e., $L = 5$, the complex- or real-valued MFT sensing matrix (blue or green lines in Fig. 5.1a) structured by the CDS of frequencies cannot satisfy MWBE condition.

Eventually, a CDS of frequencies leads to the optimized MFT sensing matrix in the conventional grid configuration if the cross-correlation function between the transmitted and demodulation signals in (3.27) is sinusoidal. Suppose that our commercial TOF camera is capable of carrying out the high-frequency TOF measurement with an emitted

sinusoidal signals. Then, a high depth resolution can be achieved through a conventional MFT acquisition ($F = 1$) with a CDS of frequencies.

Nevertheless, in a super-resolution MFT acquisition ($F = 100$), the sensing matrix constructed by the CDS of frequencies no longer possesses the optimized coherence map. As can be seen in Fig. 5.1b that the mutual coherence values of all MFT sensing matrices are approximate to one for all settings, e.g., $L = 1$ or $L = 5$ (red or blue line), complex-valued or real-valued model (blue or green line). Thus, due to the restricting condition in (3.14), an exact signal reconstruction cannot be guaranteed with high probability. At this point, we hypothesize that there exists another frequency selection which can construct a MFT sensing matrix with a better coherence histogram and eventually bring a higher stability of accurate signal reconstruction in a super-resolution configuration ($F > 1$).

5.1.3 Proposed optimization method

In this part, an optimization method is introduced to find out the frequency selection which can optimize the coherence property of the sensing matrix iteratively. Additionally, it simultaneously brings a better performance of signal reconstruction in a super-resolution MFT acquisition.

5.1.3.1 Coherence cost

Many different restricting conditions on sensing matrix, e.g., Null Space Property, RIP or Mutual Coherence for a guarantee for the high stability of an exact signal reconstruction, are documented in the CS theory (see Section 3.1). However, these strong conditions are no longer satisfied in a super-resolution MFT acquisition. After the discretization step with a large refinement factor, the mutual coherence of a super-resolution MFT sensing matrix is approximate to one (see Fig. 3.4). Therefore, we introduce an alternative coherence cost which has been proposed in many studies [30] in order to measure the quality of a coherence histogram of a sensing matrix more accurately:

$$E = ||\tilde{\boldsymbol{\Phi}}^H \tilde{\boldsymbol{\Phi}} - I||_F^2 = \mathrm{Tr}\{(\tilde{\boldsymbol{\Phi}}^H \tilde{\boldsymbol{\Phi}} - I)(\tilde{\boldsymbol{\Phi}}^H \tilde{\boldsymbol{\Phi}} - I)^H\} \tag{5.14}$$

where $\mathrm{Tr}\{\cdot\}$ denotes the trace operator and from (3.12), (5.14) is rewritten as follows:

$$E = \sum_{1 \le n \ne n' \le N} c_{nn'}^2 \tag{5.15}$$

where $c_{nn'}$ is the element of the Gram matrix $\boldsymbol{C}$ (see Section 3.4.2.1).

The equation (5.15) shows that the above coherence cost E is the sum of square of the Gram matrix (see Section 3.4.2.1). Theoretically, if this coherence cost E is smaller, then the sensing matrix comprises more incoherent columns. From this result, the stability of a good sparse recovery may become higher. At this point, minimizing the coherence cost

E may lead to the improvement of the sparse reconstruction performance. Therefore, our proposed method aims to find the frequency selection H_{opt} so that:

$$H_{opt} = \arg\min_{H} E = \arg\min_{H} \sum_{1 \le n \ne n' \le N} c_{nn'}^2 \tag{5.16}$$

5.1.3.2 Proposed frequency selection optimization

The frequency selection optimization method is a gradient steepest descent algorithm [30] which is used to update the set H iteratively for minimizing the coherence cost E. We start with a set H_0 of M random frequencies to construct the initial sensing matrix $\mathbf{\Phi}_{init}$. The coherence cost of this matrix is denoted as E_0. At iteration k, the new set H_k is achieved through updating each frequency f_i of the current set H_{k-1} sequentially with the new value:

$$f_{i,k} = f_{i,k-1} - \eta \nabla E_{f_i} \tag{5.17}$$

where η is a given step size and ∇E_{f_i} represents the gradient of E respect to f_i

$$\nabla E_{f_i} = \frac{\partial E}{\partial f_i}_{|H_{k-1}} \tag{5.18}$$

$$= \sum_{q_1=1, q_1 \ne q_2}^{N} \sum_{q_2=1}^{N} \Delta E_{q_1 q_2, f_i} \tag{5.19}$$

where

$$\Delta E_{q_1,q_2,f_i} = c_{q_1,q_2} \Delta c^*_{q_1,q_2,f_i} + \Delta c_{q_1,q_2,f_i} c^*_{q_1,q_2} \tag{5.20}$$

$$c_{q_1,q_2} = \frac{u_{q_1,q_2}}{v_{q_1,q_2}} \tag{5.21}$$

$$u_{q_1,q_2} = \sum_{p=1}^{m} \phi_{pq_1} \phi^*_{pq_2} \tag{5.22}$$

$$v_{q_1,q_2} = ||\boldsymbol{\phi}_{q_1}||_2 ||\boldsymbol{\phi}_{q_2}||_2 \tag{5.23}$$

$$||\boldsymbol{\phi}_q||_2 = \sqrt{\sum_{i=1}^{M} \phi_{iq}^2} \tag{5.24}$$

$$\Delta c_{q_1,q_2,f_i} = \frac{\Delta u_{q_1,q_2,f_i} v_{q_1,q_2} - u_{q_1,q_2} \Delta v_{q_1,q_2,f_i}}{v_{q_1,q_2}^2} \tag{5.25}$$

$$\Delta u_{q_1,q_2,f_i} = \gamma_{q_1,f_i}\phi^*_{iq_2} + \phi_{iq_1}\gamma^*_{q_2,f_i} \tag{5.26}$$

$$\begin{aligned}\Delta v_{q_1,q_2,f_i} = \frac{1}{2}\frac{\gamma_{q_1,f_i}\phi^*_{iq_1} + \phi_{iq_1}\gamma^*_{q_1,f_i}}{||\boldsymbol{\phi}_{q_1}||_2}||\boldsymbol{\phi}_{q_2}||_2 + \\ \frac{1}{2}||\boldsymbol{\phi}_{q_1}||_2\frac{\gamma_{q_2,f_i}\phi^*_{iq_2} + \phi_{iq_2}\gamma^*_{q_2,f_i}}{||\boldsymbol{\phi}_{q_2}||_2}\end{aligned} \tag{5.27}$$

$$\gamma_{q,f_i} = \sum_{l=-L}^{L} c_l d^*_l(-j2\pi l q\Delta t)e^{-j2\pi l f_i q\Delta t + jl\tau_i} \tag{5.28}$$

The proofs of (5.18) - (5.28) are presented in Appendix A.1. Suppose the step size η is fixed. After all frequencies of H_k have been achieved through (5.18) - (5.28), a new sensing matrix $\boldsymbol{\Phi}_{new}$ is constructed and then its coherence cost E_{new} is computed. If the coherence cost of the current matrix is larger than E_{new}, the current sensing matrix is replaced by the new one. Otherwise, the step size η is reduced. We repeat this process until smaller coherence cost of new sensing matrix cannot be obtained. Note that the new frequency set is restricted to $\max(H_k) = 30$ MHz, $\min(H_k) = 1$ MHz and $H_k \subset \Psi$.

5.1.3.3 Update verification process

Although the above steepest descent method can minimize the coherence cost E, it is unsure that the amount of the highly incoherent columns in the sensing matrix becomes larger. Therefore, this part proposes two additional constraints to guarantee a better coherence histogram of the new sensing matrix including:

- The mutual coherence of the new sensing matrix is smaller or at least equal to that of the current sensing matrix.
- The new sensing matrix has the amount of large coherence elements $c_{nn'}$, referred shortly as $ML(\boldsymbol{\Phi_{new}})$, that is smaller or at least equal to that of the current sensing matrix. We define $c_{nn'} \geq c_{large}$ as a large-coherence element where $0 \leq c_{large} \leq 1$ is chosen due to the super-resolution MFT settings.

Both of two conditions are verified carefully after each iteration of the steepest descent method. If all conditions on the new sensing matrix are satisfied, the new set of frequencies H_k is updated for the iteration k. Then it is used as input for the next iteration $k+1$. This procedure repeats until no frequency is updated. Algorithm 12 describes how to find the optimized set of frequencies H_{opt}.

Algorithm 12 Gradient steepest descent method for frequency selection optimization

Input: H_0, η_0
Output: H_{opt}

1: Build the matrix $\mathbf{\Phi}$ with H_0.
2: Calculate the coherence cost E_0 of the matrix $\mathbf{\Phi}$ and mutual coherence $\mu_0 = \mu_{\mathbf{\Phi}}$
3: Initialize $k = 1$
4: **while** TRUE **do**
5: Initialize $H_k = H_{k-1}$
6: **for** $i = 1$ to M **do**
7: Initialize $\eta = \eta_0$
8: Compute the gradient ∇E_{f_i} with the set H_k
9: Compute the new value $f_{i,k} = f_{i,k-1} - \eta \nabla E_{f_i}$ with $f_{i,k-1} \in H_{k-1}$
10: Build the matrix $\mathbf{\Phi}_{new}$ with the set H_k and the new value $f_{i,k}$
11: Compute E_{new} of the matrix $\mathbf{\Phi}_{new}$
12: **if** $E_{new} < E_0$ **then**
13: **if** $\mu_{\mathbf{\Phi}_{new}} < \mu_0$ and $ML(\mathbf{\Phi}_{new}) < ML(\mathbf{\Phi})$ **then**
14: Update $f_{i,k}$ for the new set H_k
15: Update $E_0 = E_{new}$, $\mu_0 = \mu_{\mathbf{\Phi}_{new}}$, $ML(\mathbf{\Phi}) = ML(\mathbf{\Phi}_{new})$ and $\mathbf{\Phi} = \mathbf{\Phi}_{new}$
16: **else**
17: Go forward to step 21
18: **end if**
19: **else**
20: Update the step size $\eta = \eta/2$
21: **if** $\eta < \eta_{min}$ **then**
22: continue;
23: **end if**
24: Go back to step 8
25: **end if**
26: **end for**
27: Set $H_{opt} = H_k$
28: **if** $H_k = H_{k-1}$ **then**
29: break;
30: **end if**
31: $k = k + 1$
32: **end while**

5.1.3.4 Initial phase-offset optimization

The equation (3.31) indicates that the structure of a MFT sensing matrix is also highly dependent on the preset phase-offset τ of each TOF measurement. Therefore, the initial

phase-offset selection optimization can improve the coherence histogram of a MFT sensing matrix. Again, the principle of the previous part is employed. A gradient steepest descent method is used for minimizing the coherence cost E through updating the phase-offset iteratively. We choose a random set of initial phase-offsets $J = \{\tau_1, \tau_2, \cdots, \tau_M\}$ for M TOF measurements. The initial phase-offset τ_i is updated at iteration k with a chosen step size $\eta_2 > 0$:

$$\tau_{i,k} = \tau_{i,k-1} - \eta_2 \nabla E_{\tau_i} \tag{5.29}$$

where ∇E_{τ_i} denotes the gradient of the coherence cost E with respect to an initial phase-offset τ_i of the set J. The computation of ∇E_{τ_i} is carried out as follows:

$$\nabla E_{\tau_i} = \frac{\partial E}{\partial \tau_i} = \sum_{q_1=1, q_1 \neq q_2}^{N} \sum_{q_2=1}^{N} \Delta E_{q_1 q_2, \tau_i} \tag{5.30}$$

where

$$\Delta E_{q_1,q_2,\tau_i} = c_{q_1,q_2} \Delta c^*_{q_1,q_2,\tau_i} + \Delta c_{q_1,q_2,\tau_i} c^*_{q_1,q_2} \tag{5.31}$$

$$\Delta c_{q_1,q_2,\tau_i} = \frac{\Delta u_{q_1,q_2,\tau_i} v_{q_1,q_2} - u_{q_1,q_2} \Delta v_{q_1,q_2,\tau_i}}{v^2_{q_1,q_2}} \tag{5.32}$$

$$\Delta u_{q_1,q_2,\tau_i} = \gamma_{q_1,\tau_i} \phi^*_{iq_2} + \phi_{iq_1} \gamma^*_{q_2,\tau_i} \tag{5.33}$$

$$\begin{aligned} \Delta v_{\tau_i,q_1,q_2} = \frac{1}{2} \frac{\gamma_{q_1,\tau_i} \phi^*_{iq_1} + \phi_{iq_1} \gamma^*_{q_1,\tau_i}}{||\boldsymbol{\phi}_{q_1}||_2} ||\boldsymbol{\phi}_{q_2}||_2 + \\ \frac{1}{2} ||\boldsymbol{\phi}_{q_1}||_2 \frac{\gamma_{q_2,\tau_i} \phi^*_{iq_2} + \phi_{iq_2} \gamma^*_{q_2,\tau_i}}{||\boldsymbol{\phi}_{q_2}||_2} \end{aligned} \tag{5.34}$$

$$\gamma_{q,\tau_i} = \sum_{l=-L}^{L} c_l d^*_l(jl) e^{-j2\pi l f_i q \Delta t + jl\tau_i} \tag{5.35}$$

The proofs of (5.30) - (5.35) are presented in Appendix A.1. At iteration k, the update of phase-offset in (5.29) repeats for all element of the set J_{k-1} to formulate the new set J_k. Similar to the above frequency selection optimization, this update is only valid if all conditions on the new sensing matrix, i.e., a smaller coherence cost, a smaller mutual coherence, a smaller amount of large coherence elements, are satisfied. Otherwise, the step size η_2 is reduced. The initial phase-offset optimization method runs until no update of J can be done. The final result is the optimized set of phase-offsets J_{opt}.

5.2 Frequency and initial phase-offset optimization

Algorithm 13 Gradient steepest descent method for frequency and phase-offset selection optimization

Input: Initialize the random set of M frequencies and phase-offsets Γ_0=$\{H_0$,$J_0\}$
Output: Γ_{opt}=$\{H_{opt}, J_{opt}\}$

1: Build the matrix $\mathbf{\Phi}$ with Γ_0
2: Calculate the coherence cost E_0 of the matrix $\mathbf{\Phi}$ and mutual coherence $\mu_0 = \mu_{\mathbf{\Phi}}$
3: Initialize $k = 1$
4: **while** TRUE **do**
5: Initialize $\Gamma_k = \Gamma_{k-1}$
6: **for** $i = 1$ to M **do**
7: Initialize $\eta_1 = \eta_{1,0}$, $\eta_2 = \eta_{2,0}$
8: Compute the gradient ∇E_{f_i} and ∇E_{τ_i} with the set Γ_k.
9: Calculate the new value $f_{i,k} = f_{i,k-1} - \eta_1 \nabla E_{f_i}$ with $f_{i,k-1} \in H_k$
10: Calculate the new value $\tau_{i,k} = \tau_{i,k-1} - \eta_2 \nabla E_{\tau_i}$ with $\tau_{i,k-1} \in J_k$
11: Build the matrix $\mathbf{\Phi}_{new}$ with the set Γ_k and the new values $f_{i,k}$, $\tau_{i,k}$
12: Compute E_{new} of the matrix $\mathbf{\Phi}_{new}$
13: **if** $E_{new} < E_0$ **then**
14: **if** $\mu_{\mathbf{\Phi}_{new}} < \mu_0$ and $ML(\mathbf{\Phi}_{new}) < ML(\mathbf{\Phi})$ **then**
15: Update $f_{i,k}$ for the new set H_k and $\tau_{i,k}$ for the new set J_k.
16: Update $E_0 = E_{new}$, $\mu_0 = \mu_{\mathbf{\Phi}_{new}}$, $ML(\mathbf{\Phi}) = ML(\mathbf{\Phi}_{new})$ and $\mathbf{\Phi} = \mathbf{\Phi}_{new}$
17: **else**
18: Go forward to step 22
19: **end if**
20: **else**
21: Update the step size $\eta_1 = \eta_1/2$ and $\eta_2 = \eta_2/2$
22: **if** $\eta_1 < \eta_{min}$ and $\eta_2 < \eta_{min}$ **then**
23: continue;
24: **end if**
25: Go back to step 8
26: **end if**
27: **end for**
28: Set $\Gamma_{opt} = \Gamma_k$
29: **if** $\Gamma_k = \Gamma_{k-1}$ **then**
30: break;
31: **end if**
32: $k = k + 1$
33: **end while**

In this part, we present a gradient steepest descent method that optimizes both frequency and initial phase-offset for minimizing the coherence cost E. This method is

the integration between the frequency selection optimization and the initial phase-offset selection optimization in the previous parts. In particular, both frequency and initial phase-offset are updated simultaneously for constructing a new sensing matrix with all satisfying conditions, i.e., a smaller coherence cost, a lower mutual coherence, a smaller amount of large coherence elements. Finally, the optimized sets Γ_{opt}=$\{H_{opt}, J_{opt}\}$ are obtained after no update can be proceeded. This method is described in detail in Algorithm .13.

5.3 Numerical results

5.3.1 CDS selection and the proposed frequency optimization method

The frequency selection optimization method described in Algorithm 12, opens an opportunity for a better MFT sensing matrix by optimizing the set of modulation frequencies iteratively. More precisely, the optimized sensing matrix has smaller coherence cost, simultaneously a lower mutual coherence and a smaller number of the large coherence elements. However, we consider whether such a better coherence histogram of this MFT sensing matrix guarantees a higher stability of good sparse support reconstruction. Numerical experiments in this part aim to indicate that the frequency selection optimization improve the relaxed support reconstruction performance for a super-resolution MFT acquisition in the large-refinement configuration. These results are then compared with those achieved by the optimization method using CDS.

Suppose that the maximum frequency of a TOF camera in this simulation is $f_{max} =$ 31 MHz. We structure a MFT system with a large refinement factor $F = 100$ and highest-order Fourier coefficient $L = 5$. From these parameters, the grid length is $\Delta r \approx$ 4.8 cm. All TOF measurements have zero phase-offsets ($\tau = 0$). There are two types of structured MFT acquisitions including:

- A CDS (31,15,7) of modulation frequencies is chosen for 15 TOF measurements ($M = 15$). The MFT sensing matrix $\mathbf{\Phi}_{CDS}$ is structured through these measurements, according to (3.31). Because the CDS comprises only integers with gcd (CDS) = 1 MHz, the ambiguity range of this model is $R_{max} = c/(2\,\text{gcd (CDS)}) =$ 150 m for a complex-valued MFT system or $R_{max} = 75$ m for a real-valued one.

- Our proposed frequency selection optimization method is used for finding the optimized frequency set or the optimized sensing matrix $\mathbf{\Phi}_{opt}$. Since this set contains frequencies from the set Ψ where gcd (Ψ) = 0.25 MHz, the ambiguity range of this model is $R_{max} = c/(2\,\text{gcd}\,(\Psi)) = 600$ m for a complex-valued MFT system or $R_{max} = 300$ m for a real-valued one. A large-coherence element is defined with $c_{large} = 0.45$ for the update verification condition in Algorithm 12.

From the above analysis, the MFT acquisition structured by our proposed frequency selection optimization method, apparently has the advantage of an extended ambiguity

range, compared with a MFT acquisition structured by the CDS of frequencies. In principle, our optimization method can select frequencies arbitrarily from a pool of available modulation frequencies, e.g., set Ψ, and hence extend the ambiguity range. Whereas, the optimization technique using CDS has a fixed ambiguity range even if the TOF camera can modulate and demodulate an extended pool of frequencies.

As shown through the numerical experiments in Section 3.4.5, a real-valued MFT acquisition has an advantage of better reconstruction results. Thus, in this simulation, both $\mathbf{\Phi}_{CDS}$ and $\mathbf{\Phi}_{opt}$ are real-valued sensing matrices. To cover the same range of interest but not override the ambiguity range, a common dimension N is set for both of them but does not exceed $N_{max} = 31F/2 = 1550$. For a deep analysis, the numerical experiments are categorized into two different cases, i.e., a large range of interest ($N = 1500$) and a short range of interest ($N = 750$).

5.3.1.1 Large range of interest

A large dimension $N = 1500$ is set commonly for both sensing matrices $\mathbf{\Phi}_{CDS} \in \mathbb{R}^{15\times1500}$ and $\mathbf{\Phi}_{opt} \in \mathbb{R}^{15\times1500}$ to cover the same range of interest. For an analysis of the coherence property, the coherence histograms of two matrices are illustrated by blue and red lines in Fig. 5.2. Apparently, there is no significant difference between two these coherence histograms. From this result, it is difficult to explore advantages and disadvantages of our proposed frequency selection optimization and the technique using CDS regarding sparse recovery performance.

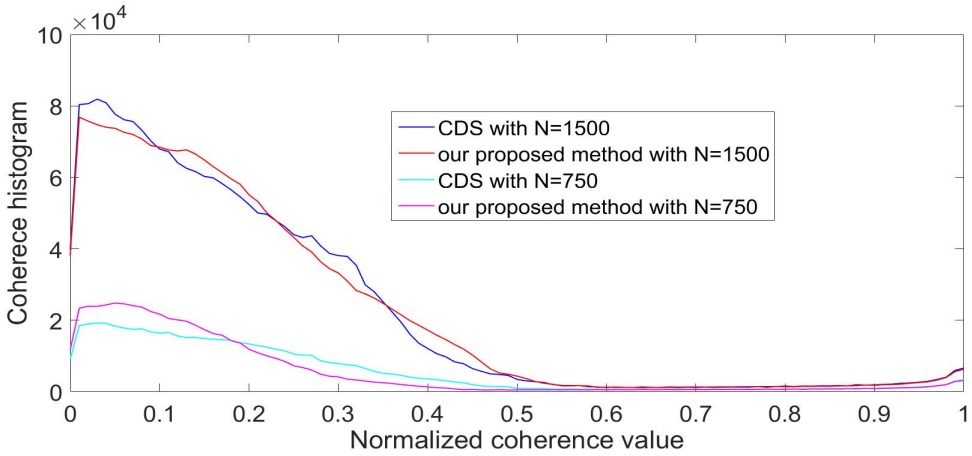

Figure 5.2. Coherence histogram of the sensing matrices structured by the CDS (31,15,7) and our proposed frequency selection optimization method. Choose $M = 15$, $F = 100$, $f_{max} = 31$ MHz

Thus, two Monte Carlo simulations are subsequently carried out with 3000 trials for each case of SNR and 500 trials for each case of MD. These experiments aim to obtain the

analysis of the reconstructed results using $\mathbf{\Phi}_{CDS}$ and $\mathbf{\Phi}_{opt}$ in the cases of various SNRs (from 5 dB to 40 dB) and various MDs (from 5 to 150 bins). Conventionally, for the analysis in the MD domain, there are two different cases of SNRs, i.e., 15 dB for a noisy case and 30 dB for a nearly noiseless case. At each iteration, the procedure of generating 3-sparse signal and noisy measurement vector is similar to the previous simulations. For a comparison, three different greedy pursuit methods, i.e., OMP3, POMP, and Ma-OMP3, are used for 3-sparse reconstruction. Fig. 5.3 and Fig. 5.4 demonstrate the relaxed support recovery rates of all three above methods with a tolerance offset $\delta = 2$ for two different MFT acquisitions $\mathbf{\Phi}_{CDS}$ and $\mathbf{\Phi}_{opt}$ in the cases of various SNRs and various MDs respectively.

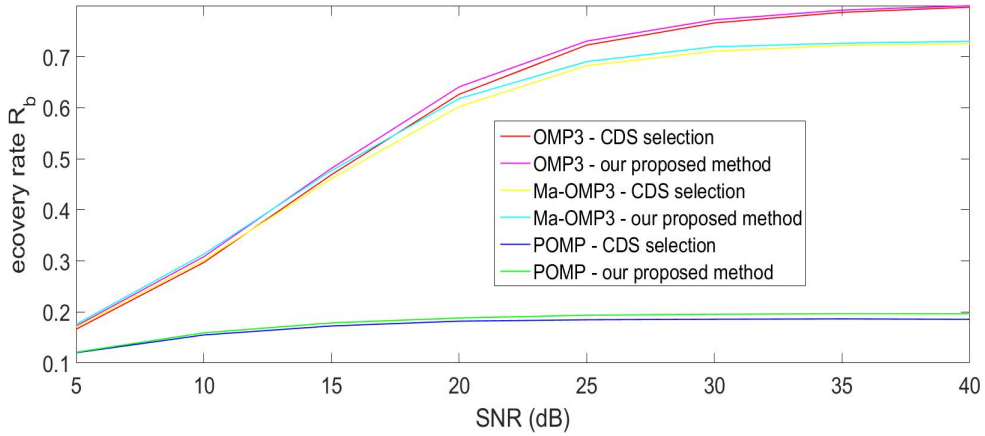

Figure 5.3. Relaxed support recovery rates ($\delta = 2$) at different SNRs (3000 trials for each SNR) for the CDS (31,15,7) and the proposed frequency optimization method with a large range of interest configuration. Choose $N = 1500, L = 5, M = 15, F = 100, K = 3$, $f_{max} = 31$ MHz

As can be seen in Fig. 5.4 that there is no significant difference between the relaxed support recovery performances using $\mathbf{\Phi}_{opt}$ (rose, cyan, and green lines) and $\mathbf{\Phi}_{CDS}$ (red, yellow, and blue lines) in all cases of various MDs. However, according to the analysis in the SNR domain in Fig. 5.3, the MFT acquisition $\mathbf{\Phi}_{opt}$ (rose, cyan, and green lines) brings the slightly higher relaxed support recovery rates in all cases of various SNRs. These results strengthen the hypothesis that our proposed frequency selection optimization is more efficient than the optimization technique based on a CDS in a super-resolution MFT acquisition with a large refinement factor. Nonetheless, the strengths of our proposed frequency selection optimization are significantly low in the case of a large range-of-interest.

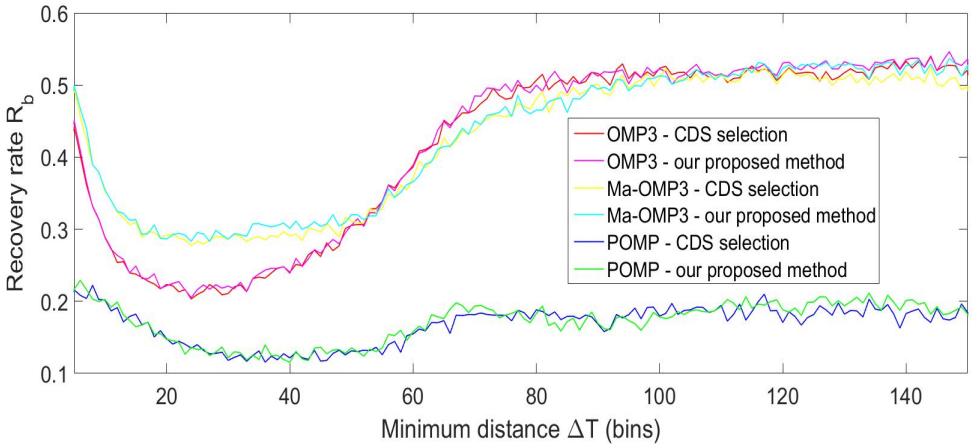

(a) 15dB

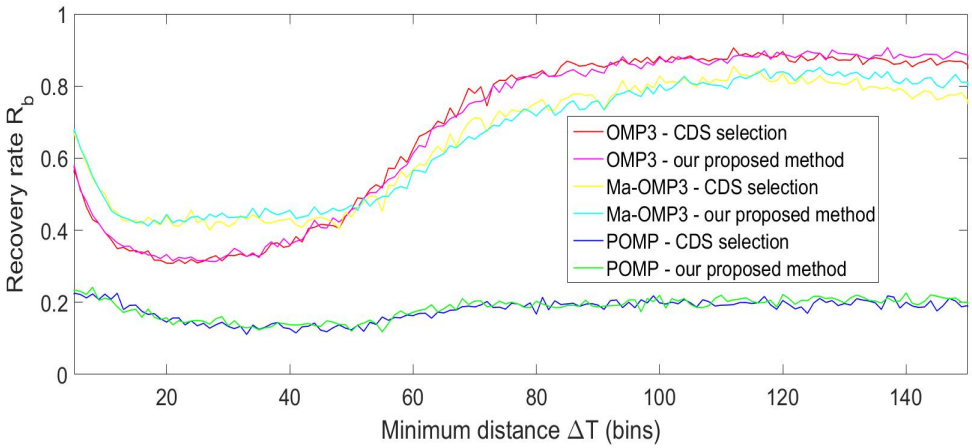

(b) 30dB

Figure 5.4. Relaxed support recovery rates ($\delta = 2$) at different MDs (500 trials for each MD) for the CDS (31,15,7) and the proposed frequency optimization method with a large range of interest configuration. Choose $N = 1500, L = 5, M = 15, F = 100, K = 3$, $f_{max} = 31$ MHz

5.3.1.2 Short range of interest

In this part, a smaller dimension $N = 750$ is configured for both real-valued MFT acquisitions with two sensing matrices $\mathbf{\Phi}_{CDS} \in \mathbb{R}^{15\times750}$ and $\mathbf{\Phi}_{opt} \in \mathbb{R}^{15\times750}$. For an analysis of the coherence property, their coherence histograms are illustrated by cyan and rose lines in Fig. 5.2. It can be seen apparently in this figure that the coherence histogram of $\mathbf{\Phi}_{opt} \in \mathbb{R}^{15\times750}$ (rose line) comprises a smaller amount of large coherence

components $ML(\mathbf{\Phi})$, compared with the coherence histogram of $\mathbf{\Phi}_{CDS} \in \mathbb{R}^{15\times750}$ (cyan line).

However, it is unsure that this property can bring a better recovery performance. And hence, two Monte Carlo simulations whose procedures are similar to two above simulations, are proceeded. They aim to achieve the analysis of the reconstructed results using two these MFT acquisitions in various SNR cases (from 5 dB to 40 dB) and various MDs (from 5 to 150 bins). Three different recovery methods, i.e., OMP3, POMP, and Ma-OMP3, are used for the sparse reconstruction. Fig. 5.5 and Fig. 5.6 demonstrate the relaxed support recovery rates R_b of all three above methods with a tolerance offset $\delta = 2$ for two MFT acquisitions $\mathbf{\Phi}_{CDS} \in \mathbb{R}^{15\times750}$ and $\mathbf{\Phi}_{opt} \in \mathbb{R}^{15\times750}$ in the cases of various SNRs and MDs respectively.

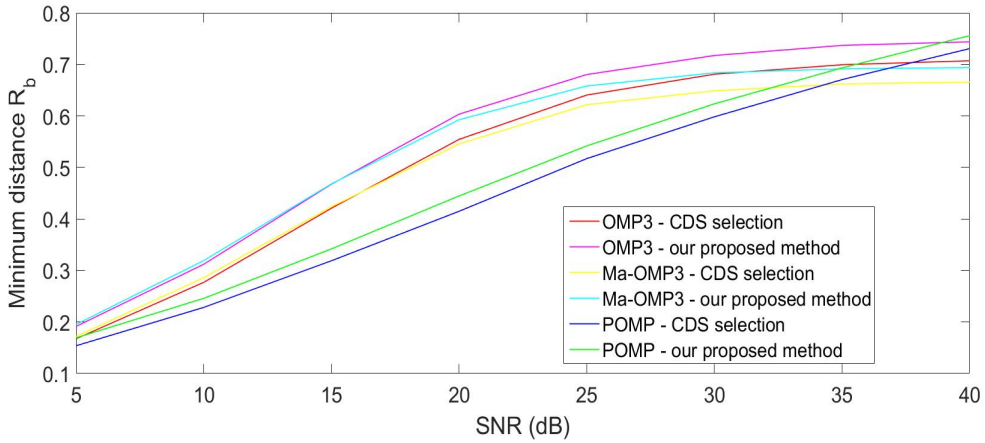

Figure 5.5. Relaxed support recovery rates ($\delta = 2$) at different SNRs (3000 trials for each SNR) for the CDS (31,15,7) and the proposed frequency optimization method with a short range of interest configuration. Choose $N = 750$, $L = 5$, $M = 15$, $F = 100$, $K = 3$, $f_{max} = 31$ MHz

It can be seen in Fig. 5.5 and Fig. 5.6 that the MFT acquisition $\mathbf{\Phi}_{opt}$ (rose, cyan and green lines) brings some advantages. More precisely, the relaxed support recovery rates of three algorithms using this model are much higher than those using the optimization technique based on a CDS (red, yellow and blue lines) in most cases of various SNRs and MDs. These results indicate that the super-resolution MFT acquisition ($F = 100$) structured by our proposed frequency selection optimization method can bring the higher stability of a good support recovery, especially in short range-of-interest applications.

Due to the previous studies [45, 50], it is unsuspected that a CDS of Fourier samples can lead to the optimized DFT sensing matrix and hence a high recovery performance. Extensively, it may also be applied to a MFT acquisition, but only in the case of a conventional grid configuration ($F = 1$). From the above numerical results, a CDS of frequencies is no longer the best choice for a super-resolution MFT acquisition with a

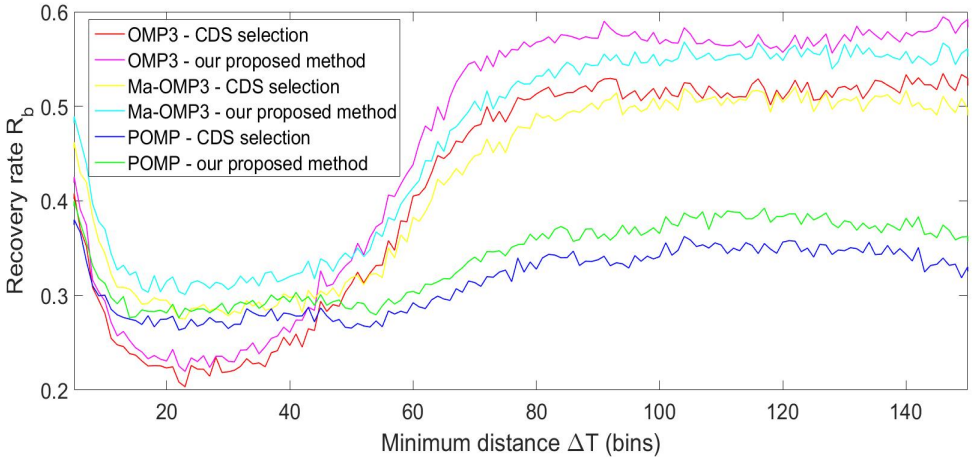

(a) 15dB

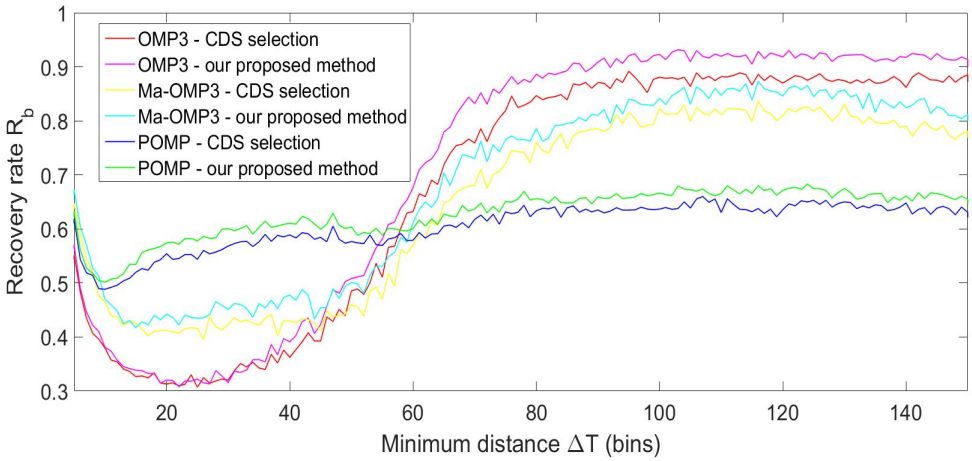

(b) 30dB

Figure 5.6. Relaxed support recovery rates ($\delta = 2$) at different MDs (500 trials for each MD) for the CDS (31,15,7) and the proposed frequency optimization method with a short range of interest configuration. Choose $N = 750, L = 5, M = 15, F = 100, K = 3$, $f_{max} = 31$ MHz

large refinement factor, i.e., $F = 100$. It seems to be possible that the poor recovery performances of MFT acquisition structured by a CDS of frequencies are due to the variation of MFT settings, e.g., the refinement factor and the dimension N. Whereas, our proposed frequency selection optimization method can find an appropriate selection of frequencies for any variation of system parameters to guarantee a higher stability of

good support recovery.

5.3.2 Free parameter settings

As stated above, our proposed frequency selection optimization method can bring potentials with any system parameters. To strengthen this argument, this part aims to evaluate this method in a super-resolution MFT acquisition with free parameter settings.

5.3.2.1 Frequency optimization

Initially, a super-resolution MFT sensing matrix $\mathbf{\Phi}_{init} \in \mathbb{R}^{20\times 500}$ is structured by a random set of 20 frequencies H_{init} and the following parameters, i.e., $N = 500$, $M = 20$, $L = 5$, $f_{max} = 30$ MHz, $F = 100$ and $\Delta r = 5$ cm. These parameters are similar to the numerical experiments in the previous chapters. Note that a CDS (30, 20) does not currently exist and hence is inapplicable in this experiment. Subsequently, the set H_{init} and the sensing matrix $\mathbf{\Phi}_{init}$ are input to our proposed frequency selection optimization method (see Algorithm 12). In this part, the initial phase-offsets are set to zero for all TOF measurements $J_{init} = 0$. After the optimization method ends, the optimized set of 20 frequencies $H_{opt,1}$ derived from the set Ψ, is used for the construction of the new MFT sensing matrix $\mathbf{\Phi}_{opt,1} \in \mathbb{R}^{20\times 500}$.

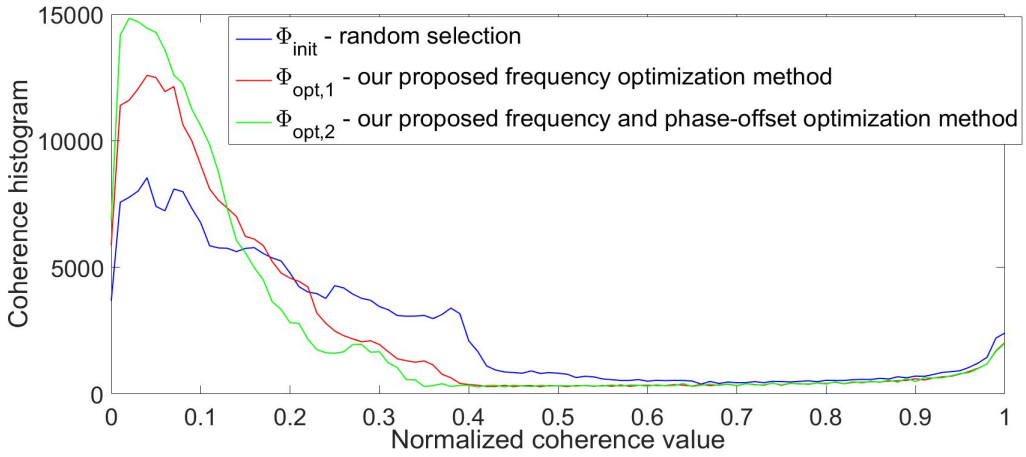

Figure 5.7. Coherence histogram of the MFT sensing matrices structured by a random selection and the proposed methods. Choose $N = 500$, $L = 5$, $M = 20$, $F = 100$, $f_{max} = 30$ MHz.

The coherence histograms of $\mathbf{\Phi}_{init}$ and $\mathbf{\Phi}_{opt,1}$ are illustrated by red and blue lines respectively in Fig. 5.7. Apparently, the Gram matrix of $\mathbf{\Phi}_{opt,1}$ contains fewer large-coherence components ($ML(\mathbf{\Phi})$).

Two Monte Carlo simulations (for $\mathbf{\Phi}_{init}$ and $\mathbf{\Phi}_{opt,1}$) are carried out with 3000 trials for each SNR and 500 trials for each MD. They are aimed to compare the reconstructed results of two different MFT acquisitions in various SNRs (from 5 dB to 40 dB) and various MDs (from 5 to 150 bins). Three different recovery methods, i.e., OMP3, POMP, and Ma-OMP3, are used for 3-sparse reconstruction. Fig. 5.8 and Fig. 5.9 demonstrate the relaxed support recovery rates of all three above methods with a tolerance offset $\delta = 2$ in the cases of various SNRs and MDs respectively.

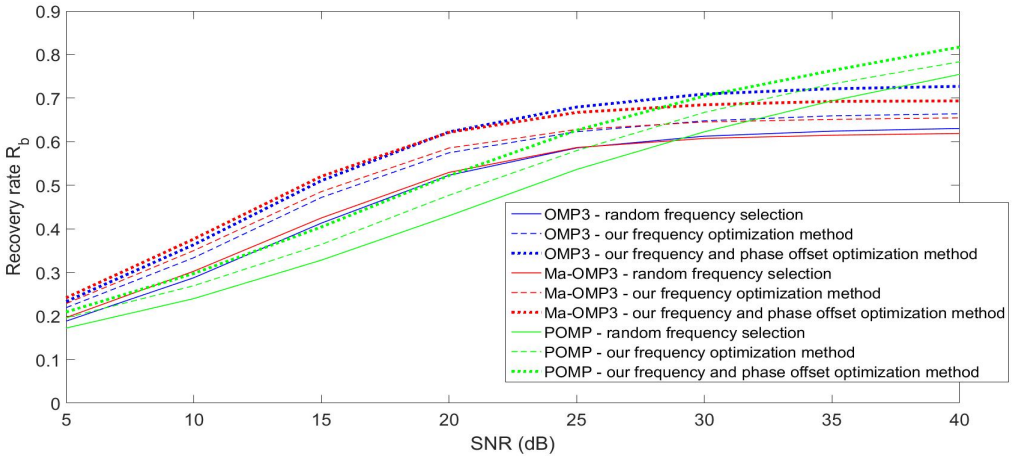

Figure 5.8. Relaxed support recovery rates ($\delta = 2$) at different SNRs (3000 trials for each SNR) for a random selection and the proposed optimization method. Choose $N = 500, L = 5, M = 20, F = 100, \Delta r = 5\text{cm}, K = 3$.

It can be seen in Fig. 5.8 and Fig. 5.9 that the optimized sensing matrix $\mathbf{\Phi}_{opt,1}$ (dashed lines) has some advantages regarding higher relaxed support recovery rates. Eventually, this MFT acquisition is more efficient than the one $\mathbf{\Phi}_{init}$ (solid lines) constructed by a random selection of frequencies. This result occurs for all three used reconstruction algorithms in all cases of various SNRs and MDs.

In summary, our proposed frequency selection optimization method is capable of designing a super-resolution MFT acquisition more efficiently with any parameter settings (N, M) and any large refinement factor. Additionally, this method may also be useful for optimizing a MFT acquisition in a conventional grid configuration (F=1) if a CDS with some setting (N, M) has been not explored yet or may not exist.

5.3.2.2 Frequency and initial phase-offset optimization

In this part, both the frequency set H and the initial phase-offset set J are optimized through our proposed method in Algorithm .13. We aim to improve the support recovery performance of the previous super-resolution MFT acquisition $\mathbf{\Phi}_{opt,1} \in \mathbb{R}^{20\times 500}$.

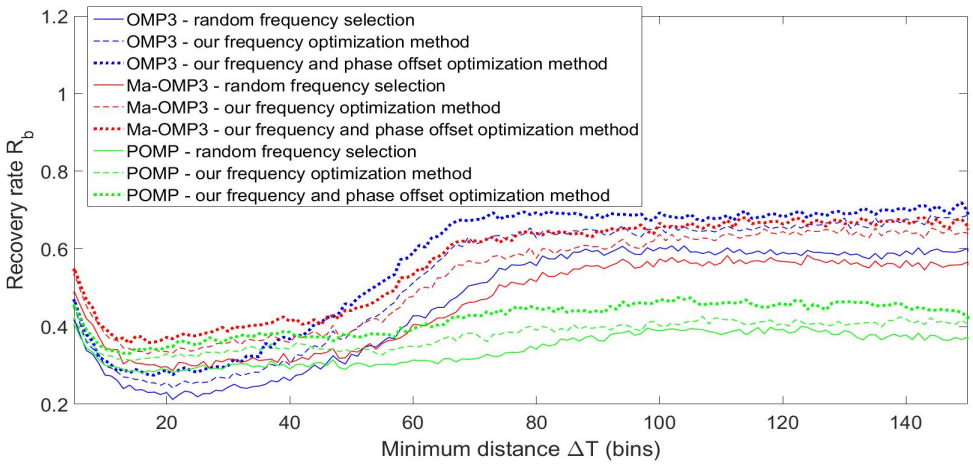

(a) 15dB

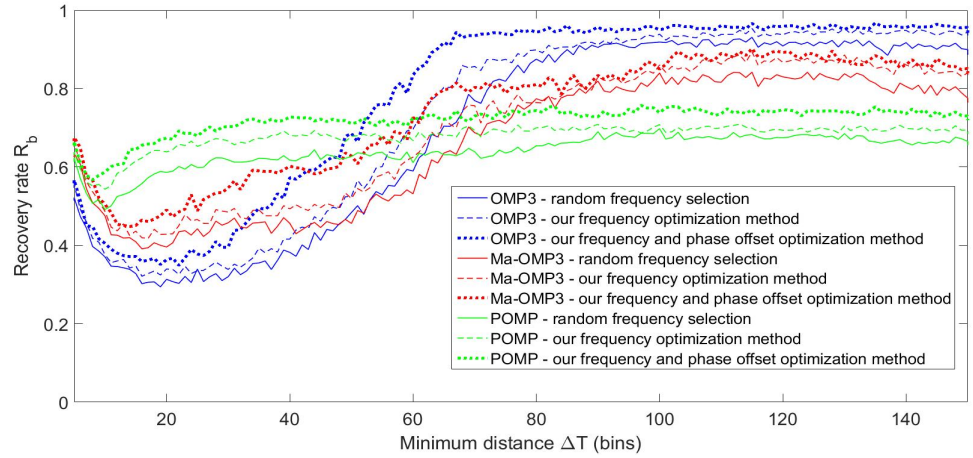

(b) 30dB

Figure 5.9. Relaxed support recovery rates ($\delta = 2$) at different MDs (500 trials for each MD) for a random selection and the proposed optimization method. Choose $N = 500, L = 5, M = 20, F = 100, \Delta r = 5\text{cm}, K = 3$.

Firstly, the optimized frequency selection $H_{opt,1}$ and the zero initial phase-offset set $J_{opt,1} = 0$ are input to Algorithm .13. After the optimization process ends, the new optimized sensing matrix $\mathbf{\Phi}_{opt,2} \in \mathbb{R}^{20\times 500}$ is constructed through the achieved sets $H_{opt,2}$ and $J_{opt,2}$. For an analysis of the coherence property, the coherence histogram of $\mathbf{\Phi}_{opt,2}$ is illustrated by green line in Fig. 5.7. Apparently, the number of large coherence

components ($ML(\mathbf{\Phi}_{opt,2})$) becomes smaller through our proposed optimization method, in comparison with the coherence histogram of $\mathbf{\Phi}_{opt,1}$ (red line).

A similar Monte Carlo simulation is carried out to analyze the reconstruction performance of the new MFT sensing matrix $\mathbf{\Phi}_{opt,2}$. Three methods, i.e., OMP3, POMP, and Ma-OMP3, are used for 3-sparse reconstruction. Subsequently, the relaxed support recovery rates of these three methods with the tolerance offset $\delta = 2$ are averaged after 3000 trials for each SNR and 500 trials for each MD. These results are then demonstrated at various SNRs (from 5 dB to 40 dB) in Fig. 5.8 and various MDs (from 5 to 150 bins) in Fig. 5.9.

It can be seen in Fig. 5.8 and Fig. 5.9 that our proposed frequency and phase-offset selection optimization $\mathbf{\Phi}_{opt,2}$ (dot lines) brings higher relaxed support recovery rates of all three reconstruction algorithms in most cases of various SNRs or MDs, compared to the frequency selection optimization method $\mathbf{\Phi}_{opt,1}$ (dashed lines) or the random frequency selection $\mathbf{\Phi}_{init}$ (solid lines).

5.4 Summary

This chapter proposed the new frequency and initial phase-offset optimization methods for a super-resolution MFT acquisition with a large refinement factor ($F \gg 1$). From the achieved numerical results, these methods are effective for optimizing the design of the super-resolution MFT sensing matrix with any parameters. In other words, they enhance the stability of accurate sparse support recovery. Besides, this chapter indicates that a CDS of frequencies is no longer the optimized one for a super-resolution MFT acquisition.

According to Fig. 5.9, if the strengths of both POMP and OMP3 can be integrated successfully as in our proposed method CMD-OMP (see Section 4.6), then a high stability of accurate support recovery can be guaranteed in the case of a high SNR. More precisely, 95% and 75% atoms are estimated accurately with an accuracy offset $\delta = 2$ in the cases of large and small MDs respectively if SNR is 30 dB. Apparently, the proposed optimization methods take a significant step towards the goals of our relaxed super-resolution CS research with $F = 100$. However, the accuracy of MPI reconstruction in a super-resolution MFT acquisition is still low in the very noisy cases, e.g., SNR=15 dB. Thus, we aim to improve this quality of sparse reconstruction through other CS techniques in next chapters.

6 Multiple measurement vector in super-resolution compressed sensing

Multiple measurement vector (MMV) modeling is a newly emerging CS technique. The sparse representation of MMV has been introduced by the neuro-magnetic inverse problems that arise in Magnetoencephalography (MEG) [70]. This approach improved the quality of the sparse recovery in several applications [71, 72, 73, 74]. Furthermore, Fang et al. [23] have recently proposed a new reconstruction algorithm for a MMV model to enhance support reconstruction performance of a super-resolution DFT-CS problem. Similarly, this chapter applies this MMV technique into our super-resolution MFT-CS acquisition with a configuration of a large refinement factor $F = 100$. Firstly, Section 6.1 introduces multiple polarization of a MFT acquisition in a CW-TOF camera and then casts it to a mathematical MMV model in Section 6.2. Secondly, we introduce many variants of OMP (OMPMMV) for solving the MMV problem in Section 6.3. Next, the modified variants of many greedy pursuits, i.e., OMP3-MMV, Ma-OMP3-MMV, POMP-MMV, are proposed in Section 6.4. The advantages of MMV techniques are shown through numerical experiments in Section 6.5 and finally concluded in Section 6.6.

6.1 Multipolarization TOF signal model

6.1.1 Polarized light

Light is an electromagnetic wave traveling through space. When light goes, the electric and magnetic fields are perpendicular to the direction of propagation. The polarization of a light simply refers to the direction of the electric field. Sunlight or other forms of natural and artificial illumination produce light waves whose electric field vectors vibrate in all planes. They are unpolarized lights. If the electric field vectors are restricted to a single plane by some polarizers, then the light is referred as plane or linearly polarized [75]. The most common source of polarized light is a laser. Eventually, the laser illumination system of a CW-TOF camera can emit or demodulate a linearly polarized optical signal. In particular, one TOF measurement at a modulation frequency f_0 and phase-offset τ in (3.28) can be rewritten for a polarized light q as follows:

$$g_{f_0,q}(\tau) = \sum_{i=1}^{K} a_{i,q}\phi_{f_0,n_i,\tau} \tag{6.1}$$

where $a_{i,q}$ is reflectivity factor of the target i for the polarized incident light q.

6.1.2 Multiple polarization

In a CW-TOF camera, multiple polarization measurements can be produced through using different polarizers at either the transmitted signals or the received radiation. Assume that there are Q polarization channels of MFT measurements. Each measurement vector corresponding to the q^{th} polarization channel will be

$$\boldsymbol{y}_q = \boldsymbol{\Phi}\boldsymbol{x}_q + \boldsymbol{\sigma}_q,\ q = 1, 2, \cdots Q \tag{6.2}$$

where $\boldsymbol{\Phi}$ is the MFT sensing matrix, $\boldsymbol{x}_q$ and $\boldsymbol{\sigma}_q$ are signal and noise vectors respectively. Clearly, when considering only a single polarization channel ($Q = 1$), the above problem reverts to the previous MFT-CS model. Assume that the transmission lines of differently polarized optical signals are similar. Then, the sparse signal vectors $\boldsymbol{x}_q$ contain the same non-zero locations for all $q \in Q$. However, according to Fresnel equations [75], an object material has different reflectivity responses to differently polarized incident lights. From this reason, the vectors $\boldsymbol{x}_q$ for all $q \in Q$ have the same non-zero locations but different magnitudes. This property of multi-polarization data leads to a MMV model with jointly sparse signal vectors.

6.2 Multiple measurement vector (MMV) model

Multiple polarization data in (6.2) can be represented through the following MMV model[71]:

$$\boldsymbol{Y} = \boldsymbol{\Phi}\boldsymbol{X} + \boldsymbol{\Sigma} \tag{6.3}$$

where finding the sparse solution $\boldsymbol{X} \in \mathbb{C}^{M\times Q} = (\boldsymbol{x}^{(1)}, \boldsymbol{x}^{(2)}, \cdots, \boldsymbol{x}^{(Q)})$ relies on the MMVs $\boldsymbol{Y} \in \mathbb{C}^{M\times Q} = (\boldsymbol{y}^{(1)}, \boldsymbol{y}^{(2)}, \cdots, \boldsymbol{y}^{(Q)})$ and the sensing matrix $\boldsymbol{\Phi} \in \mathbb{C}^{M\times N}$. The parameter Q ($Q < M$) denotes the number of measurement vectors and $\boldsymbol{\Sigma}$ is the noise matrix comprising Q noise vectors $\boldsymbol{\sigma}_q$

Similar to the single measurement vector (SMV) problem P_0 in (3.3) with $Q = 1$, the above equation system (6.3) can be solved through the following sparse problem:

$$(G_0) : \min \left| \left(\sum_{q=1}^{Q} |\boldsymbol{x}_q| \right) \right|_0 \quad \text{s.t.} \quad \boldsymbol{Y} = \boldsymbol{\Phi}\boldsymbol{X} \tag{6.4}$$

As stated in Section 3.1, the l_0-optimization problem P_0 in (3.3) is non-deterministic polynomial time (NP)-hard because of the exhausted searching for the best matching sparsest solution. Furthermore, the MMV model G_0 in (6.4) complicates the problem. Fortunately, the common sparse support or the joint-sparsity property of the signal

matrix $\boldsymbol{X}$, which are caused by multiple polarization in a CW-TOF camera, can simplify the above sparse reconstruction G_0.

In this thesis, we assume the availability of multiple polarization data or MMV data $\boldsymbol{Y}$ sharing the joint-sparse signal and a super-resolution MFT acquisition $\boldsymbol{\Phi}$. For the MMV sparse reconstruction, there are several variants of OMP which are introduced next, to decompose these sparse signal vectors efficiently [76, 73].

6.3 Conventional OMPMMV

6.3.1 Basic principle

The OMPMMV method is a variant of OMP for MMV model for finding a sparse solution $\boldsymbol{X}$ through solving the following optimization problem:

$$(Q_1) : \min ||\boldsymbol{\Phi X} - \boldsymbol{Y}||_F, \text{ subject to } \left| \left(\sum_{q=1}^{Q} |\boldsymbol{x}_q| \right) \right|_0 \leq K \tag{6.5}$$

where K is the known joint sparsity. Algorithm 14 describes in detail the operating principle of OMPMMV.

Algorithm 14 Conventional Orthogonal Matching Pursuit for MMV (OMP-MMV)

Input: $\boldsymbol{Y}$, $\boldsymbol{\Phi}$, K, $\tilde{\boldsymbol{\Phi}}$
Output: $\boldsymbol{X}$ and T
1: Initialization: $\boldsymbol{X}_0 = \emptyset, T_0 = \emptyset$, $\boldsymbol{R}_0 = \boldsymbol{Y}$, $\boldsymbol{\Gamma}_0 = \boldsymbol{R}_0$
2: **for** $t = 1$ **to** K **do**
3: Choose the column $\boldsymbol{\Phi}_i$ of $\boldsymbol{\Phi}$ which satisfies $i = \text{argmax}_k \, ||\boldsymbol{z}_k||_q$ where $\boldsymbol{z}_k^T = \tilde{\boldsymbol{\Phi}}_k^H \boldsymbol{\Gamma}_{t-1}$
4: $T_t = T_{t-1} \bigcup i$
5: Compute $\boldsymbol{X}_t = \text{argmin}_{\boldsymbol{X}} \, ||\boldsymbol{\Phi}_{T_t} \boldsymbol{X} - \boldsymbol{Y}||_F$
6: Set $\boldsymbol{R}_t = \boldsymbol{Y} - \boldsymbol{\Phi}_{T_t} \boldsymbol{X}_t$, $\boldsymbol{\Gamma}_t = \boldsymbol{R}_t$
7: **end for**
8: Set $T = T_K$ and $\boldsymbol{X} = \boldsymbol{X}_K$

Apparently, MMVs comprises many single measurement vectors (SMVs). Note that in MMV, the inner product or matching component is a vector. The best-matching atom in OMPMMV is selected at each iteration through integrating these SMV problems. According to Algorithm 14, l_q-norm of the inner product vector in step 3 is used for this integration. There are many different l_q-norms , e.g., l_1-, l_2-, l_∞-norm, and hence different variants of OMPMMV [73]. Note that the columns of a MFT sensing matrix $\boldsymbol{\Phi}$ may be not normalized. Therefore, the matrix $\tilde{\boldsymbol{\Phi}}$ which is the column-normalized version of $\boldsymbol{\Phi}$, is used for computing the matching components.

6.3.2 Recovery guarantee

The MMV problem G_0 has some restricting conditions on the sensing matrix $\boldsymbol{\Phi}$ to guarantee the stability of an exact sparse recovery [76, 73, 27].

Theorem 2. Due to [73], OMPMMV can recover the sparse signal exactly with

$$\left|\left(\sum_{q=1}^{Q}|\boldsymbol{x}_q|\right)\right|_0 \leq \frac{1+\mu}{(1+\sqrt{Q})\mu} \tag{6.6}$$

Moreover, the variant of OMPMMV with l_1-norm is proven by Chen et al. [73] can extend the above upper bound in (6.6) for an exact recovery to $\left|\left(\sum_{q=1}^{Q}|\boldsymbol{x}_q|\right)\right|_0 \leq (1+\mu^{-1})/2$. This condition is similar to that of a SMV problem in (3.14) and hence cannot be satisfied in the super-resolution CS ($F \gg 1$) as the mutual coherence of a super-resolution MFT sensing matrix is approximate to one.

6.4 Modified variants of greedy pursuits for MMV model

6.4.1 Modified OMPMMV

For the conventional OMPMMV, the matching matrix $\boldsymbol{Z} \in \mathbb{C}^{N\times Q}$ in step 4 of Algorithm 14 has its transpose represented by:

$$\boldsymbol{Z}^T = \tilde{\boldsymbol{\Phi}}^H \boldsymbol{R} \tag{6.7}$$

and its column $\boldsymbol{z}_i$:

$$\boldsymbol{z}_i = \boldsymbol{r}_i^T \tilde{\boldsymbol{\Phi}}^* \tag{6.8}$$

where $\boldsymbol{r}_i$ is the i^{th} column of the residual matrix $\boldsymbol{R}$. At an iteration, each residual column $\boldsymbol{r}_i$ derives from the measurement vector $\boldsymbol{y}_i$ and hence, it comprises observations of multiple non-zero atoms. Suppose $\boldsymbol{r}_i$ be the linear combination of K_t columns of sensing matrix $\boldsymbol{\Phi}$:

$$\boldsymbol{r}_i = \sum_{j=1}^{K_t} c_{ji}\boldsymbol{\phi}_{k_j} \tag{6.9}$$

where c_{ji} is reflective magnitude of atom j in the i^{th} measurement vector.

From (6.9), (6.8) can be rewritten:

$$\boldsymbol{z}_i = (\sum_{j=1}^{K_t} c_{ji}\boldsymbol{\phi}_{k_j})^T(\tilde{\boldsymbol{\phi}}_1^* \quad \tilde{\boldsymbol{\phi}}_2^* \quad \cdots \quad \tilde{\boldsymbol{\phi}}_N^*) \tag{6.10}$$

If all columns of $\boldsymbol{\Phi}$ are normalized and orthogonal, then:

$$\boldsymbol{\phi}_k \tilde{\boldsymbol{\phi}}_h^* = \begin{cases} 1 \neq 0 & \text{if } k = h \\ 0 & \text{if } k \neq h \end{cases} \tag{6.11}$$

From (6.10) and (6.11), if residual vector $\boldsymbol{r}_i$ contains no observation of the index k ($c_{ki} = 0$), then the matching element z_{ki} is zero. Otherwise, the absolute value of the matching element is larger than zero. From these points, non-zero atoms can be estimated through finding the largest absolute matching components

$$k_j = \arg \max_{1 \leq h \leq N} \left| (\sum_{j=1}^{K_t} c_{ji} \boldsymbol{\phi}_{k_j})^T \tilde{\boldsymbol{\phi}}_h^* \right| \tag{6.12}$$

Nevertheless, in a super-resolution MFT problem, the above atom selection procedure apparently fails due to the small incoherence of sensing matrix. Therefore, we introduce a modified variant of OMPMMV in Algorithm 15 with some modification steps to improve the accuracy of the atom selection in the MMV techniques when the sensing matrix is highly coherent. They comprise two main steps:

Algorithm 15 Modified Orthogonal Matching Pursuit for MMV joint sparse recovery - (Modified OMPMMV)

Require: $\boldsymbol{Y}$, $\boldsymbol{\Phi}$, K, $\tilde{\boldsymbol{\Phi}}$
Ensure: $\boldsymbol{X}$,T

Modified OMP-MMV - Atom Selection Module

1: Initialization: $\boldsymbol{X}_0 = \emptyset, T_0 = \emptyset$, $\boldsymbol{R}_0 = \boldsymbol{Y}$, $\boldsymbol{\Gamma}_0 = \tilde{\boldsymbol{R}}_0$
2: **for** $t = 1$ **to** K **do**
3: Choose the column a_i of matrix $\boldsymbol{\Phi}$ which satisfies $i = \text{argmax}_k \, ||\boldsymbol{z}_k||_\infty$ where $\boldsymbol{z}_k^T = \tilde{\boldsymbol{\Phi}}_k^H \boldsymbol{\Gamma}_{t-1}$
4: Insert i into set $T_t = T_{t-1} \bigcup i$
5: Compute $\boldsymbol{X}_t = \text{argmin}_{\boldsymbol{X}} \, ||\boldsymbol{\Phi}_{T_t} \boldsymbol{X} - \boldsymbol{Y}||_F$
6: Compute residual $\boldsymbol{R}_t = \boldsymbol{Y} - \boldsymbol{\Phi}_{T_t} \boldsymbol{X}_t$ and $\boldsymbol{\Gamma}_t = \tilde{\boldsymbol{R}}_t$
7: **end for**
8: Set $T = T_K$ and $\boldsymbol{X} = \boldsymbol{X}_K$

- The residual matrix $\boldsymbol{R}$ is replaced by its normalized-column version $\tilde{\boldsymbol{R}}$ for computing the matching components between the residual matrix and the columns of the sensing matrix.

$$\boldsymbol{z}_i = \frac{(\sum_{j=1}^{K_t} c_{ji} \boldsymbol{\phi}_{k_j})^T}{|| \sum_{j=1}^{K_t} c_{ji} \boldsymbol{\phi}_{k_j} ||_2} (\tilde{\boldsymbol{\phi}}_1^* \quad \tilde{\boldsymbol{\phi}}_2^* \quad \cdots \quad \tilde{\boldsymbol{\phi}}_N^*) \tag{6.13}$$

- Use l_∞-norm of the inner product for integrating MMVs.

Given k_m be the non-zero index of $\boldsymbol{x}_i$ with the largest absolute magnitude $|c_{k_m i}| = \max_{k_j} |c_{k_j i}|$. Suppose that $|c_{k_m i}| \gg |c_{k_j i}| \; \forall j \neq m$, then the matching vector $\boldsymbol{z}_i$ in (6.13) has the ${k_m}^{th}$ element:

$$|z_{k_m i}| = \Big| \frac{(\sum_{j=1}^{K_t} c_{ji} \boldsymbol{\phi}_{k_j})^T}{|| \sum_{j=1}^{K_t} c_{ji} \boldsymbol{\phi}_{k_j} ||_2} \tilde{\boldsymbol{\phi}}^*_{k_m} \Big| \approx \Big| \frac{(c_{k_m i} \boldsymbol{\phi}_{k_m})^T}{||c_{k_m i} \boldsymbol{\phi}_{k_m}||_2} \tilde{\boldsymbol{\phi}}^*_{k_m} \Big| = 1 \tag{6.14}$$

and elements at other indices $n \neq k_m$:

$$|z_{ni}| = \Big| \frac{(\sum_{j=1}^{K_t} c_{ji} \boldsymbol{\phi}_{k_j})^T}{|| \sum_{j=1}^{K_t} c_{ji} \boldsymbol{\phi}_{k_j} ||_2} \tilde{\boldsymbol{\phi}}^*_{n} \Big| = \Big|\Big| \frac{(\sum_{j=1}^{K_t} c_{ji} \boldsymbol{\phi}_{k_j})^T}{|| \sum_{j=1}^{K_t} c_{ji} \boldsymbol{\phi}_{k_j} ||_2} \Big|\Big|_2 \Big|\Big| \tilde{\boldsymbol{\phi}}^*_{n} \Big|\Big|_2 \sin\theta_n < 1 \tag{6.15}$$

From the above results, if the dynamic range of an arbitrary column vector $\boldsymbol{x}_i$ is large, then the non-zero index k_m can be estimated accurately by using the l_∞-norm of the matching component rows. The effectiveness of our proposed Modified OMP-MMV in Algorithm 15 will be proven through the next numerical comparison with other variants of OMPMMV, i.e., l_1-, l_2- and l_∞-norm.

6.4.2 Modified global optimization - GO-MMV

The thesis proposes in this part a new atom updating module GO-MMV, a variant of the global optimization (GO) which has been introduced in Section 4.2, for a MMV model as described in Algorithm 16. The operating principle of this method is correcting each non-zero index while holding others fixed. It relies on finding a replacing atom which can bring the smallest residual cost $||\boldsymbol{\Phi}_T \boldsymbol{X} - \boldsymbol{Y}||_F$. Unlike the atom selection module in the above Modified OMPMMV, the atom updating module of GO-MMV uses l_2-norm of matching components to integrate all MMVs for selecting the replacing atoms.

6.4.3 Cyclic orthogonal matching pursuit for MMV model - OMP3-MMV

We extend a variant of OMP3 for a MMV model, namely Cyclic OMPMMV (OMP3-MMV), by adding the above GO-MMV at the end of the Modified OMPMMV, as described in Algorithm 17. More precisely, GO-MMV fixes the wrongly selected indices of Modified OMPMMV. And hence, OMP3-MMV is promising to bring a better recovery performance. According to the operating principle of this method in Algorithm 16, our proposed OMP3-MMV uses l_∞-norm of the matching component vectors in atom selection module and l_2-norm of the matching component vectors in atom updating module. We refer this method shortly as OMP3-MMV (l_∞-norm, l_2-norm). Besides, there are other variants of OMP3-MMV with other settings of (l_{p_1}-norm, l_{p_2}-norm). In next numerical experiments, we aim to prove that our proposed variant OMP3-MMV (l_∞-norm, l_2-norm) has advantages regarding high support recovery performances.

Algorithm 16 Global optimization for MMV model - (GO-MMV)

Require: $\boldsymbol{Y}$, $\boldsymbol{\Phi}$, $\boldsymbol{X}$, T, $\tilde{\boldsymbol{\Phi}}$
Ensure: $\boldsymbol{X}$, T
while true **do**
  for $j = 1$ **to** length(T) **do**
    Set $T_2 = T$ and $\boldsymbol{X}_2 = \boldsymbol{X}$
    Remove the j^{th} element from T_2 and the j^{th} row from $\boldsymbol{X}_2$
      $T_2 = T_2 \setminus T_2(j)$
      $\boldsymbol{X}_2 = \boldsymbol{X}_2 \setminus \boldsymbol{X}_2(j,:)$
    Compute residual $\boldsymbol{R} = \boldsymbol{Y} - \boldsymbol{\Phi}_{T_2}\boldsymbol{X}_2$
    Choose the column i of matrix $\boldsymbol{\Phi}$ which satisfies
      $i = \text{argmax}_k \, ||\boldsymbol{z}_k||_2$ where $\boldsymbol{z}_k^T = \tilde{\boldsymbol{\Phi}}_k^H \boldsymbol{R}$
    if $i \notin T$ **then**
      Insert i into set $T_2 = T_2 \bigcup i$
    else
      continue
    end if
    Compute $\boldsymbol{X}_2 = \text{argmin}_{\boldsymbol{X}} \, ||\boldsymbol{\Phi}_{T_2}\boldsymbol{X} - \boldsymbol{Y}||_F$
    Compute residual $\boldsymbol{R}_2 = \boldsymbol{Y} - \boldsymbol{\Phi}_{T_2}\boldsymbol{X}_2$
    if $||\boldsymbol{R}_2||_F < ||\hat{\boldsymbol{R}}||_F$ **then**
      Update $T = T_2$ and $\hat{\boldsymbol{R}} = \boldsymbol{R}_2$
      Update $\boldsymbol{X} = \boldsymbol{X}_2$
    end if
  end for
  if no update in step 15 and 16 **then**
    break
  end if
end while

Algorithm 17 Cyclic Orthogonal Matching Pursuit for MMV joint sparse recovery - (OMP3-MMV)

Require: $\boldsymbol{Y}$, $\boldsymbol{\Phi}$, K, $\tilde{\boldsymbol{\Phi}}$
Ensure: $\boldsymbol{X}$, T
Initialization: $\boldsymbol{X}_0 = \emptyset, T_0 = \emptyset$, $\boldsymbol{R}_0 = \boldsymbol{Y}$, $\boldsymbol{\Gamma}_0 = \tilde{\boldsymbol{R}}_0$
$[\boldsymbol{X}, T]$ = Modified OMPMMV ($\boldsymbol{Y}$, $\boldsymbol{\Phi}$, K)
$[\boldsymbol{X}, T]$ = GO-MMV ($\boldsymbol{Y}$, $\boldsymbol{\Phi}$, $\boldsymbol{X}$, T)

6.4.4 Cyclic magnitude adjustment orthogonal matching pursuit for MMV model - Ma-OMP3-MMV

Magnitude-Adjustment Orthogonal Matching Pursuit (Ma-OMP) is a variant of non-negative OMP. As proven through the numerical results in Section 4.6, this algorithm can bring a better recovery performance at a small MD in extremely noisy cases. In this part, this method is modified for a MMV case as described in Algorithm 18.

Algorithm 18 Modified Magnitude-Adjustment Orthogonal Matching Pursuit for MMV joint sparse recovery - (Ma-OMPMMV)

Require: $\boldsymbol{Y}$, $\boldsymbol{\Phi}$, K, $\tilde{\boldsymbol{\Phi}}$
Ensure: $\boldsymbol{X}$, T
1: Initialization: $\boldsymbol{X}_0 = \emptyset, T_0 = \emptyset$, $\boldsymbol{R}_0 = \boldsymbol{Y}$, $\boldsymbol{\Gamma}_0 = \tilde{\boldsymbol{R}}_0$
2: **for** $t = 1$ **to** K **do**
3: Choose the column a_i of matrix $\boldsymbol{\Phi}$ which satisfies $i_t = \text{argmax}_k \, ||\boldsymbol{z}_k||_\infty$ where $\boldsymbol{z}_k^T = \tilde{\boldsymbol{\Phi}}_k^H \boldsymbol{\Gamma}_{t-1}$
4: Insert i_t into set $T_t = T_{t-1} \bigcup i_t$
5: Compute $a_t = \text{argmin}_{a_t} \, ||a_t \boldsymbol{\phi}_{i_t} - \boldsymbol{r}_{t-1}||_2$
6: **if** $i_t \in T_{t-1}$ **then**
7: $x_{i_t} = x_{i_t} + a_t$
8: **else**
9: $T_t = T_{t-1} \bigcup i_t$
10: $x_{i_t} = \rho a_t$
11: **end if**
12: Compute $\boldsymbol{X}_t = \text{argmin}_{\boldsymbol{X}} \, ||\boldsymbol{\Phi}_{T_t} \boldsymbol{X} - \boldsymbol{Y}||_F$
13: Compute residual $\boldsymbol{R}_t = \boldsymbol{Y} - \boldsymbol{\Phi}_{T_t} \boldsymbol{X}_t$ and $\boldsymbol{\Gamma}_t = \tilde{\boldsymbol{R}}_t$
14: **end for**
15: Set $T = T_K$ and $\boldsymbol{X} = \boldsymbol{X}_K$

Similar to the Modified OMPMMV, Ma-OMPMMV uses l_∞-norm of matching component vectors to integrate MMVs. Besides, similar to Ma-OMP, Ma-OMPMMV selects an adjustment factor of $\rho = 0.8$ for regulating the estimated non-zero magnitudes, as proven in Section 4.5.2. Subsequently, we add the GO-MMV technique to the end of the above Ma-OMPMMV to correct the wrongly selected indices. This method is referred as Ma-OMP3-MMV as described in Algorithm 19. Similar to OMP3-MMV, our proposed Ma-OMP3-MMV uses l_∞-norm and l_2-norm in atom selection and updating module respectively. Furthermore, there are other variants of Ma-OMP3-MMV with various settings of (l_{p_1}-norm, l_{p_2}-norm) to integrate MMVs.

Algorithm 19 Modified Cyclic Magnitude-Adjustment Orthogonal Matching Pursuit for MMV joint sparse recovery - (Ma-OMP3-MMV)

Require: $\boldsymbol{Y}$, $\boldsymbol{\Phi}$, K, $\tilde{\boldsymbol{\Phi}}$
Ensure: $\boldsymbol{X}$, T
1: Initialization: $\boldsymbol{X}_0 = \emptyset, T_0 = \emptyset$, $\boldsymbol{R}_0 = \boldsymbol{Y}$, $\boldsymbol{\Gamma}_0 = \tilde{\boldsymbol{R}}_0$
2: $[\boldsymbol{X}, T]$ = Ma-OMPMMV ($\boldsymbol{Y}$, $\boldsymbol{\Phi}$, K)
3: $[\boldsymbol{X}, T]$ = GO-MMV ($\boldsymbol{Y}$, $\boldsymbol{\Phi}$, $\boldsymbol{X}$, T)

6.4.5 POMP for MMV model

As proven in Chapter 3, POMP is a potential recovery algorithm to bring a better recovery performance in small MDs, especially in the nearly noiseless cases. In principle, the atom selection module of POMP inherits from OMP. Our research aims to develop a variant of POMP for a MMV model but is currently unsuccessfully. Apparently, it becomes challenging to integrate all MMVs in its atom removal module.

In this thesis, we can only use POMP for MMV data after converting it to the averaged measurement vector:

$$\boldsymbol{y}_0 = \frac{1}{Q}\sum_{q=1}^{Q}\boldsymbol{y}_q = \boldsymbol{\Phi}\frac{1}{Q}\sum_{q=1}^{Q}\boldsymbol{x}_q = \boldsymbol{\Phi}\boldsymbol{x}_0 \tag{6.16}$$

The above problem (6.16) is a converted SMV model. Therefore, OMP3, Ma-OMP3 or POMP can be used for the reconstruction of the sparse signal $\boldsymbol{x}_0$ using (6.16). From this result, we can estimate the joint-sparse support of the unknown matrix $\boldsymbol{X}$. The above implementation is similar to the numerical studies of Yang et al.[74]. The averaging operator in (6.16) is considered as temporal or spatial noise filtering techniques [42]. Thus, the converted SMV model is promising to bring higher recovery performances through the reduction of measurement noises.

6.5 Numerical results

This section carries out several numerical experiments, similar to Section 4.5. We aim to do the reconstruction performance analysis of our proposed methods for a super-resolution MFT acquisition using MMV techniques. A MMV model with $Q = 3$ is constructed on the super-resolution MFT sensing matrix $\boldsymbol{\Phi}_{opt,1} \in \mathbb{R}^{20\times 500}$ with a large refinement factor $F = 100$ and the old parameters, i.e., $L = 5$, $f_{max} = 30$ MHz. This sensing matrix is the optimized result of the proposed frequency selection optimization in Chapter. 5.

This analysis of each MMV joint-sparse reconstruction algorithm includes two main Monte Carlo simulations:

- The first one is analyzing the reconstruction capabilities of a method for a MMV model in the cases of various SNRs (from 5 dB to 50 dB). Each SNR comprises 3000 trials. At each trial, a non-negative K-joint-sparse signal matrix ($Q = 3$) is generated with each column containing K random non-zero indices ($\Delta T \geq 5$ for $\delta = 2$ or $\Delta T \geq 11$ for $\delta = 5$) and magnitudes into the range [0.1,10]. Note that three columns of this signal matrix have the common non-zero support but different non-zero magnitudes. Subsequently, the noisy MMV data is generated through (6.3) with an analyzed SNR. The relaxed support recovery rates with the tolerance offsets $\delta = 2$ and $\delta = 5$ are averaged after 3000 trials for each SNR. Finally, we obtain the support recovery performance of the reconstruction algorithm in the SNR domain.
- The second one is analyzing the reconstruction capabilities of this method for a MMV model in the cases of various MDs. The relaxed support recovery rates with the tolerance offsets $\delta = 2$ and $\delta = 5$ are averaged after 500 trials for each MD. At each trial, the procedures of signal and MMV generation are similar to the first analysis. But the joint-sparse support of the signal matrix $\boldsymbol{X}$ has MD equal to the analyzed MD value. Note that there are two cases of different SNRs for the generation of noisy MMVs, i.e., 15 dB and 30 dB. With this analysis, we obtain the support recovery performance of the method in the MD domain (from 5 to 150 bins) with two various noise levels.

6.5.1 Comparison between OMPMMV variants

Two Monte Carlo simulations are carried out in this part to obtain the reconstruction performance analysis of all six different variants of OMPMMV in the SNR and MD domains. These variants include:

- the proposed Modified OMPMMV in Algorithm 15.
- three conventional variants of OMPMMV in Algorithm 14 with different l_p-norms, i.e., l_1-, l_2-, and l_∞-norm, without normalizing the residual vectors.
- two conventional variants of OMPMMV in Algorithm 14 with different l_p-norms, i.e., l_1-, l_2-norm, with normalizing the residual vectors.

According to the achieved results in Fig. 6.1 and Fig. 6.2, we have:

- The proposed Modified OMPMMV (blue lines) brings the highest relaxed support recovery rates in all cases of different noise levels and MDs among the analyzed OMPMMV variants.
- The support recovery performances of the conventional OMPMMV with different l_p-norms, i.e., l_∞-, l_2- and l_1- norm, without normalizing the residual vectors (rose, red and green lines respectively) stay in the descending order.

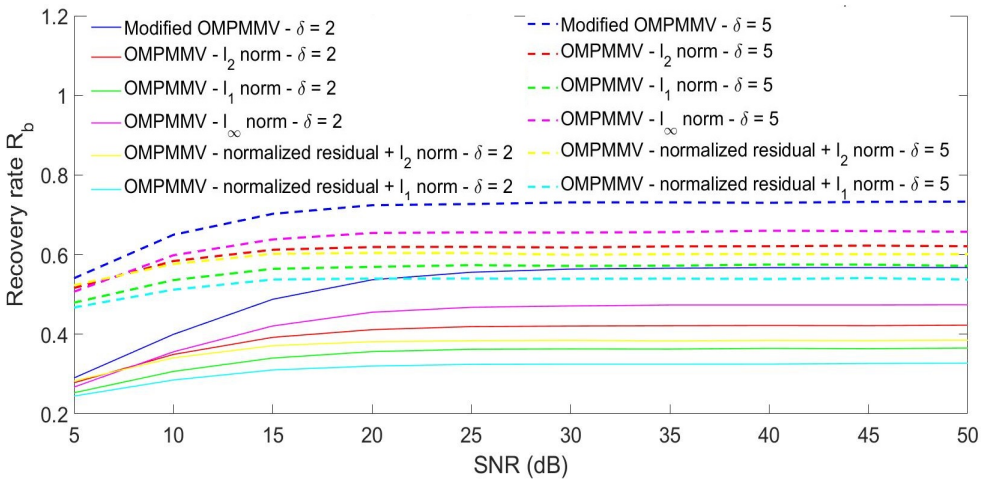

Figure 6.1. Comparison between the relaxed support recovery performances of Modified OMPMMV and the conventional variants of OMPMMV in the cases of different SNRs (3000 trials for each SNR). Choose $N = 500$, $L = 5$, $M = 20$, $Q = 3$, $f_{max} = 30$ MHz, $F = 100$, $K = 3$, $\Delta r = 5$ cm for a super-resolution MMV-MFT acquisition.

- Two remaining variants (yellow and light blue lines) with normalizing the residual vectors but other l_p-norms, i.e., l_2- or l_1- norm, have the poorest support reconstruction performances. These results reveal that the normalizing of the residual vectors is only effective if OMPMMV uses l_∞-norm of the matching rows.

6.5.2 Comparison between OMP3-MMV variants

In this part, the recovery performances of four different variants of OMP3-MMV are compared to each other in the same MMV-MFT acquisition $\mathbf{\Phi}_{opt,1}$. Four variants of OMP3-MMV are constructed with different settings (l_{p_1}-norm, l_{p_2}-norm) as mentioned in Section 6.4.3, i.e., (l_∞-norm, l_2-norm), (l_∞-norm, l_1-norm), (l_∞-norm, l_∞-norm), (l_2-norm, l_2-norm). Fig. 6.3 and Fig. 6.4 demonstrate their relaxed support recovery rates in the cases of various SNRs (3000 trials for each SNR) and various MDs (500 trials for each MD).

It can be seen in Fig. 6.3 that our proposed OMP3-MMV with (l_∞-norm, l_2-norm) (blue lines) brings the highest relaxed support recovery rates with both $\delta = 2$ and $\delta = 5$ in the cases of low SNRs (below 35 dB). Nevertheless, at a SNR of higher than 35 dB, the recovery rates of the variant of OMP3-MMV with (l_∞-norm, l_∞-norm) (red lines) are slightly higher than those of our proposed method with a small tolerance offset $\delta = 2$. This result can be explained through the highest reconstruction performances of the variant of OMP3-MMV with (l_∞-norm, l_∞-norm) in most cases of small MDs

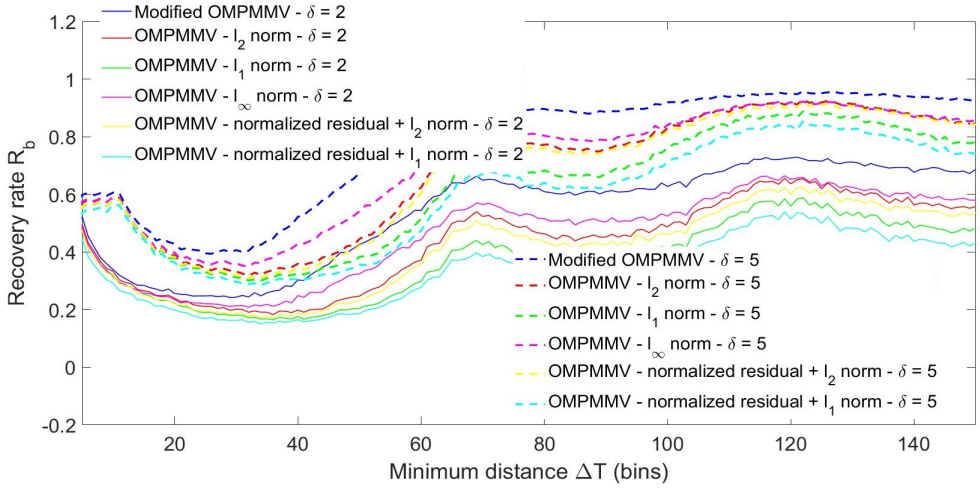

(a) 15dB

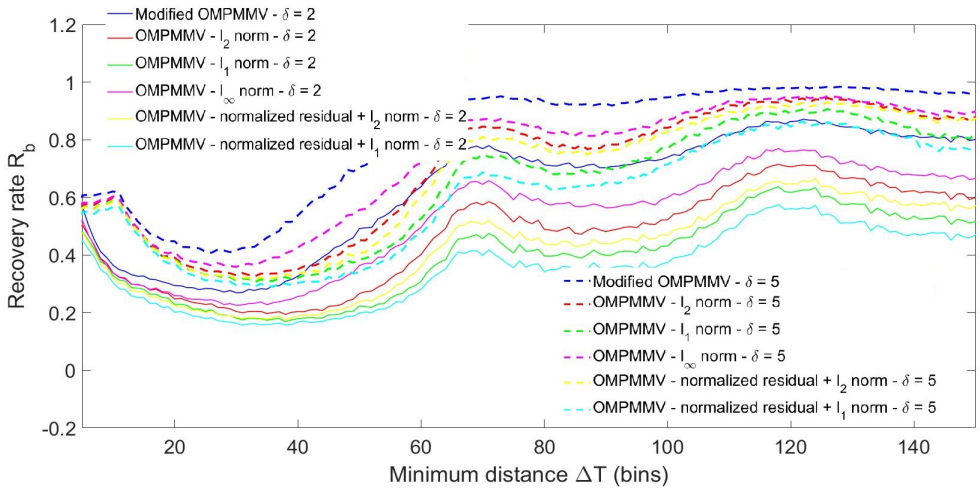

(b) 30dB

Figure 6.2. Comparison between the relaxed support recovery performances of Modified OMPMMV and the conventional variants of OMPMMV in the cases of different MDs (500 trials for each MD). Choose $N = 500$, $L = 5$, $M = 20$, $Q = 3$, $f_{max} = 30$ MHz, $F = 100$, $K = 3$, $\Delta r = 5$ cm for a super-resolution MMV-MFT acquisition.

$(10 \leq \Delta T \leq 30)$, as can be seen in Fig. 6.4b. Nevertheless, with a large offset $\delta = 5$, there seems to be no significant difference between the relaxed support recovery rates of these two variants. For an overall comparison, our proposed OMP3-MMV with (l_∞-

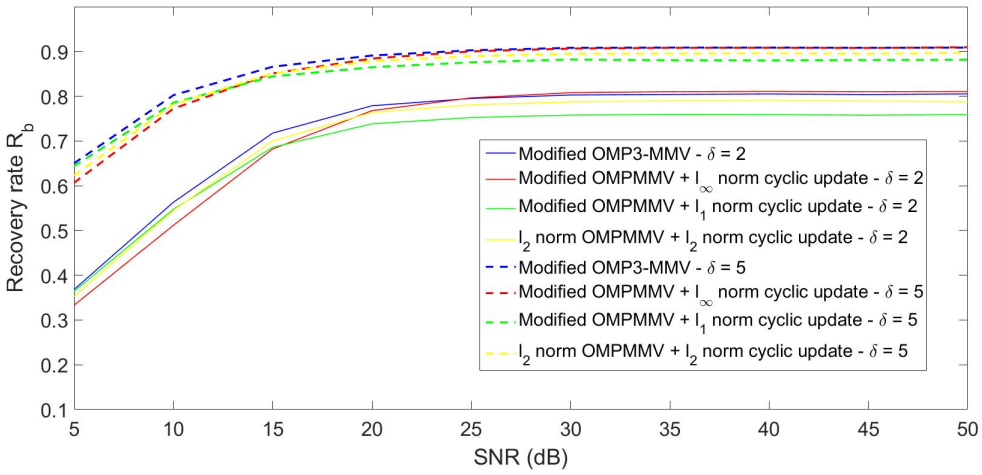

Figure 6.3. Comparison between the relaxed support recovery performances of our proposed OMP3-MMV and the other variants of OMP3-MMV in the cases of different SNRs (3000 trials for each SNR). Choose $N = 500$, $L = 5$, $M = 20$, $Q = 3$, $f_{max} = 30$ MHz, $F = 100$, $K = 3$, $\Delta r = 5$ cm for a super-resolution MMV-MFT acquisition.

norm, l_2-norm) can be considered as the best method among the analyzed variants of OMP3-MMV.

6.5.3 Comparison between Ma-OMP3-MMV variants

Similarly, this part aims to compare the reconstruction performances of many variants of Ma-OMP3-MMV for the same super-resolution MFT acquisition using MMV techniques. As mentioned in Section 6.4.4, our proposed Ma-OMP3-MMV in Algorithm 19 uses two norm operations (l_∞-norm, l_2-norm).

For a diverse comparison, two other variants of Ma-OMP3-MMV with different settings (l_{p_1}-norm, l_{p_2}-norm), i.e., (l_∞-norm, l_∞-norm) and (l_∞-norm, l_1-norm) are also analyzed in the cases of various SNRs and MDs. All achieved results of three Ma-OMP3-MMV variants are demonstrated in Fig. 6.5 and Fig. 6.6.

It can be seen in Fig. 6.5 and Fig. 6.6 that our proposed method Ma-OMP3-MMV with (l_∞-norm, l_2-norm) (blue lines) brings the highest relaxed support recovery rates ($\delta = 2$ and $\delta = 5$) in the cases of low SNRs below 35 dB or in the cases of large MDs. Whereas, the variant of Ma-OMP3-MMV with (l_∞-norm, l_∞-norm) (red lines) is the best choice among three variants in other cases. The above results are similar to those of OMP3-MMV. For an overall evaluation, our proposed method Ma-OMP3-MMV with (l_∞-norm, l_2-norm) is the best variant of Ma-OMP3-MMV for our super-resolution MMV-MFT acquisition.

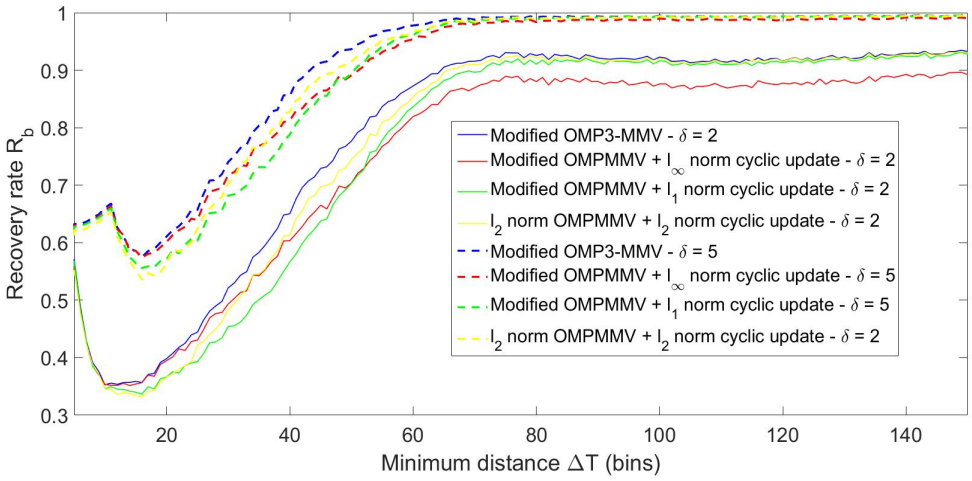

(a) 15dB

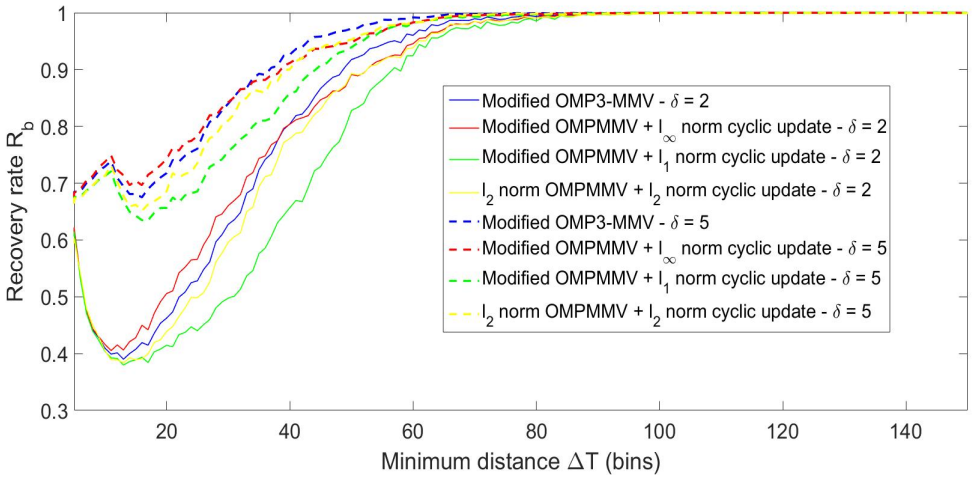

(b) 30dB

Figure 6.4. Comparison between the relaxed support recovery performances of our proposed OMP3-MMV and the other variants of OMP3-MMV in the cases of different MDs (500 trials for each MD). Choose $N = 500$, $L = 5$, $M = 20$, $Q = 3$, $f_{max} = 30$ MHz, $F = 100$, $K = 3$, $\Delta r = 5$ cm for a super-resolution MMV-MFT acquisition.

6.5.4 Comparison between MMVs and SMV

A question arises whether a super-resolution MFT acquisition using MMV techniques is actually more efficient than a SMV model. This part aims to answer this question

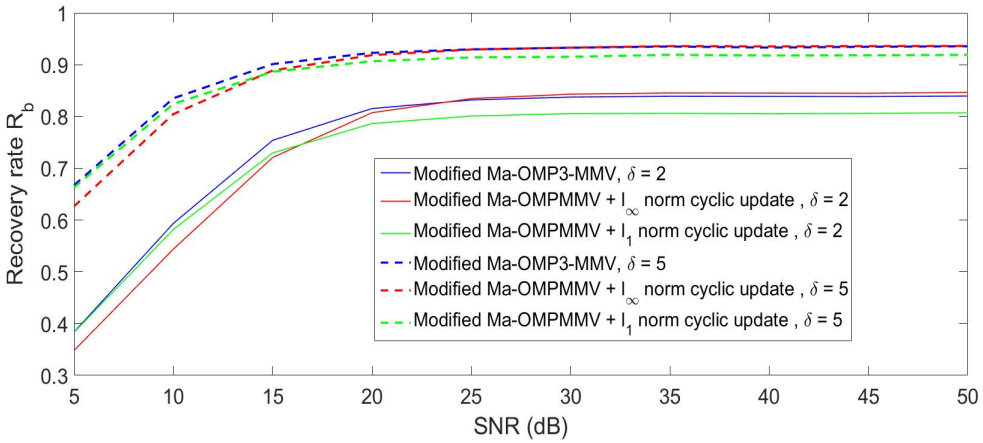

Figure 6.5. Comparison between the relaxed support recovery performances of many variants of Ma-OMP3-MMV in the cases of different SNRs (3000 trials for each SNR). Choose $N = 500$, $L = 5$, $M = 20$, $Q = 3$, $f_{max} = 30$ MHz, $F = 100$, $K = 3$, $\Delta r = 5$ cm for a super-resolution MMV-MFT acquisition.

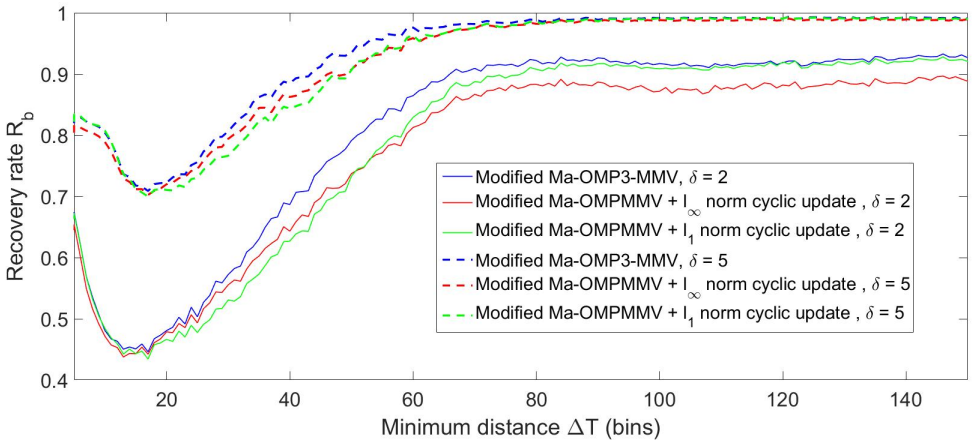

(a) 15dB

Figure 6.6. Comparison between the relaxed support recovery performances of many variants of Ma-OMP3-MMV in the cases of different MDs (500 trials for each MD). Choose $N = 500$, $L = 5$, $M = 20$, $Q = 3$, $f_{max} = 30$ MHz, $F = 100$, $K = 3$, $\Delta r = 5$ cm for a super-resolution MMV-MFT acquisition.

through numerical experiments. The above MMV model with $Q = 3$ can be considered as three SMV models sharing the same sensing matrix $\mathbf{\Phi}_{opt,1} \in \mathbb{R}^{20\times 500}$. For the

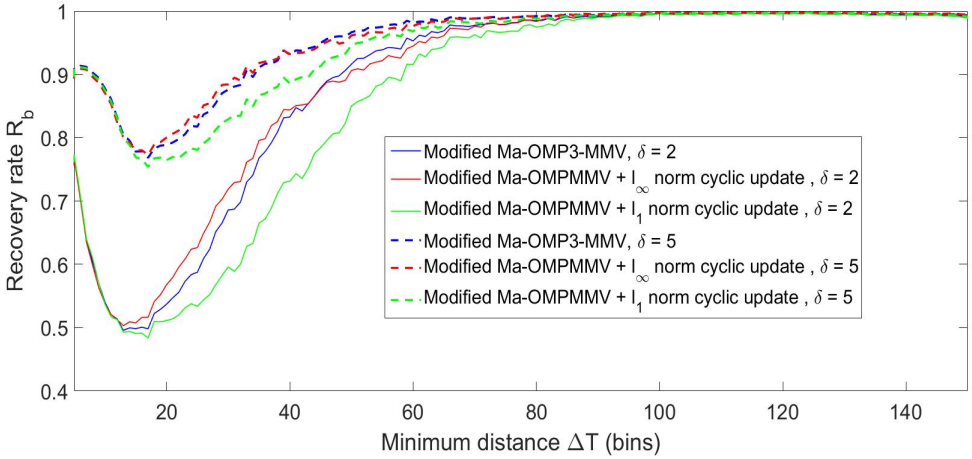

(b) 30dB

Figure 6.6. Comparison between the relaxed support recovery performances of Ma-OMP3-MMV and the other variants of Ma-OMP3-MMV in the cases of different MDs (500 trials for each MD). Choose $N = 500$, $L = 5$, $M = 20$, $Q = 3$, $f_{max} = 30$ MHz, $F = 100$, $K = 3$, $\Delta r = 5$ cm for a super-resolution MMV-MFT acquisition (cont).

construction of such MMV data, we carry out a total of 60 TOF measurements. From this point, we construct a SMV model with 60 real-valued TOF measurements at different modulation frequencies. An optimized set of 60 frequencies are found through our proposed frequency optimization method in Algorithm 12 with the same previous parameters, i.e., $N = 500, L = 5, f_{max} = 30$ MHz, $F = 100$. After the optimization phase, we obtain the optimized super-resolution MFT sensing matrix $\mathbf{\Phi}_{opt} \in \mathbb{R}^{60\times 500}$.

Two Monte Carlo simulations are carried out on the super-resolution MFT acquisition $\mathbf{\Phi}_{opt} \in \mathbb{R}^{60\times 500}$ with 3000 trials for each SNR and 500 trials for each MD. At each trial, the procedures of signal and noisy measurement vector generation are similar to Section. 4.5. Three reconstruction methods, i.e., OMP3, POMP, and Ma-OMP3, reconstruct the sparse signal based on the generated noisy measurement vector. Their relaxed support recovery rates with the tolerance offset $\delta = 2$ are then averaged after all trials. These results are demonstrated in the cases of various SNRs in Fig. 6.7 and in the cases of various MDs in Fig. 6.8. Besides, the achieved results of OMP3-MMV and Ma-OMP3-MMV collected from Fig. 6.3, Fig. 6.4 and Fig. 6.5, Fig. 6.6 are also demonstrated in Fig. 6.7 and Fig. 6.8.

Moreover, an alternative sparse reconstruction approach for MMV data is to convert it to a SMV data as described in (6.16). Subsequently, OMP3, Ma-OMP3, and POMP reconstruct the common sparse support based on the converted SMV data. Their relaxed support recovery rates with the tolerance offset $\delta = 2$ are also demonstrated in Fig. 6.7

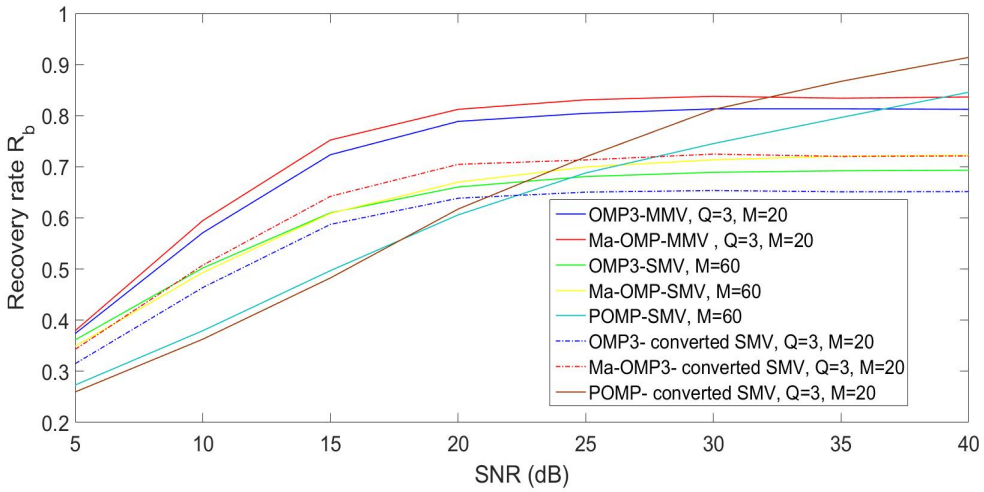

Figure 6.7. Comparison between the relaxed support recovery performances ($\delta = 2$) in MMV model and SMV model in the cases of different SNRs (3000 trials for each SNR). Choose $N = 500$, $L = 5$, $M = 20$, $Q = 3$, $f_{max} = 30$ MHz, $F = 100$, $K = 3$, $\Delta r = 5$ cm for the construction of MMV and SMV models.

and Fig. 6.8. Note that the MMV data in the previous numerical experiments (Fig. 6.3, Fig. 6.4 and Fig. 6.5, Fig. 6.6) are reused in this simulation for a correct comparison.

A comparison between the results in Fig. 6.7 and Fig. 6.8 claims that:

- The MMV model based on the MFT acquisition $\mathbf{\Phi}_{opt,1} \in \mathbb{R}^{20\times 500}$ using OMP3-MMV and Ma-OMP3-MMV (solid blue and red lines) outperforms the SMV model $\mathbf{\Phi}_{opt} \in \mathbb{R}^{60\times 500}$ using OMP3 and Ma-OMP3 (solid green and yellow lines) at most cases of various SNRs and MDs. Exceptionally, according to Fig. 6.8, the relaxed support recovery rates of OMP3-MMV (solid blue lines) are slightly lower than those of OMP3-SMV (solid green lines) in a few cases of small MDs ($\Delta T \leq 20$).

- The achieved reconstruction results of POMP based on the converted SMV data (solid brown lines) are better than those of POMP for the SMV model $\mathbf{\Phi}_{opt} \in \mathbb{R}^{60\times 500}$ (solid marine lines) in the cases of high SNRs (SNR $\geq$ 17 dB). However, they become slightly poorer in the cases of low SNRs (SNR $\leq$ 17 dB).

- The reconstructed support results of OMP3-MMV (solid blue lines) and Ma-OMP3-MMV (solid red lines) for the MMV model are much better than those of OMP3 (dashed blue lines) and Ma-OMP3 (dashed red lines) based on the converted SMV data (see (6.16)) in all cases of various SNRs and MDs. These results are due to the fact that OMPMMV variants simultaneously use Q measurement

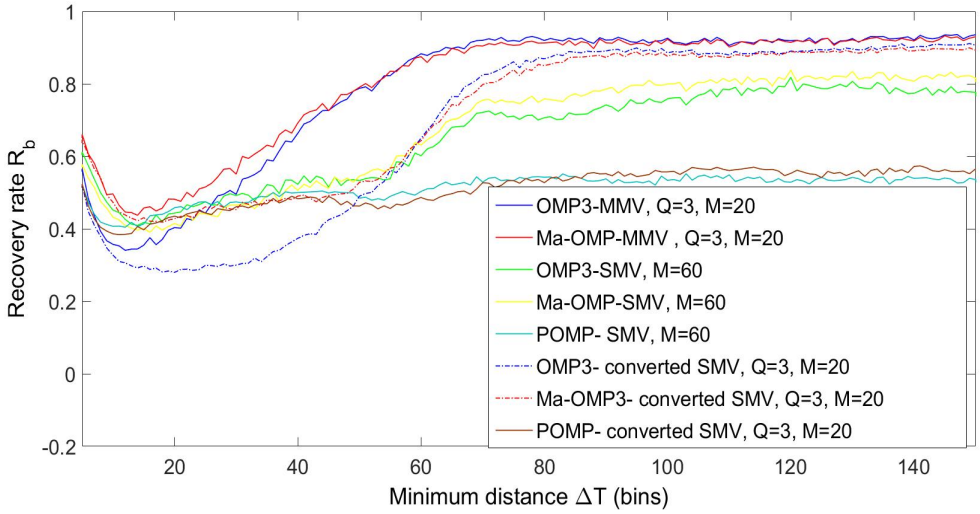

(a) 15dB, $\delta = 2$ for R_b evaluation

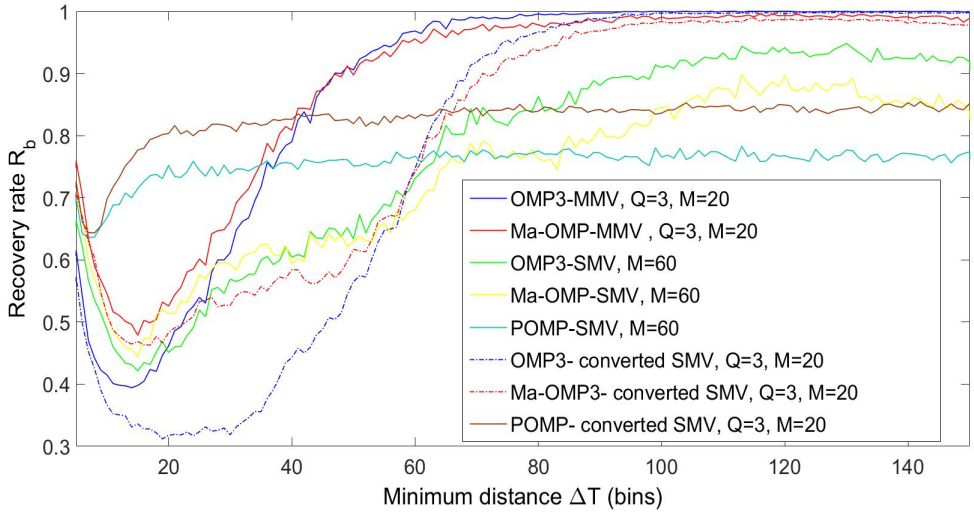

(b) 30dB, $\delta = 2$ for R_b evaluation

Figure 6.8. Comparison between the relaxed support recovery performances ($\delta = 2$) in MMV model and SMV model in the cases of different MDs (500 trials for each MD). Choose $N = 500$, $L = 5$, $M = 20$, $Q = 3$, $f_{max} = 30$ MHz, $F = 100$, $K = 3$, $\Delta r = 5$ cm for the construction of MMV and SMV models.

vectors for selecting non-zero indices. Therefore, more collected informations are

apparently effective to obtain a more accurate reconstruction of the signal support. These results have been proven similarly in the prior study of Yang et al. [74].

In summary, instead of measuring more TOF samples at different frequencies, it is more efficient to enhance the sparse support recovery performance for a super-resolution MFT acquisition through using MMV techniques.

6.5.5 Number of MMVs

The numerical experiment in this part aims to evaluate the benefits of an increase of MMV number($Q > 3$). For this reason, two Monte Carlo simulations with 3000 trials for each SNR (from 5 dB to 40 dB) and 500 trials for each MD (from 5 to 150 bins) are carried out for a new MMV model comprising six measurement vectors ($Q = 6$) sharing the same MFT sensing matrix $\mathbf{\Phi}_{opt,1} \in \mathbb{R}^{20\times 500}$.

For the above MMV model, the procedures of signal and measurement vector generation at each trial are similar to the previous simulations. Subsequently, OMP3-MMV and Ma-OMP3-MMV are used for 3-sparse reconstruction based on the MMV data. Furthermore, we use POMP for the sparse support reconstruction based on the converted SMV model in (6.16). The relaxed support recovery rates are averaged after all trials and then demonstrated in the SNR domain (see Fig. 6.9) and the MD domain (see Fig. 6.10).

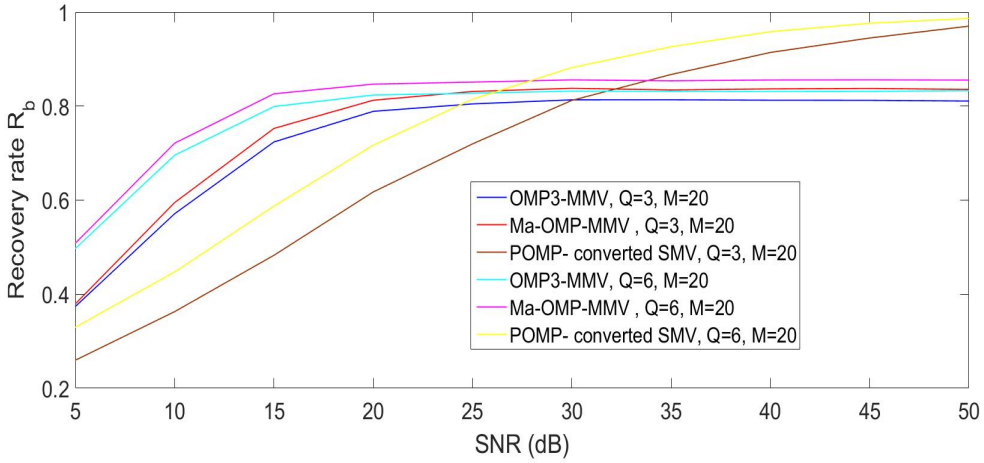

Figure 6.9. Comparison between the relaxed support recovery performances ($\delta = 2$) in two MMV models with different settings of Q in the case of different SNRs (3000 trials for each SNR). Choose $N = 500$, $L = 5$, $M = 20$, $f_{max} = 30$ MHz, $F = 100$, $K = 3$, $\Delta r = 5$ cm for the construction of MMV models

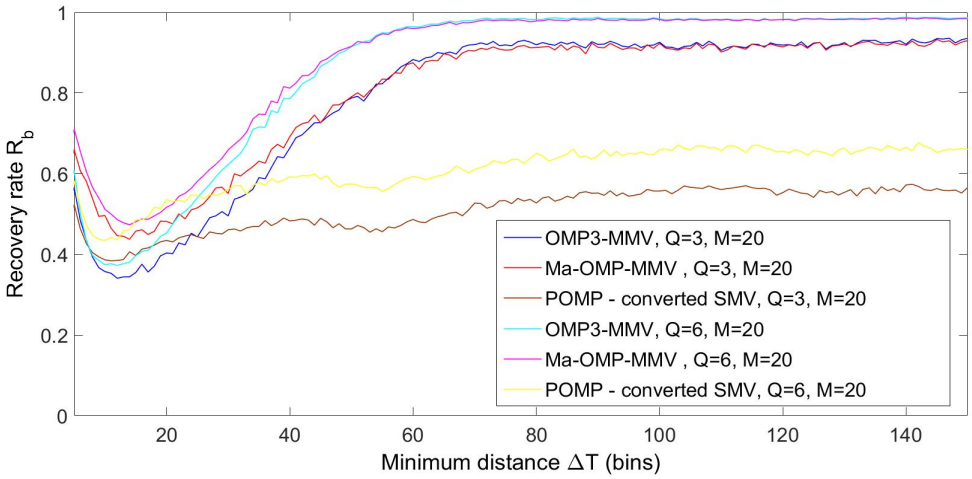

(a) 15dB, $\delta = 2$ for R_b evaluation

Figure 6.10. Comparison between the relaxed support recovery performances ($\delta = 2$) in two MMV models with different settings of Q in the cases of different MDs (500 trials for each MD). Choose $N = 500$, $L = 5$, $M = 20$, $f_{max} = 30$ MHz, $F = 100$, $K = 3$, $\Delta r = 5$ cm for the construction of MMV models

It can be seen in Fig. 6.9 and Fig. 6.10 that a larger amount of MMVs ($Q = 6$) brings the higher relaxed support recovery rates of three above reconstruction methods, i.e., OMP3-MMV, Ma-OMP3-MMV and POMP-MMV (cyan, rose and yellow lines), in all cases of various SNRs and MDs. However, a larger amount of MMVs requires more acquisition time and higher system design complexity. Thus, the amount of MMVs should be selected carefully to guarantee a good reconstruction performance as well as a fast processing speed in a super-resolution MFT acquisition.

6.6 Summary

Through the above numerical results, MMV techniques bring some significant improvements of sparse reconstruction performance in a super-resolution MFT acquisition. Besides, our modified MMV variants of greedy pursuits, i.e., OMP3-MMV, Ma-OMP3-MMV, POMP for the converted SMV model, are proven as the appropriate methods for a MMV joint sparse reconstruction. Each of them possesses some various advantages at different MDs (see Fig. 6.8). If their strengths can be integrated through our proposed method CMD-OMP, then a high stability of accurate relaxed support recovery is guaranteed with an accuracy offset $\delta = 2\Delta r$ through 60 TOF measurements ($M = 20$ and $Q = 3$):

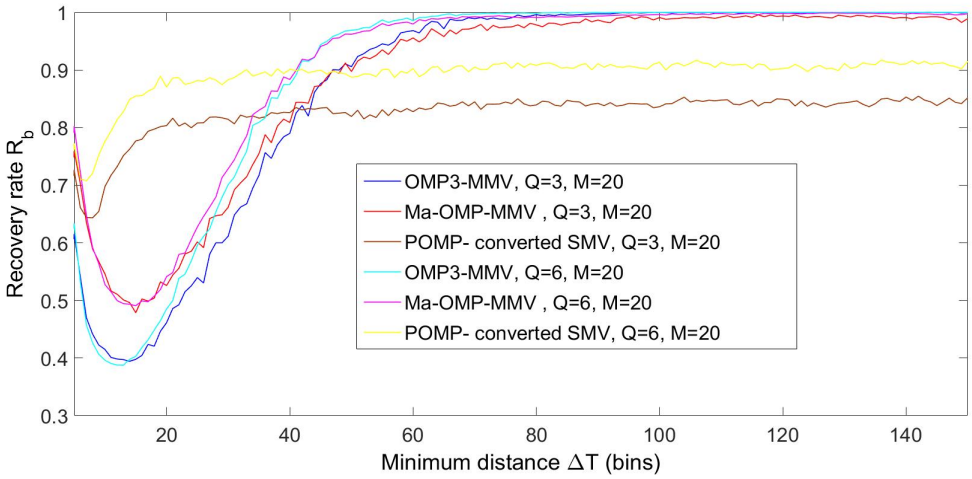

(b) 30dB, $\delta = 2$ for R_b evaluation

Figure 6.10. Comparison between the relaxed support recovery performances ($\delta = 2$) in two MMV models with different settings of Q in the cases of different MDs (500 trials for each MD). Choose $N = 500$, $L = 5$, $M = 20$, $f_{max} = 30$ MHz, $F = 100$, $K = 3$, $\Delta r = 5$ cm for the construction of MMV models (cont)

- In the cases of moderate noise levels, e.g., SNR = 30 dB, about 80% non-zero indices can be estimated accurately by POMP when $10\Delta r \leq \Delta T \leq 50\Delta r$ and about 90% atoms can be estimated accurately by OMP3-MMV when $\Delta T \geq 50\Delta r$.
- In the cases of high noise levels, e.g., SNR = 15 dB, about 50% non-zero indices can be estimated accurately by Ma-OMP3-MMV when $10\Delta r \leq \Delta T \leq 40\Delta r$ and over 80% atoms can be estimated accurately by OMP3-MMV when $\Delta T \geq 60\Delta r$.

As mentioned above, similar to a target-localization application [74], MMV data of a MFT acquisition in a TOF camera can be acquired through using different polarizers at either transmitter or receiver. However, the hardware design for such real MMV data generation is currently complicated in a commercial TOF camera system.

So far, as the targets get closer or more precisely MD is significantly small, the MPI localization usually fails even with the availability of MMV data. It seems to be possible that the poor reconstruction results at small MDs are due to the low incoherence of the super-resolution MFT sensing matrix. Thus, we will introduce a new type of TOF measurement in next chapter to enhance this incoherence.

7 Simultaneous multiple frequency acquisition

Chapter 5 optimizes a super-resolution MFT acquisition in a large refinement factor configuration successfully by selecting an appropriate set of frequencies and phase-offsets. However, these achievements are significantly small because the coherence of the sensing matrix is still high, especially at the diagonal line of the Gram matrix as shown in Fig. 5.7. From this result, the neighboring indices sharing the similar observations are hard to be estimated accurately. And hence, the support recovery performance is poor especially in noisy cases as shown in Fig. 5.8. For these reasons, in this chapter, the conventional TOF measurement, which is modulated and demodulated at a single frequency, is replaced by simultaneous multiple frequency (SMF) measurement. This new type of SMF measurement was firstly introduced by Payne et al. [29] for extending the ambiguity range of a CW-TOF camera. Whereas, we use these SMF measurements for designing a new sensing matrix with a higher incoherence. Firstly, we represent MFT acquisition and multiple-SMF acquisition under a projection matrix model. Subsequently, according to this model, we aim to design a more incoherent sensing matrix based on multiple SMF measurements through a projection matrix optimization method in Section 7.2. However, there are some restricting conditions on projection matrix regarding hardware design complexity. Therefore, we modify the optimization method to obtain the appropriate solution satisfying these conditions. The capabilities of the proposed multiple-SMF acquisition in resolving MPIs are demonstrated through numerical experiments in Section 7.3. Furthermore, it is currently challenging to carry out a real SMF measurement in a commercial TOF camera. For this reason, we introduce joint multiple frequency calibration in Section 7.4. The operating principle of this technique is similar to multiple-SMF models, but can be implemented easily in a commercial CW-TOF camera.

7.1 Projection matrix model

7.1.1 Dictionary matrix

Given that a CW-TOF camera can modulate the set Ψ of M_0 frequencies with zero phase-offsets. Then, MFT dictionary matrix $\mathbf{\Phi}_0$ comprises M_0 rows

$$\mathbf{\Phi}_0 = \begin{pmatrix} \boldsymbol{\phi}_{f_1} \\ \boldsymbol{\phi}_{f_2} \\ \vdots \\ \boldsymbol{\phi}_{f_{M_0}} \end{pmatrix} \tag{7.1}$$

where $\boldsymbol{\phi}_{f_j}$ denotes TOF correlation function response to scatterers locating at N grids with modulation frequency f_j, as described in (3.29).

7.1.2 MFT sensing matrix

So far, each TOF measurement in a MFT acquisition is a sample of cross-correlation function $g_{f_0}(\tau)$ in (3.29) between the reflected and demodulation signals at a single frequency $f_0 \in \Psi$. Suppose that this measurement has a zero phase-offset $\tau = 0$. In principle, this TOF measurement shares a row of the above dictionary matrix $\mathbf{\Phi}_0$.

If a MFT acquisition carries out M TOF measurements at different frequencies from the set Ψ, then we construct the corresponding MFT sensing matrix by picking $M < M_0$ rows of the dictionary matrix $\mathbf{\Phi}_0$. The picking relationship between the MFT sensing matrix and the dictionary matrix can be rewritten under a mathematical projection matrix model:

$$\mathbf{\Phi} = \boldsymbol{P}\mathbf{\Phi}_0 \tag{7.2}$$

where $\boldsymbol{P} \in \mathbb{R}^{M \times M_0}$ is projection matrix. In a MFT acquisition, the projection matrix $\boldsymbol{P}$ is a binary matrix whose rows each contain only one non-zero element. The non-zero location denotes the chosen modulation frequency. For instance, if an arbitrary frequency f_m is chosen for the first measurement of a MFT acquisition, then the first row of projection matrix contains one non-zero element $p_{1m} = 1$.

7.1.3 Multiple-SMF sensing matrix

SMF measurement was introduced firstly by Payne et al. [29]. This new type of TOF measurement comprises multiple parts of different modulation frequencies. Unlike the conventional CW-TOF measurement, the illumination system of a SMF model does not transmit an optical signal at one frequency, but emits a mixture of signal parts of

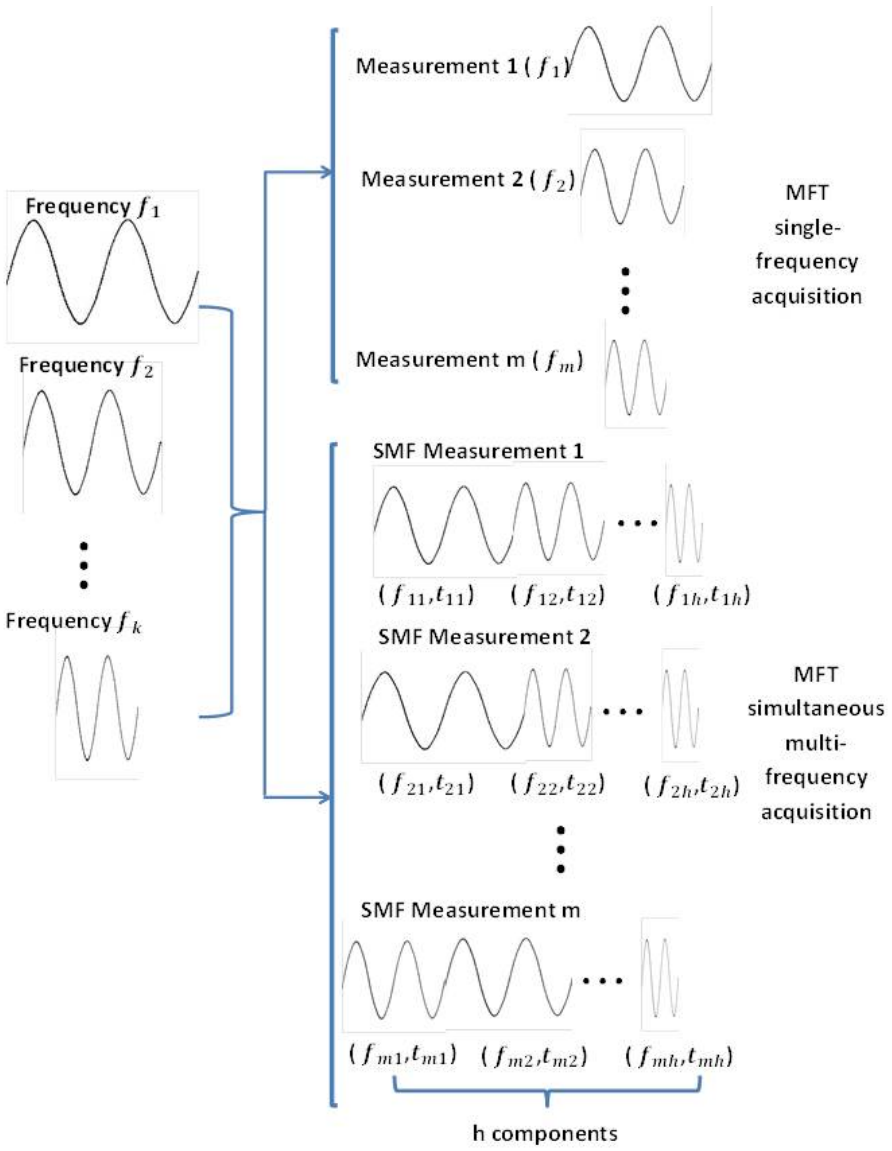

Figure 7.1. Single-frequency and simultaneous multi-frequency MFT acquisition

multiple frequencies, as described in Fig. 7.1. At receiver side, a TOF chip correlates the reflected signal parts with a similar demodulation signal mixture. In other words, each frequency part of the reflected signal is correlated with a demodulation signal part of the same frequency and exposure time. Eventually, a SMF measurement is considered as the linear combination of multiple single-frequency TOF measurements. As a result, we can represent multiple SMF measurements using the projection matrix

model (7.2). Nevertheless, the structure of projection matrix in this multiple-SMF model is different from that in a MFT acquisition. To be more precise, each row of the multiple-SMF projection matrix contains more than one non-zero entry. Suppose that a SMF measurement comprises h parts of different frequencies, then h is also the number of non-zero elements in the corresponding projection matrix row. The non-zero elements of this row denote the corresponding member frequencies of the SMF measurement. From these points, the projection matrix of multiple-SMF acquisition is no longer a binary matrix as a MFT acquisition. We aim to improve the quality of the MPI separation by designing the structure of multiple-SMF acquisition or more precisely optimizing the corresponding projection matrix.

7.2 Projection matrix optimization in SMF acquisition

As discussed above, the projection matrix representing for multiple-SMF acquisition is a sparse matrix where h denotes the largest sparsity of its rows. In this part, we introduce a projection matrix optimization method to enhance the incoherence of the corresponding multiple-SMF matrix, similar to many previous studies [77, 78, 79, 30].

7.2.1 Projection matrix optimization method

As mentioned in Section 5.1, the coherence cost E of a sensing matrix $\boldsymbol{\Phi}$ in (5.14) is a good measure to evaluate its coherence map or Gram matrix if the mutual coherence is close to one. A sensing matrix with a smaller coherence cost may bring a higher sparse reconstruction performance in a super-resolution CS problem. Therefore, we use the projection matrix optimization method which has been proposed by Abolghasemi et al. [30] for minimizing the coherence cost of the multiple-SMF sensing matrix

$$\hat{\boldsymbol{P}} = \arg\min_{\boldsymbol{P}} E \quad \text{s.t.} \quad \boldsymbol{\Phi} = \boldsymbol{P}\boldsymbol{\Phi}_{\boldsymbol{0}} \tag{7.3}$$

The optimization method uses gradient descent steepest technique to update the sensing matrix iteratively through:

$$\boldsymbol{\Phi}_{new} = \tilde{\boldsymbol{\Phi}} - \eta \boldsymbol{\nabla E} \tag{7.4}$$

where

$$\boldsymbol{\nabla E} = \frac{\partial E}{\partial \tilde{\boldsymbol{\Phi}}} = 4\tilde{\boldsymbol{\Phi}}(\tilde{\boldsymbol{\Phi}}^H \tilde{\boldsymbol{\Phi}} - \boldsymbol{I}) \tag{7.5}$$

with $\tilde{\boldsymbol{\Phi}}$ is the normalized column version of sensing matrix $\boldsymbol{\Phi}$ and η is a given step-size. This step-size value is reduced until the newly achieved sensing matrix $\boldsymbol{\Phi}_{new}$ has a smaller coherence cost $E(\boldsymbol{\Phi}_{new}) < E(\boldsymbol{\Phi})$. Subsequently, a new projection matrix $\boldsymbol{P}_{new}$

can be inferred through the following inverse linear problem:

$$\boldsymbol{\Phi}_{new} = \boldsymbol{P}_{new}\boldsymbol{\Phi}_0 \Rightarrow \boldsymbol{P}_{new} = \boldsymbol{\Phi}_{new}\boldsymbol{\Phi}_0^{-1} \tag{7.6}$$

7.2.2 Modified projection matrix modification

Nevertheless, there are some restricting conditions on the optimized projection matrix in multiple-SMF model. These conditions are highly dependent on the hardware design complexity of a commercial TOF camera for real SMF measurements. Currently, the research about such design has not been investigated yet. However, according to the operating principle of a multiple-SMF acquisition, we hypothesize in this chapter that there are two severe technical limitations including the largest amount of different parts and the magnitude adjustment. From this point, we modify the above original optimization method to avoid these problems. To be concrete, there are two modification steps on the achieved result $\boldsymbol{P}_{new}$.

7.2.2.1 Sparse matrix construction

So far, there have been no studies that build up a real TOF system for acquiring real SMF measurements. Therefore, a comparison between several practical systems can hardly be achieved. For instance, Payne et al. [29] only simulated their idea of SMF measurements comprising two different-frequency components by two sequential TOF measurements. The design complexity of this system is high if the emitted optical signal contains many different-frequency parts. For such a real SMF measurement, a CW-TOF camera requires a more complex illumination driving system and TOF modulation chip. Definitely, the amount of different-frequency parts in a SMF measurement is a crucial factor. Therefore, we hypothesize that a real CW-TOF system can modulate SMF measurements comprising only a few different-frequency parts. In other words, there is an upper bound on the number of different-frequency parts, due to hardware design complexity. This bound is equivalent to the largest sparsity of the corresponding multiple-SMF projection matrix row.

Given h be the largest sparsity of the projection matrix rows. In order to obtain the optimized projection matrix $\boldsymbol{P}_s$ which can satisfy the restricting condition on the row sparsity, the inverse linear problem (7.6) should be converted to the following optimization problem:

$$\boldsymbol{P}_s = \underset{\boldsymbol{P}}{\operatorname{argmin}} ||\boldsymbol{P} - \boldsymbol{\Phi}_{new}\boldsymbol{\Phi}_0^{-1}||_2 \quad \text{s.t.} \quad ||\boldsymbol{p}_q||_0 \leq h, \forall q \leq M \tag{7.7}$$

From (7.6), each row $\boldsymbol{\phi}_{new,q}$ of $\boldsymbol{\Phi}_{new}$ is represented by:

$$\boldsymbol{\phi}_{new,q} = \boldsymbol{p}_{s,q}\boldsymbol{\Phi}_0 \quad \forall q \leq M \tag{7.8}$$

or

$$\boldsymbol{\phi}_{new,q}^T = \boldsymbol{\Phi}_0^T \boldsymbol{p}_{s,q}^T \quad \forall q \leq M \tag{7.9}$$

According to (7.9), the optimization problem (7.7) can be solved by finding M sparse row vectors $\boldsymbol{p}_{s,q}$ in (7.9) based on the available vector $\boldsymbol{\phi}_{new,q}^T$ and matrix $\boldsymbol{\Phi}_0^T$. The largest sparsity h is a known parameter due to hardware limitation. Since $N \gg M_0$, (7.9) is an over-determined equation system. There are many sparse reconstruction methods for solving this problem (7.9). For a simplicity, we propose the greedy pursuit OMP3 in Algorithm 6 with a fast-processing speed and a high reconstruction quality since the sparsity h is known. Our solution approach for finding a sparse projection matrix $\boldsymbol{P}_s$ is shown in Algorithm 20.

7.2.2.2 Magnitude adjustment

A SMF measurement is considered as the linear combination of multiple single-frequency measurements. Each frequency component has various contribution in this SMF measurement that is represented by the amplitude of the corresponding element in the projection row. The amplitude adjustment of the projection matrix elements can be proceeded through setting the exposure times or the optical magnitudes of the frequency parts.

Notably, frequency components in a SMF measurement are periodical modulated waveforms. Therefore, the exposure time of one frequency component is equivalent to the number of periods containing in the corresponding waveform. In a SMF measurement, if the numbers are integers and the optical magnitudes of all frequency parts are equal, then the projection matrix elements representing for the frequency parts are also integers. If a TOF camera can amend the optical magnitude of each frequency part, the corresponding projection matrix element is float-valued. From these points, whether the magnitudes of multiple-SMF projection matrix elements take float or integer numbers, is highly dependent on the illumination waveform modulation capabilities of the TOF camera system. Note that a negative value of one projection matrix element represents a frequency part demodulated at a phase-offset τ of π (radians).

The achieved sparse projection matrix $\boldsymbol{P}_s$ in (7.7) contains float-valued elements. If these matrix elements are restricted to integer format, the following rounding operation should be implemented on row vectors $\boldsymbol{p}_{s,q}$ in (7.9):

$$\boldsymbol{p}_{s,int,q} = \text{round}(\boldsymbol{p}_{s,q}) \tag{7.10}$$

This procedure (7.10) repeats for M rows to obtain the projection matrix $\boldsymbol{P}_{s,int}$, whose structure possesses the integer format and the largest row sparsity h. After the calculation of the projection matrix $\boldsymbol{P}_{s,int}$, the new sensing matrix $\boldsymbol{\Phi}_{new}$ is computed again such that $\boldsymbol{\Phi}_{new} = \boldsymbol{P}_{s,int}\boldsymbol{\Phi}_0$. However, this new result of sensing matrix is only updated for the next iteration if $E(\boldsymbol{\Phi}_{new}) < E(\boldsymbol{\Phi})$. Otherwise, the step-size in (7.4) is reduced and then the previous computation procedure of $\boldsymbol{P}_{s,int}$ is repeated until the new sensing

Algorithm 20 Gradient steepest descent method for the projection matrix optimization in a multiple-SMF model

Input: The sensing matrix $\boldsymbol{\Phi}_0^{(k\times N)}$, a initial random sparse projection matrix $\boldsymbol{P}_0^{(M\times k)}$ and h

Output: The optimized sparse projection matrix $\boldsymbol{P}_{opt}$

1: Compute the measurement matrix $\boldsymbol{\Phi} = \boldsymbol{P}_0\boldsymbol{\Phi}_0$ and the column-normalized $\tilde{\boldsymbol{\Phi}}$
2: Calculate $E(\boldsymbol{\Phi})$ and set $E_{min} = E(\boldsymbol{\Phi})$
3: **while** TRUE **do**
4: Compute the gradient $\boldsymbol{\nabla E}$
5: Update the new measurement matrix $\boldsymbol{\Phi}_{new} = \tilde{\boldsymbol{\Phi}} - \eta\boldsymbol{\nabla E}$
6: **for** $q = 1$ to M **do**
7: Set $\boldsymbol{y} = \boldsymbol{\phi}_{new,q}^T$
8: Use OMP3 to find $\hat{\boldsymbol{x}} = \text{argmin}_{\boldsymbol{x}}\, ||\boldsymbol{y} - \boldsymbol{\Phi}_0^T\boldsymbol{x}||_2$ s.t. $||\boldsymbol{x}||_0 \leq h$
9: $\hat{\boldsymbol{x}} = \text{round}(\hat{\boldsymbol{x}})$ (only applied if integer-valued format is required)
10: Set $\boldsymbol{p}_{s,int,q} = \hat{\boldsymbol{x}}$
11: **end for**
12: Form the matrix $\boldsymbol{P}_{s,int}$ from M achieved rows $(\boldsymbol{p}_{s,int,1}, \boldsymbol{p}_{s,int,2} \cdots \boldsymbol{p}_{s,int,M})$
13: Update $\boldsymbol{\Phi}_{new} = \boldsymbol{P}_{s,int}\boldsymbol{\Phi}_0$
14: Calculate $E(\boldsymbol{\Phi}_{new})$
15: **if** $E(\boldsymbol{\Phi}_{new}) < E_{min}$ **then**
16: Set $E_{min} = E(\boldsymbol{\Phi}_{new})$ and $\boldsymbol{P}_{opt} = \boldsymbol{P}_{s,int}$
17: Update $\boldsymbol{\Phi} = \boldsymbol{\Phi}_{new}$ and compute $\tilde{\boldsymbol{\Phi}}$
18: **else**
19: Update $\eta = \eta/2$
20: **if** $\eta < \eta_{min}$ **then**
21: break;
22: **end if**
23: **end if**
24: **end while**

matrix $\boldsymbol{\Phi}_{new}$ acquires a smaller coherence cost. Algorithm 20 describes in details this process of optimization. The final results are the optimized projection matrix $\boldsymbol{P}_{opt}$ and the corresponding optimized multiple-SMF sensing matrix $\boldsymbol{\Phi}_{opt}$.

7.2.3 SMF model parameters

Given $\boldsymbol{\Phi}_{new,1}$ and $\boldsymbol{\Phi}_{new,2}$ be the reconstructed sensing matrices at step 5 and step 13 respectively in Algorithm 20. At each iteration, $\boldsymbol{\Phi}_{new,2}$ is the optimized multiple-SMF sensing matrix satisfying two restricting conditions, e.g., the largest amount of different-frequency parts, integer projection matrix format. Whereas, $\boldsymbol{\Phi}_{new,1}$ is the optimized

one without any restrictions. Apparently, there are some errors from the inverse sparse reconstruction in (7.7) or the rounding operation in (7.10). Therefore, $\boldsymbol{\Phi}_{new,2}$ differs from $\boldsymbol{\Phi}_{new,1}$. Theoretically, $\boldsymbol{\Phi}_{new,2}$ with two restricting conditions apparently acquires a larger coherence cost, compared to $\boldsymbol{\Phi}_{new,1}$. As a result, the sparse reconstruction performance in the multiple-SMF acquisition $\boldsymbol{\Phi}_{new,2}$ depends on the gap between two these matrices:

$$e^{(k)} = ||\boldsymbol{\Phi}_{new,1} - \boldsymbol{\Phi}_{new,2}||_2^2 = ||\boldsymbol{\Phi}_{new,1} - \boldsymbol{P}_{s,int}\boldsymbol{\Phi}_0||_2^2 \tag{7.11}$$

This gap represents how closely the achieved sensing matrix $\boldsymbol{\Phi}_{new,2}$ converges to the optimized one $\boldsymbol{\Phi}_{new,1}$. It becomes larger if the restricting conditions on multiple-SMF projection matrix are tighter, e.g., a smaller row sparsity or an integer format requirement. Therefore, these conditions play major roles in the design of a multiple-SMF sensing matrix. Moreover, the solution of the inverse problem (7.7) is also highly dependent on the structure of the dictionary matrix $\boldsymbol{\Phi}_0$ or in other words the set of possible modulation frequencies Ψ.

In both MFT and multiple-SMF model, the K-sparse reconstruction requires a few measurements. According to (3.46), more measurements are efficient to reconstruct a sparse signal accurately with a higher probability but consume more acquisition time. Therefore, the number of SMF measurements (M) is a crucial factor in a multiple-SMF model.

7.3 Numerical results

In this part, the MPI reconstruction capabilities of multiple-SMF acquisition are analyzed through several numerical experiments. We assume that SMF data is available. This analysis aims to indicate the influence of the concerned parameters, i.e., row sparsity and magnitude format (integer of float) of the projection matrix, dictionary matrix structure, the number of SMF measurements.

Initially, we construct the dictionary matrix $\boldsymbol{\Phi}_0$ with the same parameters of the previous MFT acquisition, i.e.,$N = 500, L = 5, f_{max} = 30$ MHz, $\Delta r = 5$cm) in the large refinement factor configuration $F = 100$. Suppose that all 117 available modulation frequencies in the set Ψ (see Remark 6) with $f_{max} = 30$ MHz and $f_{min} = 1$ MHz can be modulated and demodulated in these simulations and hence $M_0 = 117$.

Based on this dictionary matrix $\boldsymbol{\Phi}_0$, we run the proposed projection matrix optimization method in Algorithm 20 with different restricting conditions on the projection matrix, i.e., largest row sparsity (h), magnitude format (integer or float numbers) and the number of SMF measurements (M). An initial random projection matrix $\boldsymbol{P}_{init}$ is input to the algorithm. Note that a gradient steepest descent method only brings a local optimization solution for a non-convex problem. Therefore, we carry out a Monte Carlo simulation with 100 different initial random projection matrices to find the optimal projection matrix or more precisely the optimal multiple-SMF sensing matrix with

the smallest coherence cost.

There are four optimized projection matrices $\boldsymbol{P}_1$, $\boldsymbol{P}_2$, $\boldsymbol{P}_3$ and $\boldsymbol{P}_4$ corresponding to four different settings, as listed in Table 7.1. The construction of these matrices is based on the dictionary matrix $\boldsymbol{\Phi}_0 \in \mathbb{R}^{117\times500}$. Besides, the fifth one $\boldsymbol{P}_5$ is achieved through running the proposed projection matrix optimization method on the other dictionary matrix $\boldsymbol{\Phi}_{0,1} \in \mathbb{R}^{60\times500}$ with only 60 available frequencies. Note that these frequencies are drawn from the same set Ψ. Correspondingly, five multiple-SMF sensing matrices $\boldsymbol{\Phi}_{SMF,1}$, $\boldsymbol{\Phi}_{SMF,2}$, $\boldsymbol{\Phi}_{SMF,3}$, $\boldsymbol{\Phi}_{SMF,4}$ and $\boldsymbol{\Phi}_{SMF,5}$ are generated through (7.2) with five different optimized projection matrices.

Table 7.1. Different SMF measurement matrices with different parameter settings

Projection Matrix /Sensing matrix	h	M	M_0	Format	Coherence cost E
$\boldsymbol{P}_1/\boldsymbol{\Phi}_{SMF,1}$	5	20	117	Integer	1.6046e+004
$\boldsymbol{P}_2/\boldsymbol{\Phi}_{SMF,2}$	10	20	117	Integer	1.4571e+004
$\boldsymbol{P}_3/\boldsymbol{\Phi}_{SMF,3}$	5	20	117	Float	1.6166e+004
$\boldsymbol{P}_4/\boldsymbol{\Phi}_{SMF,4}$	5	40	117	Integer	1.3881e+004
$\boldsymbol{P}_5/\boldsymbol{\Phi}_{SMF,5}$	5	20	60	Integer	1.6347e+004

The analysis is carried out through the comparison between the above multiple-SMF acquisitions with different settings of projection matrix:

- An increase of the largest row sparsity in the projection matrix is evaluated through the comparison between two multiple-SMF models sharing two integer projection matrices $\boldsymbol{P}_1$ and $\boldsymbol{P}_2$ with different largest row sparsity values $h = 5$ and $h = 10$.
- The usefulness of optical intensity modulation system can be recognized through a comparison between two models sharing the integer projection matrix $\boldsymbol{P}_1$ and the float one $\boldsymbol{P}_3$ with the same largest row sparsity $h = 5$.
- An increase of the SMF measurement number is evaluated through the comparison between two models sharing two integer projection matrices $\boldsymbol{P}_1$ and $\boldsymbol{P}_4$ with different amounts of SMF measurements.
- The effect of the dictionary matrix structure is explored through the comparison between two models sharing two integer projection matrices $\boldsymbol{P}_1$ and $\boldsymbol{P}_5$ with the same settings but based on two different dictionary matrices $\boldsymbol{\Phi}_0 \in \mathbb{R}^{117\times500}$ and $\boldsymbol{\Phi}_{0,1} \in \mathbb{R}^{60\times500}$.

7.3.1 Coherence histogram

The coherence histograms of five multiple-SMF sensing matrices $\mathbf{\Phi}_{SMF,1}$-$\mathbf{\Phi}_{SMF,5}$ as well as the dictionary matrix $\mathbf{\Phi}_0 \in \mathbb{R}^{117\times500}$ are shown in Fig. 7.2. In this representation, if more coherence elements move closer to zero, then the sensing matrix contains a larger amount of highly incoherent columns. Firstly, as can be seen in Fig. 7.2 that the coherence histogram of the dictionary matrix $\mathbf{\Phi}_0 \in \mathbb{R}^{117\times500}$ is much worse than that of five multiple-SMF sensing matrices although it comprises a significantly large amount of TOF measurements ($M_0 = 117$). These results indicate that a multiple-SMF model leads to a highly incoherent sensing matrix.

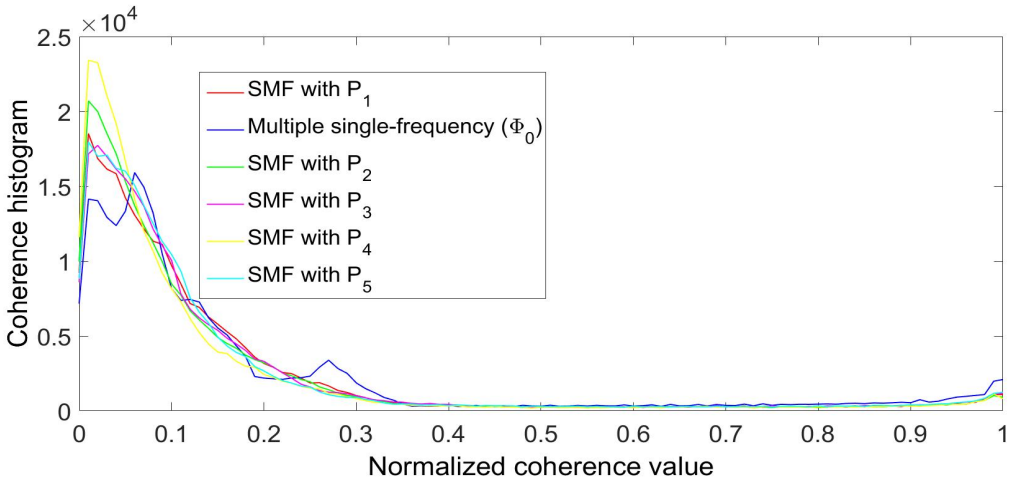

Figure 7.2. Coherence histogram of various SMF measurement matrices

Besides, as Fig. 7.2 shows, two multiple-SMF sensing matrices $\mathbf{\Phi}_{SMF,2}$ (green line) and $\mathbf{\Phi}_{SMF,4}$ (yellow line) possess better coherence histograms, in comparison to the reference one $\mathbf{\Phi}_{SMF,1}$ (red line). According to this result, an increase of the largest row sparsity in projection matrix or a larger amount of SMF measurements can enhance the incoherence of a multiple-SMF sensing matrix.

7.3.2 Support recovery performance

The above coherence histogram representations are hard to explore the strengths of a multiple-SMF model in resolving MPI problem. Therefore, we carry out two Monte Carlo simulations to analyze the reconstruction capabilities of different multiple-SMF acquisitions with 3000 trials for each SNR and 500 trials for each MD. At each trial, a non-negative 3-sparse signal is generated with random non-zero locations and magnitudes. Subsequently, the noisy measurement vector is generated randomly through the sparse signal and a multiple-SMF sensing matrix with the analyzed SNR. Two algo-

rithms, i.e., POMP and OMP3, are used sequentially for 3-sparse reconstruction. The relaxed support recovery rates with a tolerance offset $\delta = 2$ are averaged after all trials. These results are then demonstrated in Fig. 7.3 for various SNRs (from 5 dB to 40 dB) and Fig. 7.4, Fig. 7.5 for various MDs (from 5 bins to 150 bins).

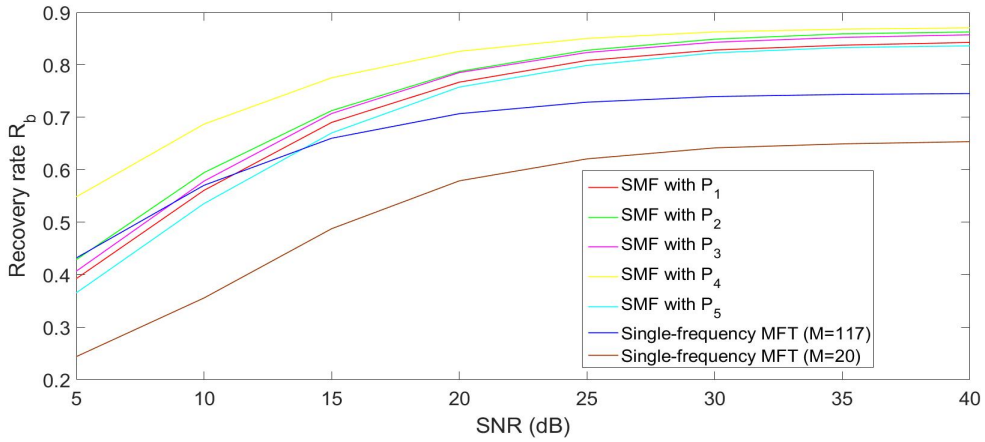

(a) OMP3

Figure 7.3. Comparison between the relaxed support recovery performances ($\delta = 2$ bins) of multiple-SMF acquisition and MFT acquisition at different SNRs (3000 trials for each SNR). Choose $N = 500$, $L = 5$, $f_{max} = 30$ MHz, $F = 100$, $\Delta r = 5$ cm, $K = 3$.

7.3.2.1 Different settings

It can be seen in Fig. 7.3, Fig. 7.4, Fig. 7.5 that:

- The multiple-SMF acquisition $\mathbf{\Phi}_{SMF,2}$ (green lines) with a larger amount of different-frequency parts ($h = 10$) brings higher relaxed support recovery rates in all cases of various SNRs and MDs, in comparison with the multiple-SMF acquisition $\mathbf{\Phi}_{SMF,1}$ (red lines) with $h = 5$. Definitely, a SMF measurement with a larger amount of different frequency-parts has more advantages in the reconstruction of MPI time profile.
- Moreover, the reconstruction performance of $\mathbf{\Phi}_{SMF,1}$ (red lines) is much poorer than that of $\mathbf{\Phi}_{SMF,4}$ (yellow lines) in the cases of various SNRs and MDs. This result indicates that a larger number of SMF measurements can enhance the quality of MPI reconstruction in a multiple-SMF acquisition.

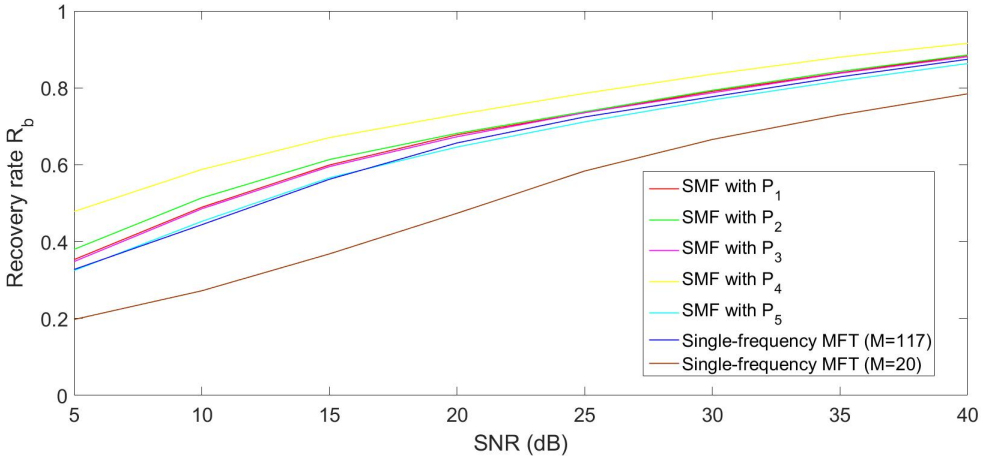

(b) POMP

Figure 7.3. Comparison between the relaxed support recovery performances ($\delta = 2$ bins) of multiple-SMF acquisition and MFT acquisition at different SNRs (3000 trials for each SNR). Choose $N = 500$, $L = 5$, $f_{max} = 30$ MHz, $F = 100$, $\Delta r = 5$ cm, $K = 3$ (cont).

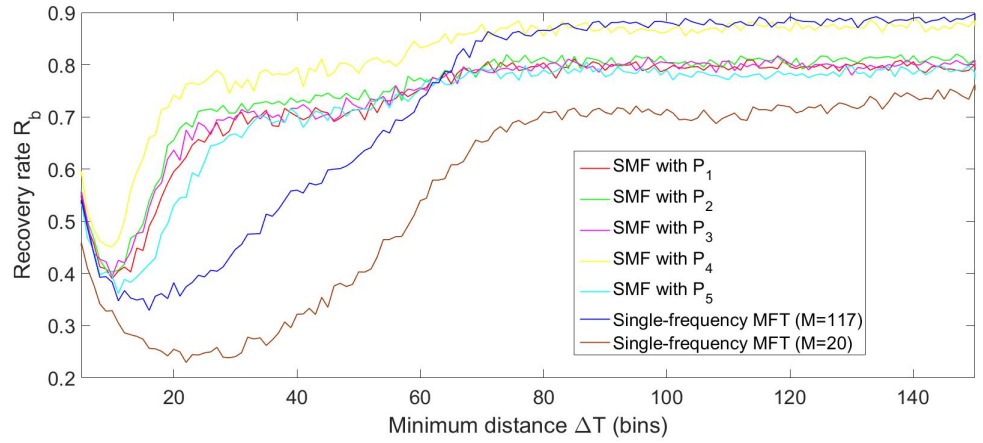

(a) OMP3 - 15dB

Figure 7.4. Comparison between the relaxed support recovery performances ($\delta = 2$ bins) of multiple-SMF acquisition and MFT acquisition at different MDs (500 trials for each MD) in the case of SNR = 15dB. Choose $N = 500$, $L = 5$, $f_{max} = 30$ MHz, $F = 100$, $\Delta r = 5$ cm, $K = 3$.

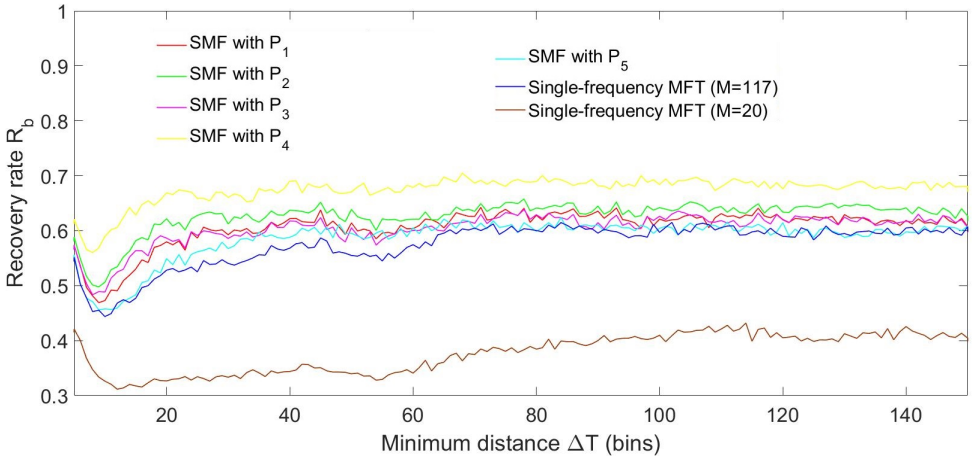

(b) POMP - 15dB

Figure 7.4. Comparison between the relaxed support recovery performances ($\delta = 2$ bins) of multiple-SMF acquisition and MFT acquisition at different MDs (500 trials for each MD) in the case of SNR = 15dB. Choose $N = 500$, $L = 5$, $f_{max} = 30$ MHz, $F = 100$, $\Delta r = 5$ cm, $K = 3$ (cont).

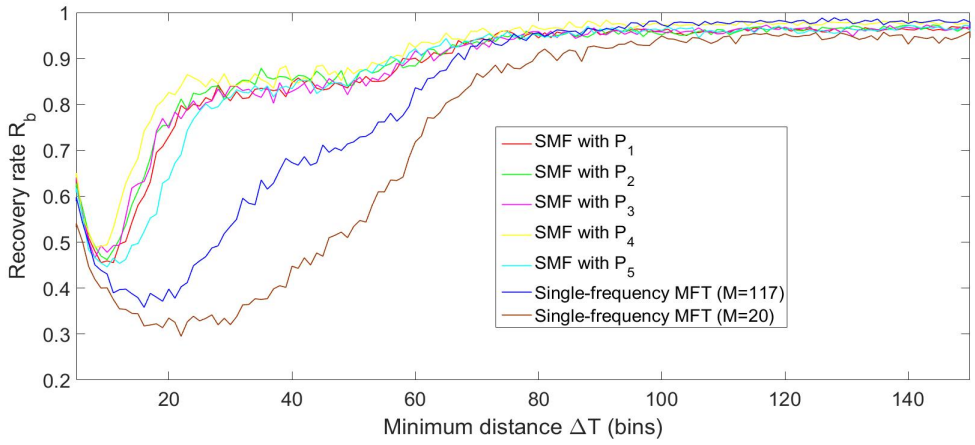

(a) OMP3 - 30dB

Figure 7.5. Comparison between relaxed support recovery performances ($\delta = 2$ bins) of multiple-SMF acquisition and MFT acquisition at different MDs (500 trials for each MD) in the case of SNR = 30dB. Choose $N = 500$, $L = 5$, $f_{max} = 30$ MHz, $F = 100$, $\Delta r = 5$ cm, $K = 3$.

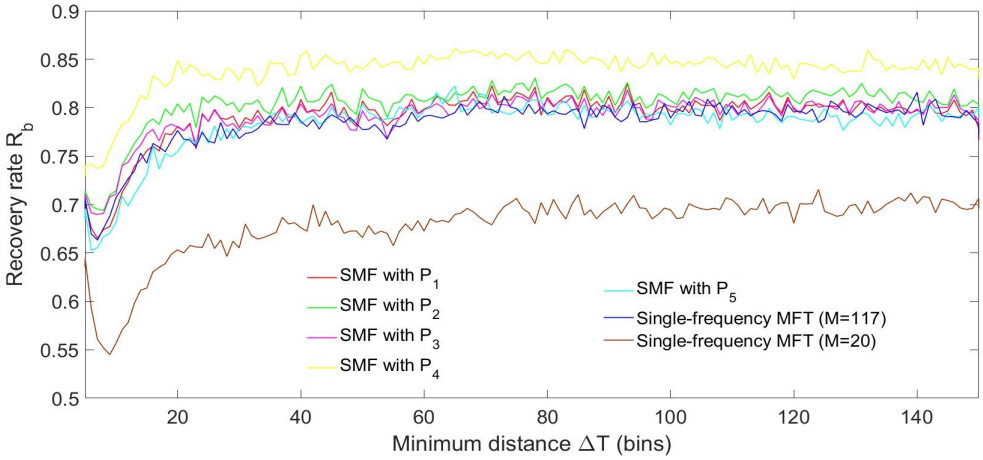

(b) POMP - 30dB

Figure 7.5. Comparison between relaxed support recovery performances ($\delta = 2$ bins) of multiple-SMF acquisition and MFT acquisition at different MDs (500 trials for each MD) in the case of SNR = 30dB. Choose $N = 500$, $L = 5$, $f_{max} = 30$ MHz, $F = 100$, $\Delta r = 5$ cm, $K = 3$ (cont).

- Additionally, the sensing matrix $\mathbf{\Phi}_{SMF,3}$ (rose lines) sharing the float-valued projection matrix $\boldsymbol{P}_3$ brings slightly higher relaxed support recovery rates of OMP3 in all cases of various SNRs and MDs, in comparison with $\mathbf{\Phi}_{SMF,1}$ (red lines). However, the reconstruction performances of POMP using both two multiple-SMF models $\mathbf{\Phi}_{SMF,3}$ and $\mathbf{\Phi}_{SMF,1}$ seem to be similar. From these results, the hardware for optical intensity modulation seems unnecessary in the development of a multiple-SMF acquisition.

- A comparison between the reconstruction results of $\mathbf{\Phi}_{SMF,5}$ (cyan lines) and $\mathbf{\Phi}_{SMF,1}$ (red lines) claims that a multiple-SMF acquisition which is constructed with a larger set of modulation frequencies, can bring the higher quality of MPI time profile reconstruction. As a result, the pool of available modulation frequencies in a CW-TOF camera should be extended for a multiple-SMF acquisition.

7.3.2.2 Multiple-SMF acquisition and MFT acquisition

The reconstruction results of the MFT acquisition $\mathbf{\Phi}_{opt,1}$ with the same parameters ($N = 500, L = 5, f_{max} = 30$ MHz, $F = 100$, $\Delta r = 5$ cm, $K = 3$) are collected from Fig. 5.8 and Fig. 5.9. Then, these results are compared to those of the multiple-SMF models in Fig. 7.3 for various SNRs and Fig. 7.4, Fig. 7.5 for various MDs. A comparison between these results claims that a multiple-SMF acquisition is more efficient than

a MFT acquisition with the same amount of measurements. Definitely, the relaxed support recovery rates of four different multiple-SMF models $\mathbf{\Phi}_{SMF,1}$, $\mathbf{\Phi}_{SMF,2}$, $\mathbf{\Phi}_{SMF,3}$ and $\mathbf{\Phi}_{SMF,5}$ (red, green, rose, cyan lines) are much higher than those of the MFT acquisition $\mathbf{\Phi}_{opt,1}$ (brown lines).

Moreover, we analyze another MFT acquisition sharing the dictionary matrix $\mathbf{\Phi}_0$ with 117 TOF measurements. Two similar Monte Carlo simulations are carried out with 3000 trials for each SNR and 500 trials for each MD to obtain the reconstruction results of this MFT acquisition in the cases of various SNRs and MDs. The generation procedures of 3-sparse signals and measurement vectors are similar to the previous numerical experiments. OMP3 and POMP are used for the 3-sparse reconstruction. The achieved relaxed support recovery rates with a tolerance offset $\delta = 2$ are demonstrated in Fig. 7.3 for SNR domain and Fig. 7.4, Fig. 7.5 for MD domain.

As can be seen in Fig. 7.3 and Fig. 7.4a that the reconstruction results of OMP3 using the MFT acquisition $\mathbf{\Phi}_0$ (blue lines) are better than those of OMP3 using four multiple-SMF acquisitions (red, green, rose, cyan lines) in the cases of low SNRs and large MDs. In other cases, multiple-SMF acquisitions have more advantages regarding higher reconstruction performances. Especially, according to Fig. 7.4b and Fig. 7.5b, the reconstruction results of POMP using four multiple-SMF acquisitions are better than those of POMP using the MFT acquisition $\mathbf{\Phi}_0$ (blue lines) in most cases of different SNRs and MDs. These numerical results indicate that a MFT acquisition is ineffective for resolving MPI problem even if carrying out more TOF measurements. These poor performances of a MFT acquisition are caused by the high coherence of a super-resolution MFT sensing matrix with a large refinement factor. Whereas, the proposed multiple-SMF acquisition can guarantee a high stability of accurate sparse support reconstruction through only a few SMF measurements.

7.3.2.3 Different reconstruction methods

In this part, we analyze the recovery performance of three different reconstruction algorithms, i.e., OMP3, POMP, and Ma-OMP3, in a typical multiple-SMF acquisition $\mathbf{\Phi}_{SMF,1}$. Similarly, two Monte Carlo simulations are carried out with 3000 trials for each SNR (from 5 dB to 40 dB) and 500 trials for each MD (from 5 to 150 bins). At each trial, we repeat the procedures in the previous numerical experiments for generating randomly 3-sparse signal and noisy SMF measurement vector.

Subsequently, three above methods reconstruct 3-sparse signal based on the measurement vector and the multiple-SMF sensing matrix $\mathbf{\Phi}_{SMF,1}$. The relaxed support recovery rates with $\delta = 2$ are averaged after all trials and then demonstrated in Fig. 7.6 for various SNRs and Fig. 7.7 for various MDs.

As can be seen in Fig. 7.6 that the relaxed support recovery rates of OMP3 (blue lines) are higher than those of Ma-OMP3 (green lines) in the cases of various SNRs in a super-resolution multiple-SMF acquisition $\mathbf{\Phi}_{SMF,1}$. Whereas, the reconstruction results

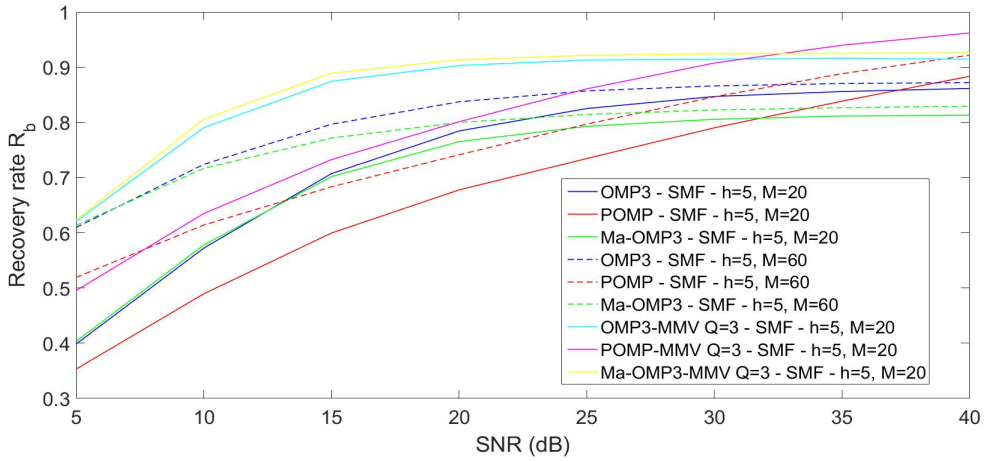

Figure 7.6. Comparison between the relaxed support recovery performances ($\delta = 2$ bins) of different reconstruction methods for the multiple-SMF model at different SNRs (3000 trials for each SNR). Choose $N = 500$, $L = 5$, $f_{max} = 30$ MHz, $F = 100$, $\Delta r = 5$ cm, $K = 3$.

of POMP (red lines) are the poorest ones among three analyzed methods in most cases of different SNRs. Additionally, as Fig. 7.7 shows, POMP and Ma-OMP3 outperform in the cases of small MDs while OMP3 inversely does in the cases of large MDs. Ma-OMP3 brings a better relaxed support recovery performance than POMP does in the cases of large MDs. These results are similar to the numerical analysis of a MFT acquisition in Section 4.5.

Moreover, as Fig. 7.7 shows, POMP and OMP3 possess their advantages in the cases of different MDs. From these results, if these strengths can be integrated efficiently in the proposed method CMD-OMP as described in Section. 4.6, then we can even enhance the stability of accurate signal reconstruction in a multiple-SMF model. This result is similar to that in a MFT acquisition. However, the tuning border for the selection between POMP and OMP3 in a multiple-SMF model is different from that of a MFT acquisition in Section. 4.6. For instance, when SNR is 15dB, the tuning point is approximately 20 bins in Fig. 7.6 for the multiple-SMF model $\mathbf{\Phi}_{SMF,1}$ while that for the MFT acquisition $\mathbf{\Phi}_{opt,1}$ is about 45 in Fig. 4.8.

In Section 4.6, the tuning border can be estimated through a numerical analysis. It demonstrates the relaxed support recovery rates of both OMP3 and POMP with the tolerance offset $\delta = 2$ in two domains of SNRs (5 dB to 50 dB) and MDs (from 5 to 150 bins). Similarly, Fig. 7.8 shows the similar results for two multiple-SMF models $\mathbf{\Phi}_{SMF,1}$ and $\mathbf{\Phi}_{SMF,4}$. In this figure, the red color region denotes the cases where POMP outperforms OMP3 and inversely the green one denotes the cases where OMP3 has better performances. As can be seen in Fig. 7.8a that the tuning MD value of the multiple-

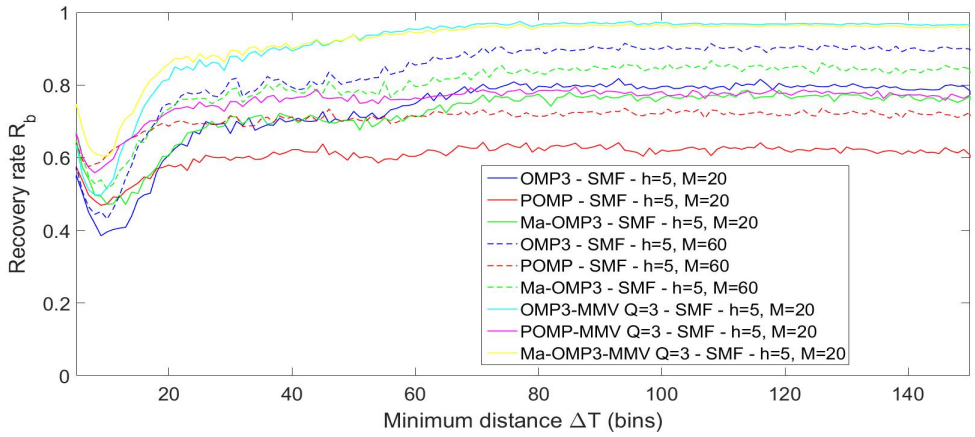

(a) 15dB

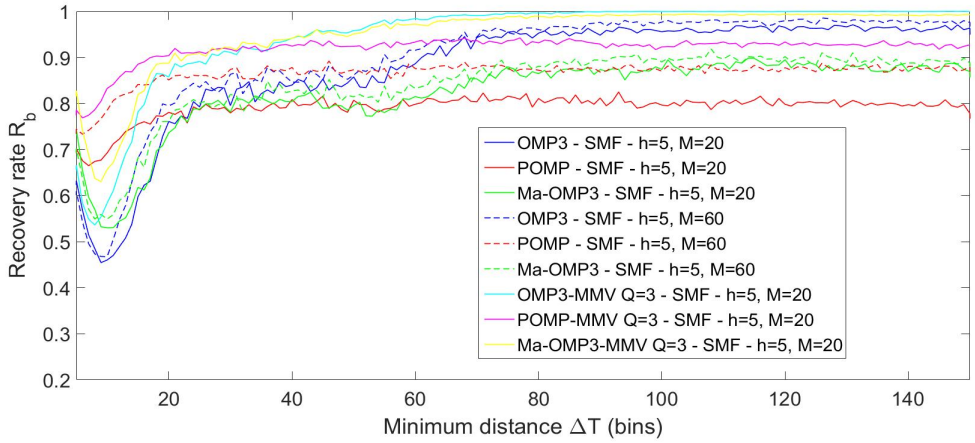

(b) 30dB

Figure 7.7. Comparison between the relaxed support recovery performances ($\delta = 2$ bins) of different reconstruction methods for the multiple SMF model at different MDs (500 trials for each MD). Choose $N = 500$, $L = 5$, $f_{max} = 30$ MHz, $F = 100$, $\Delta r = 5$ cm, $K = 3$.

SMF acquisition $\mathbf{\Phi}_{SMF,1}$ is minimal (about 20 bins) in a highly noisy case. Whereas, the acquisition $\mathbf{\Phi}_{SMF,4}$ with more SMF measurements acquires a smaller tuning value (approximately 15 bins in Fig. 7.8b). These results indicate that OMP3 individually can bring a high stability of a good support recovery in most cases of various MDs for a multiple-SMF acquisition. Therefore, in a multiple-SMF acquisition, CMD-OMP in

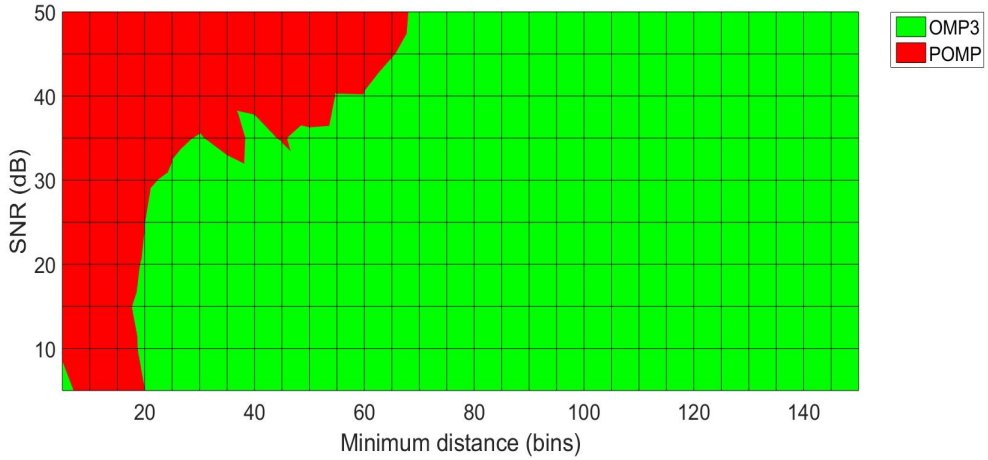

(a) $\boldsymbol{P}_1$

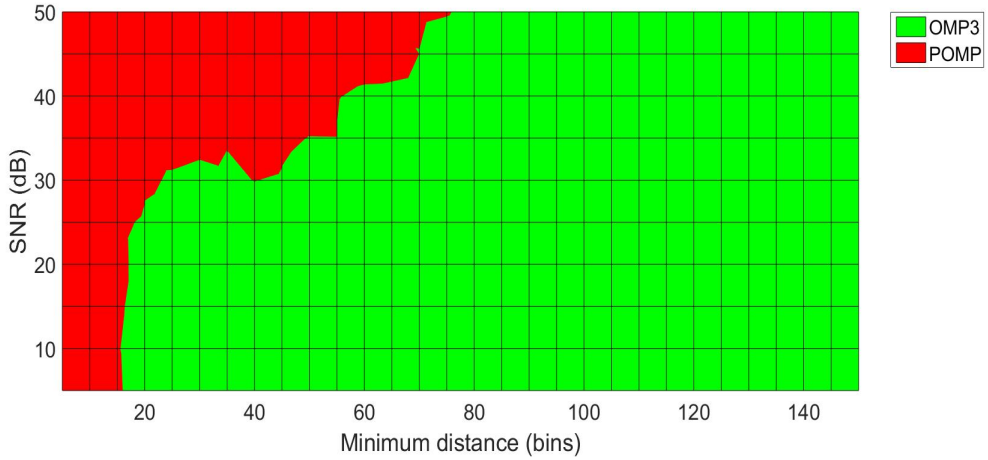

(b) $\boldsymbol{P}_4$

Figure 7.8. Tuning border image of the relaxed support recovery rates ($\delta = 2$) between POMP and OMP3 for the multiple SMF model in the super-resolution configuration. Choose $N = 500$, $L = 5$, $f_{max} = 30$ MHz, $F = 100$, $\Delta r = 5$ cm, $K = 3$.

Algorithm. 11 should configure Δ_{tuning} and F_0 so that OMP3 is frequently selected for most scenarios.

7.3.3 Multiple-SMF acquisition using MMV techniques

As mentioned in Chapter 6, MMV data in a MFT acquisition can be generated through multiple polarization techniques. In principle, these techniques are applicable for a multiple-SMF acquisition system at either transmitter or receiver side. Therefore, in this part, we resolve MPIs through a multiple-SMF acquisition using MMV techniques.

Two Monte Carlo simulations are carried out with 3000 trials for each SNR (from 5 dB to 40 dB) and 500 trials for each MD (from 5 to 150 bins). In these numerical experiments, we assume that MMVs ($Q = 3$) comprising multiple-SMF measurements sharing the sensing matrix $\mathbf{\Phi}_{SMF,1}$ are available. At each trial, the procedures of a 3-joint-sparse signal matrix and MMV generation are similar to the previous simulations in Section 6.5. OMP3-MMV, Ma-OMP3-MMV in Chapter 6 are used to reconstruct the joint-sparse signal based on the MMV data. Moreover, we also use POMP on the converted SMV data as described in (6.16) for sparse support recovery. After all trials, the relaxed support recovery rates of all three above methods are averaged and then demonstrated for various SNRs in Fig. 7.6 and for various MDs in Fig. 7.7.

For further comparison, we construct a multiple-SMF acquisition of 60 SMF measurements $\mathbf{\Phi}_{SMF,6}$ without MMV techniques. This acquisition is optimized through the proposed projection matrix optimization method in Algorithm. 20. Definitely, it has the same amount of SMF measurements as the above multiple-SMF acquisition using MMV techniques ($M = 20, Q = 3$). The previous parameters are maintained with $h = 5, N = 500, f_{max} = 30$ MHz, $F = 100$, $\Delta r = 5$ cm. The similar Monte Carlo simulations are carried out for achieving the recovery performances of OMP3, POMP, and Ma-OMP3 in a multiple-SMF acquisition $\mathbf{\Phi}_{SMF,1}$ without MMV techniques. The achieved results are demonstrated in various SNRs (see Fig. 7.6) and various MDs (see Fig. 7.7).

A comparison between the results in Fig. 7.6 and Fig. 7.7 claims that a multiple-SMF model using MMV techniques ($M = 20, Q = 3$) outperforms a multiple-SMF model ($M = 60$) without MMV techniques in most cases of SNRs and MDs. These results illustrate the effectiveness of MMV techniques as well as many proposed variants of OMPMMV methods, i.e., OMP3-MMV, Ma-OMP3-MMV and even POMP based on the converted SMV data. This multiple-SMF model using MMV techniques can guarantee a high stability of a good relaxed support recovery ($\delta = 2\Delta r$) even in highly noisy environments with only 60 SMF measurements. For instance, at SNR of 15 dB, about 60% atoms are estimated successfully by Ma-OMP3-MMV when the MD is minimal ($\Delta T = 10$ bins). This success rate becomes higher with 80% using Ma-OMP3-MMV when $\Delta T = 20$ bins and then over 90% using OMP3-MMV when $\Delta T \geq 40$ bins.

7.3.4 Relaxed super-resolution problem

Our primary goal in this thesis is to guarantee the high stability of good relaxed support recovery in all cases of various MDs in noisy cases. As proven previously, a super-resolution multiple-SMF acquisition using MMV techniques with a large refinement factor $F = 100$ brings a high 3-sparse support recovery performance through 60 SMF measurements. We expect that a relaxed super-resolution factor can be achieved through this technique. Therefore, a Monte Carlo simulation is carried out in this part to obtain the recovery performance at various MDs in a multiple-SMF acquisition $\mathbf{\Phi}_{SMF,1}$ using MMV techniques, similar to the previous numerical experiment in Fig. 7.7 but with a fixed SNR of 20 dB. At each trial, we generate a joint-sparse signal matrix whose each column contains only two non-zero atoms ($K = 2$). This simulation aims to evaluate the capabilities of a multiple-SMF acquisition using MMV techniques in the discrimination of two-target. The achieved relaxed support recovery rates with two tolerance offsets $\delta = 2$ and $\delta = 5$ are shown in Fig. 7.9.

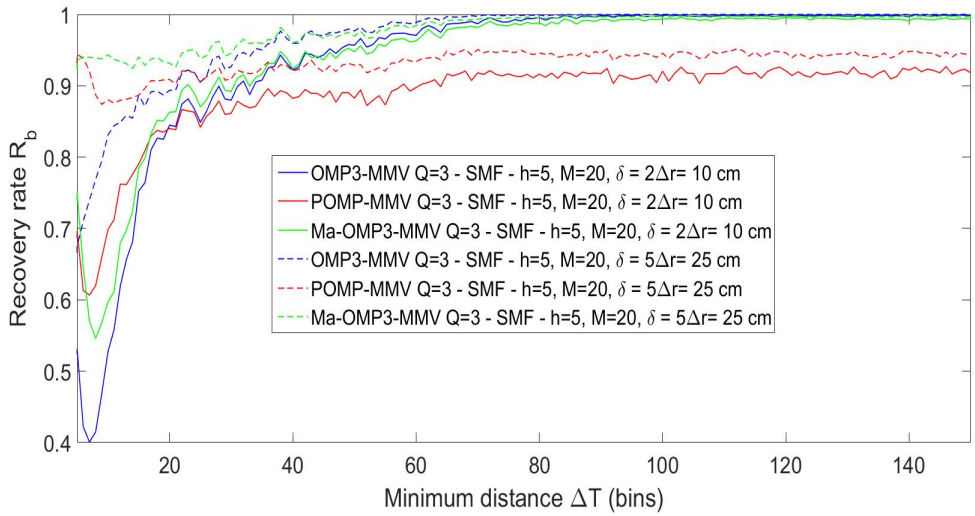

Figure 7.9. Relaxed support recovery performances ($\delta = 2$) for a MMV-SMF model (Q=3) at different MDs (500 trials for each MD) with SNR= 20dB. Choose $N = 500$, $L = 5$, $f_{max} = 30$ MHz, $F = 100$, $\Delta r = 5$ cm, $K = 2$, $h = 5$, $M = 20$.

It can be seen Fig. 7.9 that a multiple-SMF acquisition using MMV techniques guarantees a high stability of accurate target localization despite the large refinement factor $F = 100$ is large. For instance, if $f_{max} = 30$ MHz, then:

- About 70% atoms separated by $10\Delta r = 50$ cm can be localized accurately with an accuracy offset of $\delta = 2\Delta r = 10$ cm. This success rate can be increased up to 90% for the cases of large MDs ($30\Delta r = 150$ cm).

- If the accuracy requirement of a TOF application is low with $\delta = 5\Delta r = 25$ cm, about 95% atoms can be localized accurately in all cases of various MD $\Delta T \geq 2\delta + 1 = 55$ cm.

Furthermore, the above properties in numbers would be even improved if a new TOF camera can carry out a SMF measurement containing higher-frequency parts.

7.3.5 Summary

The multiple-SMF acquisition is an effective solution to successfully resolve a MPI problem in a TOF camera which can modulate only a low-frequency acquisition. It brings the highly reliable reconstruction results in a highly noisy case through only a few SMF measurements. Thus, this accurate time profile reconstruction can be maintained with a video frame rate. However, a SMF measurement simultaneously issues new challenges regarding the system design complexity. Apparently, the implementation of a real SMF measurement is currently hard for a commercial CW-TOF camera. For this purpose, we require the following new hardware design:

- A new illumination system for emitting a mixed optical signal comprising multiple frequency parts.
- A new chip design for measuring the cross-correlation between the reflected and demodulation signal mixtures comprising multiple corresponding parts.

7.4 Joint multiple frequency calibration

As mentioned above, a currently commercial TOF camera hardly acquires a SMF measurement. Therefore, we introduce an alternative way in this part to replace a real multiple-SMF acquisition but still guarantee the usefulness of our proposed projection matrix optimization. Firstly, $M_0 = 117$ frequency TOF measurements are carried out to generate the full measurement vector $\boldsymbol{y}_0 = \boldsymbol{\Phi}_0 \boldsymbol{x}$ sharing the dictionary matrix $\boldsymbol{\Phi}_0$. Subsequently, we formulate a calibration vector $\boldsymbol{z}$ through combining all measurements of $\boldsymbol{y}_0$:

$$\boldsymbol{z} = \boldsymbol{P}\boldsymbol{y}_0 = \boldsymbol{P}\boldsymbol{\Phi}_0\boldsymbol{x} + \boldsymbol{P}\boldsymbol{\sigma} = \boldsymbol{\Phi}\boldsymbol{x} + \boldsymbol{n} \tag{7.12}$$

where $\boldsymbol{P}$ is projection matrix which can be optimized by our proposed projection matrix optimization method in Algorithm 20. For this reason, this technique is named in this thesis as joint multiple-frequency calibration method, similar to the previous study of Fornaro et al. [80] in tomographic SAR. In principle, this calibration technique can enhance the incoherence of the calibration matrix $\boldsymbol{\Phi}$ and eventually improve the sparse reconstruction results without hardware updates. Additionally, there are no restricting

conditions on this projection matrix since this technique is not limited by hardware design. However, according to the calibration process in (7.12), the measurement noises $\boldsymbol{\sigma}$ may be enhanced through scaling with the projection matrix. Therefore, this technique only brings benefits if the enhancement of measurement noise is insignificant. From these points, despite no restricting conditions, the structure of the projection matrix, e.g. the row sparsity, also plays a significant role in this joint multiple-frequency calibration method.

7.4.1 Numerical results

In this part, two Monte Carlo simulations are carried out with 3000 trials for each SNR (from 5 dB to 60 dB) and 500 trials for each MD (from 5 to 150 bins). At each trial, we carry out 117 TOF measurements $\boldsymbol{y}_0$ sharing the dictionary matrix $\boldsymbol{\Phi}_0$. The MFT dictionary matrix is constructed with the parameters, i.e., $N = 500, L = 5, f_{max}$ = 30 MHz, $F = 100$ and $\Delta r = 5$ cm. The procedures of 3-sparse signal vector and measurement vector are similar to the previous simulations for a MFT acquisition in Chapter 4. These numerical experiments aim to compare the reconstruction results before and after the calibration process.

Firstly, two algorithms POMP and OMP3 are used for the sparse support reconstruction based on the measurement vector $\boldsymbol{y}_0$ and the dictionary matrix $\boldsymbol{\Phi}_0$. The achieved results are shown in Fig. 7.10 and Fig. 7.11. Secondly, according to 7.12, we generate the calibration vectors $\boldsymbol{z}$ with four different projection matrices $\boldsymbol{P}_1$, $\boldsymbol{P}_2$, $\boldsymbol{P}_3$, $\boldsymbol{P}_4$. These matrices are collected from the previous multiple-SMF numerical experiments with the setting parameters listed in Table.7.1. Similarly, POMP and OMP3 are used for the sparse support recovery based on the calibration vectors $\boldsymbol{z}$ and the calibration matrix $\boldsymbol{\Phi}$ in (7.12). The achieved results are also demonstrated in Fig. 7.10 and Fig. 7.11.

A comparison between the reconstruction results before and after calibration in Fig. 7.10 and Fig. 7.11 claims that the joint multiple-frequency calibration is only efficient for the algorithm OMP3 in some cases. Concretely, the calibration technique brings better support recovery performance of OMP3 in the cases of high SNRs (SNR $\geq$ 30 dB for $\boldsymbol{P}_1$-$\boldsymbol{P}_3$ and SNR $\geq$ 25 dB for $\boldsymbol{P}_4$). Whereas, it causes negative influences on the sparse recovery results of POMP in most cases of various SNRs and MDs (see Fig. 7.10a and Fig. 7.11a). These results indicate that the enhancement of measurement noises in (7.12) is challenging in the joint multiple-frequency calibration.

Besides, unlike the multiple-SMF acquisition in the previous section, a larger row sparsity of projection matrix is inefficient to enhance the recovery quality through the joint multiple-frequency calibration. As can be seen in Fig. 7.10 and Fig. 7.11 that the reconstruction results of OMP3 and POMP after calibration with $\boldsymbol{P_2}$ ($h = 10$, green lines) are even worse than those after calibration with $\boldsymbol{P_1}$ ($h = 5$, blue lines). Whereas, a larger amount of rows in the projection matrix $\boldsymbol{P_4}$ (rose lines) can improve the reconstruction performance, compared to the calibration with $\boldsymbol{P_1}$ ($h = 5$, blue lines).

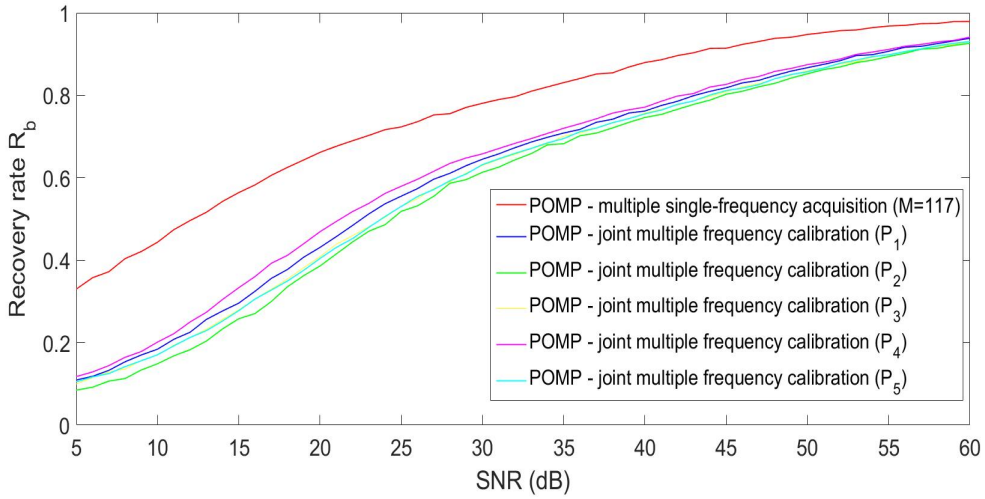

(a) POMP

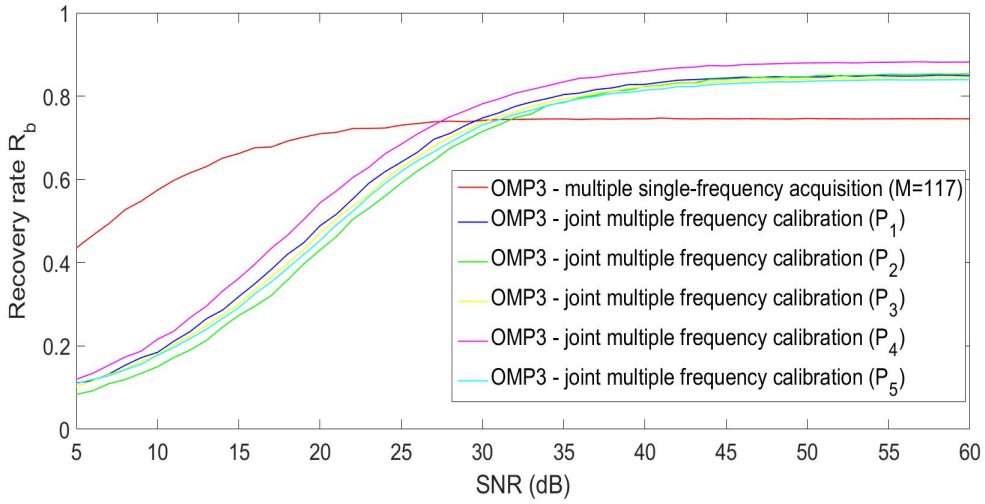

(b) OMP3

Figure 7.10. Relaxed support recovery performances ($\delta = 2$) of OMP3 and POMP after joint multiple-frequency calibration with different projection matrices at different SNRs (3000 trials for each SNR). Choose $N = 500$, $L = 5$, $f_{max} = 30$ MHz, $F = 100$, $\Delta r = 5$ cm, $K = 3$.

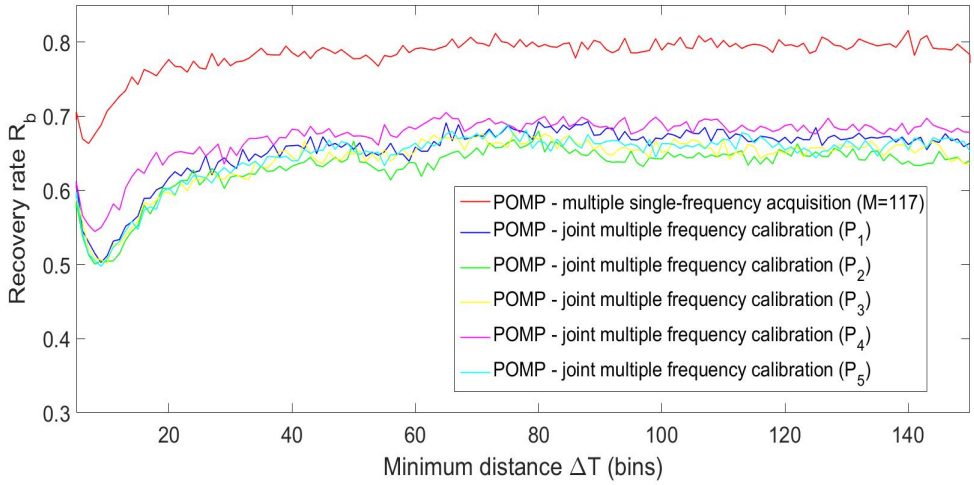

(a) POMP

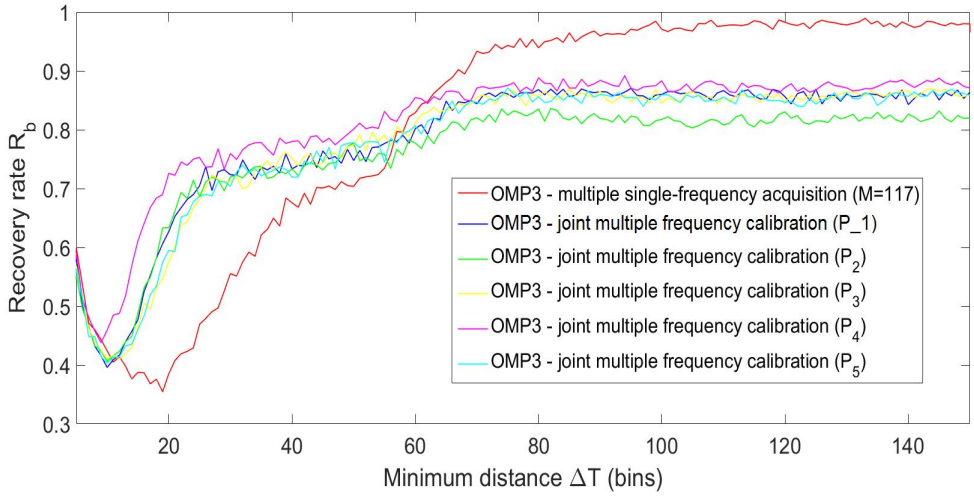

(b) OMP3

Figure 7.11. Relaxed support recovery performances ($\delta = 2$) of OMP3 and POMP after joint multiple-frequency calibration with different projection matrices at different MDs (500 trials for each MD) with SNR=30 dB. Choose $N = 500$, $L = 5$, $f_{max} = 30$ MHz, $F = 100$, $\Delta r = 5$ cm, $K = 3$.

7.4.2 Summary

Without any hardware design for a real SMF measurement, the joint multiple-frequency calibration is an efficient method to improve the support reconstruction results of OMP3

in a MFT acquisition. According to the operating principle, this calibration technique is considered as an alternative solution to prove the capabilities of a real multiple-SMF model for resolving MPIs in Chapter 8. However, this technique requires a significant amount of slightly noisy TOF measurements.

8 Experimental results

This chapter carries out several practical experiments to strengthen the arguments of a super-resolution MFT acquisition that have been inferred from the previous numerical results.

8.1 PMD Multicam System and measurement matrix formulation

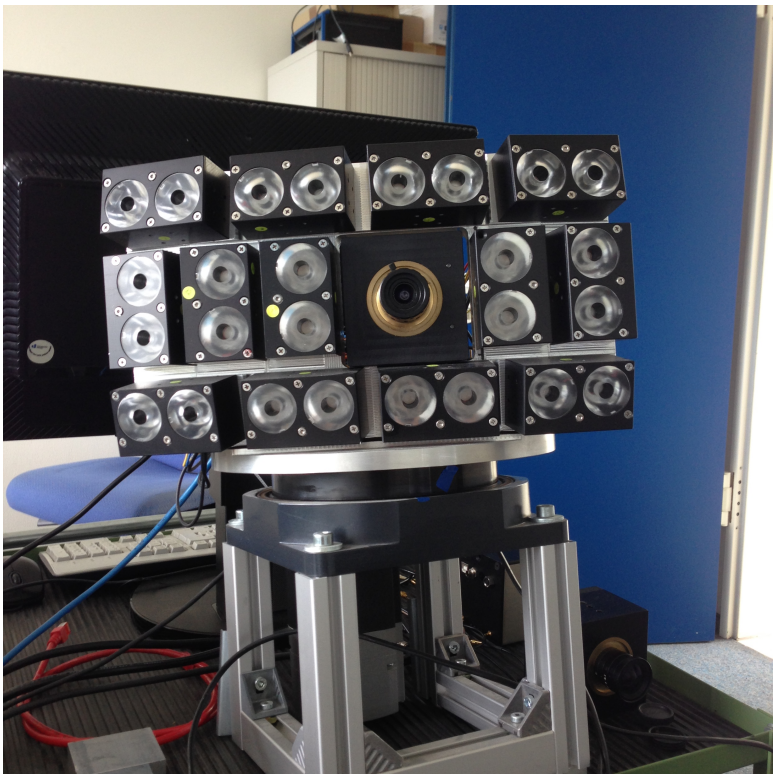

Figure 8.1. Multicam System

The ZESS Multicam system [2] in Fig. 8.1 with a commercial PMD 19k camera chip [4] can carry out TOF measurements at different modulation frequencies in the set Ψ

(see Remark 6) from 1 MHz to 30 MHz with a frequency step of 0.25 MHz. This set has been used in most previous numerical experiments. Theoretically, this PMD chip can carry out a higher-frequency (up to 60 MHz) TOF measurement. But this measurement is highly noisy with low confidentiality and low demodulation contrast.

As explained in Section 2.2, a TOF measurement is one sample of cross-correlation between the reflected and demodulation signals at a phase-offset τ. In a PMD 19K chip [4], this sample can be computed through the subtraction between two samples of channel A and channel B:

$$C_\tau = C_{\tau,A} - C_{\tau,B} \tag{8.1}$$

8.1.1 PMD Multicam System

Each measurement in a MFT acquisition is a TOF sample in (8.1) at one modulation frequency. This measurement is an intensity sample achieved from the integration process of the reflected optical signal. Thus, its accuracy suffers from the saturation problem. For restricting a huge amount of incident photons, the exposure time of each TOF measurement should be set short enough. We set 100-microsecond exposure time for the low-frequency acquisitions (1 - 10 MHz) and a longer exposure time for the higher ones to maintain a high demodulation contrast. Eventually, a MFT acquisition comprising M TOF measurements at different frequencies, consumes a short acquisition time for a K-sparse reconstruction. More precisely, the acquisition time of 20 TOF measurements only takes a few milliseconds for the reconstruction of 2 MPIs in the next practical experiments.

Nevertheless, since the exposure time is short, the TOF measurement C_{τ,f_0} is relatively noisy at a high-frequency modulation in a PMD 19k camera. Low demodulation contrast or photon shot noises can cause errors in a TOF measurement [5]. Therefore, in our real MFT model, two samples C_τ and $C_{\tau+\pi}$ are used for a more robust correlation sample:

$$g_{\tau,f_0} = C_{\tau,f_0} - C_{\tau+\pi,f_0} \tag{8.2}$$

A TOF measurement in (8.5) acquires a doubled acquisition time but reduced measurement noises in this thesis. For the future development of a practical MFT system, we aim to design a TOF imaging chip to read out a robust TOF intensity sample in only one acquisition in order not to slow down the overall system speed.

8.1.2 Dictionary matrix formulation

Each row of MFT dictionary matrix in (3.31) is the response of the cross-correlation function to N grids at a modulation frequency. With f_{max}= 30 MHz, a grid system possesses a grid length of 5 m in the conventional grid configuration to guarantee the high stability of exact support recovery. However, this grid length is impractical with low

depth resolution and big mismatch model errors. The reconstruction of target depths are hence extremely inaccurate. For this reason, we configure the grid system with a smaller grid length of $\Delta r = 5$ cm. This setting is equivalent to a large refinement factor $F = 100$. For a short-range application, a small dimension $N = 200$ is set for the construction of MFT dictionary matrix to cover a range of interest of 10 m.

Besides, for the construction of a real MFT dictionary matrix, the Fourier coefficient estimation of the cross-correlation function is necessary. In our ZESS Multicam system, the optical output lies somewhere between a square wave and a sinusoidal one. Thus, the high-order harmonic components vary at different modulation frequencies and are entirely different from the theoretical equation (3.41). The high-order harmonics of the cross-correlation function at each modulation frequency are measured through a practical experiment [15]. Firstly, we mount the Multicam system accurately 1m ahead of a highly-reflecting object, e.g., white paper. Next, several TOF measurements are carried out at one frequency with different phase-shifts θ (in degrees) of the transmitted optical signal. This phase-shift is generated by an external pulse generator (Agilent 81150A). The achieved TOF samples at one frequency f_0 can be mathematically represented by:

$$g_{\theta,f_0} = \sum_{l=1}^{L} c_l d_l^* \cos(l\theta\pi/180) \tag{8.3}$$

For our ZESS Multicam system, only five harmonics ($L = 5$) are concerned because the magnitudes of higher-order ones are significantly small. Note that even-order components are very close to zero. Eventually, only three variables or three odd-order harmonic coefficients (1^{st}, 3^{rd}, 5^{th} harmonics) are unknown in (8.3). We collect 24 samples at different equi-stepped phase-shifts (from 0° to 345° with a step of 15°) for the estimation of three odd-order coefficients through the following inverse linear equation problem:

$$\hat{\boldsymbol{z}} = \underset{\boldsymbol{z}}{\operatorname{argmin}} \, ||\boldsymbol{g} - \boldsymbol{G}\boldsymbol{z}||_2 \tag{8.4}$$

where $\boldsymbol{g}$ is the measurement vector of 24 samples, $\boldsymbol{G}$ is the measurement matrix formulated from (8.3) and $\boldsymbol{z}$ is variable vector of three expected Fourier coefficients. Apparently, (8.4) is an overdetermined equation system which can be easily solved through a least mean squares minimization method. The achieved results are Fourier coefficients of the cross-correlation function at a modulation frequency. The above estimation process repeats for 117 modulation frequencies in the set Ψ to construct the real-valued dictionary matrix $\boldsymbol{\Phi}_0 \in \mathbb{R}^{117\times 200}$.

8.2 Transparent object imaging

MPIs are generated by transparent object imaging in our practical experiments. Particularly, several transparent objects are put between the Multicam system and one opaque

object. A lot of transparent objects imply a lot of MPIs. These setups are similar to the practical experiments of Bhandari et al. [6]. In our experiments, we put only one transparent bottle between the ZESS Multicam system and a white wall to simulate two real MPIs (one from the bottle and one from the wall as described in Fig. 8.2). More

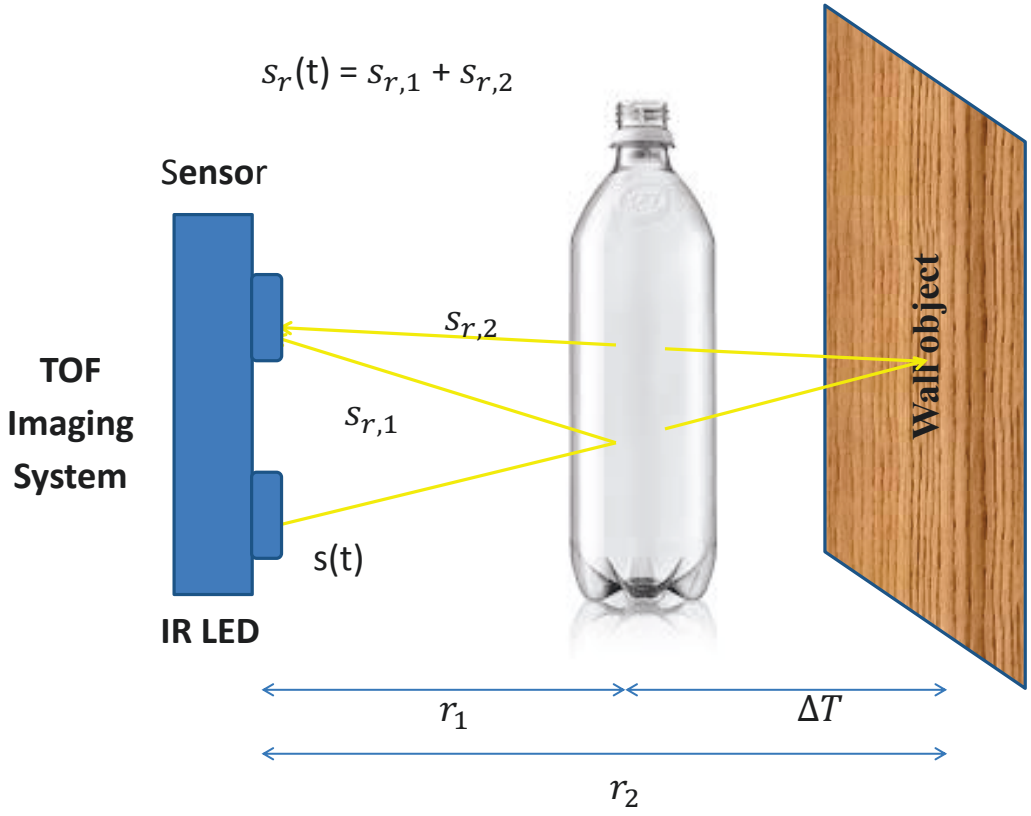

Figure 8.2. Transparent object imaging with two reflecting components from a transparent bottle and a wall.

precisely, there is more than one reflection from two sides (front and back) of the bottle. Nevertheless, the diameter of the bottle is significantly small (approximately 10 cm = 2 Δr) and hence multiple light rays scattered from the bottle are considered as one scatterer. And hence, the number of MPIs is only two ($K = 2$) in this setup. Moreover, this transparent object imaging with such complex scattering property is common in many real-life scenes. These errors are considered as mismatch model errors caused by the scene structure.

Apparently, the above scattering scene with only two MPIs seems to be more simple than that in the previous studies, e.g., [6]. Their research has reconstructed more MPIs

but not concerned about the minimum separation between MPIs yet. Whereas, MD between targets is the most crucial factor in our analysis. It is challenging to setup more MPIs since most of the optical energy is distorted through multiple transparent objects. From this point, the amplitudes of signals reflected from far objects are extremely tiny if the number of scatters is large. Thus, the above setup comprising only two MPIs is convenient for adjusting MD.

In our MPI setup, the bottle and the wall are positioned on different grid points to avoid mismatch model errors caused by grid system as described in Fig. 3.2. Therefore, their actual locations, r_1 (bottle) and r_2 (wall) respectively, are represented by two ordinal numbers of the corresponding grids, named as bins in our analysis. For instance, the target position of 3m is equivalent to 60 bins $\equiv 60\Delta r$ where $\Delta r = 5$ cm is the grid length in space. The locations of the bottle and the wall vary in nine scenarios E1-E9 as listed in Table 8.1. Apparently, the distance separation between the bottle and the wall $\Delta R = r_2 - r_1 = \Delta T \Delta r$ denotes minimum distance between scatterers in each scenario. For the reconstruction of MPIs, we carry out 20 TOF measurements with the set $\Gamma_0 = (H_0, J_0)$ of 20 random frequencies (H_0) and zero phase-offsets ($J_0 = 0$). Subsequently, we collect the achieved TOF samples C_0 for the measurement vector $\boldsymbol{y} \in \mathbb{R}^{20}$. The sensing matrix $\boldsymbol{\Phi} \in \mathbb{R}^{20\times 200}$ is extracted from the dictionary matrix $\boldsymbol{\Phi}_0 \in \mathbb{R}^{117\times 200}$ through the randomly chosen frequencies. Based on the achieved measurement vector and sensing matrix, a variety of CS algorithms recover the 2-sparse signal with a known sparsity $K = 2$. This sparse reconstruction can be implemented sequentially or simultaneously for all pixels. For the evaluation of the support reconstruction performance, only two largest-magnitude atoms of the reconstructed signal are concerned.

After the sparse reconstruction of a greedy pursuit with a known $K = 2$, the sparse support of the reconstructed signal comprises at most two ordinal indices (in bins). These indices denote the estimated locations of the bottle and the wall ($\hat{r}_1$ and $\hat{r}_2$) in the grid system. Subsequently, they are then compared with the actual ones (r_1 and r_2). For both visual and numerical comparison, we demonstrate the following images and histograms:

- The recovered depth image of the transparent bottle, e.g. Fig. 8.3, Fig. 8.5 and Fig. 8.7, comprises all pixels where the location of the bottle is estimated accurately. In this analysis, we evaluate the reconstructed sparse support under the relaxed condition with a tolerance offset $\delta = 5$ bins. In other words, this image demonstrates the region of the transparent bottle that has the estimated support index in the range $\hat{r}_1 \in [r_1 - 5\Delta r, r_1 + 5\Delta r]$. This result is equivalent to 25 cm accuracy bound. This low accuracy of MPI reconstruction is due to that the exposure time for each TOF measurement is significantly short in order not to override the dynamic range of our TOF chip. We should build up a TOF camera system for measuring the TOF correlation more accurately in the future to improve this accuracy bound. The pixel color denotes the estimated ordinal index $\hat{r}_1$. Black pixels

Table 8.1. Nine scenarios E1-E9 with different MDs, 1 bin = $\Delta r = 5$ cm

Experiment	r_1 (bins)	r_2 (bins)	ΔR (bins) $r_2 - r_1$
E1	1 m=20Δr	3.7 m=74Δr	54
E2	1.4 m=28Δr	4.4 m=88Δr	60
E3	1 m=20Δr	4.2 m=84Δr	64
E4	0.9 m=18Δr	4.55 m=91Δr	73
E5	1.6 m=32Δr	5.4 m=108Δr	76
E6	0.8 m=16Δr	4.8 m=96Δr	80
E7	1.1 m=22Δr	5.4 m=108Δr	86
E8	0.9 m=18Δr	5.4 m=108Δr	90
E9	0.7 m=20Δr	5.4 m=108Δr	94

denote the region of missing detection. This image is used for a visual evaluation of the reconstruction performance of the foreground transparent object.

- The reconstruction histogram of transparent bottle region, e.g. Fig. 8.4, Fig. 8.6 and Fig. 8.8, lists the reconstructed support indices of all pixels in the transparent imaging region. This result comprises the estimated depths of both bottle and wall ($\hat{r}_1$ and $\hat{r}_2$). The yellow lines at r_1 and r_2 show the actual locations of two objects. The reconstruction result of a CS algorithm is better if the distribution of the histogram stays more densely around these yellow lines.

- The count of accurately estimated atoms (shortly count n), e.g. Table. 8.2, denotes how many locations of the wall as well as the bottle image points in the transparent imaging region are reconstructed accurately with a tolerance offset $\delta = 2\Delta r = 10$ cm. In other words, it counts all estimated support indices satisfying $\hat{r}_1 \in [r_1 - 2, r_1 + 2]$ or $\hat{r}_2 \in [r_2 - 2, r_2 + 2]$. The ratio n/n_{total} denotes the relaxed support recovery rate for each scenario where n_{total} is the number of object locations (both wall and bottle) in the transparent imaging region which should be estimated. For instance, if the transparent imaging region comprises 10 pixels, then $n_{total} = 10K = 20$.

Besides, the reflection properties of the transparent region in each scenario have influences on the reconstruction quality. Especially, the ratio between the reflective mag-

nitudes of the bottle and the wall (a_1 and a_2 respectively)

$$rt = \frac{a_1}{a_2} \tag{8.5}$$

represents the dynamic range through

$$DR = max(rt, \frac{1}{rt}) \tag{8.6}$$

In our visual representation, this ratio is demonstrated additionally by a color image for each scenario:

- red if $0.2 < rt < 5$
- dark red if $0.05 \leq rt \leq 0.2$ or $5 \leq rt \leq 20$
- blue and yellow if $rt < 0.05$
- light blue if $rt > 20$

As a result, red pixels represent small DR cases while the other ones represent large DR cases. Apparently, most region surrounding the bottle is colored with dark red or yellow because there is only one reflective component from the wall in this region. Furthermore, this reflective property image also indicates the ground-truth transparent bottle shape.

8.3 Comparison of various reconstruction methods

8.3.1 POMP and OMP3

In this part, the reconstruction capabilities of two previously introduced greedy pursuits OMP3 and POMP are analyzed in the cases of various MDs (E1-E9). In each scenario, their sparse reconstruction relies on the achieved measurement vector and the available sensing matrix $\mathbf{\Phi} \in \mathbb{R}^{20\times200}$ collected from 20 TOF measurements with the set Γ_0 of random frequencies and zero phase-offsets. We assume the known sparsity $K = 2$. The achieved counts n are given in Table 8.2. Besides, the recovered depth images of the transparent bottle and the reconstruction histogram of the transparent bottle region are also demonstrated in the following figures, i.e, scenario E1 in Fig. 8.3 and Fig. 8.4, scenario E4 in Fig. 8.5 and Fig. 8.6, scenario E8 in Fig. 8.7 and Fig. 8.8.

8.3.1.1 Scenario E1

Firstly, the scenario E1 is an example of a small MD case $\Delta T = 2.7$ m $= 54\Delta r$. Fig. 8.3a illustrates the inhomogeneous reflective property of the transparent bottle region in this

Table 8.2. Numerical count n for the comparison between OMP3 and POMP in nine scenarios E1-E9

Experiment	OMP3			POMP		
	Small DR	Large DR	Sum	Small DR	Large DR	Sum
E1	26/702 0.037	126/378 0.333	152/1080 0.1407	223/702 0.317	90/378 0.238	313/1080 0.29
E2	40/326 0.123	78/164 0.475	118/490 0.241	28/326 0.086	55/164 0.335	83/490 0.169
E3	52/756 0.069	116/396 0.293	168/1152 0.146	157/756 0.208	70/396 0.177	227/1152 0.197
E4	414/958 0.432	130/388 0.335	544/1346 0.404	293/958 0.306	103/388 0.265	396/1346 0.294
E5	245/390 0.628	126/250 0.504	371/640 0.579	81/390 0.207	74/250 0.296	155/640 0.242
E6	463/1308 0.354	148/522 0.283	611/1830 0.334	303/1308 0.232	96/522 0.184	399/1830 0.218
E7	347/750 0.463	105/320 0.328	452/1070 0.422	148/750 0.197	69/320 0.215	217/1070 0.203
E8	341/662 0.515	177/430 0.411	518/1092 0.474	148/662 0.223	102/430 0.237	250/1092 0.229
E9	609/1642 0.37	146/742 0.197	755/2384 0.317	435/1642 0.265	153/742 0.206	588/2384 0.246

scenario. Besides, as Fig. 8.3b shows, the traditional four-phase stepping method (see (2.10)) brings poor reconstruction performances of object locations. Apparently, the bottle depth estimation seems to be not robust through this traditional algorithm. Only the bottle region where the reflecting component from the wall is significantly small (light blue or dark red pixels in Fig. 8.3a), can acquire accurate depth reconstruction.

This result indicates the problem of MPIs in a commercial TOF camera with wrong depth estimation of the traditional method.

Subsequently, the reconstruction results of OMP3 and POMP based on the MFT acquisition are shown in Fig. 8.3c and Fig. 8.3d respectively. TOF measurements are carried out at a random set of 20 frequencies H_0 and zero phase-offsets $J_0 = 0$ ($\Gamma_0 = (H_0, J_0)$). A comparison between these results in two figures reveals that POMP recovers the depth of the bottle accurately with a higher probability in this scenario of a small MD. Additionally, according to the histogram in Fig. 8.4a, the object locations in the bottle region reconstructed by POMP (red part) distributes more densely around the yellow reference lines. Furthermore, the relaxed support recovery rate of POMP with the count n of 313 in Table 8.2 is higher than that of OMP3 with only 152. These results indicate the better sparse reconstruction performance of POMP in the case of a small MD, compared to the traditional four-phase stepping method (green part) and OMP3 (blue part)

Nevertheless, a comparison between the results in Fig. 8.4a claims that the reconstruction results of OMP3 (blue parts) based on the MFT measurements are poorer than those of the traditional four-phase method (green parts). Apparently, a MFT acquisition with randomly chosen frequencies and phase-offsets cannot guarantee a good support recovery with a high probability.

Besides the scenario E1, we also have two other scenarios E2-E3 for the cases of small MDs. Similarly, according to Table 8.2, POMP outperforms OMP3 in E3. Nevertheless, the results of OMP3 are better than those of POMP in E2. It seems to be possible that the poorer performance of POMP are due to that this small MD value of 60 stays in the tunning region between OMP3 and POMP (see Fig. 4.11).

8.3.1.2 Scenario E4

Secondly, the scenario E4 represents the case of a medium MD ($\Delta T = 73\Delta r$). This MD value resides in the tuning region between POMP and OMP3 (see Fig. 4.11). Due to the comparison between the results of OMP3 and POMP in Fig. 8.5c and Fig. 8.5d, it can be seen that OMP3 is more efficient than POMP in this scenario. Furthermore, as Table 8.2 shows, the count n of OMP3 (544) is significantly higher than that of POMP (396). Nevertheless, their reconstruction histograms (red and blue parts) in Fig. 8.6a seem to be similar. Unlike the scenario E1, the reconstruction results of both methods using the MFT acquisition are better than those of the traditional four-phase method.

When MD gets larger, OMP3 has a better recovery performance than POMP. These results can be seen in Table 8.2 through the counts n in several scenarios E5-E7.

(a) Reflecting property image

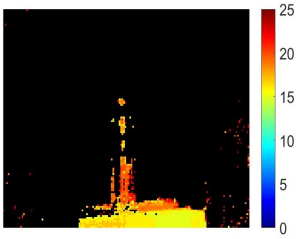

(b) Traditional four-phase method

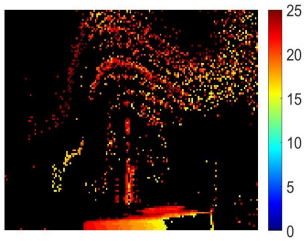

(c) (Γ_0) OMP3

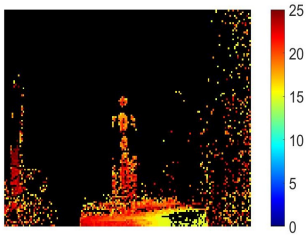

(d) (Γ_0) POMP

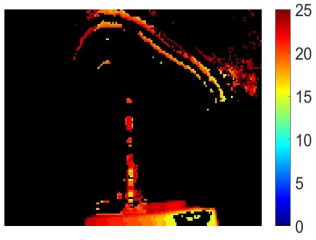

(e) (Γ_0) CMD-OMP

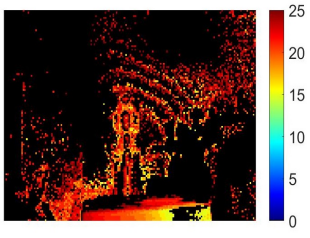

(f) (Γ_1) OMP3

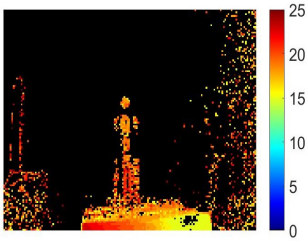

(g) (Γ_1) POMP

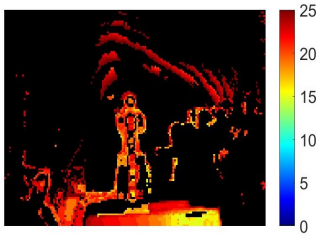

(h) (Γ_1) CMD-OMP

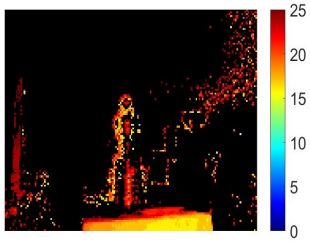

(i) (Γ_2) OMP3

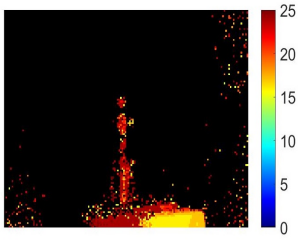

(j) (Γ_2) POMP

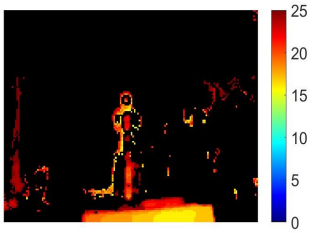

(k) (Γ_2) CMD-OMP

Figure 8.3. The recovered depth images of the transparent bottle using different recovery methods (traditional four-phase method, OMP3, POMP, CMD-OMP) and different super-resolution MFT models (random frequency selection Γ_0, frequency selection optimization Γ_1, frequency and phase-offset selection optimization Γ_2) at a small MD $\Delta T = 54\Delta r$ in scenario E1.

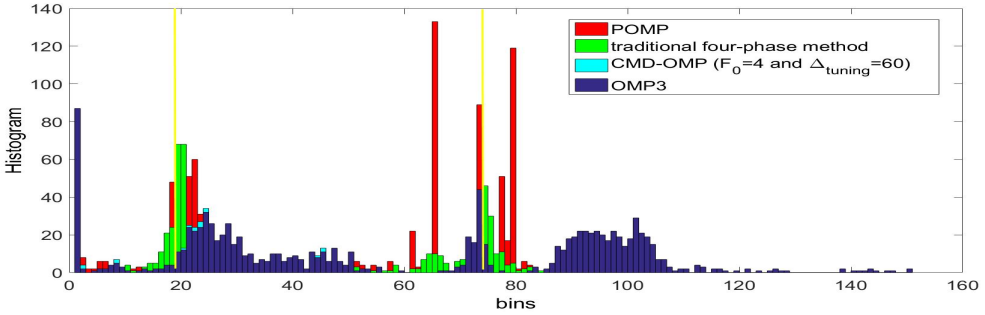

(a) Comparison between reconstruction results of POMP, OMP3, traditional four-phase method and CMD-OMP using the MFT model structured by random frequency selection and zero phase-offsets Γ_0

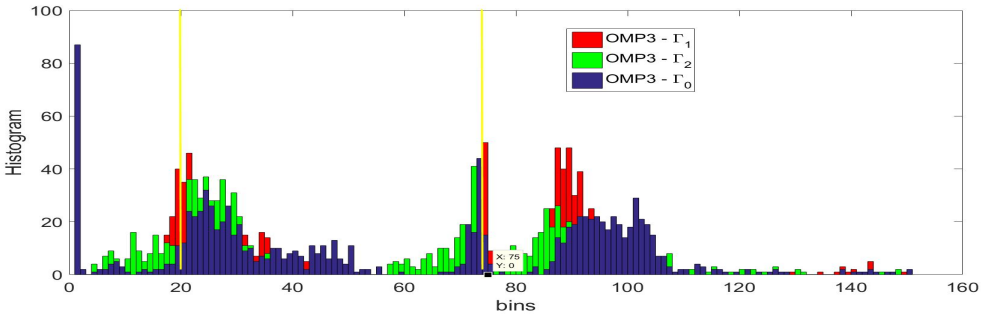

(b) Comparison between reconstruction results of OMP3 using different MFT models structured by Γ_0, Γ_1 and Γ_2

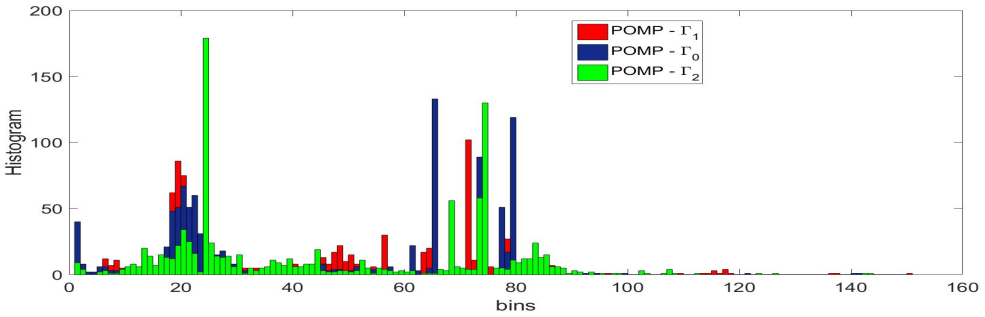

(c) Comparison between reconstruction results of POMP using different MFT models structured by Γ_0, Γ_1 and Γ_2

Figure 8.4. Histogram of the reconstructed support results into the transparent bottle region of different recovery methods (traditional four-phase method, OMP3, POMP, CMD-OMP) using different super-resolution MFT models (random frequency selection Γ_0, frequency selection optimization Γ_1, frequency and phase-offset selection optimization Γ_2) at a small MD $\Delta T = 54\Delta r$ in scenario E1.

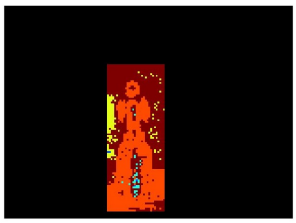

(a) Reflecting property image

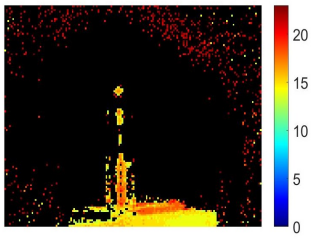

(b) Traditional four-phase method

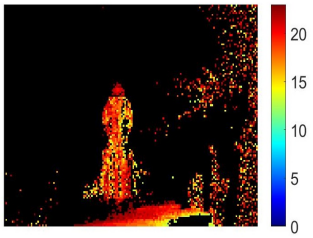

(c) (Γ_0) OMP3

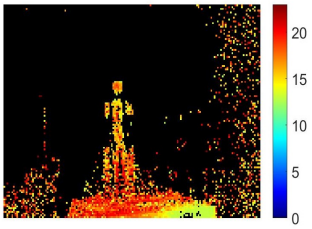

(d) (Γ_0) POMP

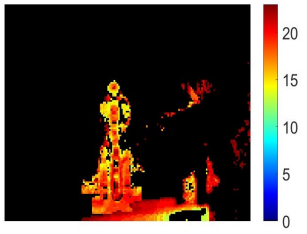

(e) (Γ_0) CMD-OMP

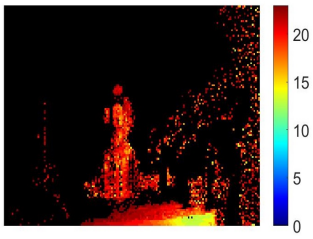

(f) (Γ_1) OMP3

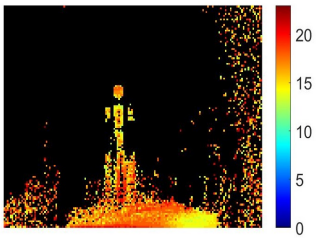

(g) (Γ_1) POMP

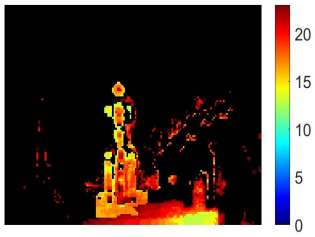

(h) (Γ_1) CMD-OMP

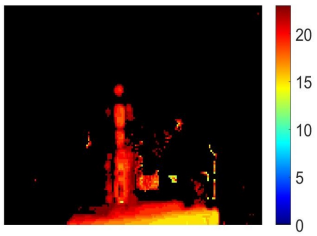

(i) (Γ_2) OMP3

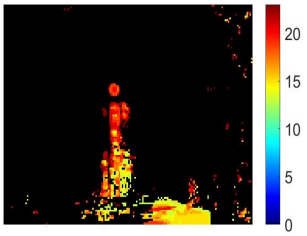

(j) (Γ_2) POMP

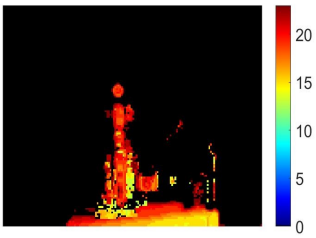

(k) (Γ_2) CMD-OMP

Figure 8.5. The recovered depth images of the transparent bottle using different recovery methods (traditional four-phase method, OMP3, POMP, CMD-OMP) and different super-resolution MFT models (random frequency selection Γ_0, frequency selection optimization Γ_1, frequency and phase-offset selection optimization Γ_2) at a medium MD $\Delta T = 73\Delta r$ in scenario E4.

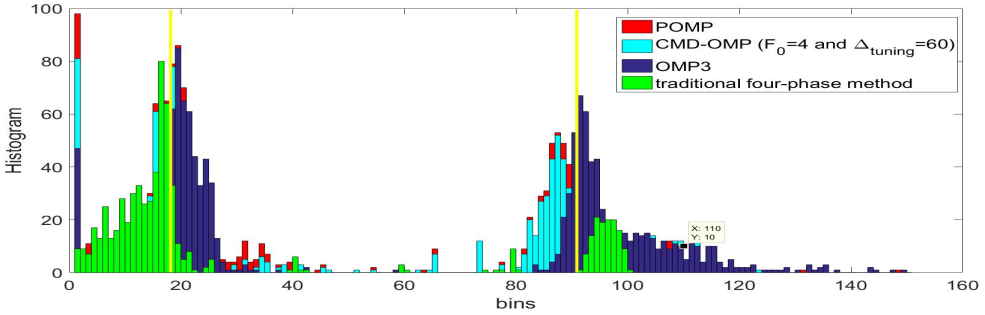

(a) Comparison between reconstruction results of POMP, OMP3, traditional four-phase method and CMD-OMP using the MFT model structured by random frequency selection and zero phase-offsets Γ_0

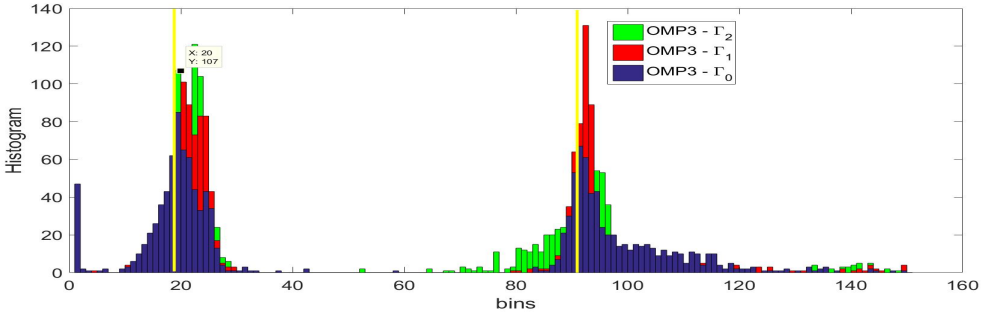

(b) Comparison between reconstruction results of OMP3 using different MFT models structured by Γ_0, Γ_1 and Γ_2

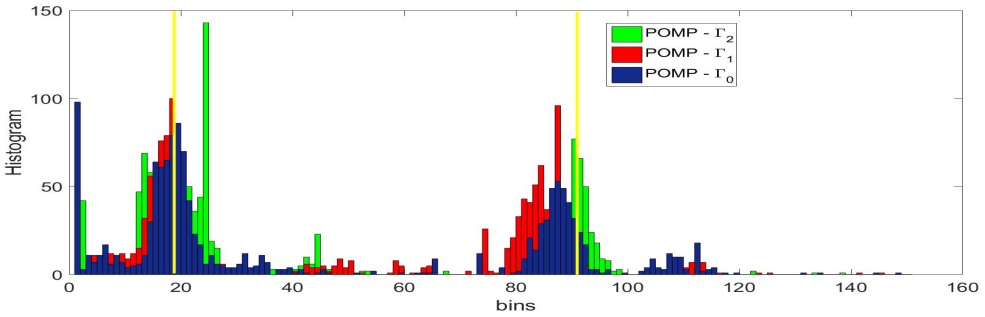

(c) Comparison between reconstruction results of POMP using different MFT models structured by Γ_0, Γ_1 and Γ_2

Figure 8.6. Histogram of the reconstructed support results into the transparent bottle region of different recovery methods (traditional four-phase method, OMP3, POMP, CMD-OMP) using different super-resolution MFT models (random frequency selection Γ_0, frequency selection optimization Γ_1, frequency and phase-offset selection optimization Γ_2) at a medium MD $\Delta T = 73\Delta r$ in scenario E4.

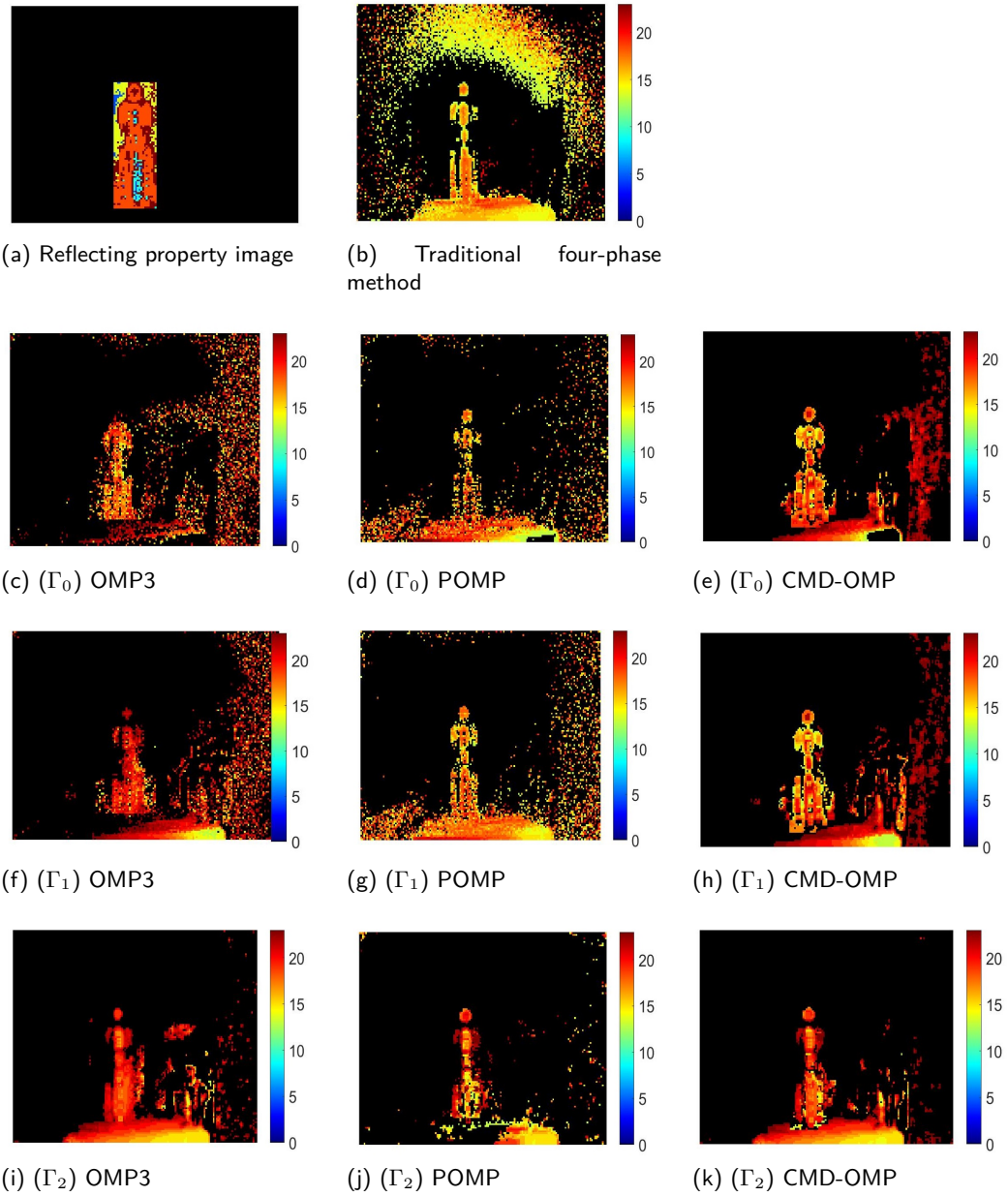

(a) Reflecting property image (b) Traditional four-phase method

(c) (Γ_0) OMP3 (d) (Γ_0) POMP (e) (Γ_0) CMD-OMP

(f) (Γ_1) OMP3 (g) (Γ_1) POMP (h) (Γ_1) CMD-OMP

(i) (Γ_2) OMP3 (j) (Γ_2) POMP (k) (Γ_2) CMD-OMP

Figure 8.7. The recovered depth images of the transparent bottle using different recovery methods (traditional four-phase method, OMP3, POMP, CMD-OMP) and different super-resolution MFT models (random frequency selection Γ_0, frequency selection optimization Γ_1, frequency and phase-offset selection optimization Γ_2) at a large MD $\Delta T = 90\Delta r$ in scenario E8.

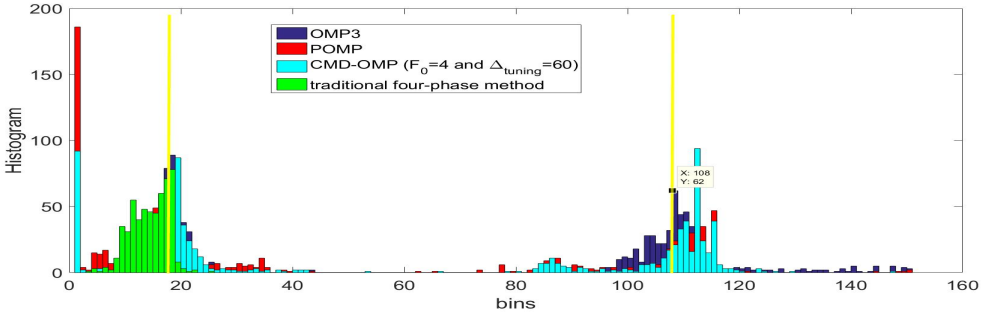

(a) Comparison between reconstruction results of POMP, OMP3, traditional four-phase method and CMD-OMP using the MFT model structured by random frequency selection and zero phase-offsets Γ_0

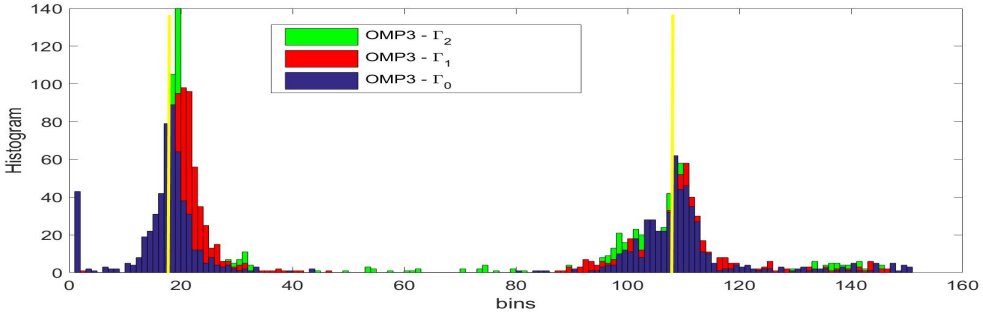

(b) Comparison between reconstruction results of OMP3 using different MFT models structured by Γ_0, Γ_1 and Γ_2

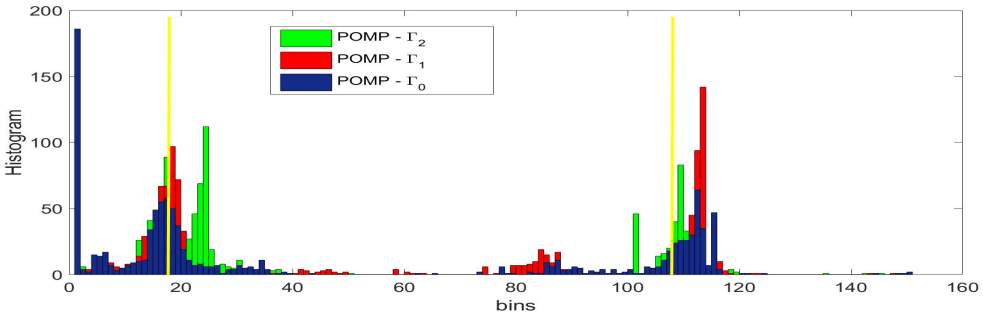

(c) Comparison between reconstruction results of POMP using different MFT models structured by Γ_0, Γ_1 and Γ_2

Figure 8.8. Histogram of the reconstructed support results into the transparent bottle region of different recovery methods (traditional four-phase method, OMP3, POMP, CMD-OMP) using different super-resolution MFT models (random frequency selection Γ_0, frequency selection optimization Γ_1, frequency and phase-offset selection optimization Γ_2) at a large MD $\Delta T = 90\Delta r$ in scenario E8.

8.3.1.3 Scenario E8

Thirdly, the scenario E8 is an example of large MD case. A comparison between the results between Fig. 8.7c and Fig. 8.7d claims that OMP3 outperforms POMP in the case of large MD. Additionally, according to Table 8.2, the count n of OMP3 (518) is significantly higher than that of POMP (250). Furthermore, the similar results of the scenario E9 in Table 8.2 indicate again the better reconstruction performance of OMP3 in such cases of large MDs.

Due to a high coherence of MFT sensing matrix constructed by the randomly chosen frequencies, the reconstruction results of POMP (red part) using the MFT acquisition in Fig. 8.8a are even poorer than those of the traditional four-phase method (green part).

8.3.1.4 Dynamic ranges

Additionally, it can be seen apparently in Table 8.2 that the reconstruction performances of OMP3 and POMP highly depend on the dynamic range in each scenario. In general, POMP outperforms OMP3 in the cases of a small MD. However, as Table 8.2 shows, this strength of POMP only occurs in the cases of a small DR. Whereas, if DR is large, then OMP3 outperforms POMP in most cases of various MDs.

8.3.2 BPIC

BPIC is a l_1 optimization technique with a noise constraint as defined in (3.5). For a further comparison, this method is used for sparse reconstruction based on the available MFT measurement vector and the sensing matrix in nine above scenarios E1-E9. Note that the upper bound ϵ on the noise variance is unknown in these real TOF measurements. In this experiment, we set two different bounds:

$$\epsilon = \frac{||\boldsymbol{y}||_2}{a_{BPIC}} \tag{8.7}$$

where $a_{BPIC} = 5$ or $a_{BPIC} = 10$ for MPI reconstruction using BPIC. The counts n achieved by BPIC in nine scenarios are given in Table 8.3.

A comparison between the results in Table 8.2 and Table 8.3 reveals that BPIC cannot outperform both OMP3 and POMP in all scenarios though this algorithm consumes much computation time for the time profile reconstruction of the entire image. Apparently, it is not an appropriate reconstruction method for a real MFT acquisition. In comparison to the numerical results in Fig. 4.7, it seems possible that the poor performances of BPIC are due to the inaccurate prediction of noise variance.

Table 8.3. Numerical count n of BPIC in nine scenarios E1-E9

Experiment	BPIC ($a_{BPIC} = 5$)			BPIC ($a_{BPIC} = 10$)		
	Small DR	Large DR	Sum	Small DR	Large DR	Sum
E1	53/702	90/378	143/1080	71/702	94/378	165/1080
E2	18/326	67/164	85/490	33/326	44/164	77/490
E3	96/756	122/396	218/1152	103/756	124/396	227/1152
E4	151/958	65/388	216/1346	144/958	78/388	222/1346
E5	172/390	106/250	278/640	139/390	103/250	242/640
E6	231/1308	89/522	320/1830	252/1308	94/522	346/1830
E7	135/750	53/320	188/1070	126/750	50/320	176/1070
E8	142/662	53/430	195/1092	179/662	70/430	249/1092
E9	475/1642	94/742	569/2384	490/1642	123/742	613/2384

8.3.3 Ma-OMP3

Table 8.4 shows the relaxed support recovery rates (count n) of Ma-OMP3. A comparison between the results achieved by OMP3, POMP, and Ma-OMP3 in Table 8.4 and Table 8.2 indicates that Ma-OMP3 outperforms OMP3 and POMP in several cases (E2, E3, E5, E7, E8, E9). However, it cannot outperform POMP in the case a small MD, e.g., E1. These results coincide with the numerical ones in Fig. 4.7.

8.3.4 Supportive affects of LO techniques

As proven by the numerical results in Fig. 4.6 and Fig. 4.7, LO techniques with a small LO range can bring the improvements of reconstruction performances in most cases of various SNRs and MDs. Therefore, in this part, this technique is used to fix the incorrectly estimated indices of OMP3, Ma-OMP3, and POMP. Table 8.4 and Table 8.5 demonstrate the relaxed support reconstruction rates (counts n) of OMP3, Ma-OMP3, and POMP with the support of LO technique. A small LO range of 5 bins is configured for a short searching time.

However, unlike the numerical results, the relaxed support recovery performances of Ma-OMP3 and OMP3 with the support of LO technique become poorer in most scenarios. According to the comparison between the results in the cases of different DRs

Table 8.4. Numerical count n of Ma-OMP3 in nine scenarios E1-E9

Experiment	Ma-OMP3			Ma-OMP3+ LO(5)		
	Small DR	Large DR	Sum	Small DR	Large DR	Sum
E1	28	111	139	71	62	133
E2	137	75	212	139	23	162
E3	128	87	215	129	71	200
E4	380	137	517	409	70	479
E5	263	118	381	255	49	304
E6	384	150	534	434	98	532
E7	363	103	466	346	76	422
E8	354	174	528	336	78	424
E9	633	163	796	644	138	782

Table 8.5. Numerical count n of OMP3 and POMP with the support of LO technique in nine scenarios E1-E9

Experiment	OMP3+ LO(5)			POMP+ LO(5)		
	Small DR	Large DR	Sum	Small DR	Large DR	Sum
E1	27	132	159	173	46	219
E2	77	75	152	27	21	48
E3	47	138	185	163	37	200
E4	413	129	542	241	36	277
E5	248	125	373	126	46	172
E6	454	147	601	272	164	336
E7	347	103	450	208	44	252
E8	348	176	524	234	57	291
E9	626	152	778	500	90	590

in Table 8.2, Table 8.4 and Table 8.5, it seems possible that LO techniques cause bad results in the cases of large DRs.

8.3.5 Summary

The above practical results indicate the following properties of several proposed greedy pursuit methods in a real super-resolution MFT acquisition:

- POMP and OMP3 have their advantages in the cases of different MDs. POMP outperforms OMP3 in the cases of small MDs while OMP3 does inversely in the cases of large MDs. An appropriate selection between them brings potentials for a higher stability of accurate support reconstruction in all scenarios.
- The reflective property of a real transparent object imaging is usually inhomogeneous. A good reconstruction method should guarantee a high performance in all cases of various DRs.
- It is hard to predict the upper bound on noise variance in real TOF measurements accurately. Therefore, BPIC is inefficient for time profile reconstruction with long computation time.
- LO technique only brings a slightly small improvement of support recovery rates in the cases of small DRs. With an inhomogeneous reflectivity property, this atom updating technique seems to be inefficient for fixing the wrongly estimated atoms of OMP3 and Ma-OMP3 in transparent object imaging.

8.4 CMD-OMP

As can be seen in Table.8.2 that OMP3 and POMP possess their advantages at various MDs. In this part, we integrate their strengths through our proposed method CMD-OMP in Algorithm 11 in the above super-resolution MFT acquisition. Similar to Section 4.6, there are four various settings (F_0, Δ_{tuning}) for different variants of CMD-OMP in this analysis. Table.8.6 demonstrates the counts n of four CMD-OMP variants in all 9 scenarios. As can be seen in Table.8.6 that:

- In six cases (E2, E4, E5, E6, E7, E8, E9), the CMD-OMP variant with the setting (4, 84) brings the best recovery performances among four variants. These good results are due to that this variant of CMD-OMP selects OMP3 as the prerequisite reconstruction algorithm.
- Inversely, the CMD-OMP variant with the setting (10, 60) brings the best performance among four variants in two remaining scenarios E1 and E3. This variant of CMD-OMP uses POMP the most frequently.

Table 8.6. Numerical count n of CMD-OMP variants with different settings

Experiment	$F_0 = 4$		$F_0 = 10$	
	$\Delta_{tuning} = 60$	$\Delta_{tuning} = 84$	$\Delta_{tuning} = 60$	$\Delta_{tuning} = 84$
E1	196	148	291	156
E2	118	118	86	117
E3	226	155	224	152
E4	407	529	393	518
E5	229	371	164	373
E6	391	594	415	594
E7	226	417	218	354
E8	257	370	246	273
E9	600	736	588	595

As explained previously, CMD-OMP only uses up the strengths of POMP and OMP3. And hence its recovery results lie somewhere between those of two these member methods. Therefore, it can be seen apparently in Fig.8.3e, Fig.8.5e and Fig.8.7e that CMD-OMP cannot outperform POMP in the cases of small MDs or OMP3 in the cases of large ones. Apparently, CMD-OMP is an efficient reconstruction method for a complex scattering scene comprising many different cases of MPIs with various MDs. Whereas, if either OMP3 or POMP is used individually for the MPI reconstruction of this scene, the achieved results are good at some pixels but inversely poor at other ones. CMD-OMP variants bring the balanced results to guarantee a higher stability of accurate MPI reconstruction.

8.5 Frequency and phase-offset selection optimization

So far, the TOF measurements are carried out with the set $\Gamma_0 = (H_0, J_0)$ of 20 random frequencies (H_0) and zero phase-offsets ($J_0 = 0$). As mentioned in Section 5.3.2, the proposed frequency selection optimization method in Algorithm 12 explored the optimized set of frequencies $H_{opt,1}$ which constructs a more highly incoherent MFT sensing matrix $\mathbf{\Phi}_1$. This matrix can be inferred from the dictionary matrix through the set of frequencies $H_{opt,1}$ and zero phase-offsets J_0. Set $\Gamma_1 = (H_{opt,1}, J_0)$.

Furthermore, the optimized sets of frequencies and phase-offsets $\Gamma_2 == (H_{opt,2}, J_{opt,2})$

have been found in Section 5.3.2 through the proposed frequency and phase-offset selection optimization method in Algorithm 13. These sets are promising for constructing a MFT sensing matrix $\mathbf{\Phi}_2 \in \mathbb{R}^{20\times 200}$ with a better coherence histogram, in comparison to $\mathbf{\Phi}_1$ (Γ_1). The matrix is similarly inferred from the dictionary matrix $\mathbf{\Phi}_0$, according to the set Γ_2.

As proven in the numerical results in Fig. 5.8 and Fig. 5.9, two MFT acquisitions $\mathbf{\Phi}_1$ and $\mathbf{\Phi}_2$ can bring better support recovery performances of a CS algorithm. Thus, this part aims to carry out the real MFT experiments to strengthen these arguments. In particular, we collect TOF measurements at the frequency set $H_{opt,1}$ with zero phase-offsets as well as the frequency set $H_{opt,2}$ with non-zero phase-offsets $J_{opt,2}$ for nine scenarios E1-E9. At each scenario, there are two available measurement vectors $\boldsymbol{y}_1$ ($\mathbf{\Phi}_1$) and $\boldsymbol{y}_2$ ($\mathbf{\Phi}_2$). Note that for the generation of a TOF measurement with a non-zero phase-offset, we use an external pulse generator (Agilent 81150A) to shift the phase of the transmitted optical signal.

Based on the achieved measurement vectors and the corresponding sensing matrix $\mathbf{\Phi}_1$ or $\mathbf{\Phi}_2$, three algorithms OMP3, POMP and CMD-OMP resolve MPIs with a known sparsity $K = 2$. The achieved relaxed support recovery rates with $\delta = 2$ or the count n for both two MFT acquisitions are given in Table 8.7. The recovered depth images of the transparent bottle using three methods in the scenarios E1, E4 and E8 are demonstrated in the third and fourth rows of Fig. 8.3, Fig. 8.5 and Fig. 8.7 respectively. For a further comparison between three MFT acquisitions, their reconstruction histograms are shown in Fig. 8.4b, Fig. 8.6b and Fig. 8.8b for OMP3 and in Fig. 8.4c, Fig. 8.6c and Fig. 8.8c for POMP.

As can be seen in Fig. 8.3c, Fig. 8.3f and Fig. 8.3i that the depth images of the bottle recovered by OMP3 using the optimized sets Γ_1 and Γ_2 look more robust than those using the random set Γ_0 in the case E1 of a small MD. Moreover, these results are even better than those of the traditional four-phase method in Fig. 8.3b. Besides, two these optimized MFT acquisitions bring the similar improvement of reconstruction performance of POMP in the case E8 of a large MD (see Fig. 8.7c, Fig. 8.7f and Fig. 8.7i). Apparently, MFT acquisition with the optimized set of frequencies or phase-offsets reconstructs MPI more efficiently, compared to the traditional phase-stepping acquisition.

In scenario E4, there is no significant difference between the recovered bottle depth images of all three MFT acquisitions in Fig. 8.5c, Fig. 8.5f and Fig. 8.5i. Whereas, the reconstruction histograms of OMP3 (see Fig. 8.6b) and POMP (see Fig. 8.6c) using the optimized sets Γ_1 and Γ_2 stay more densely around the yellow line r_2. From this result, two MFT acquisitions $\mathbf{\Phi}_1$ and $\mathbf{\Phi}_2$ apparently bring the more accurate reconstruction of the wall. Inversely, according to the reconstruction histograms of OMP3 and POMP (see Fig. 8.4b and Fig. 8.4c in the scenario E1 and see Fig. 8.8b and Fig. 8.8c in the scenario E8), two these MFT acquisitions bring the more accurate reconstruction of the bottle in two other scenarios.

Moreover, a probabilistic comparison between the counts n in Table 8.7 and Table 8.2

Table 8.7. Numerical count n of OMP3 and POMP using the frequency or phase-offset optimization.

Experiment	Γ_1		Γ_2	
	OMP3	POMP	OMP3	POMP
E1	281	343	192	272
E2	236	134	200	194
E3	385	396	424	297
E4	647	316	520	435
E5	386	139	332	294
E6	572	403	688	590
E7	510	247	595	510
E8	448	302	573	362
E9	786	635	1172	860

indicates that both Γ_1 and Γ_2 can bring higher support recovery performances of both OMP3 and POMP in all scenarios, compared to the random set Γ_0. Nevertheless, there are a few exceptional cases where the counts n of either OMP3 or POMP become lower, e.g., E4, E5, E6 with Γ_1 or E4, E5 with Γ_2. It seems to be possible that these occasionally poor results are due to the optimization errors between the simulation and practical results. Notably, the practical and numerical dictionary matrices do not coincide since the harmonic components of the real TOF cross-correlation function differ from those of the numerical ones in (3.41), especially at high modulation frequencies.

In summary, both two above optimization methods show their capabilities for designing the optimized super-resolution MFT acquisition. Concretely, they apparently bring higher support recovery performances of both OMP3 and POMP in most cases of various MDs, compared with the previous random sets of frequencies and phase-offsets Γ_0. From these results, the proposed CMD-OMP method also inherits some benefits from these improvements. As can be seen in Fig. 8.3h, Fig. 8.5h and Fig. 8.7h using the MFT acquisition $\mathbf{\Phi}_1$ or Fig. 8.3k, Fig. 8.5k and Fig. 8.7k using the MFT acquisition $\mathbf{\Phi}_2$ that the recovered depth images of the transparent bottle using CMD-OMP acquire a higher accuracy.

Besides, as proven through the numerical results in Fig. 5.9, the optimized set of frequencies and phase-offsets Γ_2 with a more highly incoherent sensing matrix $\mathbf{\Phi}_2$ is promising to bring better reconstruction results, compared with the MFT acquisition using only the frequency optimization method Γ_1. However, according to Table 8.7,

the counts n of OMP3 or POMP using the MFT acquisition $\mathbf{\Phi}_2$ are lower in many cases of small and medium MDs (E1-E5). It seems to be possible that the occasionally poorer performances of Γ_2 are due to mismatch errors between the numerical and real dictionary matrices as explained before. Whereas, in the cases of large MDs (E6-E9), the MFT acquisition $\mathbf{\Phi}_2$ is apparently a more efficient measurement scheme with higher counts n of both OMP3 and POMP. In summary, under the probabilistic evaluation, the frequency and phase shift optimization method apparently brings a better design of a practical super-resolution MFT acquisition. These results would become significantly better if the real dictionary matrix coincides with the theoretical one.

8.6 SMF and joint multiple-frequency calibration

As mentioned in Chapter 7, a TOF camera system should modulate and demodulate simultaneously multiple-frequency parts for a real SMF measurement. However, the hardware design for such implementation, similar to the studies of Payne et al. [29], is significantly complicated and still under our investigation. In this part, we carry out the joint multiple-frequency calibration technique which have been proposed in Section 7.4. Its operating principle is similar to a multiple-SMF acquisition with the optimization of the projection matrix. Therefore, this technique is considered as a temporary way to prove the effectiveness of a multiple-SMF acquisition in resolving MPI problem.

As proven through the numerical results in Section 7.4, this technique is only useful if the measurement noise is considerably low. Whereas, TOF measurements of a commercial PMD camera at high modulation frequencies are highly noisy and less reliable with low demodulation contrast [4]. Therefore, only TOF measurements with frequencies up to 15 MHz are carried out in this experiment to ensure low measurement noises. Since the refinement factor remains with $F = 100$, decreasing the highest modulation frequency causes no significant difference, apart from a larger grid length. Thus, the achieved results acquire good demonstration but do not lose the generality.

In this experiment, there are five scenarios B1-B5 with different MDs as listed in Table 8.8. According to the operating principle of joint multiple-frequency calibration technique in Section 7.4, we carry out 57 TOF measurements from 1 MHz to 15 MHz with a phase step of 0.5 MHz to construct the measurement vector $\boldsymbol{y}_0$ sharing a dictionary matrix $\mathbf{\Phi}_{0,2}$ for each scenario. Note that the practical dictionary matrix $\mathbf{\Phi}_{0,2}$ is picked from the above dictionary matrix $\mathbf{\Phi}_0$ with the same parameters $N = 200, L = 5$. However, for maintaining $F = 100$ with $f_{max} = 15$ MHz, we set a grid spacing to 10 cm ($\Delta r = 10$ cm). Note that the range $[r_1 - 5\Delta r, r_1 + 5\Delta r]$ is still applied for the recovered depth image of the transparent bottle and the count n comprises all estimated atom indices in $[r_1 - 2\Delta r, r_1 + 2\Delta r]$ or $[r_2 - 2\Delta r, r_2 + 2\Delta r]$, similar to the previous experiments.

Notably, the real dictionary matrix $\mathbf{\Phi}_{0,2}$ is different from the numerical one in Section 7.3. Therefore, we run the projection matrix optimization method in Algorithm. 20

Table 8.8. SMF model : five scenarios with different MDs, $f_{max} = 15$ MHz, F=100, $\Delta r = 10$ cm

Experiments	r_1	r_2	$r_2 - r_1$
B1	1m ($10\Delta r$)	5.5m ($55\Delta r$)	4.5m ($45\Delta r$)
B2	1.8m ($18\Delta r$)	5.5m ($55\Delta r$)	3.7m ($37\Delta r$)
B3	1.6m ($16\Delta r$)	4.3m ($43\Delta r$)	2.7m ($27\Delta r$)
B4	1.1m ($11\Delta r$)	4.6m ($46\Delta r$)	3.5m ($35\Delta r$)
B5	0.8m ($8\Delta r$)	3.7m ($37\Delta r$)	2.9m ($29\Delta r$)

on this real dictionary matrix $\boldsymbol{\Phi}_{0,2}$ to find five optimized real projection matrices $\hat{\boldsymbol{P}}_1$ - $\hat{\boldsymbol{P}}_5$ with different setting parameters as listed in Table 7.1. Additionally, an optimized integer projection matrix $\hat{\boldsymbol{P}}_6$ with the setting parameters $M = 20$ and $h = 3$ is also explored for a further comparison. Subsequently, at each scenario, the measurement vector $\boldsymbol{y}_0$ is converted to several calibration vectors $\boldsymbol{z}$ through the calibration process in (7.12) with six different projection matrices $\hat{\boldsymbol{P}}_1$ - $\hat{\boldsymbol{P}}_6$. Based on these calibration vectors, the sparse time profile of MPIs (transparent bottle and opaque wall) is then recovered by POMP and OMP3 in five scenarios B1-B5. The achieved counts n are given in Table 8.9 and Table 8.10 respectively.

Table 8.9. The count n of POMP with different settings of joint multiple-frequency calibration

	POMP						
Experiment	$\boldsymbol{\Phi}_{0,2}$	$\hat{\boldsymbol{P}}_1$	$\hat{\boldsymbol{P}}_2$	$\hat{\boldsymbol{P}}_3$	$\hat{\boldsymbol{P}}_4$	$\hat{\boldsymbol{P}}_5$	$\hat{\boldsymbol{P}}_6$
B1	366	276	265	338	334	373	283
B2	191	94	174	158	191	207	143
B3	224	145	137	189	199	131	135
B4	506	441	407	500	365	301	437
B5	555	482	414	666	448	404	793

Table 8.10. The count n of OMP3 with different settings of joint multiple-frequency calibration

Experiment	OMP3						
	$\boldsymbol{\Phi}_{0,2}$	$\hat{\boldsymbol{P}}_1$	$\hat{\boldsymbol{P}}_2$	$\hat{\boldsymbol{P}}_3$	$\hat{\boldsymbol{P}}_4$	$\hat{\boldsymbol{P}}_5$	$\hat{\boldsymbol{P}}_6$
B1	123	376	261	416	390	276	190
B2	43	152	186	163	225	196	74
B3	31	220	161	213	207	171	45
B4	223	664	429	606	507	407	264
B5	123	736	479	881	570	985	428

According to Table 8.9, the counts n of POMP after the joint multiple-frequency calibration with different settings are lower than those based on the MFT acquisition $\boldsymbol{\Phi}_{0,2}$ before the calibration. The enhanced noise variance causes these poor reconstruction results of the calibration technique. These practical results coincide with the numerical ones in Fig. 7.11a. Whereas, OMP3 apparently brings a better support recovery performance after the calibration in all scenarios.

Besides, the comparison between the reconstruction results of OMP3 after many different calibrations in Table 8.10 reveals that:

- Compared to $\hat{\boldsymbol{P}}_1$, the calibration with $\hat{\boldsymbol{P}}_2$ with a larger row sparsity brings poorer reconstruction results of OMP3. It seems to be possible that these poor performances of $\hat{\boldsymbol{P}}_2$ is due to the enhanced noise variance. Whereas, a smaller row sparsity ($h = 3$) in $\hat{\boldsymbol{P}}_6$ can restrict the enhancement of the noise but not enhance the incoherence of the calibration matrix $\boldsymbol{\Phi}$. As a result, the reconstruction results after the calibration with $\hat{\boldsymbol{P}}_6$ are poorer than those with $\hat{\boldsymbol{P}}_1$ in all scenarios. Eventually, an appropriate value of h should be chosen carefully for the joint multiple-frequency calibration to bring the highest reconstruction performance of OMP3.

- The comparison between the counts n of OMP3 after the calibrations $\boldsymbol{P}_4$ and $\boldsymbol{P}_1$ reveals that a larger amount of the projection matrix rows does not guarantee the improvement of reconstruction quality in all scenarios.

- Whereas, there is no significant difference between the counts n of OMP3 after the calibrations using the real-valued projection matrix $\hat{\boldsymbol{P}}_3$ and the integer one $\hat{\boldsymbol{P}}_1$.

Furthermore, the strengths of joint multiple-frequency calibration are also demonstrated through the recovered depth image of the transparent bottle using OMP3 in

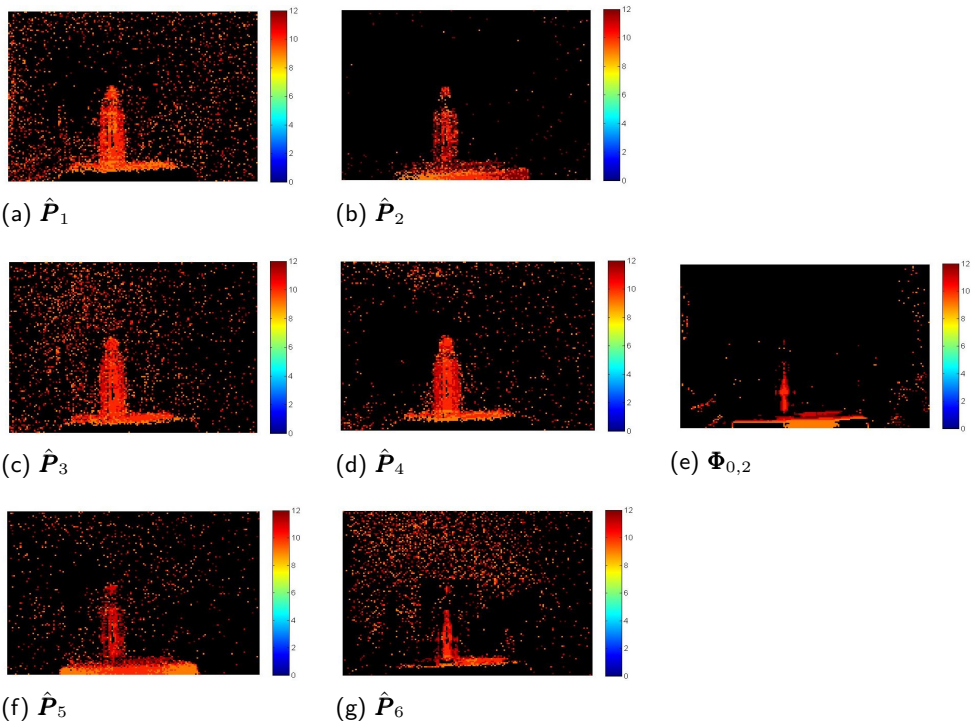

(a) $\hat{\boldsymbol{P}}_1$ (b) $\hat{\boldsymbol{P}}_2$ (c) $\hat{\boldsymbol{P}}_3$ (d) $\hat{\boldsymbol{P}}_4$ (e) $\boldsymbol{\Phi}_{0,2}$ (f) $\hat{\boldsymbol{P}}_5$ (g) $\hat{\boldsymbol{P}}_6$

Figure 8.9. Joint multiple frequency calibration: the recovered depth images of transparent bottle using OMP3 in scenario B1.

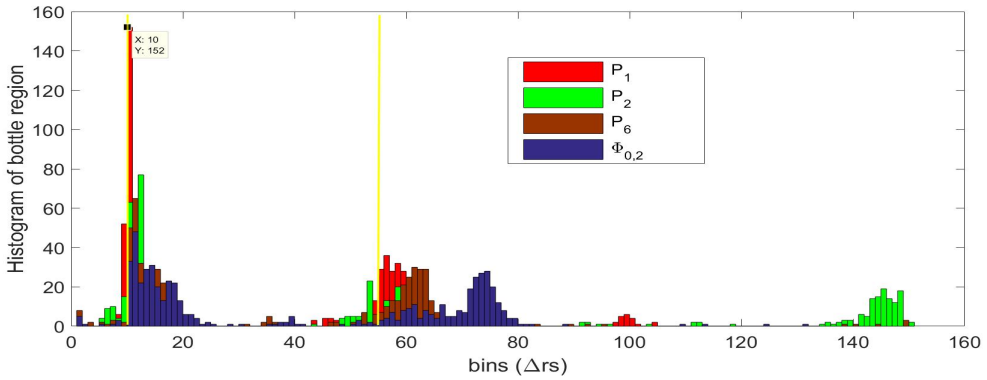

(a) Different row sparsity values

Figure 8.10. The joint multiple frequency calibration: the histogram of reconstruction results using OMP3 in scenario B1.

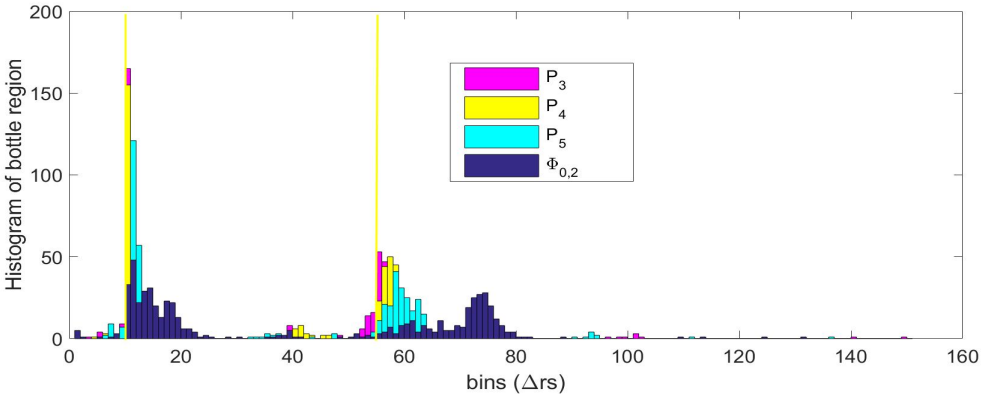

(b) Other settings of calibration matrix

Figure 8.10. The joint multiple frequency calibration: the histogram of reconstruction results using OMP3 in scenario B1 (cont).

scenario B1 in Fig. 8.9. After the calibration with $\hat{\boldsymbol{P}}_1$, $\hat{\boldsymbol{P}}_3$ and $\hat{\boldsymbol{P}}_4$, the depth images of the bottle region are reconstructed more accurately although MD in this scenario is medium ($\Delta T = 45\Delta r$). Additionally, as can be seen in Fig. 8.10, the reconstruction histograms of the reconstruction results in scenario B1 after the calibration technique stay more densely around the yellow reference lines which represent the actual depths of the bottle and the wall.

In summary, the joint multiple-frequency calibration technique based on multiple less noisy TOF measurements brings higher recovery performances of OMP3. Through these practical results and the numerical results in Section 7.3, we can insist that a SMF model is apparently efficient to enhance the stability of a good relaxed support recovery in a large refinement factor configuration. Therefore, if we can develop a practical TOF camera system in the future for real SMF measurements, the time profile of near-distant MPIs will be reconstructed successfully even though SMF measurements contain only low-frequency parts.

8.7 Summary

This chapter carried out several practical experiments to realize a MFT acquisition through our ZESS Multicam camera. Two MPIs are set up through the transparent bottle imaging. However, this setup apparently causes more than two MPIs because of the complex scattering properties of the bottle. This scenario is a good example of a real scattering scene where the number of MPIs or the signal sparsity is hard to predict accurately. Therefore, the practical results achieved through this transparent object

imaging guarantee not only the confidentiality of our numerical analysis but also the effectiveness of a MFT acquisition in real scattering scenes. Apparently, we can resolve two largest-magnitude MPIs though the sparse reconstruction suffers from the wrong prediction of sparsity information.

Besides, the reconstruction of MPI time profile in our practical experiments suffers from the inappropriate hardware design. Typically, we use our Multicam system for acquiring a depth image through the traditional four-phase algorithm. Thus, this system cannot produce a robust TOF correlation measurement at a high frequency with a high demodulation contrast. In our experiments, we concerned about the saturation problem and hence cannot set a long exposure time for each TOF measurement. Moreover, the mismatch model errors caused by the inaccurate construction of dictionary matrix also present significant challenges. For these reasons, we only verified the reconstruction results under the accuracy bound of 25 cm. In the future, we aim to develop a new type of TOF camera for acquiring a TOF or SMF correlation measurement more accurately.

According to the above practical results, POMP and OMP3 have their advantages in a super-resolution MFT acquisition in the cases of various MDs. POMP outperforms at small MDs, but inversely OMP3 does at large ones. The proposed method CMD-OMP is an efficient solution to guarantee the high stability of a good support recovery. Besides, the experimental and numerical results indicated that CMD-OMP even outperforms the l_1-optimization method in a super-resolution CS problem.

Additionally, the proposed frequency and phase-offset selection optimization method is capable of designing super-resolution MFT sensing matrices with higher incoherence. In other words, these MFT acquisitions, i.e., $\mathbf{\Phi}_1$ and $\mathbf{\Phi}_2$ in Section. 8.5, bring better reconstruction results of many different algorithms, e.g., OMP3, POMP. Despite mismatch model errors between the practical and numerical dictionary matrices, the advantages of the optimization methods can be apparently demonstrated through practical results, similar to the numerical ones in Section 5.3.

Finally, we carried out successfully the joint multiple-frequency calibration by a real TOF camera. The achieved results coincide with the numerical results in Section 7.4. Apparently, this calibration technique enhances the stability of a good relaxed support recovery using OMP3. However, such high performance only occurs when the sparse reconstruction of OMP3 relies on the less noisy measurements. Whereas, it seems to be possible that the poor performances of POMP are due to the enhanced noise variance after the calibration process. Apparently, this technique is only an alternative way to demonstrate the capabilities of a multiple-SMF acquisition in resolving near-distant MPIs. Our goal in the future is to build up a TOF camera system for acquiring real SMF measurements. We expect to resolve MPIs with a high depth accuracy and depth resolution through a real multiple-SMF model comprising only low-frequency parts.

9 Conclusion

MPI is currently a crucial issue that causes inaccuracies of the depth estimation in a commercial CW-TOF camera. This thesis introduced a MFT acquisition to resolve the MPIs through a CS model. In a conventional grid system configuration ($F = 1$), the reconstruction of MPI time profile is accurate with a high probability and requires only a few of TOF measurements. However, this model with low-frequency measurements leads to a large grid spacing system, e.g., 30 MHz is equivalent to a spatial grid length of 5 m. Eventually, it cannot be applied to a real-life scene since the depth accuracy and resolution are significantly low. More concisely, the accurate localization of near targets seems to be impossible. Therefore, an increase of TOF modulation frequency is an essential task in the development of a TOF camera for a real MFT acquisition. Nevertheless, the hardware design for such frequency increase is extremely complicated with the current technology.

Without hardware updates, the super-resolution CS technique is an efficient approach for solving the above high-frequency problems through a grid refinement process. However, this technique causes poor sparse reconstruction performances because the super-resolution MFT sensing matrix is highly coherent. Therefore, the high stability of a perfect support recovery is hard to maintain in such a large-refinement-factor configuration. In this thesis, we introduced a relaxed metric to gauge the reconstructed support more accurately. From this point, we improved the relaxed support recovery performance in a super-resolution MFT acquisition at $F = 100$ by optimizing the MFT sensing matrix design and using the appropriate super-resolution CS reconstruction methods. We tried to not only reduce mismatch model errors but also obtain a high relaxed super-resolution factor. More concisely, the localization of near targets becomes accurate with a tolerance offset. This offset denotes the depth accuracy requirement of a TOF application.

9.1 Super-resolution compressed sensing algorithms

In this thesis, we proposed three greedy pursuit methods, i.e., OMP3, POMP, and Ma-OMP3. These algorithms can guarantee a moderate stability of an accurate support recovery in a MFT acquisition with the configuration of a large refinement factor as well as maintain a high frame-rate. But, they require a predicted sparsity of the observed scene. Interestingly, three above methods have their various advantages in some cases of different MDs. More precisely, POMP and Ma-OMP3 outperform at small MDs while OMP3 inversely does at large ones. Their reconstruction capabilities have been proven

through numerical and practical experiments. From these results, we proposed a new method CMD-OMP to use up these strengths. In particular, CMD-OMP predicts the MD in a scenario and then select POMP or OMP3 for a good support recovery in an appropriate case. Under a probabilistic evaluation, this integration method outperforms the individual ones, i.e., OMP3 and POMP and even some available super-resolution CS algorithms, e.g., BLOOMP, BPIC, SURE-IR. On the other hand, CMD-OMP consumes a short computation time and hence is potential for a high frame-rate reconstruction. In the future, the member algorithms, i.e., OMP3 and POMP can be replaced by other methods which bring better recovery performances in some cases of specific MDs. Therefore, our future research aims to explore such new algorithms to enhance the reconstruction quality of CMD-OMP.

Moreover, the thesis also introduced MMV techniques and some modified variants of OMPMMV to enhance the quality of the reconstruction results in a super-resolution MFT acquisition. Their strengths have been demonstrated through the numerical experiments in Section 6.5. However, these MMV techniques require high hardware design complexity for acquiring multiple polarization data in a TOF acquisition. Thus, a new TOF camera system for multi-polarized light modulation and demodulation is currently under our investigation.

9.2 Super-resolution MFT sensing matrix design

Several various CS techniques have been applied in this thesis for optimizing the structure of a super-resolution MFT sensing matrix with the higher incoherence.

Firstly, we proposed the frequency and phase-offset selection optimization method. Through the numerical and practical experiments, this technique successfully explored an optimized set of frequencies and phase-offsets which can structure a super-resolution MFT sensing matrix with a smaller coherence cost. Through this acquisition, the support reconstruction performances of both OMP3 and POMP are improved. Especially, this technique is flexible to apply for any parameter settings (N, M).

Secondly, we introduced a multiple-SMF acquisition which has been proven through the numerical experiments to enhance the incoherence of the sensing matrix through the projection matrix optimization method. Through this property, the multiple-SMF acquisition can bring higher support recovery performances of any reconstruction algorithms. Their achieved reconstruction results are apparently better than those achieved by the frequency and phase-offset selection optimization method. Nevertheless, a real SMF measurement is complicated to acquire through a commercial CW-TOF camera. Thus, we used the joint multiple-frequency calibration in the practical experiments to demonstrate the effectiveness of a real multiple-SMF acquisition successfully. To be concrete, according to the results in Section. 8.6, this calibration technique can improve the reconstruction quality of OMP3 in a super-resolution CS problem.

9.3 Relaxed super-resolution factor

According to the numerical results of a multiple-SMF acquisition using MMV model in Fig. 7.9, the high stability of an accurate target localization with a tolerance offset can be guaranteed even in noisy environments (SNR = 20 dB). In particular, this type of acquisition with a large refinement factor $F = 100$ has the following properties:

- About 70% atoms separated by a small MD of $10\Delta r$ are localized accurately with an accuracy offset of $2\Delta r$. This rate can be increased up to 90% if target separation is larger than $30\Delta r$.
- For a larger accuracy offset of $5\Delta r$ or a looser depth accuracy requirement, about 95% atoms are localized accurately in all cases of various MDs $\Delta T \geq 2\delta{+}1 = 11\Delta r$.

Typically, if $f_{max} = 30$ MHz, then the depth accuracy and resolution are 5 m in a conventional MFT acquisition. We wish to increase the modulation frequency of a TOF camera system, but the hardware design for such an increase is significantly complicated. Therefore, from the above results, a relaxed super-resolution factor can be achieved through our proposed super-resolution CS techniques. More precisely, our techniques can increase the depth resolution of MPI reconstruction up to a few tens of cms. Whereas, these properties in numbers are still improved linearly through the future development of a TOF camera with a higher modulation-frequency modulation and demodulation. For instance, if $f_{max} = 300$ MHz, then the relaxed depth resolution could reach up to a few cms. In summary, our relaxed super-resolution CS techniques in this thesis are efficient to resolve near-distant MPIs through a low-cost CW-TOF camera with short acquisition and computation time. On the other hand, some of these solution approaches are also useful for many other CS applications sharing a DFT sensing matrix, e.g., target localization through radar processing, high-frequency component extraction from low-frequency samples.

A Appendix

A.1 Derivative of E(f_i) w.r.t. f_i

$$\nabla E_{f_i} = \frac{\partial E}{\partial f_i} \tag{A.1}$$

$$= \frac{\partial}{\partial f_i} \sum_{q_1=1, q_1 \neq q_2}^{N} \sum_{q_2=1}^{N} c_{q_1 q_2} c^*_{q_1 q_2} \tag{A.2}$$

$$= \sum_{q_1=1, q_1 \neq q_2}^{N} \sum_{q_2=1}^{N} \frac{\partial}{\partial f_i} c_{q_1 q_2} c^*_{q_1 q_2} \tag{A.3}$$

$$= \sum_{q_1=1, q_1 \neq q_2}^{N} \sum_{q_2=1}^{N} \Delta E_{q_1, q_2, f_i} \tag{A.4}$$

where

$$\begin{aligned} \Delta E_{q_1, q_2, f_i} &= \frac{\partial}{\partial f_i} c_{q_1 q_2} c^*_{q_1 q_2} \\ &= c_{q_1 q_2} \frac{\partial c^*_{q_1 q_2}}{\partial f_i} + \frac{\partial c_{q_1 q_2}}{\partial f_i} c^*_{q_1 q_2} \\ &= c_{q_1 q_2} \Delta c^*_{q_1 q_2, f_i} + \Delta c_{q_1 q_2, f_i} c^*_{q_1 q_2} \end{aligned} \tag{A.5}$$

and

$$c_{q_1 q_2} = \frac{\sum_{p=1}^{m} \phi_{p q_1} \phi^*_{p q_2}}{||\boldsymbol{\phi}_{q_1}||_2 ||\boldsymbol{\phi}_{q_2}||_2} \tag{A.6}$$

where $\boldsymbol{\phi}_q$ is the q^{th} column of the sensing matrix $\boldsymbol{\Phi}$.

Then set

$$u_{q_1, q_2} = \sum_{p=1}^{m} \phi_{p q_1} \phi^*_{p q_2} \tag{A.7}$$

and

$$v_{q_1, q_2} = ||\boldsymbol{\phi}_{q_1}||_2 ||\boldsymbol{\phi}_{q_2}||_2 \tag{A.8}$$

From (A.6):

$$\Delta c_{q_1 q_2, f_i} = \frac{\partial c_{q_1 q_2}}{\partial f_i} = \frac{\Delta u_{q_1,q_2,f_i} v_{q_1,q_2} - u_{q_1,q_2} \Delta v_{q_1,q_2,f_i}}{v_{q_1,q_2}^2} \tag{A.9}$$

where

$$\Delta u_{q_1,q_2,f_i} = \frac{\partial}{\partial f_i} \sum_{p=1}^{m} \phi_{pq_1} \phi_{pq_2}^* \tag{A.10}$$

and

$$\Delta v_{q_1,q_2,f_i} = \frac{\partial ||\boldsymbol{\phi}_{q_1}||_2}{\partial f_i} ||\boldsymbol{\phi}_{q_2}||_2 + ||\boldsymbol{\phi}_{q_1}||_2 \frac{\partial ||\boldsymbol{\phi}_{q_2}||_2}{\partial f_i} \tag{A.11}$$

A.1.1 Computation of $\Delta u_{i,q_1,q_2}$

Only the element ϕ_{iq} contains the frequency variable f_i so only its derivative respect to f_i is non-zero:

$$\frac{\partial(\phi_{pq})}{\partial f_i} = \begin{cases} \sum_{l=-L}^{L} c_l d_l^* (-j2\pi l q \Delta t) e^{-j2\pi l f_i q \Delta t + j l \tau_i} & \text{if } p = i \\ 0 & \text{if } p \neq i \end{cases} \tag{A.12}$$

Set $\gamma_{q,f_i} = \sum_{l=-L}^{L} c_l d_l^* (-j2\pi l q \Delta t) e^{-j2\pi l f_i q \Delta t + j l \tau_i}$ and then replace (A.12) into (A.10):

$$\Delta u_{i,q_1,q_2} = \gamma_{q_1,f_i} \phi_{iq_2}^* + \phi_{iq_1} \gamma_{q_2,f_i}^* \tag{A.13}$$

A.1.2 Computation of $\Delta v_{i,q_1,q_2}$

Set:

$$\begin{aligned} \Upsilon_{i,q} &= \frac{\partial ||\boldsymbol{\phi}_q||_2}{\partial f_i} \\ &= \frac{\partial \sqrt{\sum_{p=1}^{m} \phi_{pq} \phi_{pq}^*}}{\partial f_i} \\ &= \frac{\partial \sqrt{u_{q,q}}}{\partial f_i} \\ &= \frac{\Delta u_{i,q,q}}{2\sqrt{u_{q,q}}} \\ &= \frac{\Delta u_{i,q,q}}{2||\boldsymbol{\phi}_q||_2} \end{aligned} \tag{A.14}$$

Replace (A.13) into (A.14):

$$\Upsilon_{i,q} = \frac{\gamma_{q,f_i}\phi^*_{iq} + \phi_{iq}\gamma^*_{q,f_i}}{2||\boldsymbol{\phi}_q||_2} \tag{A.15}$$

Replace (A.15) into (A.11):

$$\begin{aligned}\Delta v_{i,q_1,q_2} = &\frac{\gamma_{q_1,f_i}\phi^*_{iq_1} + \phi_{iq_1}\gamma^*_{q_1,f_i}}{2||\boldsymbol{\phi}_{q_1}||_2}||\boldsymbol{\phi}_{q_2}||_2 + \\ &\frac{\gamma_{q_2,f_i}\phi^*_{iq_2} + \phi_{iq_2}\gamma^*_{q_2,f_i}}{2||\boldsymbol{\phi}_{q_2}||_2}||\boldsymbol{\phi}_{q_1}||_2\end{aligned} \tag{A.16}$$

A.2 Derivative of E(τ_i) w.r.t. τ_i

$$\nabla E_{\tau_i} = \frac{\partial E}{\partial \tau_i} \tag{A.17}$$

$$= \sum_{q_1=1, q_1\neq q_2}^{N}\sum_{q_2=1}^{N}\frac{\partial}{\partial f_i}c_{q_1q_2}c^*_{q_1q_2} \tag{A.18}$$

$$= \sum_{q_1=1, q_1\neq q_2}^{N}\sum_{q_2=1}^{N}\Delta E_{q_1,q_2,\tau_i} \tag{A.19}$$

The computation of $\Delta E_{q_1,q_2,\tau_i}$ is similar to the computation of $\Delta E_{q_1,q_2,f_i}$ from (A.5)-(A.16) but γ_{q,f_i} is replaced by $\gamma_{q,\tau_i} = \sum_{l=-L}^{L} c_l d^*_l(jl)e^{-j2\pi l f_i q\Delta t + jl\tau_i}$.

Bibliography

[1] G. Alenyà, S. Foix, and C. Torras, "Tof cameras for active vision in robotics," *Sensors and Actuators A: Physical*, vol. 218, pp. 10–22, 2014.

[2] R. Lange, *3D Time-of-Flight Distance Measurement with Custom Solid-State Image Sensors in CMOS/CCD-Technology*. PhD thesis, University of Siegen, 2000.

[3] A. Kolb, E. Barth, R. Koch, and R. Larsen, "Time-of-Flight Cameras in Computer Graphics," *Computer Graphics Forum*, 2010.

[4] T. M. B. B. H. Kraft, J. Frey, "3D-Camera of High 3D-Frame Rate, Depth-Resolution and Background Light Elimination Based on Improved PMD (Photonic Mixer Device)-Technologies ," tech. rep., PMDTechnologies GmbH, 2004.

[5] T. Instruments, *Introduction to the Time-of-Flight(ToF) System Design*. Texas Instruments, 2014.

[6] A. Bhandari, A. Kadambi, R. Whyte, C. Barsi, M. Feigin, A. A. Dorrington, and R. Raskar, "Resolving multi-path interference in time-of-flight imaging via modulation frequency diversity and sparse regularization," *CoRR*, vol. abs/1404.1116, 2014.

[7] M. Feigin, R. Whyte, A. Bhandari, A. Dorington, and R. Raskar, "Modeling wiggling as a multi-path interference problem in amcw tof imaging," *Opt. Express*, no. 15, pp. 19213–19225, 2015.

[8] S. Fuchs, "Multipath interference compensation in time-of-flight camera images," in *20th International Conference on Pattern Recognition, ICPR 2010, Istanbul, Turkey, 23-26 August 2010*, pp. 3583–3586, 2010.

[9] R. Whyte, L. Streeter, M. J. Cree, and A. A. Dorrington, "Resolving multiple propagation paths in time of flight range cameras using direct and global separation methods," *Optical Engineering*, vol. 54, no. 11, p. 113109, 2015.

[10] D. Jimenez, D. Pizarro, M. Mazo, and S. Palazuelos, "Modelling and correction of multipath interference in time of flight cameras," in *2012 IEEE Conference on Computer Vision and Pattern Recognition*, pp. 893–900, June 2012.

[11] F. Heide, M. B. Hullin, J. Gregson, and W. Heidrich, "Low-budget transient imaging using photonic mixer devices," *ACM Trans. Graph.*, vol. 32, July 2013.

[12] M. Feigin, A. Bhandari, S. Izadi, C. Rhemann, M. Schmidt, and R. Raskar, "Resolving multipath interference in kinect: An inverse problem approach," *IEEE Sensors Journal*, vol. 16, no. 10, pp. 3419–3427, 2016.

[13] A. Kadambi, R. Whyte, A. Bhandari, L. Streeter, C. Barsi, A. Dorrington, and R. Raskar, "Coded time of flight cameras: Sparse deconvolution to address multipath interference and recover time profiles," *ACM Trans. Graph.*, vol. 32, pp. 167:1–167:10, Nov. 2013.

[14] A. A. Dorrington, J. P. Godbaz, M. J. Cree, A. D. Payne, and L. V. Streeter, "Separating true range measurements from multi-path and scattering interference in commercial range cameras," 2011.

[15] V. N. Xuan, K. Hartmann, W. Weihs, and O. Loffeld, "Multi-target super-resolution using compressive sensing arguments for multipath interference recovery," in *2016 4th International Workshop on Compressed Sensing Theory and its Applications to Radar, Sonar and Remote Sensing (CoSeRa)*, pp. 148–152, 2016.

[16] G. A. Howland, D. J. Lum, M. R. Ware, and J. C. Howell, "Photon counting compressive depth mapping," *Opt. Express*, vol. 21, pp. 23822–23837, Oct 2013.

[17] M. Heredia Conde, K. Hartmann, and O. Loffeld, "A compressed sensing framework for accurate and robust waveform reconstruction and phase retrieval using the photonic mixer device," *IEEE Photonics Journal*, vol. 7, no. 3, pp. 1–16, 2015.

[18] A. Seel, A. Davtyan, U. Pietsch, and O. Loffeld, "Norm-minimized scattering data from intensities," in *2016 International Conference on Communications (COMM)*, pp. 455–460, 2016.

[19] E. J. Candes, J. Romberg, and T. Tao, "Robust uncertainty principles: exact signal reconstruction from highly incomplete frequency information," *IEEE Transactions on Information Theory*, 2006.

[20] H. Stahl, J. Mietzner, and R. F. H. Fischer, "A sub-nyquist radar system based on optimized sensing matrices derived via sparse rulers," in *Compressed Sensing Theory and its Applications to Radar, Sonar and Remote Sensing (CoSeRa), 2015 3rd International Workshop on*, pp. 36–40, 2015.

[21] A. Fannjiang and W. Liao, "Mismatch and resolution in compressive imaging," *CoRR*, vol. abs/1109.0660, 2011.

[22] E. J. Candès and C. Fernandez-Granda, "Towards a mathematical theory of super-resolution," *CoRR*, vol. abs/1203.5871, 2012.

[23] J. Fang, H. Duan, J. Li, H. Li, and R. S. Blum, "Super-resolution compressed sensing: A generalized iterative reweighted L2 approach," *CoRR*, vol. abs/1412.2477, 2014.

[24] V. N. Xuan, K. Hartmann, W. Weihs, and O. Loffeld, "Combined based on minimum distance orthogonal matching pursuit method for support recovery improvement in super-resolution compressed sensing," in *2016 4th International Workshop on Compressed Sensing Theory and its Applications to Radar, Sonar and Remote Sensing (CoSeRa)*, pp. 257–261, 2016.

[25] E. J. Candes and M. B. Wakin, "An introduction to compressive sampling," *IEEE Signal Processing Magazine*, vol. 25, pp. 21–30, March 2008.

[26] D. L. Donoho and X. Huo, "Uncertainty principles and ideal atomic decomposition," *IEEE Transactions on Information Theory*, vol. 47, no. 7, pp. 2845–2862, 2001.

[27] J. Chen and X. Huo, "Theoretical results on sparse representations of multiple-measurement vectors," *IEEE Transactions on Signal Processing*, vol. 54, no. 12, pp. 4634–4643, 2006.

[28] J. Ding, L. Chen, and Y. Gu, "Robustness of orthogonal matching pursuit for multiple measurement vectors in noisy scenario," in *2012 IEEE International Conference on Acoustics, Speech and Signal Processing (ICASSP)*, pp. 3813–3816, 2012.

[29] A. D. Payne, A. P. Jongenelen, D. A. A. Dorrington, M. J. Cree, and P. D. A. Carnegie, "Multiple frequency range imaging to remove measurement ambiguity," in *9th Conference on Optical 3-D Measurement Techniques*, pp. 139 – 148, 2009.

[30] V. Abolghasemi, S. Ferdowsi, B. Makkiabadi, and S. Sanei, "On optimization of the measurement matrix for compressive sensing," in *Signal Processing Conference, 2010 18th European*, pp. 427–431, 2010.

[31] M. D. Adams, "Coaxial range measurement - current trends for mobile robotic applications," *IEEE Sensors Journal*, vol. 2, pp. 2–13, Feb 2002.

[32] R. Horaud, M. E. Hansard, G. D. Evangelidis, and C. Ménier, "An overview of depth cameras and range scanners based on time-of-flight technologies," *Mach. Vis. Appl.*, vol. 27, no. 7, pp. 1005–1020, 2016.

[33] S. B. Gokturk, H. Yalcin, and C. Bamji, "A time-of-flight depth sensor - system description, issues and solutions," in *2004 Conference on Computer Vision and Pattern Recognition Workshop*, pp. 35–35, June 2004.

[34] G. J. Iddan and G. Yahav, "Three-dimensional imaging in the studio and elsewhere," in *Proceedings of the Conference on Three-Dimensional Image Capture and Applications IV, San Jose, CA, USA, January 20, 2001*, pp. 48–55, 2001.

[35] Y. Surrel, "Design of algorithms for phase measurements by the use of phase stepping," *Appl. Opt.*, vol. 35, pp. 51–60, Jan 1996.

[36] Z. M. Daniel Malacara, Manuel Servin, *Interferogram Analysis for Optical Testing Second Edition*. 2005.

[37] M. Lindner and A. Kolb, *Lateral and Depth Calibration of PMD-Distance Sensors*, pp. 524–533. Berlin, Heidelberg: Springer Berlin Heidelberg, 2006.

[38] T. Kahlmann, F. Remondino, and H. Ingensand, "Calibration for increased accuracy of the range imaging camera SwissRanger," in *International Archives of Photogrammetry, Remote Sensing and Spatial Information Sciences,* (Isprs, ed.), vol. Vol. XXXVI, (Dresden, Germany), 2006.

[39] A. D. Payne, A. A. Dorrington, M. J. Cree, and D. A. Carnegie, "Improved linearity using harmonic error rejection in a full-field range imaging system," in *Proceedings of the Conference on Three-Dimensional Image Capture and Applications 2008, San Jose, CA, USA, January 28-29, 2008*, p. 68050D, 2008.

[40] A. D. Payne, A. A. Dorrington, and M. J. Cree, "Illumination waveform optimization for time-of-flight range imaging cameras," 2011.

[41] V. N. Xuan, W. Weihs, and O. Loffeld, "Illumination, phase step optimization and improvements in simultaneous multiple frequency measurement for time-of-flight sensors," in *2015 International Conference on 3D Imaging (IC3D)*, pp. 1–6, Dec 2015.

[42] L. Li, "Filtering for 3d time-of-flight sensors," tech. rep., Texas Instruments, 01 2016.

[43] D. Droeschel, D. Holz, and S. Behnke, "Multi-frequency phase unwrapping for time-of-flight cameras," in *2010 IEEE/RSJ International Conference on Intelligent Robots and Systems*, pp. 1463–1469, 2010.

[44] D. Freedman, E. Krupka, Y. Smolin, I. Leichter, and M. Schmidt, "SRA: fast removal of general multipath for tof sensors," *CoRR*, vol. abs/1403.5919, 2014.

[45] M. F. Duarte and Y. C. Eldar, "Structured compressed sensing: From theory to applications," *IEEE Transactions on Signal Processing*, vol. 59, no. 9, pp. 4053–4085, 2011.

[46] H. Rauhut, "Compressive sensing and structured random matrices," *Theoretical Foundations and Numerical Methods for Sparse Recovery, De Gruyter, Radon Series Comp. Appl. Math.*, 2011.

[47] S. S. Chen, D. L. Donoho, and M. A. Saunders, "Atomic decomposition by basis pursuit," *SIAM Rev.*, vol. 43, pp. 129–159, Jan. 2001.

[48] E. J. Candes and T. Tao, "Decoding by linear programming," *IEEE Transactions on Information Theory*, vol. 51, pp. 4203–4215, Dec 2005.

[49] E. Candes, "The restricted isometry property and its implications for compressed sensing," *Comptes Rendus Mathematique*, vol. 346, pp. 589–592, May 2008.

[50] P. Xia, S. Zhou, and G. Giannakis, *Achieving the Welch bound with difference sets*, vol. III. Institute of Electrical and Electronics Engineers Inc., 2005.

[51] D. L. Donoho and M. Elad, "Optimally sparse representation in general (non-orthogonal) dictionaries via l1 minimization," in *PROC. NATL ACAD. SCI. USA 100 2197,Äi202*, 2002.

[52] J. A. Tropp, "Greed is good: algorithmic results for sparse approximation," *IEEE Transactions on Information Theory*, vol. 50, pp. 2231–2242, Oct 2004.

[53] M. Heredia Conde and O. Loffeld, "Fast approximate construction of best complex antipodal spherical codes," *ArXiv e-prints*, p. 23, 2017.

[54] H. Zörlein and M. Bossert, "Coherence optimization and best complex antipodal spherical codes," *CoRR*, vol. abs/1404.5889, 2014.

[55] W. Yin, S. Osher, D. Goldfarb, and J. Darbon, "Bregman iterative algorithms for l1-minimization with applications to compressed sensing," *SIAM J. Img. Sci.*, vol. 1, pp. 143–168, Mar. 2008.

[56] E. van den Berg and M. P. Friedlander, "Probing the pareto frontier for basis pursuit solutions," *SIAM J. Sci. Comput.*, vol. 31, pp. 890–912, Nov. 2008.

[57] R. Tibshirani, "Regression shrinkage and selection via the lasso," *Journal of the Royal Statistical Society, Series B*, vol. 58, pp. 267–288, 1994.

[58] Y. Nesterov, "Smooth minimization of non-smooth functions," *Math. Program.*, vol. 103, pp. 127–152, May 2005.

[59] J. Yang and Y. Zhang, "Alternating direction algorithms for l1-problems in compressive sensing," *SIAM J. Sci. Comput.*, vol. 33, no. 1, pp. 250–278, 2011.

[60] O. Loffeld, A. Seel, M. Heredia Conde, and L. Wang, "A nullspace based l1 minimizing kalman filter approach to sparse cs reconstruction," in *11th European Conference on Synthetic Aperture Radar (EUSAR 2016)*, pp. 1–5, 2016.

[61] D. Needell, "Topics in compressed sensing," *CoRR*, vol. abs/0905.4482, 2009.

[62] T. T. Cai and L. Wang, "Orthogonal matching pursuit for sparse signal recovery with noise," *IEEE Trans. Information Theory*, vol. 57, no. 7, pp. 4680–4688, 2011.

[63] D. L. Donoho, "Superresolution via sparsity constraints," *SIAM Journal on Mathematical Analysis*, vol. 23, no. 5, pp. 1309–1331, 1992.

[64] T. Instruments, "Introduction to the Time-of-Flight (ToF) System Design," tech. rep., Texas Instruments, 2012.

[65] E. Candes and J. Romberg, "Sparsity and incoherence in compressive sampling," 2006.

[66] A. Fannjiang and W. Liao, "Coherence-pattern guided compressive sensing with unresolved grids," *CoRR*, vol. abs/1106.5177, 2011.

[67] B. L. Sturm, M. G. Christensen, and R. Gribonval, "Cyclic pure greedy algorithms for recovering compressively sampled sparse signals," in *Conference Record of the Forty Fifth Asilomar Conference on Signals, Systems and Computers, ACSCC 2011, Pacific Grove, CA, USA, November 6-9, 2011*, pp. 1143–1147, 2011.

[68] C. L. Lawson and R. J. Hanson, *Solving least squares problems*, vol. 15 of *Classics in Applied Mathematics*. Philadelphia, PA: Society for Industrial and Applied Mathematics (SIAM), 1995. Revised reprint of the 1974 original.

[69] S. D. Cohen, "Generators in cyclic difference sets," *Journal of Combinatorial Theory, Series A*, vol. 51, no. 2, pp. 227 – 236, 1989.

[70] B. I. F. Gorodnitsky, J. S.George, "Neuromagnetic source imaging with focuss: a recursive weighted minimum norm algorithm," *Electroencephalography and Clinical Neurophysiology*, vol. 95, no. 4, pp. 231–251, 1995.

[71] S. F. Cotter, B. D. Rao, K. Engan, and K. Kreutz-Delgado, "Sparse solutions to linear inverse problems with multiple measurement vectors," *IEEE Transactions on Signal Processing*, vol. 53, no. 7, pp. 2477–2488, 2005.

[72] Q. Ling and Z. Tian, "Decentralized support detection of multiple measurement vectors with joint sparsity," in *2011 IEEE International Conference on Acoustics, Speech and Signal Processing (ICASSP)*, pp. 2996–2999, 2011.

[73] J. Chen and X. Huo, "Sparse representations for multiple measurement vectors (mmv) in an over-complete dictionary," in *Proceedings. (ICASSP '05). IEEE International Conference on Acoustics, Speech, and Signal Processing, 2005.*, vol. 4, pp. iv/257–iv/260 Vol. 4, March 2005.

[74] J. Yang, A. Bouzerdoum, F. H. C. Tivive, and M. G. Amin, "Multiple-measurement vector model and its application to through-the-wall radar imaging," in *2011 IEEE International Conference on Acoustics, Speech and Signal Processing (ICASSP)*, pp. 2672–2675, May 2011.

[75] E. Hecht, *Optics, 2nd Edition*. Addison-Wesley, 1987.

[76] J. Ding, L. Chen, and Y. Gu, "Performance of orthogonal matching pursuit for multiple measurement vectors," *CoRR*, vol. abs/1109.6390, 2011.

[77] T. Hong, S. Li, H. Bai, and Z. Zhu, "An efficient algorithm for designing projection matrix in compressive sensing based on alternating optimization," vol. 125, 01 2016.

[78] Q. Li, Z. Zhu, S. Tang, L. Chang, and G. Li, "Projection matrix optimization based on svd for compressive sensing systems," in *Proceedings of the 32nd Chinese Control Conference*, pp. 4820–4825, July 2013.

[79] G. Li, Z. Zhu, D. Yang, L. Chang, and H. Bai, "On projection matrix optimization for compressive sensing systems," *IEEE Transactions on Signal Processing*, vol. 61, pp. 2887–2898, June 2013.

[80] G. Fornaro, A. M. Guarnieri, A. Pauciullo, and S. Tebaldini, "Joint multi-baseline sar interferometry," *EURASIP Journal on Advances in Signal Processing*, vol. 2005, no. 20, p. 186503, 2005.

Selbständigkeitserklärung

Ich erkläre, dass ich die vorliegende Arbeit selbständig und nur unter Verwendung der angegebenen Literatur und Hilfsmittel angefertigt habe.

Siegen, den 11. Dezember 2017 Vinh Nguyen Xuan